FABRICATION AND CHARACTERIZATION OF NANOSCALE PERIODIC FERROMAGNETIC STRUCTURES ON SUPERCONDUCTING THIN FILMS

A Dissertation

by

WONBAE BANG

Submitted to the Office of Graduate and Professional Studies of
Texas A&M University
in partial fulfillment of the requirements for the degree of

DOCTOR OF PHILOSOPHY

Chair of Committee,	Winfried Teizer
Committee Members,	Igor F. Lyuksyutov
	Donald G. Naugle
	Haiyan Wang
Head of Department,	George R. Welch

August 2015

Major Subject: Physics

ABSTRACT

This research investigates the transport properties of ferromagnetic nanostructures made by nickel or cobalt on superconducting thin films. The superconducting thin films were covered by an insulating layer, and the periodic ferromagnetic nanostructures were fabricated on top of the insulating layer. On separate superconducting thin films, periodic ferromagnetic nanostructures were embedded into the thin films. The photolithography method was used to make contact pads for a four-probe measurement. In order to fabricate the magnetic nanostructures, an Electron Beam Lithography (EBL) system was utilized. The nanoscale patterns were filled with ferromagnetic materials by using a thermal evaporating method or an electroplating technique. The superconducting properties were measured at low temperature (2.0 K<T<8.0 K) for low temperature superconductors and at high temperature (85.0 K<T<90.0 K) for high temperature superconductors with a Physical Property Measurement System (PPMS). Scanning Electron Microscopy (SEM) and an Atomic Force Microscopy (AFM) were used to characterize the nanoscale structures. Magnetic Force Microscopy (MFM) was also used to study their magnetic properties.

Superconductivity and ferromagnetism seems mutually exclusive states, however the superconducting and the ferromagnetic states show new and exciting properties when the two states affect each other at the nanoscale: hysteresis and enhanced superconductivity. Both the ferromagnetic nanostructures on the superconducting thin films and the embedded ferromagnetic nanosized arrays in the superconducting thin films exhibited an enhanced critical current density and critical magnetic field. Both of the samples also showed hysteresis and a field matching effect by the artificial ferromagnetic nanostructures when an external magnetic field was applied.

The superconducting thin films with the ferromagnetic nanostructures system may be useful for power cable and other low magnetic field applications.

DEDICATION

I dedicate my dissertation to my loving parents and brother for their unstinting support. I specially dedicate this dissertation to my precious wife and daughter; their words greatly encouraged me throughout the entire doctorate program.

ACKNOWLEDGEMENTS

I am deeply grateful to my advisor Dr. Winfried Teizer for his great advice and skills as a scientist. I would like to thank Dr. Igor F. Lyuksyutov for sharing his deep theoretical knowledge and offering financial support for my interesting research. Moreover, I would like to thank my committee members Dr. Donald G. Naugle, and Dr. Haiyan Wang for their valuable ideas and time for my research. I would also like to thank many people for their cooperation: Dr. Sung Oh Woo, Dr. Kyongwan Kim, Dr. Kelley T. Reaves, Andrew L. Liao, and Jaehyoung Son from the Nanolab. Finally, I would like to thank Dr. K. D. D. Rathnayaka and Tyler D. Morrison in Dr. Naugle's lab for their kind technical assistance.

NOMENCLATURE

FSH	Ferromagnet-Superconductor Hybrid
BCS	Bardeen, Cooper, and Schrieffer
λ	London penetration depth
ξ	Coherence length
κ	Ginzburg-Landau parameter
MR	Magnetoresistance
LTS	Low temperature superconductors
HTS	High temperature superconductors
PPMS	Physical Property Measurement System
EBL	Electron Beam Lithography
NPGS	Nanometer Pattern Generation System
SEM	Scanning Electron Microscope
AFM	Atomic Force Microscopy
MFM	Magneto Force Microscopy
VSM	Vibrating Sample Magnetometer
PMMA	Polymeathyl metacrylate
IPA	Isopropyl alcohol
PR	Photoresist
UV	Ultraviolet
MIBK	Methyl Isobutyl Ketone

SCE	Saturated Calomel Electrode
Ag/AgCl	Silver-Silver Chloride Electrode
WE	Working electrode
CE	Counter electrode
RE	Reference electrode
DI water	Deionized water
T_C	Critical temperature
I_C	Critical current
J_C	Critical current density
H_{C2}	Second critical field
R	Resistance
T/T_C	Reduced temperature
l	Mean free path
ρ	Resistivity
$YBa_2Cu_3O_{7-\delta}$	YBCO
$SrTiO_3$	STO

TABLE OF CONTENTS

Page

LIST OF FIGURES

LIST OF TABLES

1. INTRODUCTION*

In 1911, superconductivity was first observed in mercury by Kamerlingh Onnes in Leiden, Netherlands. The superconducting phenomenon is a ground-breaking scientific discovery. Many materials with superconducting properties are significant in solid state physics research. This surprising discovery entails that the electrical resistivity of many metals and alloys drops abruptly to zero when the specimen is cooled to a sufficiently low temperature [1]. Moreover, the superconducting phenomenon depends on the critical current (I_C) and the critical magnetic field (H_C) of the materials [1-5]. Even though superconductors have to be cooled to retain superconductivity, superconductor technology can be employed for sensitive devices for detection or measurements such as Superconducting QUantum Interference Device (SQUID), Magnetic Resonance Imaging (MRI), and Nuclear Magneto Resonance (NMR) [1, 2, 4].

Scientists have spent much time and effort researching superconductivity for over a century. In particular, superconductivity and its coexistence with ferromagnetic systems have been studied both theoretically and experimentally. Superconductivity and ferromagnetism seem to be mutually exclusive states. However, they show interesting

---

* Part of the data reported in this subchapter is reprinted with permission from "Instability-driven formation of domains in the intermediate state of type-I superconductors" by V. Jeudy and C. Gourdon, 2006. *Europhys. Lett.*, **75** (3), pp. 482-489, Copyright [2010] by EDP sciences

* Part of the data reported in this subchapter is reprinted with permission from "The direct observation of individual flux lines in type II superconductors" by U. Essmann and H. Träuble, 1967. *Phys. Lett.*, 24A (10), 526-527, Copyright [2015] by Elsevier

* Reprinted with permission from Introduction to Magnetic Materials, by B. D. Cullity and C. D. Graham, 2008, John Wiley and Sons, Inc., Hoboken, New Jersey. Copyright [2009] by the Institute of Electrical and Electronics Engineers, Inc.

properties when they coexist in a nanoscale system, such as hysteresis and enhanced superconductivity [6, 7].

One of the fascinating issues for potential applications in this area is the control and reduction of the dissipation of superconducting properties produced by vortex motion in the superconducting thin films. Vortex pinning has been an interesting subject in the field of superconductivity because the vortex pinning phenomenon can be determined by size and geometry of ferromagnetic structures, thickness modulation of the superconducting thin films, or magnetic particles. Thus, the vortex dynamics may act in association with the matching of the vortex lattice and artificial structures.

The studies of the vortex motion in Ferromagnet-Superconductor Hybrid (FSH) systems were focused on magnetic fields from magnetic dots (shaped like coins) array or magnetic films [6-9]. The ferromagnetic structures of the systems in the studies were directly created on the superconducting thin films. In this case, it is not easy to understand what contributions of the mechanism, such as proximity effect, magnetic interaction, or mechanical distortion, affect the observed anisotropy in the FSH systems [6-8, 10, 11]. In contrast to the previous studies, in this work superconducting thin films in FSH systems will be isolated from ferromagnetic nanostructures by a deposited insulating layer to avoid the proximity effect and mechanical distortion. However, in case of embedded FSH systems, ferromagnetic nanostructures interface the superconducting thin films directly without being separated by an insulating layer.

Even though thin film devices are made from the same superconducting materials, small variations in its fabrication process might significantly change the properties of the devices. The enhancement of the superconducting thin film devices provides an opportunity to understand the intrinsic properties of the materials from which they are made. Advanced techniques for nanostructure fabrication have allowed two characteristic lengths of superconducting materials, the coherence length ξ and the penetration depth λ, to be comparable to the thickness of superconducting thin films and the geometry of artificial periodic nanosized arrays.

A superconducting power cable provides a higher efficiency than a conventional cable because it does not generate electrical losses and heat. If a ferromagnetic structure is fabricated on the superconducting power cable, it enhances the control of the power cable's superconducting properties. In addition, enhanced efficiency may be expected in the superconducting power cable.

1.1 Type I superconductors

Superconductors are classified in two types, type I superconductors and type II superconductors, depending on their behavior in an external magnetic field.

In 1933, Meissner and Ochsenfeld found that if a normal metal sample is cooled below its transition temperature, the sample excludes the magnetic field. Also, they discovered that a magnetic field is excluded from entering a superconductor [1, 2, 5].

If a superconducting sample maintains $B = 0$ (where B is the magnetic flux density) inside the sample, this is called the Meissner effect

$$B = H + 4\pi M = 0 \quad \text{(in cgs unit)} \tag{1}$$

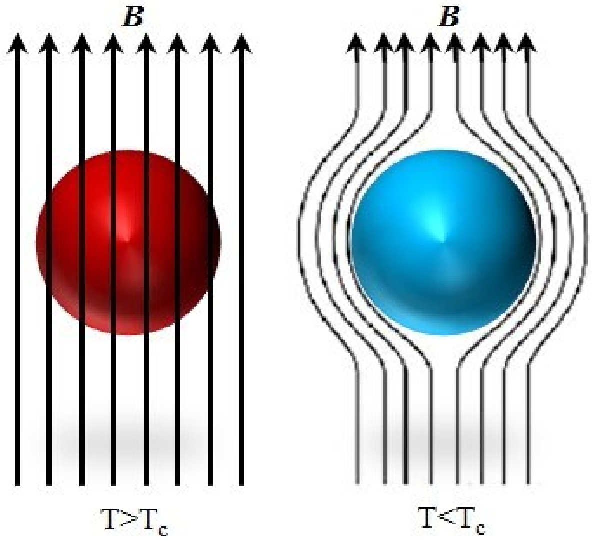

Figure 1. Schematics of constant magnetic field lines on a spherical superconductor above its transition temperature (a) and expelled magnetic field by the superconductor below its transition temperature (b).

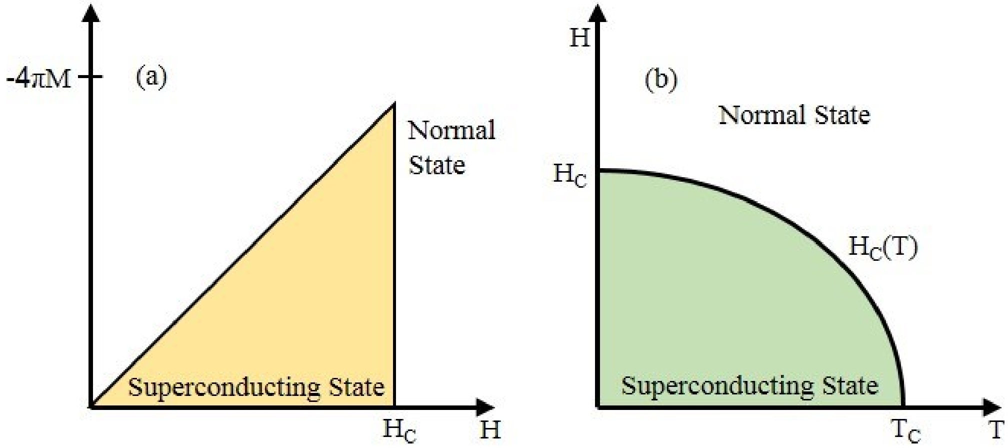

Figure 2. Magnetization as a function of external magnetic field of type I superconductors (a) and critical magnetic field as a function of temperature of type I superconductors (b).

where H is the external magnetic field and M is the magnetization. The Meissner effect is displayed in Figure 1.

The existence of the Meissner effect implies that the superconducting property can be destroyed by H_C. Many pure materials have this property; they are called type I superconductors or soft superconductors. Figure 2 (a) shows that type I superconductors have a sudden transition at their H_C when they are placed in an external magnetic field. Type I superconductors display the superconducting phenomenon (or Meissner effect) below their H_C and lose the superconductivity above the H_C. Temperature also plays a key role in type I superconductors can be seen in Figure 2 (b), which explains that type I superconductors return to their normal state when the external magnetic field increases above their $H_C(T)$ [1, 4, 5].

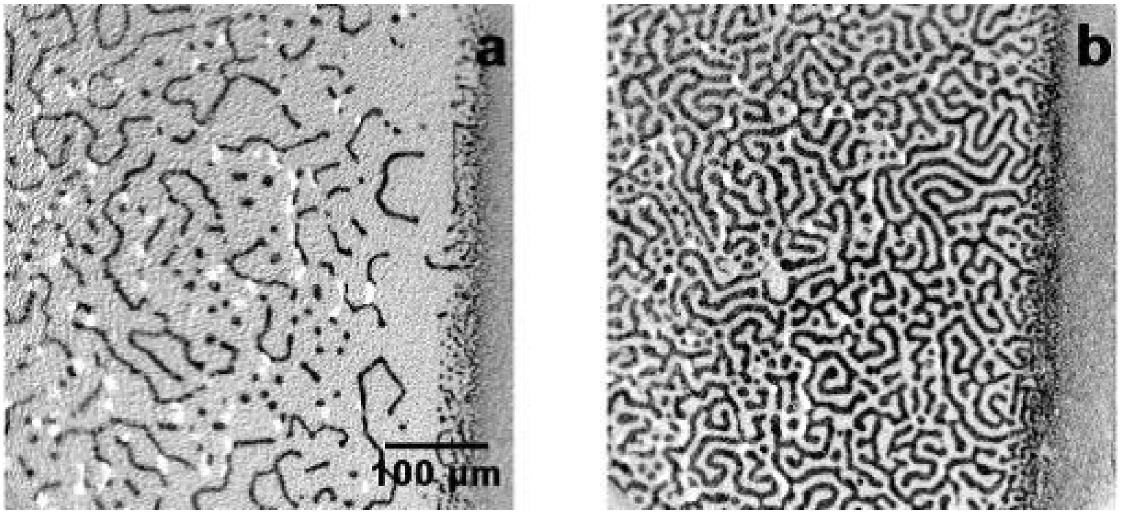

Figure 3. Magneto-optical images of the intermediate state; h=0.105 (a) and h=0.345 (b) (reprinted with permission) [13].

Type I superconductors show an intermediate state that is formed by long meander lamellae and normal state flux tubes [12-14]. The intermediate state in type I superconductors depends on the demagnetizing factor or shape of the specimens such as thin films [5]. Figure 3 illustrates example images of the intermediate state in type I superconductors by magneto-optical imaging technique. The sample is a 10 μm thick In film with different external magnetic fields; h=0.105 (a) and h=0.345 (b). h (reduced applied field) and $H_C(T)$ are defined by

$$h = \frac{H_0}{H_c(T)} \tag{2}$$

$$H_C(T) = H_C(0)\left[1 - \left(\frac{T}{T_C}\right)^2\right] \tag{3}$$

where T_C is its critical temperature or transition temperature [13]. T_C of the sample is 3.41 K.

1.2 Type II superconductors

The other type of superconductor is called a type II superconductor. As an external magnetic field is applied, type II superconductors start to gradually lose their superconductivity at the lower critical magnetic field H_{C1}. In accordance with this property, type II superconductors are also called hard superconductors. Alloys are commonly type II superconductors. Moreover, type I superconductors can become to type II superconductors when alloyed [1, 2, 5]. At the upper critical magnetic field H_{C2}, superconductivity in the sample is completely lost, and the sample becomes a normal conductor above H_{C2}, as shown in Figure 4 (a).

The region between H_{C1} and H_{C2} is the mixed state or vortex state. In this phase, the normal state and the superconducting state of the materials coexist, and the external magnetic field partially penetrates into the thin samples in uniform vortices, as shown in Figure 5 [1, 2, 5, 15].

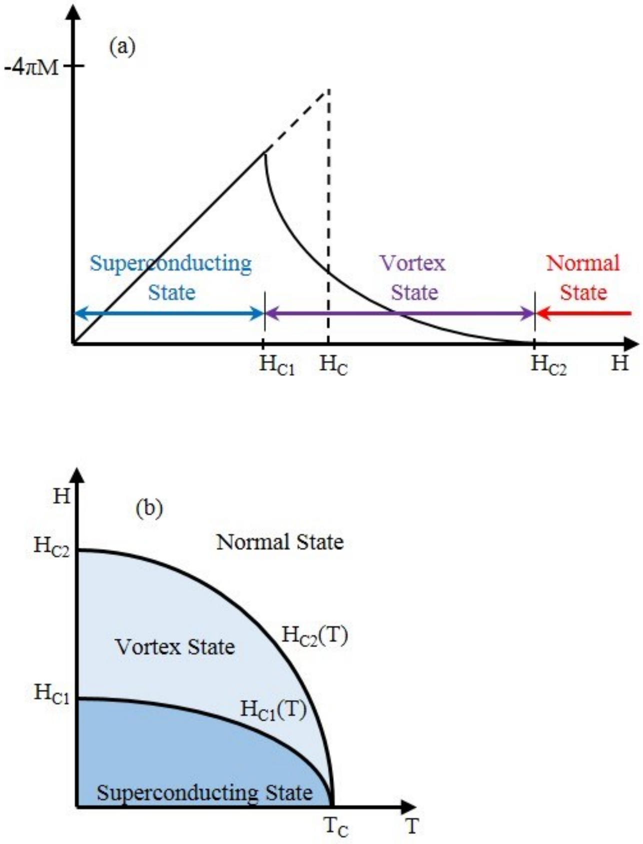

Figure 4. Magnetization as a function of external magnetic field of type II superconductors (a) and H_Cs as a function of temperature of type II superconductors (b).

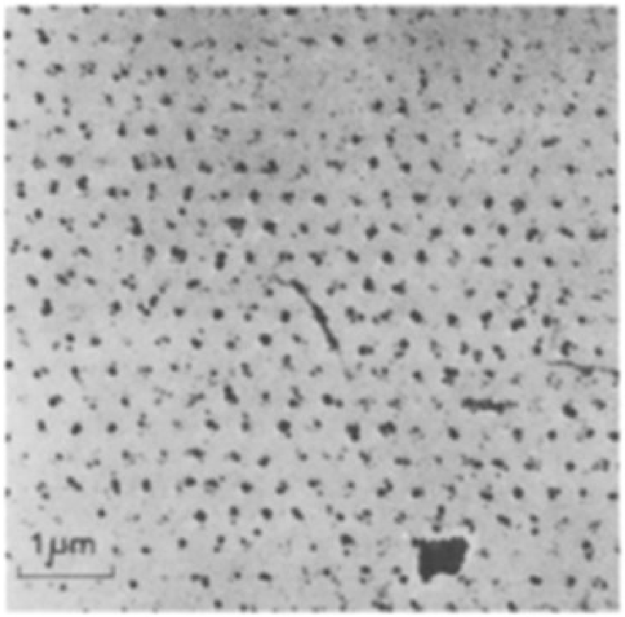

Figure 5. An image of triangular lattice of flux lines on the surface of a Pb-4%In rod at 1.1 K (reprinted with permission) [15].

1.3 Two characteristic lengths

This subchapter introduces two significant characteristic lengths in superconductors that will play an important role in the analyses of superconducting thin films.

One of the characteristic lengths in superconductors is the coherence length ξ. This ξ is an essential length to characterize superconductors. ξ measures the distance within which the superconducting electron concentration cannot change drastically [1]. Furthermore, ξ determines the radius of vortex core.

Equations (4) and (5) are the Ginzburg-Landau differential equations [5].

$$\alpha\psi + \beta|\psi|^2\psi + \frac{1}{2m^*}\left(\frac{\hbar}{i}\nabla - \frac{e^*}{c}\boldsymbol{A}\right)^2 \psi = 0 \tag{4}$$

$$\boldsymbol{J} = \frac{e^*\hbar}{2m^*i}(\psi^*\nabla\psi - \psi\nabla\psi^*) - \frac{e^{*2}}{m^*c}\psi^*\psi\boldsymbol{A} \tag{5}$$

where e^* is the charge of a superconducting electron pair (2e), m^* is the mass of a superconducting electron pair (2m), and $\hbar$ is the reduced Planck's constant. In order to simplify equation (4), fields are assumed to be zero, and ψ are assumed to be real. Equation (4) then becomes

$$\frac{\hbar^2}{2m^*|\alpha|}\frac{d^2f}{dx^2} + f - f^3 = 0 \tag{6}$$

where $f = \frac{\psi}{\psi_\infty}$ (a normalized wavefunction) and $\psi_\infty^2 = -\frac{\alpha}{\beta} > 0$. Equation (6) makes ξ, which is called the Ginzburg-Landau coherence length

$$\xi(T) = \left(\frac{\hbar^2}{2m^*\alpha(T)}\right)^{\frac{1}{2}} \tag{7}$$

where α is an expansion coefficient [5]. The electric current density in this theory is

$$\boldsymbol{J} = \frac{ne^*}{m^*}\left(\hbar\nabla\varphi - \frac{e^*}{c}\boldsymbol{A}\right) \tag{8}$$

where φ is the phase of field and $\boldsymbol{A}$ is a vector potential. When the curl of both sides is employed in equation (8) to obtain the London equation, the electric current density is given by

$$\nabla \times \boldsymbol{J} = -\frac{ne^{*2}}{m^*c}\boldsymbol{B} \tag{9}$$

According to the Meissner effect, ***B*** and ***J*** are zero inside a superconductor. Therefore,

$$\hbar\nabla\varphi - \frac{e^*}{c}\boldsymbol{A} = 0 \tag{10}$$

By using the Stokes' theorem on equation (10), $\phi = \frac{2\pi\hbar cs}{e^*}$ is obtained. ϕ is the flux quantum in a superconductor. *s* is the multiplicity constant of $\frac{2\pi\hbar c}{e^*}$.

$$\phi_0 = \frac{2\pi\hbar c}{e^*} \cong 2.0678 \times 10^{-7}\text{gauss}\cdot\text{cm}^2 \quad \text{(in cgs unit)} \tag{11}$$

This flux quantum is also called a fluxon or fluxoid [1, 5].

Superconductors can be classified by the ratio $\frac{l}{\xi_0}$. l is the electron mean free path of a sample in the normal state. ξ_0 is an intrinsic coherence length at 0 K. If the mean free path of the sample is longer than the intrinsic coherence length ($l \gg \xi_0$), the sample is in the clean limit and can be described as a pure material. In contrast, if the mean free path of the sample is shorter than the intrinsic coherence length ($l \ll \xi_0$), the sample is in the dirty limit and can be described as an impure material [3]. By this characterization, equation (7) can be expressed as

$$\xi(T) = 0.74\frac{\xi_0}{(1-t)^{\frac{1}{2}}} \qquad \text{(clean limit)} \tag{12}$$

$$\xi(T) = 0.855\left(\frac{\xi_0 l}{1-t}\right)^{\frac{1}{2}} \qquad \text{(dirty limit)} \tag{13}$$

where *t* is $\frac{T}{T_C}$. Equation (12) is for the clean limit, and equation (13) is for the dirty limit.

Both in the clean and dirty limits $\xi(T)$ as a function of temperature fit equation (12) and (13) near T_C.

The other characteristic length is the penetration depth λ that is independent of ξ. It measures the depth of penetration of the magnetic fields. If thickness of a thin film sample is much less than the λ, an applied external magnetic field uniformly penetrates the thin film. This phenomenon indicates that the Meissner effect cannot be completed in the thin film. Equation (14) is another expression [1, 5] of the London equation

$$\boldsymbol{J} = -\frac{c}{4\pi\lambda_L^2}\boldsymbol{A} \tag{14}$$

By taking the curl of both sides, equation (14) then can be written as

$$\nabla \times \boldsymbol{J} = -\frac{c}{4\pi\lambda_L^2}\boldsymbol{B} \tag{15}$$

Finally, the London penetration depth λ_L (in cgs unit) is obtained by comparison with equation (9) and (15) which is given by

$$\lambda_L = \left(\frac{m^* c^2}{4\pi n e^{*2}}\right)^{\frac{1}{2}} \tag{16}$$

where n is the number density of superconducting electrons [1, 16].

The Bardeen, Cooper, and Schrieffer (BCS) theory [17] predicts that the penetration depth in the dirty limit ($l \ll \xi_0$) is given by

$$\lambda_{eff}(l, T) = \lambda_L(T)\left(\frac{\xi_0}{J(0,T)l}\right)^{\frac{1}{2}} \tag{17}$$

where the range of the function $J(0,T)$ is from 1 at $T \approx 0$ to 1.33 at $T \approx T_C$ [5]. Equation (17) can be written by

$$\lambda_{eff}(l, 0) = \lambda_L(0)\left(\frac{\xi_0}{l}\right)^{\frac{1}{2}} \tag{18}$$

at *T*=0 K. $\lambda_L(0)$ in equation (18) is the λ_L at 0 K [18]. In addition, λ also can be written in the clean limit for equation (19) and the dirty limit for equation (20) with coefficients determined from the BCS theory. These expressions are valid in the limit near T_C [5].

$$\lambda_L(T) = \frac{\lambda_L(0)}{[2(1-t)]^{\frac{1}{2}}} \qquad \text{(clean limit)} \qquad (19)$$

$$\lambda_{eff}(l,T) = \lambda_L(T)\left(\frac{\xi_0}{1.33l}\right)^{\frac{1}{2}} \qquad \text{(dirty limit)} \qquad (20)$$

Two critical magnetic fields H_{C1} and H_{C2} can be estimated by using λ, ξ, and the flux quantum [1, 5].

$$H_{C1} \cong \frac{\Phi_0}{\pi\lambda^2} \qquad (21)$$

$$H_{C2} \cong \frac{\Phi_0}{2\pi\xi^2} \qquad (22)$$

Furthermore, type I superconductors and type II superconductors can be classified by the ratio of $\kappa = \frac{\lambda}{\xi}$, which is called the Ginzburg-Landau parameter.

For $\kappa = \frac{\lambda}{\xi} < \frac{1}{\sqrt{2}}$, the surface energy of the boundary between the superconducting region and the normal region is positive. Therefore, the system will minimize the boundary area, and the magnetic field will be expelled from the material. This is known as a type I superconductor.

On the contrary, for $\kappa = \frac{\lambda}{\xi} > \frac{1}{\sqrt{2}}$ (i.e. the boundary between type I and II is at H_{C1}=H_{C2}), the boundary has negative surface energy. The material will be unstable and will break into small domains to maximize the boundary area. Therefore, the sample is distinguished as a type II superconductor [5, 19, 20]. Figures 6 (a) and (b) show dependences of the magnetic field *B* and the number of superconducting electrons n_s near the boundary of a superconductor with a normal material for two types of superconductors: type I and type II [1, 4, 5].

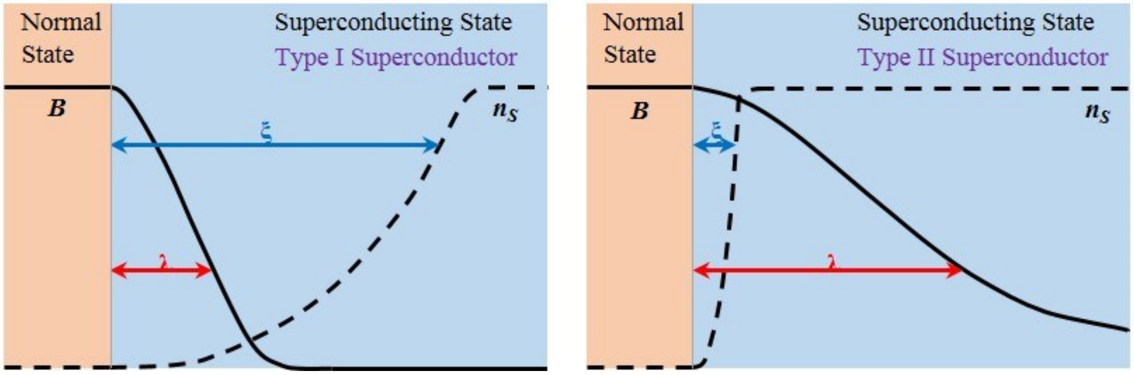

Figure 6. Variation of the magnetic field and the number of superconducting electrons for type I superconductors (a) and type II superconductors (b).

The history of superconducting materials is illustrated in Figure 7. Low temperature superconductors (LTS) are generally pure materials, and the LTS have relatively simple structures. κ is smaller than $\frac{1}{\sqrt{2}}$ in most LTS. This means that ξ of the LTS is greater than its λ. On the contrary, high temperature superconductors (HTS) are frequently cuprates that consist of copper-oxygen planes, for instance $YBa_2Cu_3O_{7-\delta}$

(YBCO), which was discovered in 1987 [21]. λ in the HTS is much larger than ξ, which means that κ is greater than $\frac{1}{\sqrt{2}}$ in the HTS.

In this research, Sn and $Pb_{82}Bi_{18}$ have been chosen as LTS and YBCO as HTS.

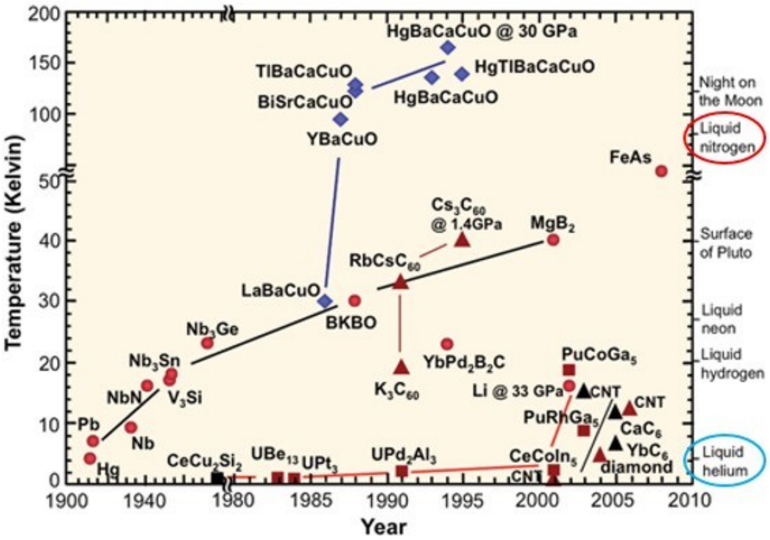

Figure 7. History of the superconductor materials [22].

1.4 Ferromagnetic materials

Ferromagnetism is one type of magnetism. A long range ordering phenomenon at the atomic level occurs in ferromagnetic materials such as Ni and Co. The phenomenon causes the unpaired spins of the atoms to line up parallel with each other in a domain. The magnetization of the randomly oriented domains tend to align with an external magnetic field, as shown in Figure 8. The magnetization of the ferromagnetic materials increases with the magnitude of the external magnetic field since ferromagnetic materials are composed of small domains where the vector sum is the total magnetic moment. The highest value of the magnetization is called the saturation magnetization (M_S). The magnetization of ferromagnetic materials is retained after the removal of the external magnetic field. They typically show some magnetization after being subjected to the external magnetic field, and they tend to remember their magnetic history. This property is called hysteresis.

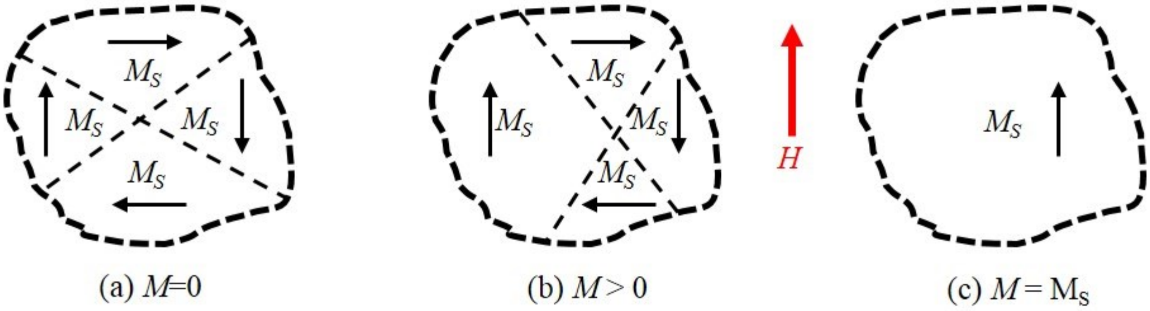

Figure 8. Magnetization by an external magnetic field (reprinted with permission) [23].

Magnetization depends on temperature. The relation between magnetization and temperature is determined by a quantum mechanical Brillouin function $B(J,a')$ [23, 24]. The relation can be expressed as

$$\frac{\sigma}{\sigma_0} = \frac{2J+1}{2J} coth\left(\frac{2J+1}{2J}\right) a' - \frac{1}{2J} coth\frac{a'}{2J} \tag{23}$$

where σ is the specific magnetization and σ_0 is the specific magnetization at 0 K. a' is $\frac{\mu_H H}{kt}$ where H is an external magnetic field, μ_H is a permeability at H, k is the Boltzmann constant, and t is temperature. The equation of the molecular field line is written as

$$\frac{\sigma}{\sigma_0} = \left(\frac{J+1}{3J}\right)\left(\frac{T}{T_{Curie}}\right)a' \tag{24}$$

where T_{Curie} is the Curie temperature. For special case, $J = \frac{1}{2}$ and after combining equation (23) and (24)

$$\frac{\sigma_S}{\sigma_0} = tanh\left(\frac{\frac{\sigma_S}{\sigma_0}}{\frac{T}{T_C}}\right) \tag{25}$$

Therefore, the magnetization of ferromagnetic materials increases with decrease of temperature below the Curie temperature [23].

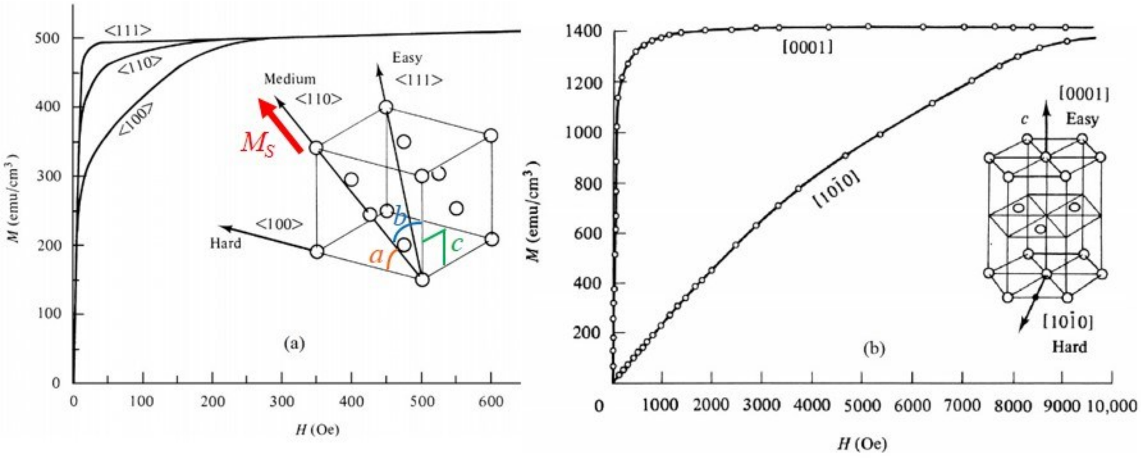

Figure 9. Magnetization curves of Ni single crystals (a) and Co single crystals (b) (reprinted with permission) [23].

Crystal anisotropy and shape anisotropy affect the magnetic properties in the shape of the *M-H* curves, as displayed in Figure 9 [23, 25, 26]. Knowledge of the magnetic anisotropy is important because the anisotropy is used to design ferromagnetic structures on experimental samples.

Table 1. Crystal anisotropy energies for various directions in a cubic crystal (reprinted with permission) [23].

$[uvw]$	*a*	*b*	*c*	α_1	α_2	α_3	*E*
[100]	0°	90°	90°	1	0	0	K_0
[110]	45°	45°	90°	$1/\sqrt{2}$	$1/\sqrt{2}$	0	$K_0+K_1/4$
[111]	54.7°	54.7°	54.7°	$1/\sqrt{3}$	$1/\sqrt{3}$	$1/\sqrt{3}$	$K_0+K_1/3+K_2/27$

Ni has a face centered cubic (fcc) structure. For Ni, Figure 9 (a) elucidates that the direction of easy magnetization is <111>, and the direction of hard magnetization is <100>. If M_S makes angles *a*, *b*, *c* with the crystal axes in a cubic crystal, and $\alpha_1, \alpha_2, \alpha_3$ are the cosines of the angles, the crystal anisotropy energy is given by

$$E = K_0 + K_1(\alpha_1^2\alpha_2^2 + \alpha_2^2\alpha_3^2 + \alpha_3^2\alpha_1^2) + K_2(\alpha_1^2\alpha_2^2\alpha_3^2) + \cdots \qquad (26)$$

where $K_0, K_1, K_2 \cdots$ are constants for a specific material at a particular temperature [23, 24]. The colored letters in Figure 9 (a) illustrate the angles between M_S and the crystal axes in case of an example of M_S along the [110] direction. Higher orders are neglected.

Table 1 provides the value of the crystal anisotropy energy when the M_S vector lies in a specific direction [uvw]. By using Table 1, the E of Ni can be computed with anisotropy constants for Ni: $K_1=-0.5$ and $K_2=-0.2$. As a result, the easy axis of magnetization is matched the experimental results with the calculation.

On the other hand, Figure 9 (b) demonstrates magnetization curves of Co. The Co has a hexagonal close-packed (hcp) structure, and the direction of easy magnetization is the c-axis. The crystal anisotropy energy for hcp can be written as

$$E = K_0 + K_1 sin^2\theta + K_2 sin^4\theta + \cdots \tag{27}$$

where θ is an angle between the M_S vector and the c axis [23, 24]. When θ=0° the energy E is minimum; in contrast when θ=90° the energy E is maximum. Anisotropy constants for Co are K_1=45 and K_2=15.

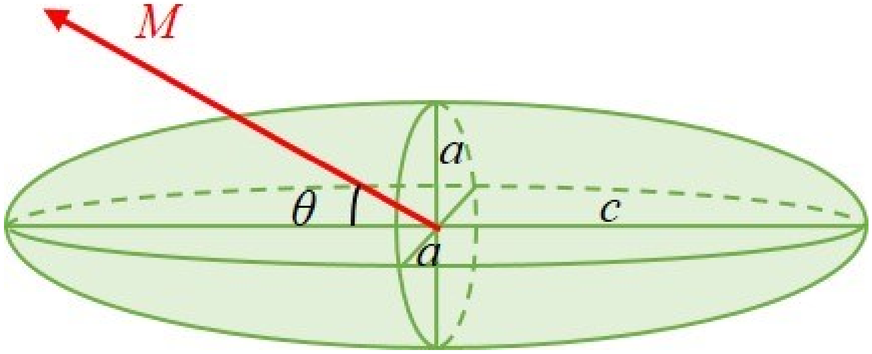

Figure 10. A schematic of a prolate ellipsoid (reprinted with permission) [23].

The magnetostatic energy E_{ms} is given by

$$E_{ms} = \frac{1}{2}M^2N_C + K_sM^2sin^2\theta \tag{28}$$

where $K_s = \frac{1}{2}(N_a - N_c)M^2$ is the shape anisotropy constant, and N_a and N_c are the demagnetizing coefficients of a axis and c axis of the sample, respectively [23, 24]. The same applied magnetic fields magnetize a sample to the same extent in any direction if the sample is a sphere. This means that N_a and N_c are the same, thus K_s will be zero. On the other hand, if c is the long axis, as given in Figure 10, it is easier to magnetize the sample along a long axis (c axis) than along a short axis (a axis). As a result, K_s is negative, and therefore the magnetostatic energy E_{ms} is lessened. The demagnetizing field along the short axis is stronger than along the long axis. This phenomenon indicates that the shape of the sample can be a source of magnetic anisotropy. This is called shape anisotropy.

1.5 Vortex motion in the Ferromagnet-Superconductor Hybrid

Properties of type II superconductors were discussed in subchapter 1.2. Type II superconductors expel applied external magnetic fields up to H_{C1}, and then tolerate partial magnetic fields in steps of the flux quantum, until H_{C2} is reached. At H_{C2}, type II superconductors lose their superconductivity. There is a mixed or vortex state in type II superconductors when the magnetic fields are between H_{C1} and H_{C2}. [2].

Superconductors and ferromagnets are mutually exclusive states of matter. However, the FSH can dramatically change superconductivity in nanoscale systems.

An effect of commensurability on transport properties occurs for magnetic dot arrays covered by a superconducting thin film [27-30]. A vortex lattice pinned by an external magnetic field competes with artificial periodic arrays. The peaks in I_C and resistances at values of the magnetic fields correspond to a vortex lattice commensurate with the artificial periodic array [31-35].

Vortex pinning at the vortex state in type II superconductors has been studied for practical applications. Various artificial magnetic periodic arrays were fabricated on superconductors to enhance the vortex pinning [9, 36-40]. Superconductivity in the vortex state is destroyed by most of the artificial magnetic periodic arrays to induce the flux quantum in the region. Vortex pinning by the periodic magnetic array depends on numerous factors such as magnetization of the array, aspect ratio of the nanorods and nanostripes, magnetic orientation, strength of the stray field, and so forth [7].

A. A. Abrikosov predicted that the flux entering a type II superconductor is in the form of quantized vortices [19]. The Abrikosov vortex lattice parameters are given by

$$a_{\triangle} = 1.075\left(\frac{\phi_0}{B}\right)^{\frac{1}{2}} \tag{29}$$

$$a_{\square} = \left(\frac{\phi_0}{B}\right)^{\frac{1}{2}} \tag{30}$$

where ϕ_0 is the flux quantum, and $a_{\triangle}$ represents the lattice constant, which is the distance of nearest neighbor of a triangular vortex array in equation (29). On the other hand, $a_{\square}$ represents the other lattice, which is the distance of nearest neighbor of a square vortex array in equation (30) [5]. Figures 11 (a) and (b) schematically represent a triangular vortex lattice and a square vortex lattice, respectively. The green and the red spots in Figures 11 (a) and (b) indicate the vortices in a type II superconductor, and the blue arrows around the spots indicate supercurrents. The matching field effect is due to the periodic nanostructure being matched by the corresponding triangular or square vortex lattice. This implies that when a perpendicular external magnetic field creates an integer number of the flux quantum per unit cell of dot shaped magnetic arrays, the vortex pinning becomes stronger indicating periodic oscillations in magnetoresistances (*MR*) and I_C [36, 38, 39]. Therefore, the flux quantum per unit cell of the pinning spots, which reduce the *MR* and increase the I_C near the sample's T_C results from applied the external magnetic fields.

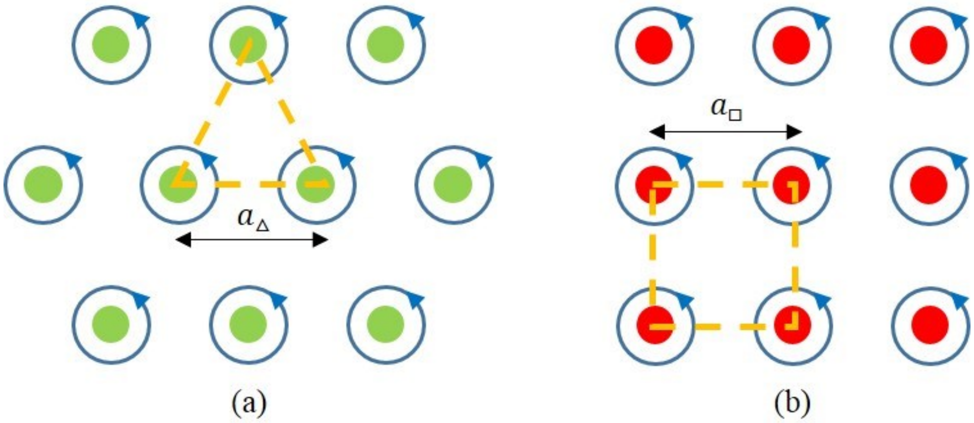

Figure 11. Schematics of a triangular vortex lattice (a) and a square vortex lattice (b).

Periodic vortex pinning with thickness modulation of superconducting thin films was first observed by Daldini [27]. Morgan and Ketterson [41] first observed direct experimental evidence that vortex pinning by magnetic dots is different from Geoffroy's [28] and Otani's results [30]. They magnetized their hybrid samples in nonmagnetic pinning centers by a magnetic dot array with perpendicular magnetization [41]. They showed a strong asymmetry of the pinning properties in I_C as a function of the external magnetic fields. The magnetic vortices can be pinned to a periodic magnetic array on the surface of a superconducting thin film which has then been studied extensively [7, 9, 10, 36, 38, 40].

In this study, artificial periodic ferromagnetic nanostructures are fabricated on superconducting thin films or embedded into superconducting thin films.

1.6 Field compensation effect in the Ferromagnet-Superconductor Hybrid

A field compensation effect is discussed in this subchapter. The ferromagnetic nanostructures on a superconducting thin film are exposed to an external homogeneous magnetic field. The magnetic field distribution is created by magnetized artificial ferromagnetic nanostructures. The magnetic field distribution depends on geometry and crystalline orientation of the nanostructures. Also, the thickness of the superconducting thin films affect the magnetic field distribution [36, 42]. When the ratio of $\frac{t}{d}$ is less than 1, where t is the thickness of the superconducting thin film, and d is the diameter of the magnetic nanostructure, the magnetic fields inside the superconducting thin film are directed normal to the surface of the thin film. And the magnetic field inside the superconducting thin film is close to the field at the surface of nanostructures. The direction of the field between the nanostructures will be changed by the field inside the superconducting thin film. Therefore, the superconducting thin film under the magnetic nanostructures provides an opportunity to observe the field compensation effect in which an external magnetic field is applied parallel to the nanostructures. The magnetic field from the nanostructures will reduce the external magnetic field in the parts of the superconducting thin film between the nanostructures [7, 36, 42, 43]. The field compensation effect is illustrated in Figure 12, which describes a simple superconducting (SC) thin film and ferromagnetic (FM) rods with insulating (IN) layers on a SiO_2/Si substrate.

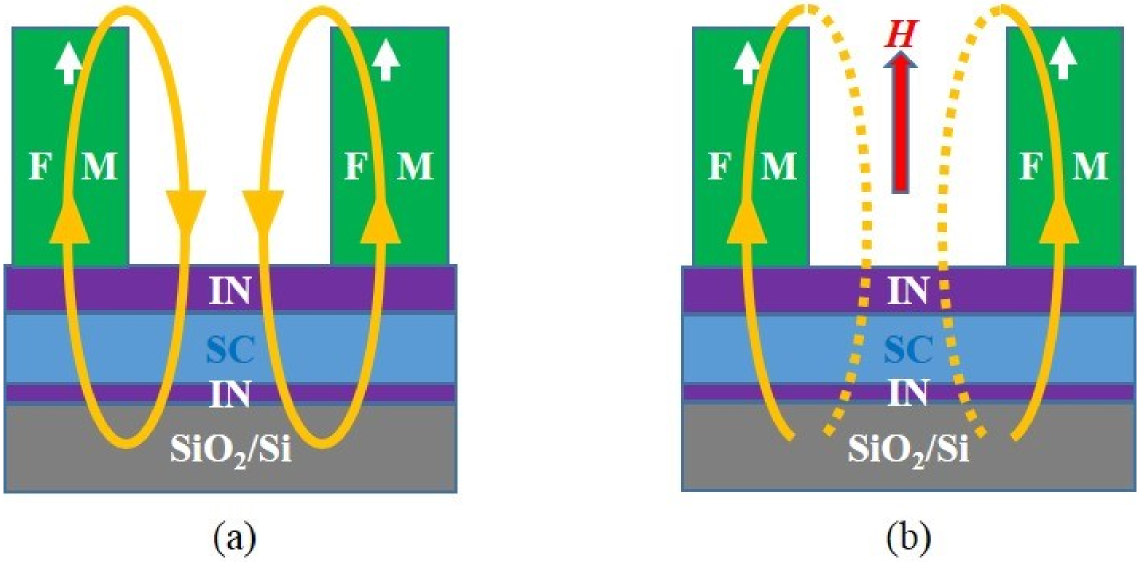

Figure 12. Schematics of the field compensation effect without external magnetic fields (a) and with external magnetic fields (b).

2. DESIGN AND FABRICATION OF FERROMAGNET-SUPERCONDUCTOR HYBRID SAMPLES

In this chapter, the design and fabrication of FSH samples are discussed. Firstly, the fabrication process of the superconducting thin films and nanosized ferromagnetic structures is elucidated. Slightly different processes for LTS FSH samples between nanoscale ferromagnetic structures on superconducting thin films and embedded nanosized ferromagnetic structures into superconducting thin films are a requirement for this specific type of research. Moreover, a similar process for HTS FSH samples is discussed. Secondly, the photolithography for the fabrication of contact pads connected to a Physical Property Measurement System (PPMS) puck is studied. In addition, an Electron Beam Lithography (EBL) process is discussed for fabrication of microsized and nanosized patterns. Finally, how to grow ferromagnetic nanostructures by thermal evaporation and an electroplating method is investigated.

2.1 Fabrication procedures

There are three different processes that depend on the FHS sample's structures. Firstly, the FSH preparation for LTS thin films is discussed. A 300 nm ± 0.5% oxide layer on an N-type Si wafer is used as a substrate. The substrate is cleaned by spraying acetone, isopropyl alcohol (IPA), and drying with nitrogen gas. This substrate is baked on a hot plate at 120 °C for five minutes to remove the remaining IPA on the surface of the substrate. Patterns for the contact pads, interfacing specific FSH sample regions, for the PPMS (Model 6000, Quantum Design) measurements are made by using photolithography. The photoresist (PR) (Microposit S1827 by Electronic Materials) is designed for microscale patterning. The thermal evaporation system is used to deposit 3 nm Cr on the patterned substrate, which serves as an adhesive layer between SiO_2 and the Au layer. Then 15~20 nm Au is thermally evaporated on top of the Cr. After lift-off in acetone, the Au electrode pads are ready to be connected to the PPMS system. A spin coater is utilized to spread a polymethyl methacrylate (PMMA) layer on the surface of the substrate where three rectangular patterns for superconducting thin films are drawn at the center of the substrate by EBL. These rectangular patterns, for the superconducting thin films, have four protruding legs. The legs are extended further by additional EBL patterning, thus connecting the legs to the Au contact pads used for a four-probe measurement. A 3 nm thick Ge film is thermally evaporated at room temperature as an adhesion layer between SiO_2 and the superconducting thin film, such as Sn or $Pb_{82}Bi_{18}$. Then 30~100 nm of the superconducting thin film is thermally evaporated on top of the Ge adhesion layer in a high vacuum system (8.7×10^{-8} torr). Throughout evaporation the superconducting thin films, the samples are cooled by filling the cold trap to which the samples is mounted with liquid nitrogen (77 K). After warming the substrate in the evaporator chamber to room temperature, 20 nm Ge is thermally evaporated on the substrate at room temperature. Unlike the previous Ge layer, this Ge layer will function as an insulator between the superconducting thin films and the ferromagnetic

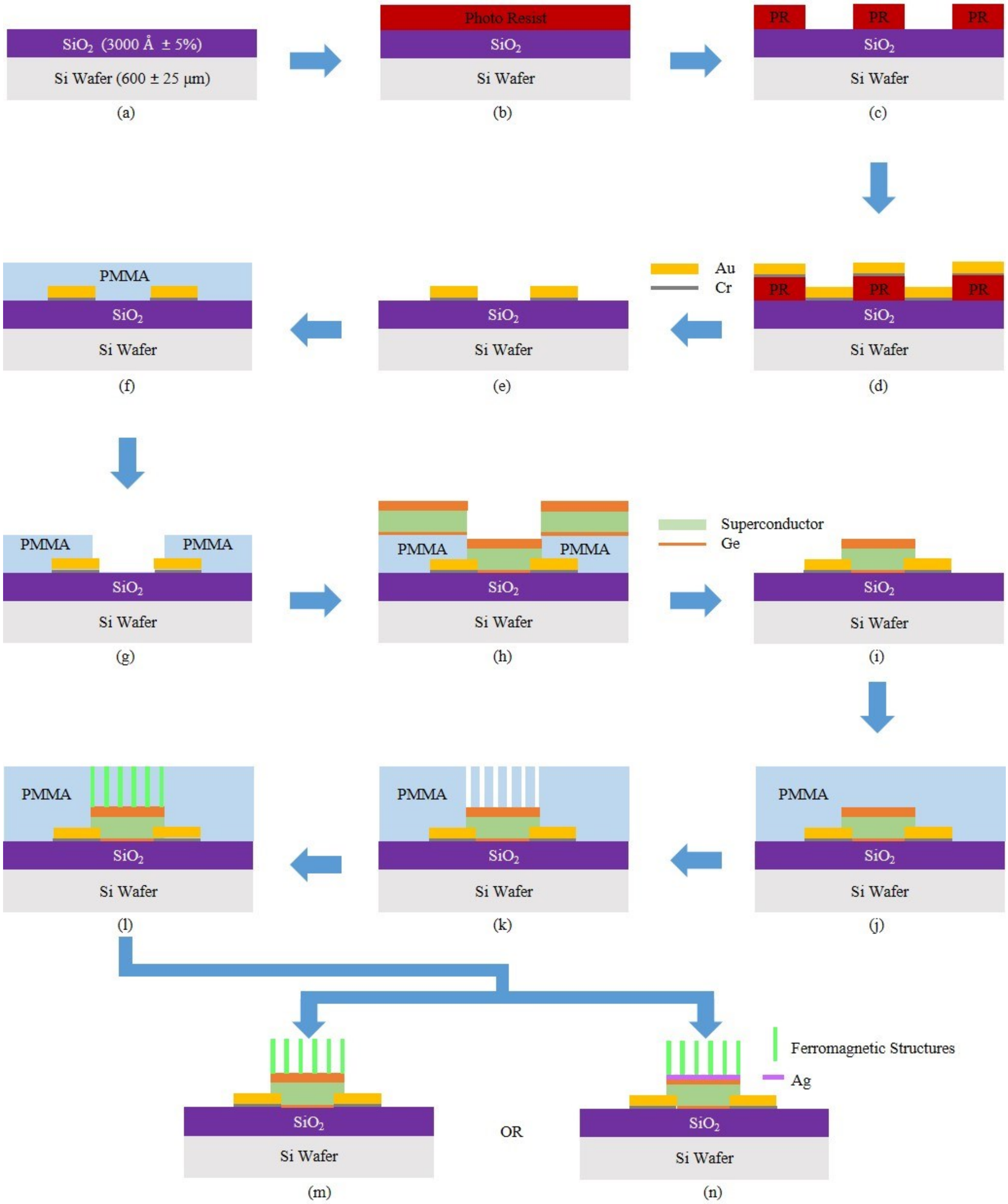

Figure 13. Procedure of the FSH for LTS thin films: a substrate (a), photoresist spin-coating (b), photolithography (c), thermal evaporation (d), lift-off (e), PMMA spin-coating (f), EBL (g), thermal evaporation (h), lift-off (i), PMMA spin-coating (j), EBL (k), thermal evaporation or electroplating (l), lift-off (m), and lift-off (n).

nanostructures. After the lift-off step, the superconducting thin films are coated with PMMA in preparation for the next process. Patterns of nanostripes or nanorods, for growing nanosized ferromagnetic structures, are drawn in the PMMA above the Ge insulating layer by EBL. Ni or Co are grown into the patterns by using either the thermal evaporator or the electroplating system. Figure 13 shows the procedure for the preparation of FSH samples for LTS thin films. A layer of 15~20 nm Ag as a counter electrode (CE) is needed to grow the nanosized ferromagnetic structures by the electroplating system, as shown in Figure 13 (n).

The second process for FSH preparation involves embedded ferromagnetic nanostructures within the superconducting thin films. The fabrication processes for this process are the same up to Figure 13 (g). Figure 14 illustrates the fabrication procedure of the embedded FSH samples for LTS thin films. As seen in Figure 14 (l), Ni or Co nanostructures are grown at room temperature by using an electroplating method. Afterward, superconducting thin films are deposited by thermal quench condensation, as shown in Figure 14 (p).

The last process for FSH preparation for HTS thin films will now be described. A 100 nm $YBa_2Cu_3O_{7-\delta}$ (abbreviated YBCO) epitaxial thin films on $SrTiO_3$ (abbreviated STO) (100) single crystal substrates were purchased from MTI Corporation. YBCO films on STO crystal substrates are cleaned by using acetone, then IPA, and drying with nitrogen gas. The YBCO films are first coated with photoresist and then placed on a hot plate at 120 °C for five minutes for prebaking. The photolithography method is performed to make four legged rectangular patterns on the YBCO films.

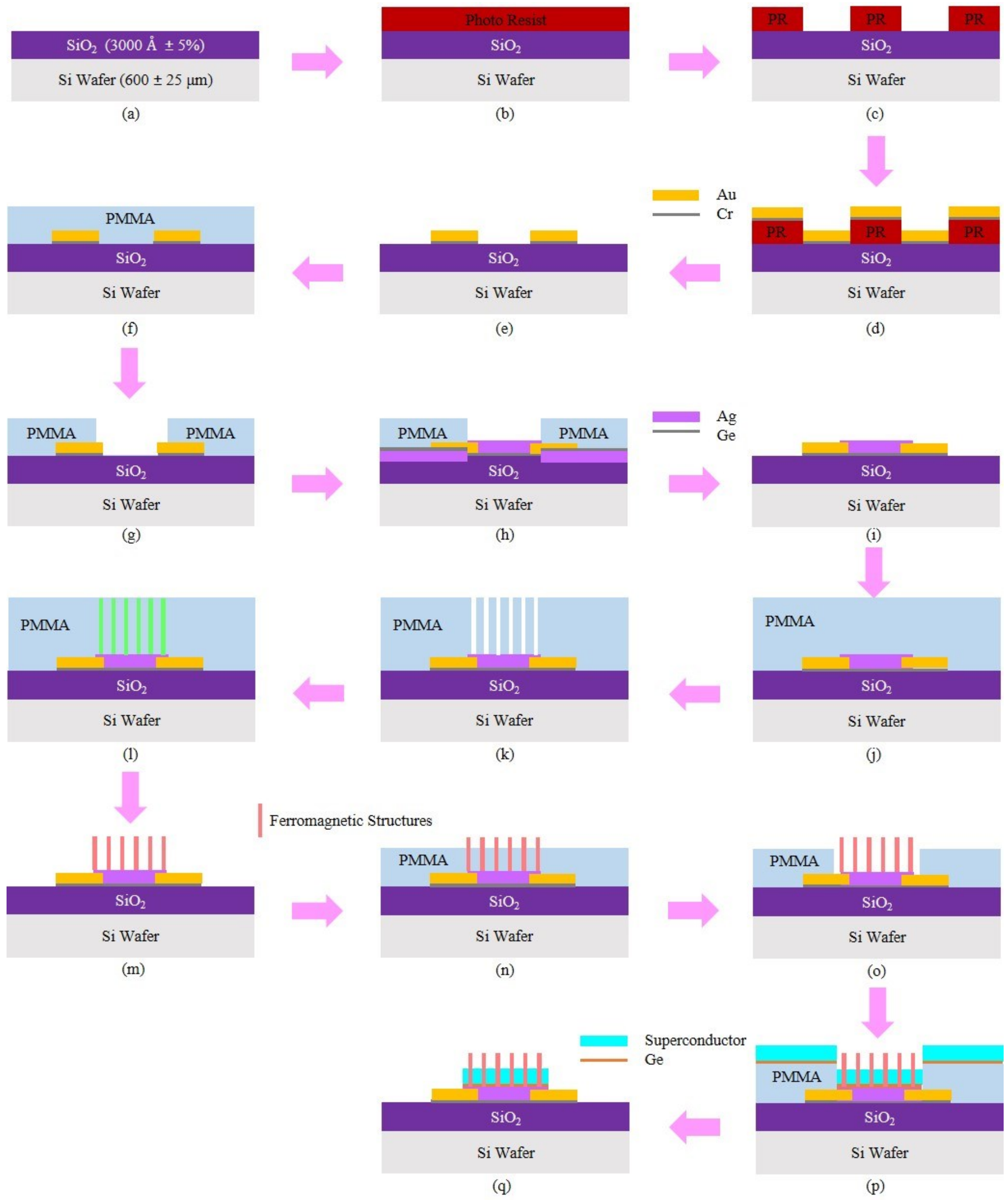

Figure 14. Procedure of the embedded FSH for LTS thin films: a substrate (a), photoresist spin-coating (b), photolithography (c), thermal evaporation (d), lift-off (e), PMMA spin-coating (f), EBL (g), thermal evaporation (h), lift-off (i), PMMA spin-coating (j), EBL (k), electroplating (l), lift-off (m), PMMA spin-coating (n), EBL (o), thermal evaporation (p), and lift-off (q).

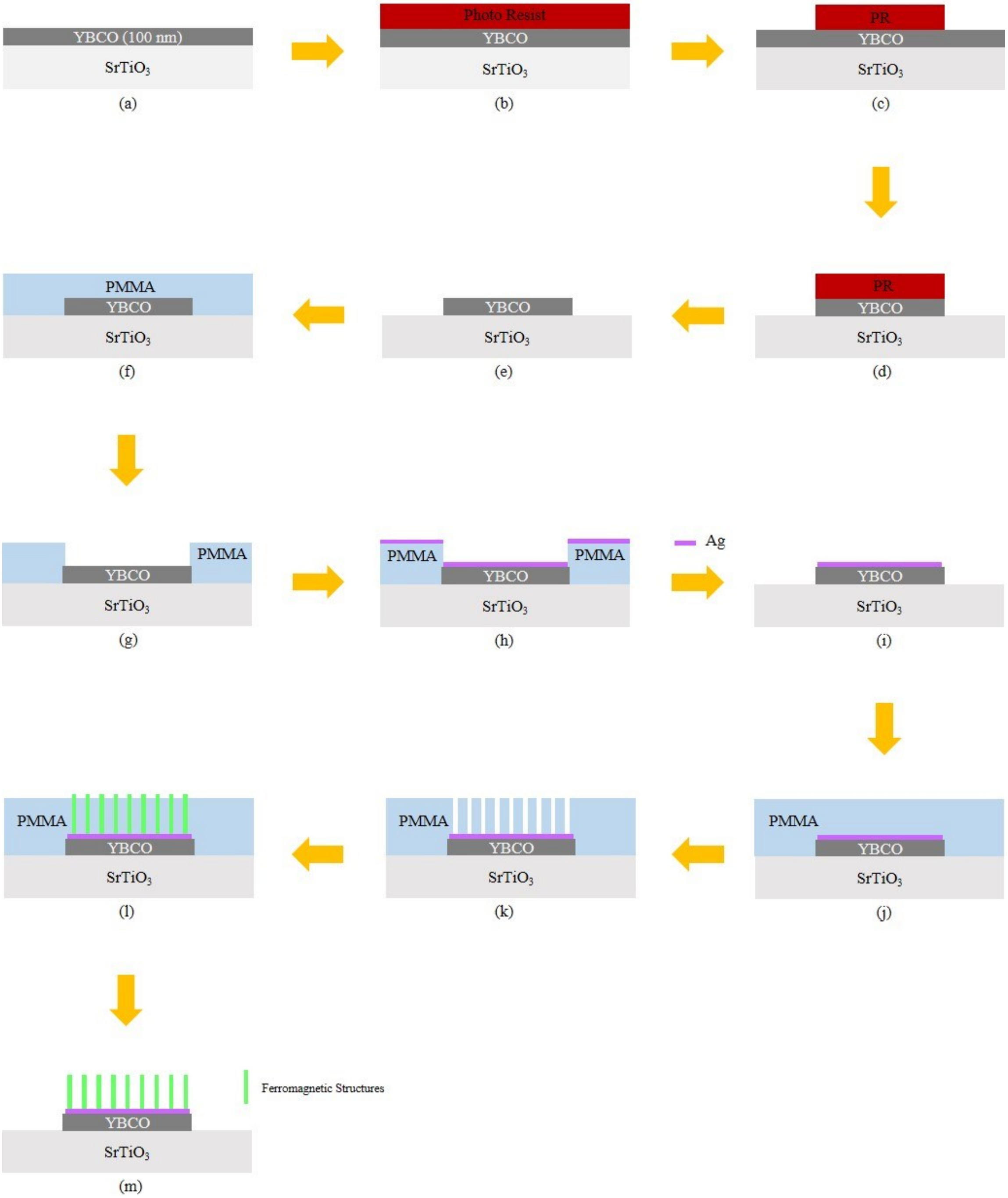

Figure 15. Procedure of the YBCO FSH for HTS thin films: a substrate (a), photoresist spin-coating (b), photolithography (c), wet etching (d), lift-off (e), PMMA spin-coating (f), EBL (g), thermal evaporation (h), lift-off (i), PMMA spin-coating (j), EBL (k), thermal evaporation or electroplating (l), and lift-off (m).

After the photolithography, the patterned samples are etched in an about 1% diluted nitric acid bath for about two seconds to remove unnecessary YBCO surrounding the PR patterns. Lift-off of the remaining PR in acetone reveals a four legged rectangular YBCO films. A 10~20 nm Ag layer is then deposited on the YBCO films by thermal evaporation at room temperature. This Ag layer serves as protective layer to preserve the chemical composition of the YBCO films and also function as a CE for electroplating, as shown in Figure 15 (i). A thermally deposited Ag layer on top of the YBCO films results in the increase of critical temperature (T_C). However, Ag layers thinner than 20 nm do not change T_C of the YBCO thin films [44]. If the YBCO films lose oxygen, they lose their superconducting properties. This means that the resistance of YBCO films does not drop to zero. Therefore, the YBCO films have to retain a proper ratio of oxygen to exhibit the superconductivity. Figure 15 shows the procedure for the YBCO FSH sample fabrication.

2.2 Photolithography

Photolithography is a process of transferring microsized patterns on a mask to a flat surface. The role of photolithography is to fabricate electrical contacts to connect to transistors which make up integrated circuits [45]. In this research, patterns of contact pads connected with the PPMS puck are created on SiO_2 substrates by photolithography. Steps of photolithography technique for this study are indicated in Figure 16.

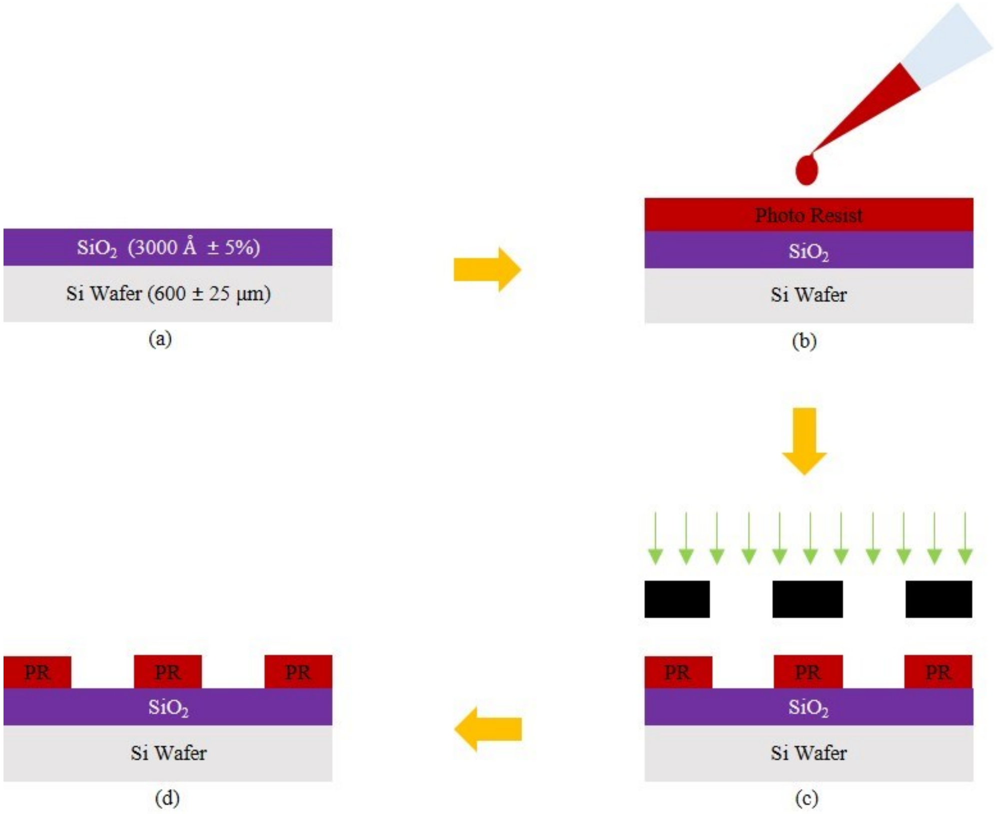

Figure 16. Cleaning a substrate (a), photoresist spin-coating (b), UV light exposure (c), and development (d).

A 1 cm x 1 cm SiO_2 substrate was cleaned to remove water and some contaminations on surface of the substrate by using acetone, IPA, and drying with nitrogen gas, as shown in Figure 16 (a). In order to eliminate the remaining IPA on the surface, the substrate was baked on a hot plate at 120 °C for five minutes.

PRs are light-sensitive materials whose chemical structure changes when the PRs are exposed to light. There are two types of PRs, positive and negative PR, as shown in Figure 17. For the positive type, regions exposed to the light change their chemical properties to make them more soluble in the developer, as seen in Figure 17 (c). In contrast, the negative type PR behaves in the opposite manner. This means that unexposed regions of the negative PR are soluble in the developer, as shown in Figure 17 (d) [45, 46].

In this project, Microposit S1827 by Electronic Materials was used as a positive PR. The PR was dropped on the clean substrate by using a pipette, as shown in Figure 16 (b).

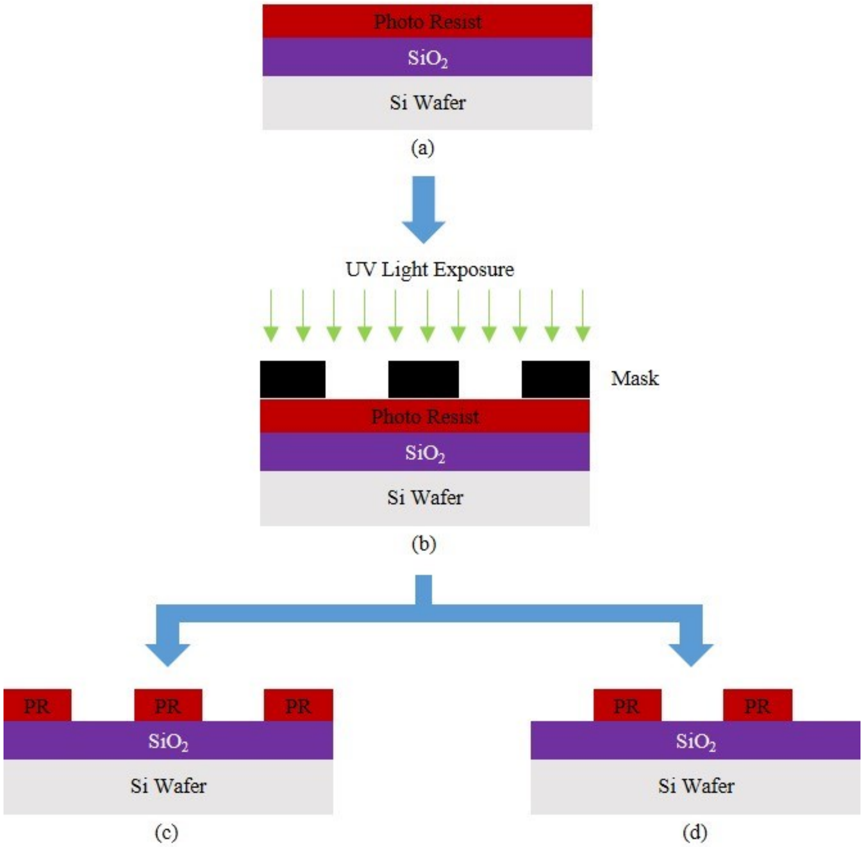

Figure 17. PR spin-coating (a), UV light exposure (b), a positive PR reaction (c), and a negative PR reaction (d).

Figure 18. A picture of the spin coater.

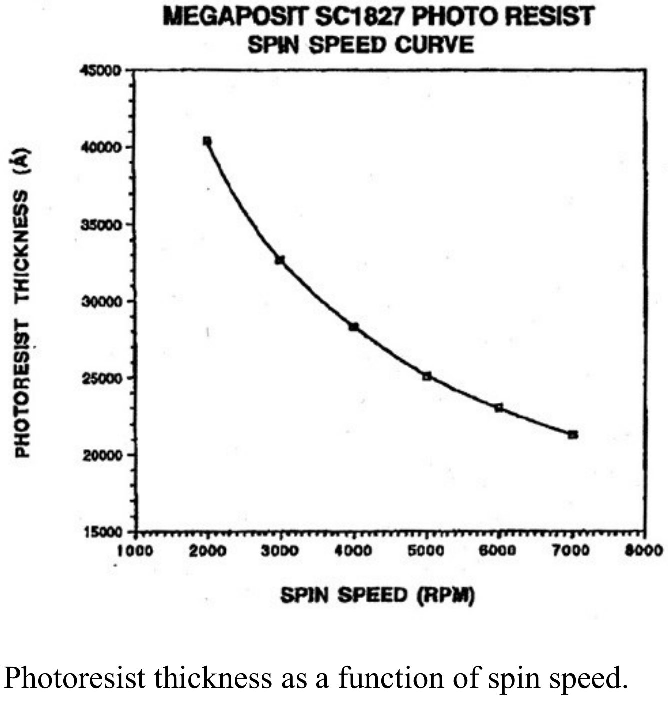

Figure 19. S1827 Photoresist thickness as a function of spin speed.

A spin-coater (WS-650S-6NPP/LITE, Laurell), which is displayed in Figure 18, was operated to uniformly spread the PR on the substrate. The thickness of the coated PR can be controlled by concentration of the PR and spin speed (rpm). Figure 19 indicates thickness of the PR as a function of spin speed for the S1827 PR [47]. The PR was spread at 5,000 rpm for 60 seconds at room temperature to achieve a 2,500 nm PR layer.

In addition, the PR coated substrate was prebaked at 120 °C for 60 seconds because the density of the PR is not sufficient to support later processing. The prebaking makes rids the surface of solvent to obtain a larger density of the PR [48]. Figure 16 (c) indicates the next process; exposure to ultraviolet (UV) light.

One of the important pieces of equipment in the photolithography is the mask aligner. A mask aligner (Q4000 IR, Quintel) for the photolithography process was employed, which is illustrated in Figure 20. A mercury short arc lamp (Advanced Radiation Corporation) was used to provide a 360 nm to a 400 nm wavelength UV light in the mask aligner when the lamp was at 350 Watt [49].

To operate in the contact mode on the mask aligner, the designed film mask was attached to a flat blank quartz mask. The PR coated substrate was exposed to UV light for 35 seconds.

The last step of photolithography is development. The substrate was dipped into the developer, which was MF-319 by Electronic Materials, shaken in a smooth and consistent manner for 35 seconds at room temperature. Then, the substrate was rinsed by

Figure 20. A picture of the mask aligner.

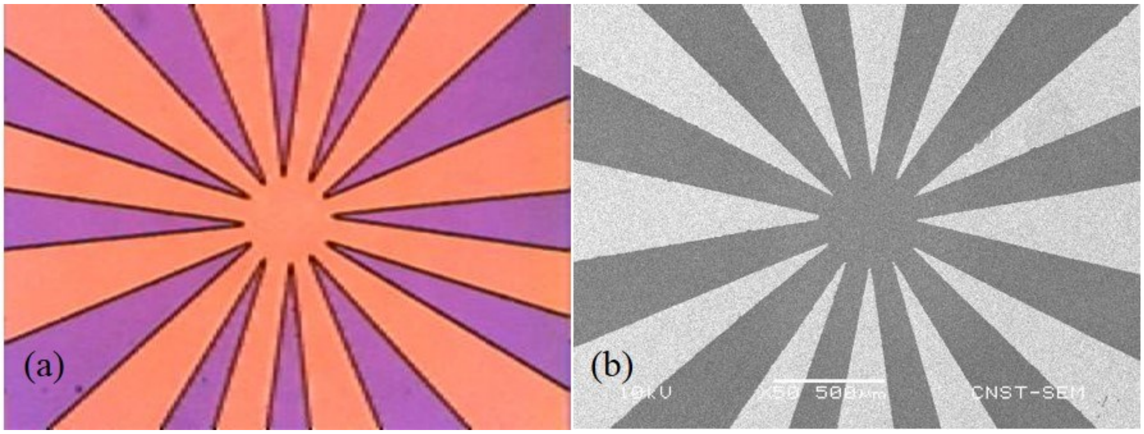

Figure 21. An image of the patterns for contact pads after photolithography by optical microscope (a) and an SEM image of the pattern after Cr and Au evaporation (b).

spraying DI water (Deionized water) for 60 seconds, and the substrate was dried by blowing nitrogen gas. After this photolithography process, a Au and a Cr thin films will be thermally evaporated on the patterned substrate. The thermal evaporation technology will be discussed later in this chapter. Figure 21 (a) shows an optical microscope image of the design of the photolithographic patterns for contact pads after the development. Figure 21 (b) illustrates an SEM image in which the clean lighter regions indicate the proper deposition of a 3 nm thick Cr thin film and a 15 nm thick Au thin film by utilizing thermal evaporation at room temperature.

2.3 Electron beam lithography

The scales of semiconductor integrated circuits are getting smaller, which means reducing to nanosized products. In modern fabrication, miniaturization has been the main issue regarding the techniques. The Electron Beam Lithography (EBL) technique is one of the most generally operated lithographic technologies for nanoscale fabrications. Advancements in EBL techniques has allowed users to design high resolution nanometer scale features directly onto substrates [50, 51].

In this research, a Scanning Electron Microscope (SEM), JSM-6460 by JEOL, and a PCD beam blanker by Deben for the EBL have been used. The SEM system is composed of an electron gun, objective lens aperture, vacuum chamber, and the Nanometer Pattern Generation System (NPGS), as shown in Figure 22. The NPGS is an easy and powerful tool for operation of the SEM for EBL [52]. The sample holding

Figure 22. A picture of the Electron Beam Lithography system.

stage moves in the nanometer scale during an electron beam exposure. In order to interface the NPGS to the SEM system, patterns have to be designed by drawing in DesignCAD. For the step in Figure 13 (g) and Figure 14 (g), the EBL was used to make rectangular patterns for superconducting thin films on the substrate.

The EBL process begins with a coat of PMMA on the substrate using the spin coater (G3-8 Spincoat, Cookson Electronics), which is shown in Figure 23. 3% 950PMMA C by Microchem was diluted in Chlorobenzene. Samples were spun at 1,700 rpm with a spin time of 60 seconds. Then, the substrate was prebaked at 120 °C for 90 seconds. The final thickness of the PMMA was around 321 nm, as shown in Figure 24 (c).

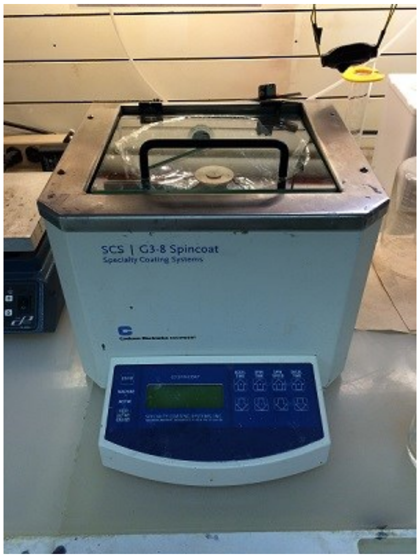

Figure 23. A picture of the spin coater.

Figure 24 provides three dimensional Atomic Force Microscope (AFM) (Bruker Dimension Icon AFM, from the MCF at TAMU) images for calibration of the thickness of PMMA with various spin coater speeds and PMMA concentrations. Scan size of the AFM images are 10 µm x 10 µm and 15 µm x 15 µm. The tapping mode was used to avoid damaging the samples. When 1%, 2%, and 6% PMMA concentration were employed with the same spin speed at 5,000 rpm, the PMMA layers thickened, 70 nm, 97 nm, and 805 nm, respectively, as shown in Figures 24 (a), (b), and (d). However, when the spin speed was increased from 1,700 rpm to 5,000 rpm, PMMA layers thinned from 1,117 nm to 805 nm, respectively, as shown in Figure 24 (d) in comparison with Figure 24 (e). Just as we discussed controlling thickness of the PR, it is known that the thickness of the PMMA also depends on spin speed and concentration of the PMMA in the Chlorobenzene.

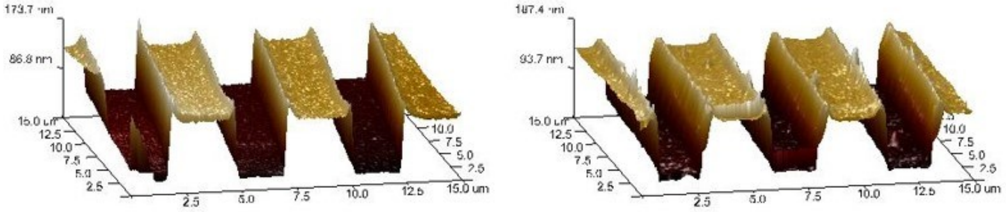

(a)
Scan Size: 15 μm x 15 μm
PPMA 1% with 5000 rpm
Thickness: 70 nm

(b)
Scan Size: 15 μm x 15 μm
PPMA 2% with 5000 rpm
Thickness: 97 nm

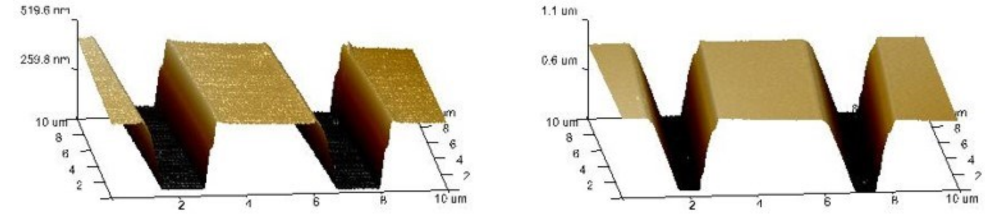

(c)
Scan Size: 10 μm x 10 μm
PPMA 3% with 1700 rpm
Thickness: 321 nm

(d)
Scan Size: 10 μm x 10 μm
PPMA 6% with 5000 rpm
Thickness: 805 nm

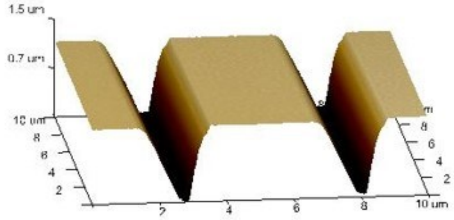

(e)
Scan Size: 10 μm x 10 μm
PPMA 6% with 1700 rpm
Thickness: 1,117 nm

Figure 24. Three dimensional AFM images of 1% PMMA with 5,000 rpm (a), 2% PMMA with 5,000 rpm (b), 3% PMMA with 1,700 rpm (c), 6% PMMA with 5,000 rpm (d), and 6% PMMA with 1,700 rpm (e).

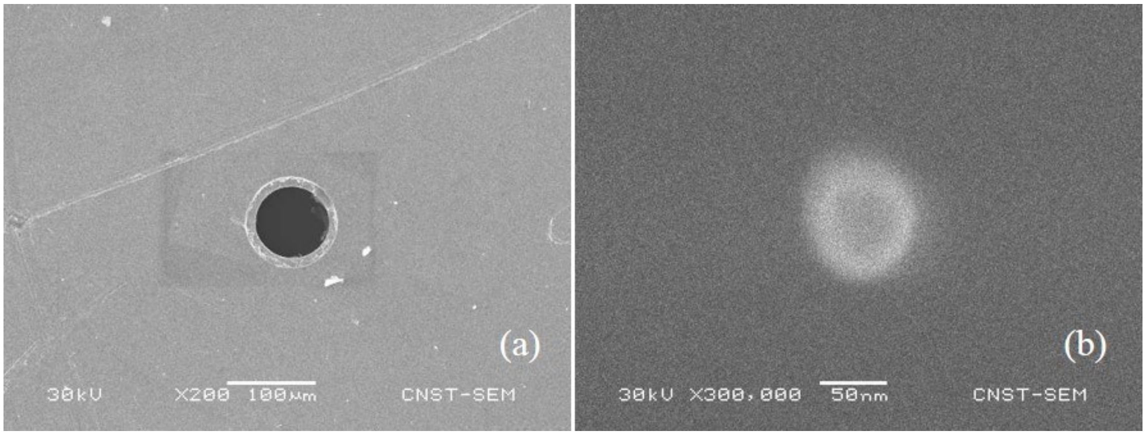

Figure 25. SEM images of the faraday cup (a) and a contamination spot (b).

Afterward, coated PMMA was exposed to an electron beam to make the patterns. Before drawing the patterns, the electron beam has to be optimized. In order to optimize the electron beam, the beam current was checked with a Faraday cup at maximum magnification (300,000x). The current was monitored and measured with a Keithley 6485 picoammeter. When the electron beam was adjusted, the beam status was confirmed by burning a contamination spot. The contamination spot should be a bright circle in the SEM mode. If there is no spot, or the spot is like an ellipse, additional focus adjustment is necessary. Figure 25 (a) shows the faraday cup on the sample stage, and Figure 25 (b) displays a well-defined contamination spot after the electron beam optimization. By adjusting the spot size, the beam currents can be tuned. Patterning time depends on the beam current; high beam currents decrease the patterning times, while low beam currents increase the patterning times. For drawing the rectangular superconducting thin film patterns, the beam current was 210 pA. The accelerating voltage was 30 kV, and the area dosages were from 350~400 μC/cm^2 for the patterns.

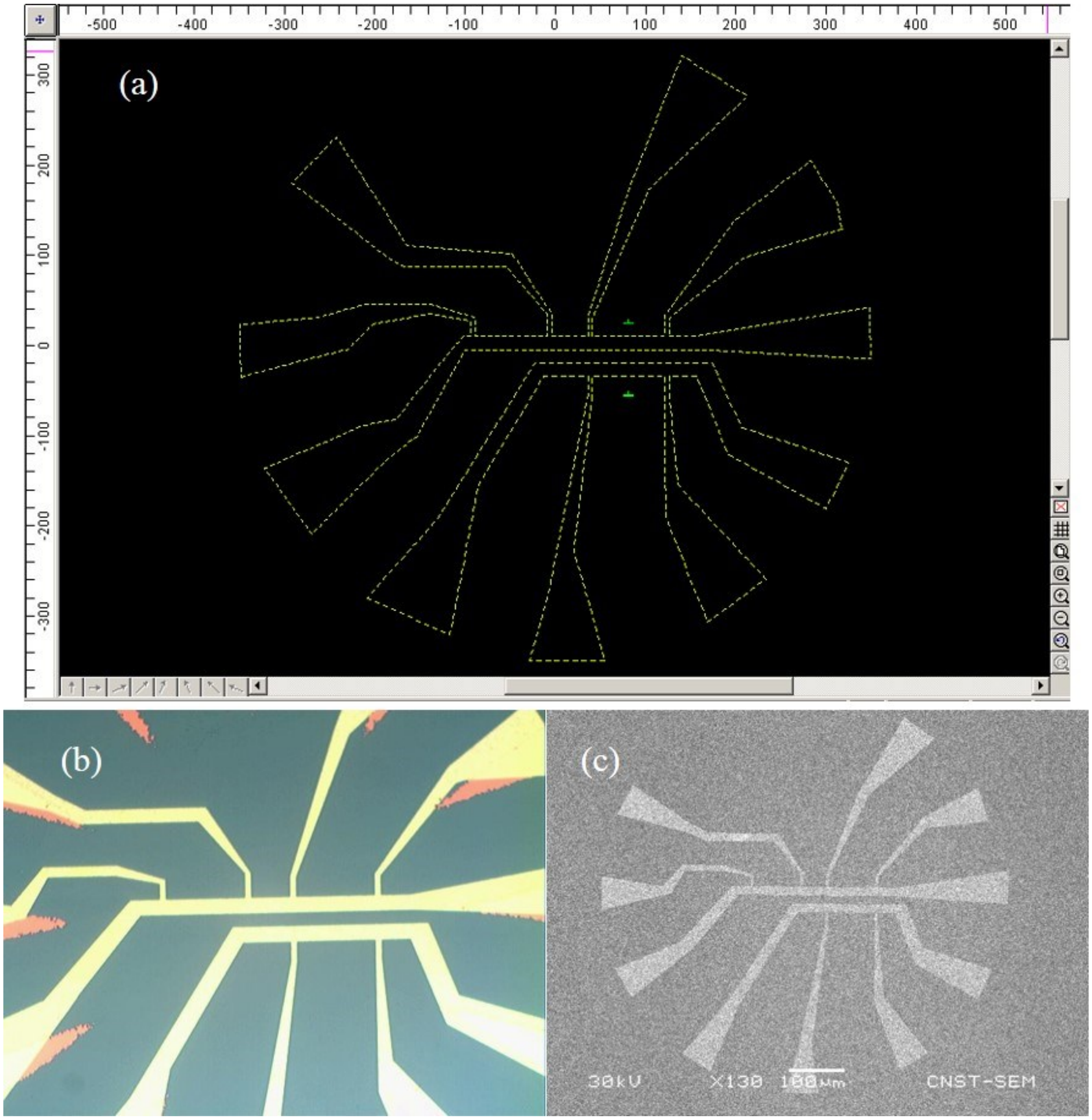

Figure 26. Captured images of a rectangular superconducting thin films pattern by DesignCAD (a), an optical microscope (b), and an SEM (c).

Finally, the EBL patterned substrate was ready to move to development step. The developer was a ratio of 1:3=Methyl Isobutyl Ketone (MIBK): IPA [53, 54]. The electron beam exposed substrate was dipped in the developer for 60 seconds at room temperature. The substrate was gently shaken by hand throughout the development. After the development process, the patterned substrate was rinsed by spraying IPA and dried with nitrogen gas.

Figure 26 shows different types of images of the rectangular superconducting thin films' pattern. There are three rectangular samples on the images. Superconducting thin films will be grown simultaneously on the three rectangular patterns. The three superconducting samples will be connected to three channels of a PPMS puck. Therefore, the physical properties can be measured at the same time in the PPMS. Figure 26 (a) displays a DesignCAD version of the pattern, and markings in the picture indicates 20 μm. The superconducting thin films have 84.33 μm length and 15.50 μm width. The ends of all the patterns overlay parts of the Au contact pads. Therefore, applied currents will be able to flow through the superconducting thin films. Figures 26 (b) and (c) illustrate an optical microscope image and an SEM image of the EBL patterns, respectively.

Now, details of patterning for nanosized stripes and rods by using the EBL is elucidated. The procedure was briefly introduced in Figures 13 (j) and (k). These steps were carried out on the rectangular superconducting thin films.

To start making nanoscale structures up to 805 nm height, a different concentration of the PMMA was used, which was 6% 950PMMA C by Microchem.

The PMMA was coated on the substrate by using the spin coater. The spin speed of the spin coater was 5,000 rpm, and the spinning time was 60 seconds. After the PMMA was spread, the substrate was placed on top of the hot plate for prebaking at 120 °C for 90 seconds. Thickness of the PMMA layer was around 805 nm, as displayed in Figure 24 (d). However, if around 321 nm height of the ferromagnetic structures are needed, the condition can be changed from 6% PMMA with 5,000 rpm to 3% PMMA with 1,700 rpm. The goal of this process is to create a high aspect ratio nanoscale structures such as 1:3 or 1:4.

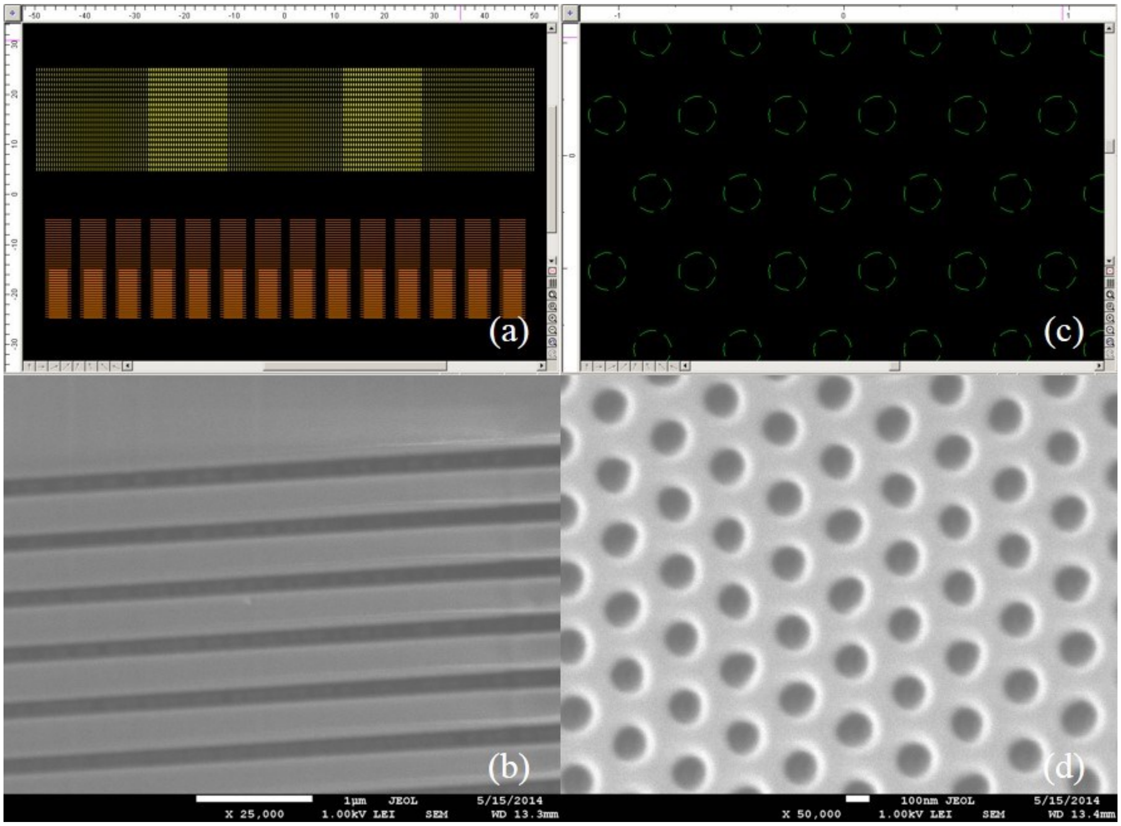

Figure 27. The design for nanostripes (a) and an SEM image of the nanostripes pattern (b), the design for nanorods (c), and an SEM image of the nanorods pattern (d).

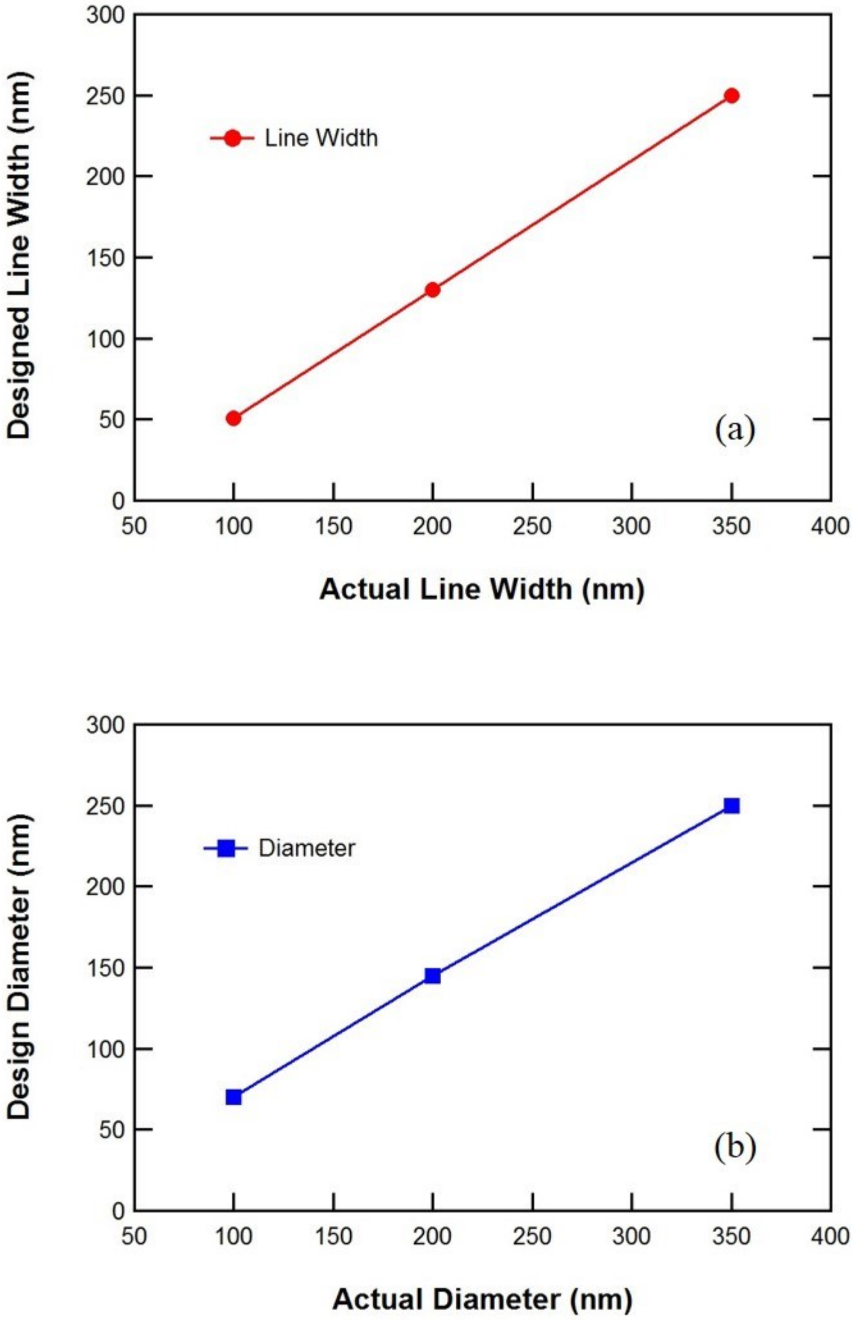

Figure 28. Calibration for line widths (a) and diameters (b).

Designs of the lines and the dots in DesignCAD program were smaller than the actual line width and diameter, respectively after EBL, because electrons from the electron beam were scattered inside the PMMA layer [55, 56]. Figure 27 (a) displays a design for the stripes, and (b) displays an SEM image for the stripes after the EBL. Figure 27 (c) illustrates a design for the rods, and (d) illustrates an SEM image for the rods after the EBL. Figure 28 shows designed line width versus actual line width (a) and designed diameter versus actual diameter (b). Both of them indicate that there is a scattering of electrons in the PMMA. For example, in order to make a 200 nm diameter pattern, the design in DesignCAD should be a 140 nm diameter.

Area dosage is another significant factor for resolution of the stripe patterning [57-59]. In order to investigate the resolution limit of the EBL, a 6% PMMA with 5,000 rpm for around 800 nm of the PMMA thickness, and a 30 kV electron beam exposure were employed. For drawing nanostripe patterns, the beam current was 10 pA. The development condition was the same as aforementioned with a ratio of 1:3=MIBK:IPA and gentle shaking for 60 seconds at room temperature. The designed pattern had a 200 nm width with a 400 nm period stripe. The stripe patterned on the same substrate, which was a Si wafer with a SiO_2 layer. Figure 29 depicts optical microscope images of dissimilar area dosage exposure by the EBL on the substrate. 20 nm of Ni was deposited on the patterned substrate with a thermal evaporator. In the examination, several different area dosages were applied to parallel stripe patterns, as shown in Figure 30 and perpendicular stripe patterns, as shown in Figure 31. From the SEM images in Figure 30

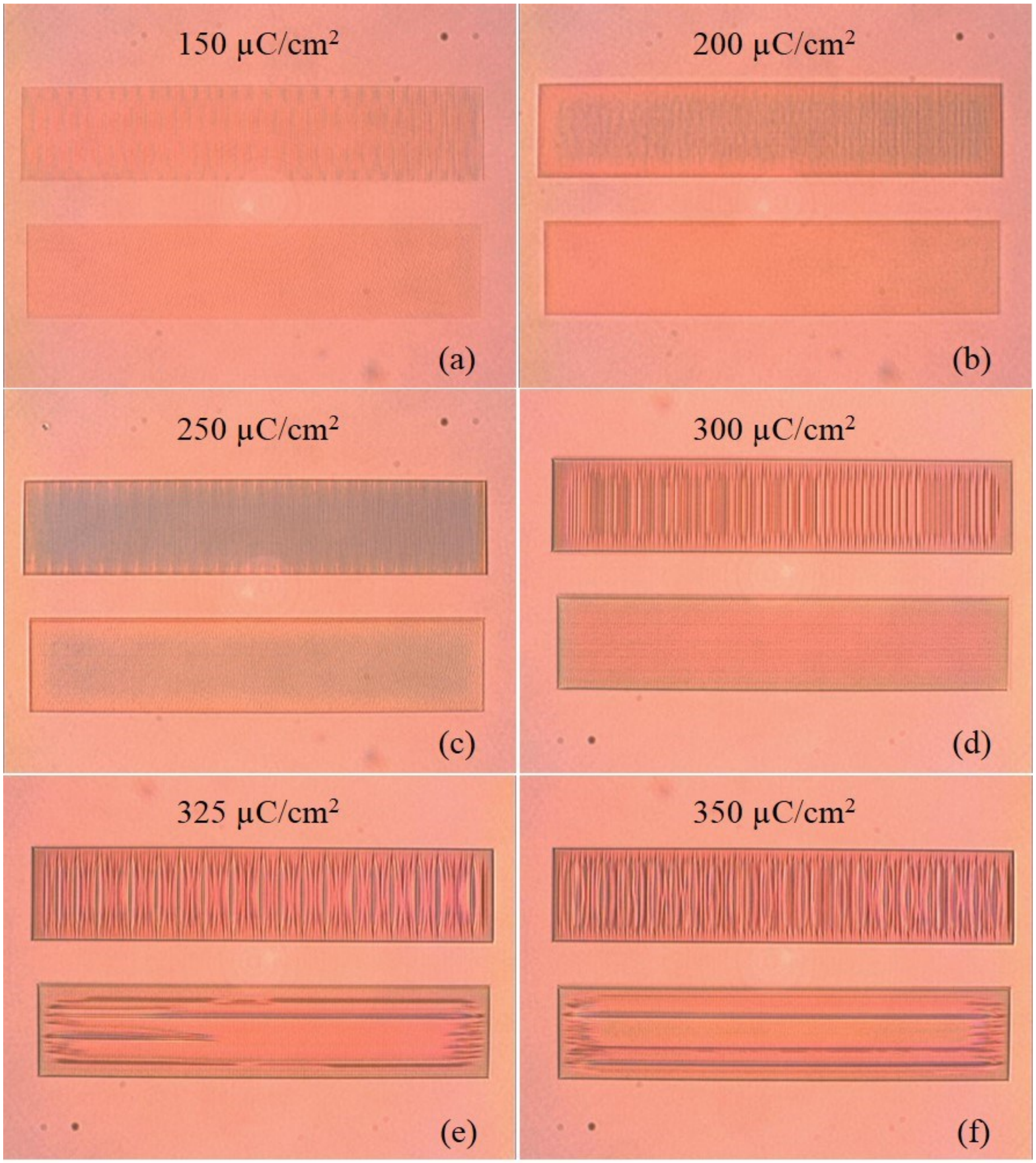

Figure 29. Optical microscope images of various area dosages of parallel and perpendicular stripes during an EBL; 150 μC/cm^2 (a), 200 μC/cm^2 (b), 250 μC/cm^2 (c), 300 μC/cm^2 (d), 325 μC/cm^2 (e), and 350 μC/cm^2 (f).

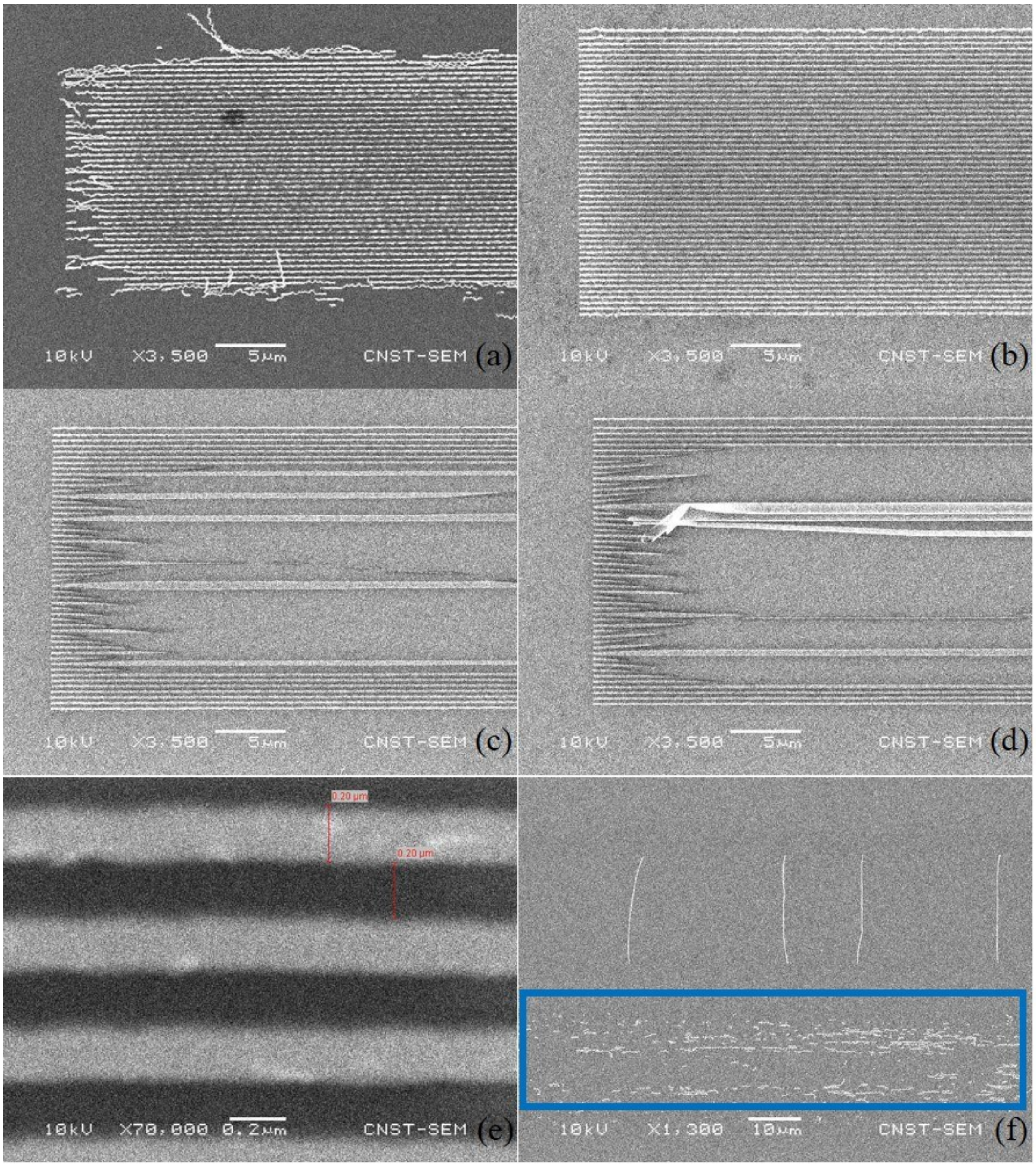

Figure 30. SEM images of various area dosage of parallel stripes during an EBL; 250 μC/cm^2 (a), 300 μC/cm^2 (b), 325 μC/cm^2 (c), 350 μC/cm^2 (d), close-up image of 300 μC/cm^2 (e), and in the blue square 200 μC/cm^2 (f).

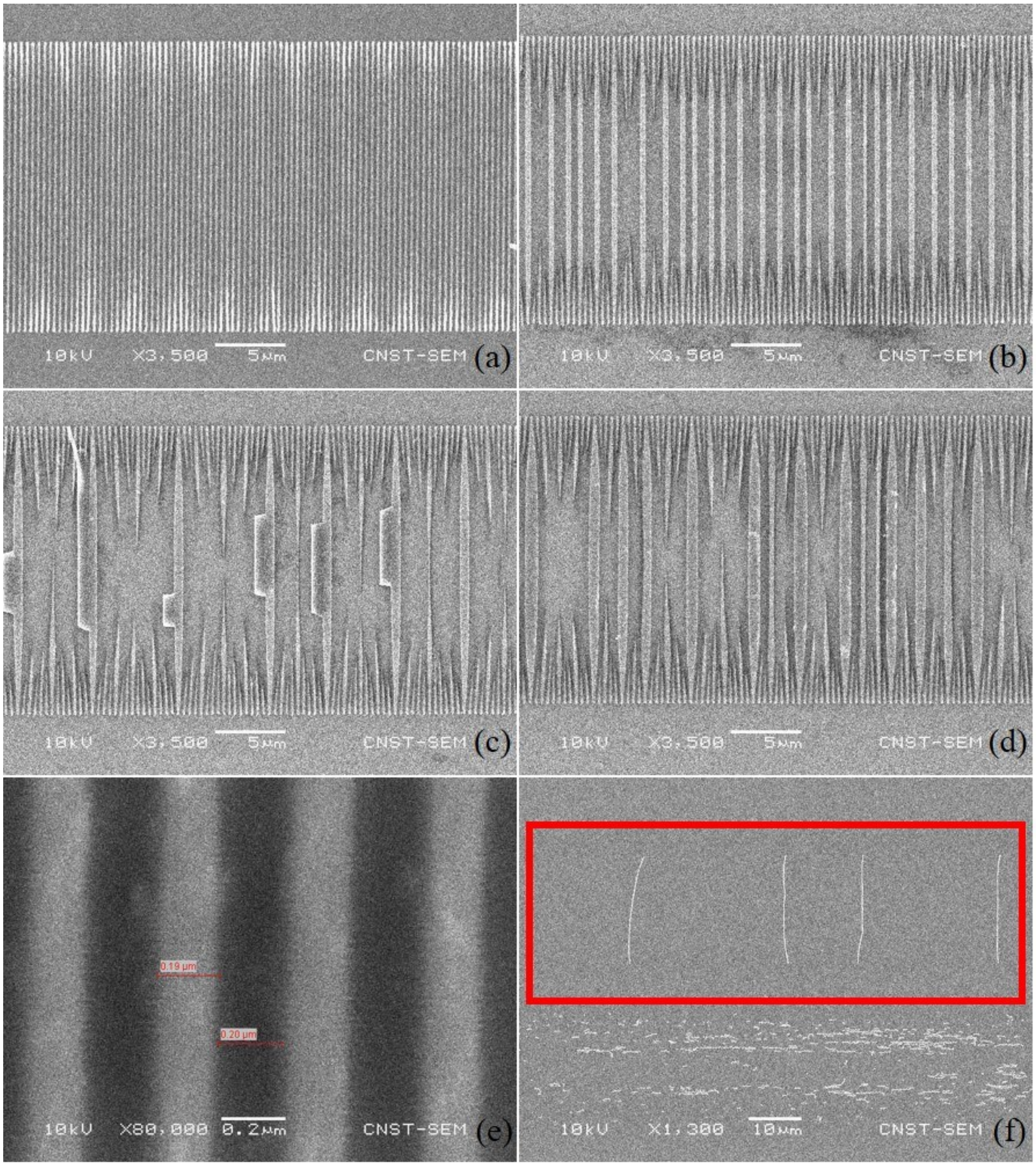

Figure 31. SEM images of various area dosage of perpendicular stripes during an EBL; 250 µC/cm^2 (a), 300 µC/cm^2 (b), 325 µC/cm^2 (c), 350 µC/cm^2 (d), close-up image of 250 µC/cm^2 (e), and in the red square 200 µC/cm^2 (f).

and Figure 31, fabrication of nanostripe patterns by the EBL was strongly dependent on the applied area dosage [57-59]. Factors of the patterning damages are classified as underexposure, overexposure, micellization, and collapse [57].

Figure 30 (f) and Figure 31 (f) are the same SEM images for a 200 $\mu C/cm^2$ which are given clearly underexposed patterns. This damage results in insufficient exposure to generate the stripe patterns. A mild underexposed pattern is shown in Figure 30 (a). Figure 30 (c) for a 325 $\mu C/cm^2$ and (d) for a 350 $\mu C/cm^2$ of parallel stripes obviously illustrate some examples of collapsed pattern of the interline walls. The same evidence for the collapse are displayed in Figure 31 (b) for a 300 $\mu C/cm^2$, (c) for a 325 $\mu C/cm^2$, and (d) for a 350 $\mu C/cm^2$. This type of damage shows that the patterning lines bend or misplace the interline walls. In this case, the proximity effects are strongly considered in the collapsed pattern. Decreasing exposure of the electron beam can be expected when the lines get closer, because the scattering of electrons in the lines make an additional energy deposition. Thus, the forces of attraction between lines exceed those of anchoring the PMMA to the substrate [57, 60]. Figure 30 (b) for 300 $\mu C/cm^2$ for the parallel pattern and Figure 31 (a) for 250 $\mu C/cm^2$ for the perpendicular pattern prove suitable area dosage for a well-defined 200 nm width with a 400 nm period of 800 nm thick nanostripes. Figure 30 (e) and Figure 31 (e) display the close-up images of Figure 30 (b) and Figure 31 (a), respectively.

2.4 Thermal evaporation

Technology of creating thin films is a broad branch of the generic technology that has to do with surface coatings. Moreover, the technology covers various thickness ranges from a few angstroms to a few microns. One of the most commonly used thin films technology is thermal evaporation. The thermal evaporation technique has been widely used for a fabrication of nanoscale devices. In general, the thermal evaporation method is a simple process in which a heated source is vaporized and deposited on a substrate located a distance above at certain conditions such as pressure, temperature and type of substrate [61-63]. The simple principle of the thermal evaporation is that thermal energy is impacted to atoms of the metal sources. So, they efficiently evaporate when their temperature is raised to their evaporation points [64].

Furthermore, thin film deposition systems usually are vacuum systems. The vacuum is an important part of the evaporation method. The aim of vacuum science and technology is to reduce the number of atoms and molecules in the chamber. For example, if there are too many gas atoms and molecules between a Au source and a substrate, the Au to gas collisions would be so high that the Au could not possibly be able to reach the substrate because of energy loss due to the collisions. Hence, the vacuum system is required to prevent this phenomenon during evaporation. Physical phenomena, such as molecular density or mean free path, are changed in the various vacuum regimes. Several pressure ranges are known as low vacuum (atmosphere to 25 Torr), medium vacuum (25 to $1\text{x}10^{-3}$ Torr), high vacuum ($1\text{x}10^{-3}$ to $1\text{x}10^{-9}$ Torr), and ultra-high vacuum (beyond 1×10^{-9} Torr). As the vacuum increases, the molecular density of the residual materials decreases, and mean free paths of the materials increase as well [64-67].

The details of the thermal evaporation technique, which was used to grow superconducting thin films, insulating layers, and contact pads, are now reviewed. Figure 32 displays that the thermal evaporator system, which was employed for this project. It consists of a rotary mechanical pump, diffusion pump, and vacuum chamber. The combination of the mechanical pump and the diffusion pump allows the mechanical pump to maintain the diffusion pump outlet pressure, because the diffusion pump cannot directly pump the gases out from the chamber without fore pumping [64].

Figure 32. A picture of the thermal evaporator system.

Table 2. The evaporation sources.

Material	Purity	Type of Boat	Deposition Temperature
Au	99.99%	Tungsten Boat	Room Temperature
Ag	99.99%	Tungsten Boat	Room Temperature
Ge	99.999%	Tungsten Basket	Room Temperature
Sn	99.992%	Tungsten Boat	Quench Condensation
$Pb_{82}Bi_{18}$	99.99%	Tungsten Boat	Quench Condensation
Ni	99.9+%	Alumina coated Tungsten Boat	Room Temperature
Co	99.9+%	Alumina coated Tungsten Boat	Room Temperature
Cr	99.9%	Cr-plated Tungsten Rod	Room Temperature

In the process of the evaporation, the base pressure in the evaporator's chamber reached at 8.7×10^{-8} Torr with liquid nitrogen in the cold trap of the diffusion pump. To evaporate Au, Ag, Ge, Sn, and $Pb_{82}Bi_{18}$ sources, tungsten evaporation boats or baskets were used, because they provided an efficient manner of reaching high temperatures with low currents. Additionally, alumina coated tungsten boats were employed for the evaporation of Ni and Co. The advantages of using the alumina coated tungsten boats are good heat transfer and the inertness of alumina with most metals [68]. For Cr evaporation, Cr-plated tungsten rods were used for deposition of a Cr adhesive layer between Au contact pads and SiO_2 substrate. All the sources and boats are indicated in Table 2. The deposition rates of Au, Ag, Ge, Ni, Co and Cr were about 0.10 nm/sec.

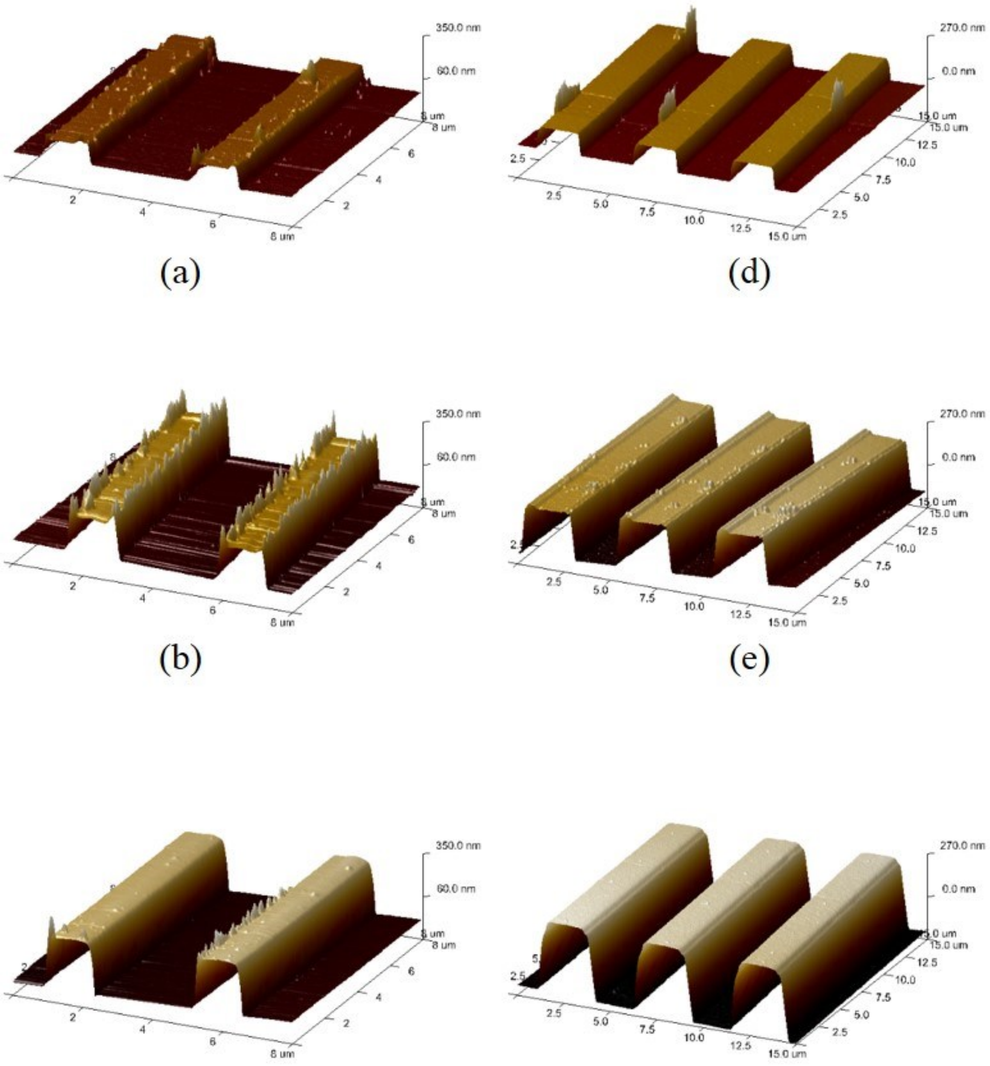

(a) (d)

(b) (e)

(c) (f)

Figure 33. Three dimensional AFM images of 123 nm Ni (scan size 8 μm x 8 μm) (a), 246 nm Ni (b), 341 nm Ni (c), 140 nm Co (scan size 15 μm x 15 μm) (d), 302 nm Co (e), and 440 nm Co (f).

On the other hand, the deposition rates of the superconducting materials, Sn and $Pb_{82}Bi_{18}$, were about 0.30 nm/sec.

For evaporation of the superconducting thin films, the quench condensation technique was used to get advantages of films consisting of clusters or grains in the early stages of the evaporations [69-73]. The temperature for the quench condensation in this research was 150~200 K. Some copper wires were connected between the sample mount of the substrate and the cold trap. The cold trap was cooled down by filling it with liquid nitrogen. Although the substrate was linked to the cold trap, the temperature of the substrate did not reach 77 K (liquid nitrogen temperature) because of radiation from the chamber walls at room temperature.

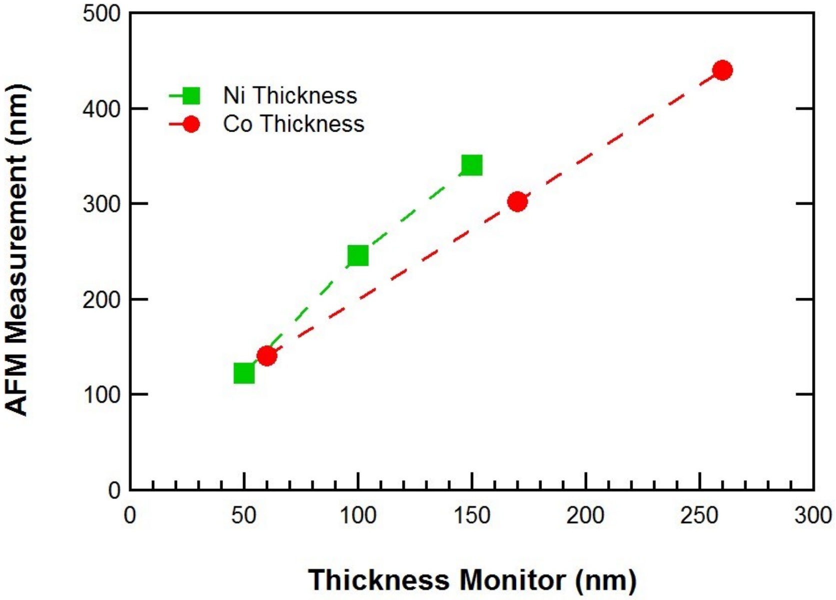

Figure 34. Thickness measurements by an AFM as a function of thickness monitor reading for the Ni and Co evaporations.

Thicknesses of the thin films were monitored during all the thermal evaporation with a quartz crystal microbalance (QCM). The thicknesses of the thermally evaporated Ni and Co were calibrated with several different depositions. Figure 33 displays three dimensional AFM images of different thicknesses of Ni and Co thin films. Additionally, since the films were deposited at the same deposition rate, it is obvious that the thicknesses of the thin films are proportional to the deposition times. In Figure 34, the results of measurement by an AFM in the tapping mode indicate that the real thicknesses of the thermally evaporated Ni and Co thin films were twice as thick as the QCM reading.

2.5 Electroplating

Electroplating or electrodeposition is one of many widely used techniques for metal coatings in science and engineering. The electroplating technology is the fabrication of thin films for protecting easily corroded surfaces, creating surfaces with particular properties, or researching physical properties of thin films. The electroplating technique provides relatively cost and time effective method, because it does not require high vacuum systems or high temperatures. Also, the electroplating method is easier and faster than a physical or chemical deposition process in a vacuum system [74, 75]. Therefore, the electroplating technique has been applied for fabrication of microelectromechanical systems (MEMS) or nanostructures.

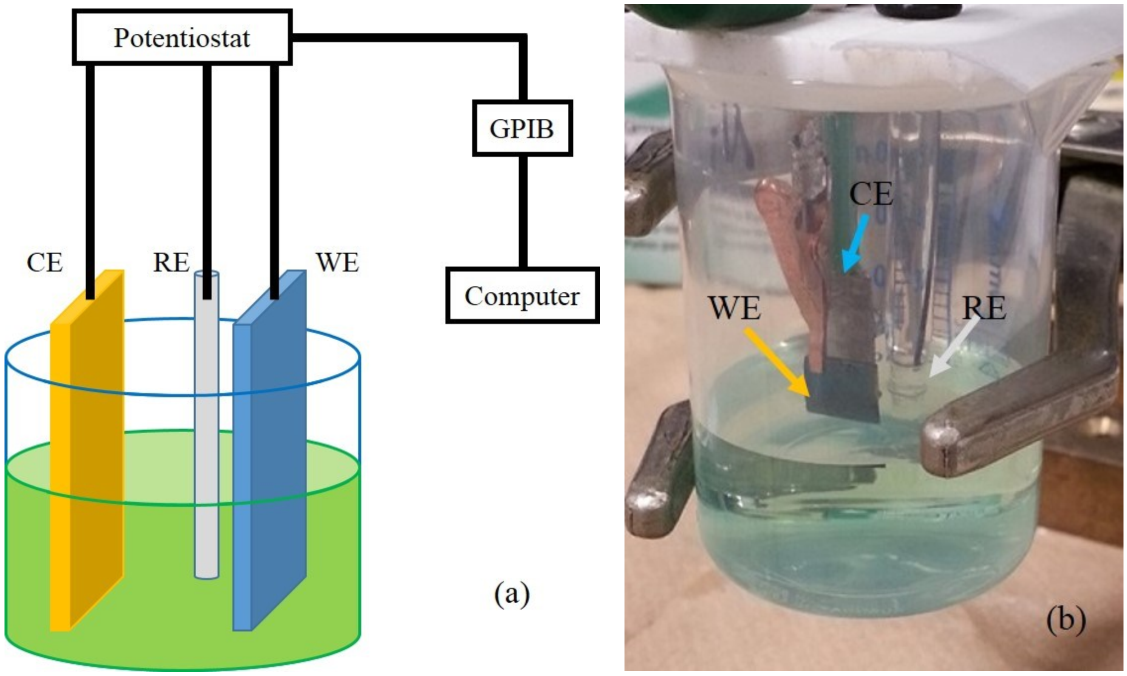

Figure 35. A schematic view of a three-electrode cell (a) and a picture of the electroplating setup for the Ni electroplating (b).

Basically, the electroplating method is the process of a metal coating on a metal surface by applying constant currents or potentials. In an electrochemical cell, there are two electrodes which are separated by at least one electrolyte phase. Also, in the electrochemical cell, a potential difference can be measured between the electrodes. Hence, the control and measurement of the potential in the cell is one of the most important parts of electrochemistry experiments. The electrodes in a three-electrode system are a combination of a working electrode (WE), counter electrode (CE), and reference electrode (RE). In general, chemical reactions in the cell consist of two independent half-reactions. The half-reactions in the cell describe the real chemical alterations at two electrodes. At the corresponding electrode, each half-reaction replies to the interfacial difference of the electrical potential. One of these reactions occurs at a WE. A WE is that at which the reaction of interest occurs. Some inert materials such as Au, Pt, or Ag can be used for a general WE. The other reaction takes place at a CE that has essentially continuous composition. A RE is a stable electrode for electrical potential. Moreover, a RE is used for the potentials measurement and control in the cell. The saturated calomel electrode (SCE) and the silver-silver chloride (Ag/AgCl) electrodes are common REs from an experimental standpoint. Additionally, there is one another electrode that is called a CE or an auxiliary electrode. A CE is typically made of an inert material such as Au, Pt, or graphite. The role of a CE is source of electrons. This CE does not react in the electrochemical solution, because the applied current is passed between a WE and CE [74].

In this research, a conventional three-electrode cell, which was composed of a WE, CE, and RE, was used to make ferromagnetic nanostructures. Figure 35 (a) shows a typical three-electrode cell. The three-electrode cell is the most universal electrochemical cell setup. The WE separates from the CE. The RE is placed as close as possible to the surface of the WE. The potential difference between the WE and the RE is monitored and controlled all the time. Furthermore, the potential difference is specified by the experimenters. The potential difference between the WE and the CE generally is not measured. A potentiostat is used to measure the difference of electrical potential between the RE and the WE. It has a high input impedance, so that a negligible current is drawn through the RE. Thus, its potential will remain constant [74, 76].

Table 3. Composition of the Ni electrolyte (a) and Co electrolyte (b).

Ni Electrolyte	
Materials	Quantity
$NiSO_4 \cdot 6H_2O$	15.00 g/L
H_3BO_3	6.77 g/L
D.I. Water	1.00 L

(a)

Co Electrolyte	
Materials	Quantity
$CoSO_4 \cdot 7H_2O$	120.00 g/L
H_3BO_3	45.00 g/L
D.I. Water	1.00 L

(b)

A SI 1286, Solartron was used as a potentiostat and power supply in this study. Temperature of the electrolytes was 21 ± 1 °C [77-79]. The WE was made of a thermally evaporated Ag thin film to carry out the electroplating. Thickness of the Ag WE was 15~20 nm. The Ag/AgCl as RE was purchased from BASi Corporation. The CE was a Ni plate or Co plate for Ni or the Co electroplating, respectively.

For Ni electroplating, the Ni electrolyte was composed of Nickel (II) sulfate hexahydrate ($NiSO_4 \bullet 6H_2O$), and Boric acid (H_3BO_3). The solid $NiSO_4 \bullet 6H_2O$ and H_3BO_3 were dissolved in DI water on a stirrer. Figure 35 (b) displays the three-electrode setup for the Ni electroplating.

For the Co electroplating, a single bath was used that contained Cobalt (II) sulfate heptahydrate ($CoSO_4 \bullet 7H_2O$), and Boric acid (H_3BO_3). These chemicals also were dissolved in DI water with stirring. The boric acid in both electrolyte was used to keep the pH ~3.5. The composition of the Ni electrolyte and Co electrolyte are seen in Table 3 [80].

A constant potential of -1.20 V was applied for 12 seconds for the electroplating of Ni nanostructures. Another constant potential of -0.90 V was applied to grow the Co nanostructures for 120 seconds [77-79, 81]. The thicknesses of the electroplated thin films or the nanosized structures were proportional to the electroplating time. Figure 36 depicts the steady potentials as a function of the electroplating time of the Ni and Co nanorods or nanostripes.

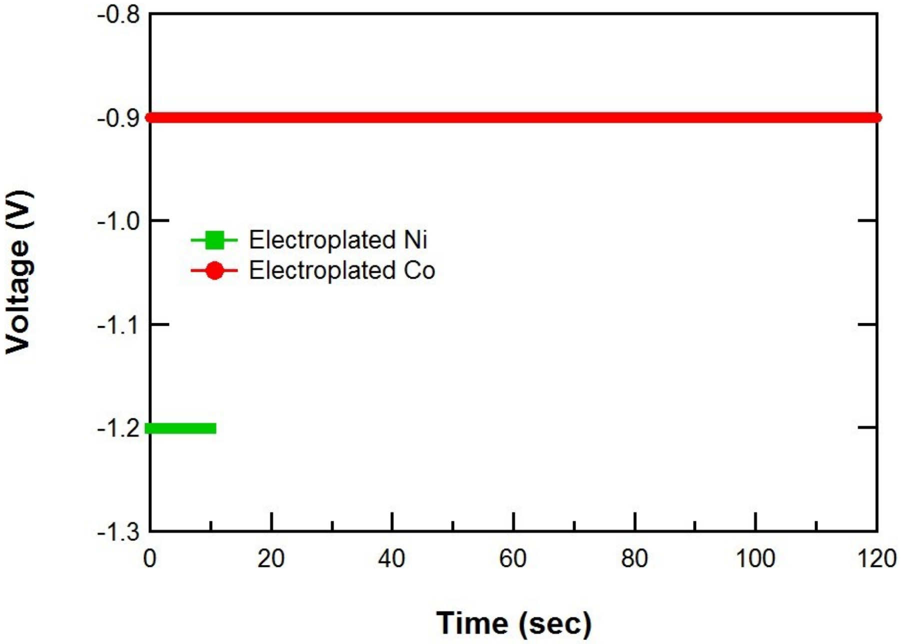

Figure 36. Applied potential as a function of electroplating time for Ni (-1.20 V) and Co (-0.90 V).

3. OBSERVATION OF THE FABRICATED SAMPLES

Observation of the samples has played an important role in the fabrication of FSH samples. Evaluation of the samples has provided opportunities for structure modification and quality enhancement. In this chapter, thickness dependence of the Sn thin films' surface is investigated. An SEM and an AFM were utilized to examine the surface of the Sn thin films. In order to see nanoscale Ni and Co arrays, an SEM and an MFM were used. Finally, SEM images of the completed FSH samples are seen.

3.1 Surface of the Sn thin films

A thermal evaporation was carried out to deposit various thicknesses of Sn thin films. The substrate was a Si wafer with a SiO_2 layer. A 3 nm Ge interlayer was deposited using the thermal evaporator between the SiO_2 and the Sn thin films as an adhesive layer. Liquid nitrogen was filled into the cold trap of the sample mount in the evaporation chamber for quench condensation throughout the Sn evaporation. The thickness of the thin films were controlled by deposition times and monitored by a QCM in real time. For these Sn thin films, the deposition rate was around 0.11 nm/sec, and base pressure in the evaporator chamber was at 8.7×10^{-8} Torr.

Figures 37 (a) and (b) show three dimensional AFM images of the surface of SiO_2 and the 3 nm insulating Ge layer, respectively. The scan size is 450 nm x 450 nm for the SiO_2 and 3.0 μm x 3.0 μm for the Ge thin film. AFM scans were operated in the tapping mode. The Si wafer with the SiO_2 layer substrate was sufficiently flat to grow high quality thin films. The root mean squared (RMS) surface roughness of the substrate was 0.153 nm. For the 3 nm Ge layer, the surface roughness was 0.331 nm.

Figure 38 displays SEM (JEOL JSM-7500F, from the MCF at TAMU) images (80,000x) and AFM amplitude error mode images (scan size 1.0 µm x 1.0 µm) for 30 nm, 50 nm, and 100 nm thick Sn thin films. The SEM images in Figures 38 from (a) to (c) indicate that the Sn films grow similarly to layer-plus-island mode (or Stranski-Krastanov mode). The Sn films were grown layer-by-layer up to a stable wetting layer. Subsequent growth revealed three dimensional islands growing on the Sn rich layer [82-84].

Two dimensional and three dimensional AFM images of surface of the Sn films are shown in Figure 39. These images display the surface roughness increasing with the Sn films' thickness.

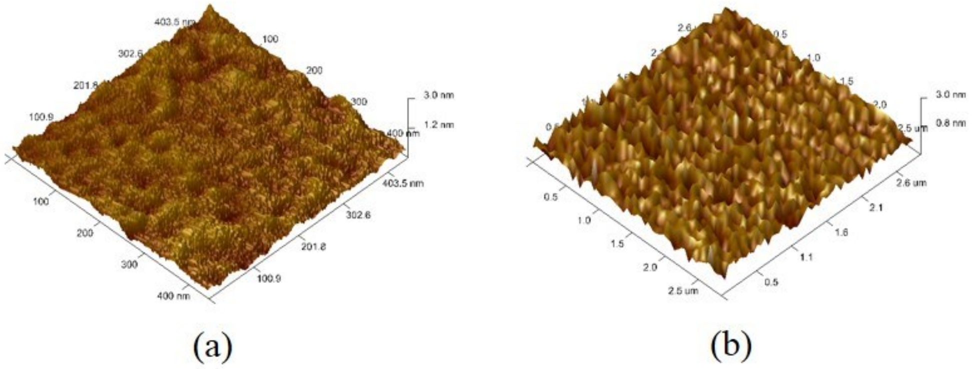

(a) (b)

Figure 37. Three dimensional AFM images for the surface of SiO_2 (a) and 3 nm Ge thin film (b).

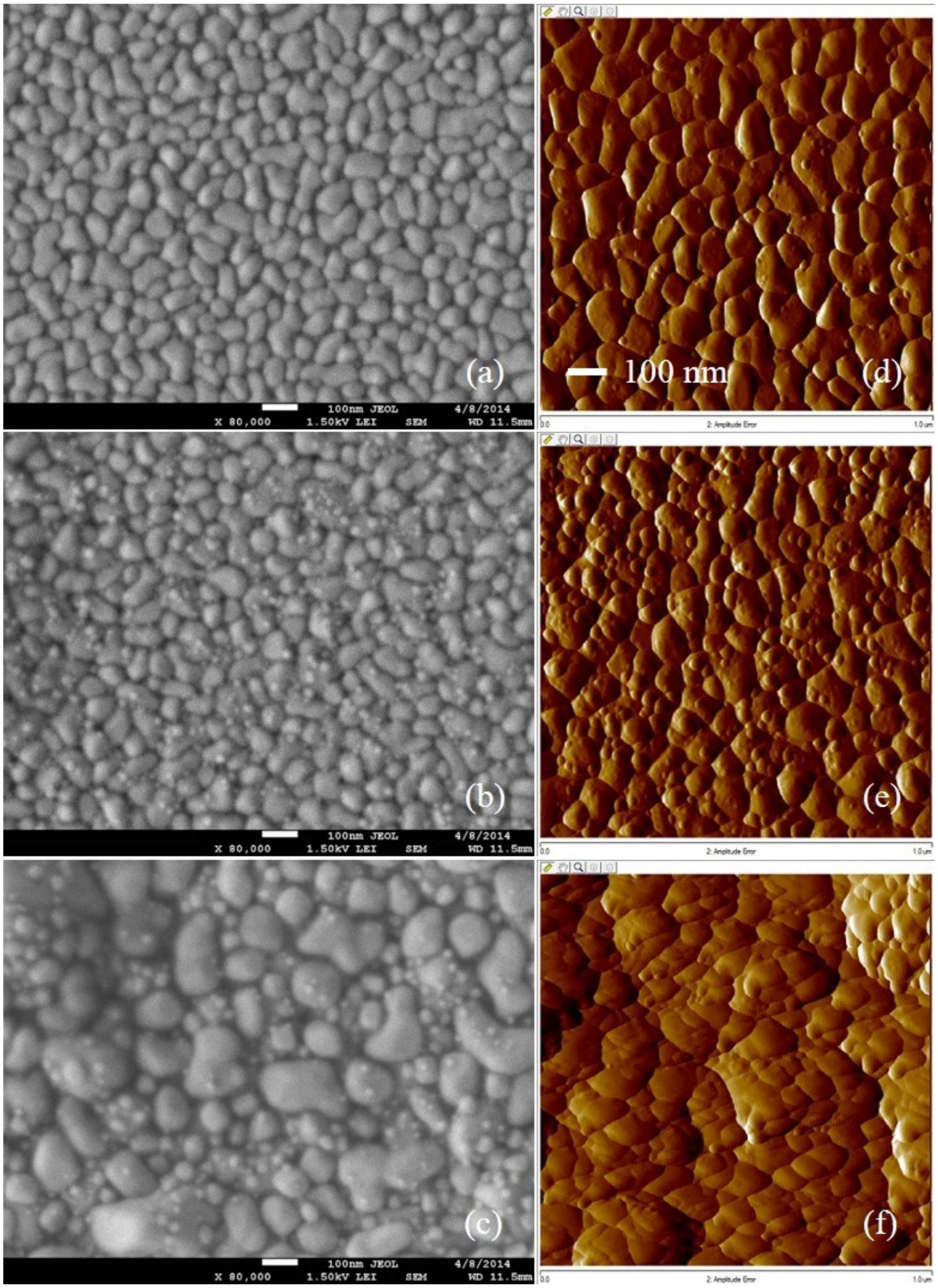

Figure 38. SEM images of 30 nm Sn (a), 50 nm Sn (b), and 100 nm Sn (c) and AFM amplitude error images of 30 nm Sn (d), 50 nm Sn (e), and 100 nm Sn (f).

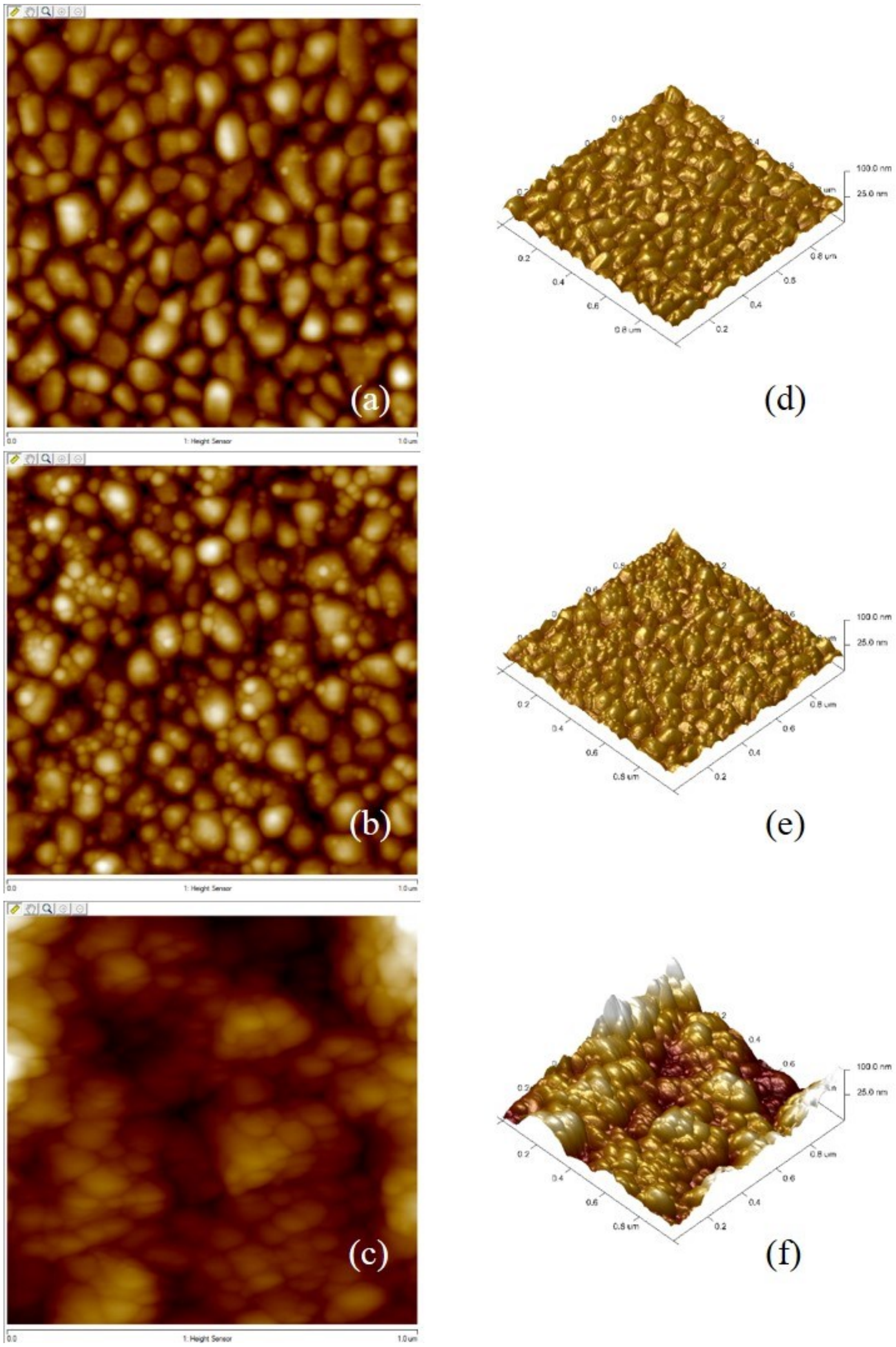

Figure 39. Two dimensional AFM images of 30 nm Sn (a), 50 nm Sn (b), and 100 nm Sn (c) and three dimensional AFM images of 30 nm Sn (d), 50 nm Sn (e), and 100 nm Sn (f).

Morphological grain sizes of the AFM images were measured [85]. The results demonstrated that the morphological grain size increased with the Sn film thickness. Figure 40 displays the surface roughness and the morphological grain size as a function of the Sn film thickness. The diameter of the grain size increases with the thickness of the Sn films, and results in the decrease of the surface density of islands [83]. Thus, surface roughness and grain sizes of the Sn films depend on the thickness of the films [86-88].

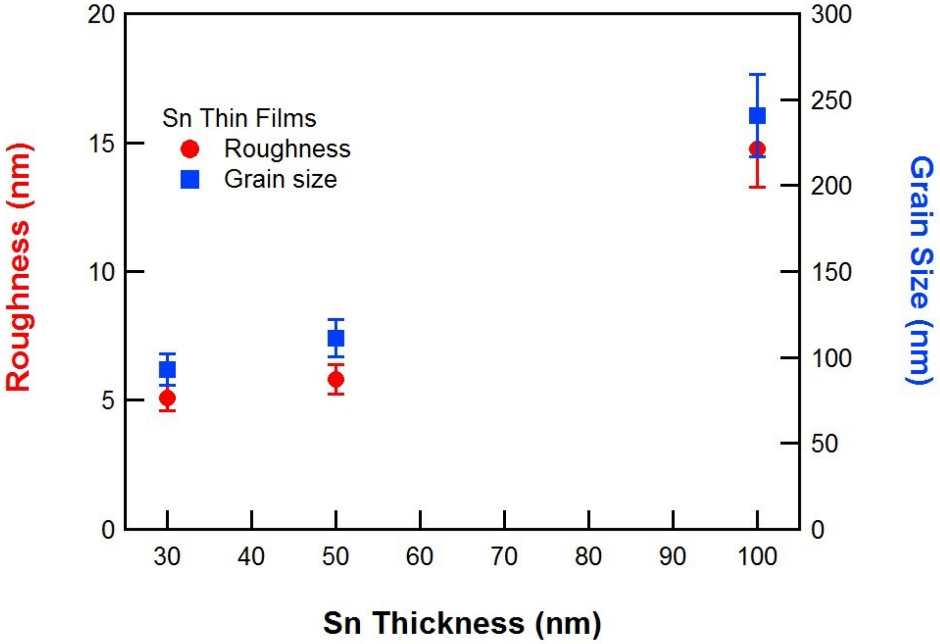

Figure 40. Surface roughness and grain size as a function of thickness of the Sn films.

3.2 Thermally evaporated ferromagnetic nanostructures

Ferromagnetic nanostructures were fabricated by thermal evaporation. SEM images in Figure 41 depict parallel Ni stripes and perpendicular Ni stripes on top of a Sn film. There was a 20 nm Ge insulating layer between the Sn film and the Ni nanostripes. The fabrication process of the Ni nanostripes was discussed in subchapter 2.4. The Ni nanostripes were designed to have a 100 nm width and a 500 nm period. The thickness of the Ni nanostripes was 121 nm. Figure 41 proves that the thermally evaporated Ni nanostripes were well-defined.

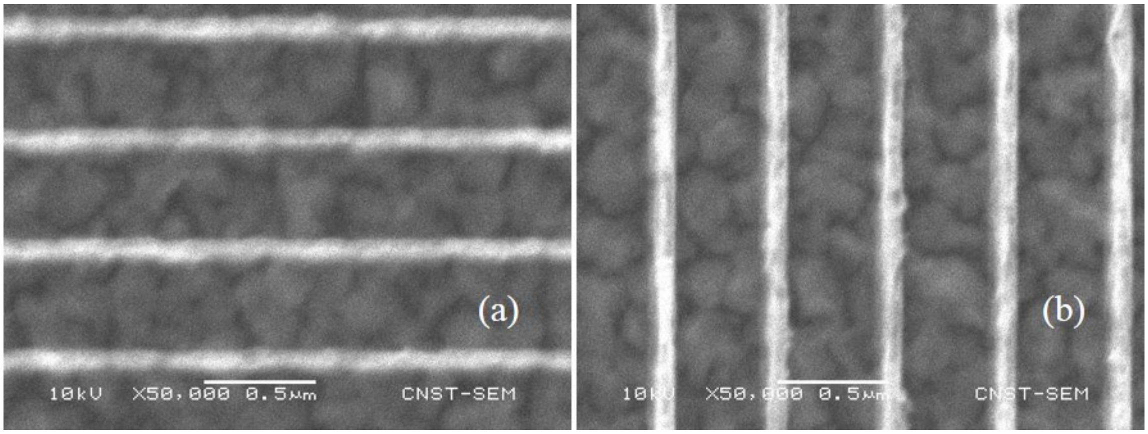

Figure 41. SEM images of thermally evaporated Ni with a 100 nm width and a 500 nm period stripes for a parallel sample (a) and perpendicular sample (b).

A Bruker Dimension Icon AFM, from the MCF at TAMU, was used as a Magnetic Force Microscope (MFM). MFM images, as shown in Figure 42, elucidate that the intensity of magnetization depends on the height of Ni stripes when the width of the lines are the same. Ni nanostripes were created with a 100 nm width and a 500 nm period. The sample in Figure 42 (a) has a 121 nm height, and the sample in Figure 42 (b) has a 250 nm height. Thus, if a high aspect ratio of nanosized ferromagnetic structures can be fabricated, an effect of the nanostructures on superconducting thin films would be clearly seen. The MFM images exhibit some lighter parts on the nanostripes that is because of a rough superconducting layer underneath the thermally evaporated Ni nanostripes.

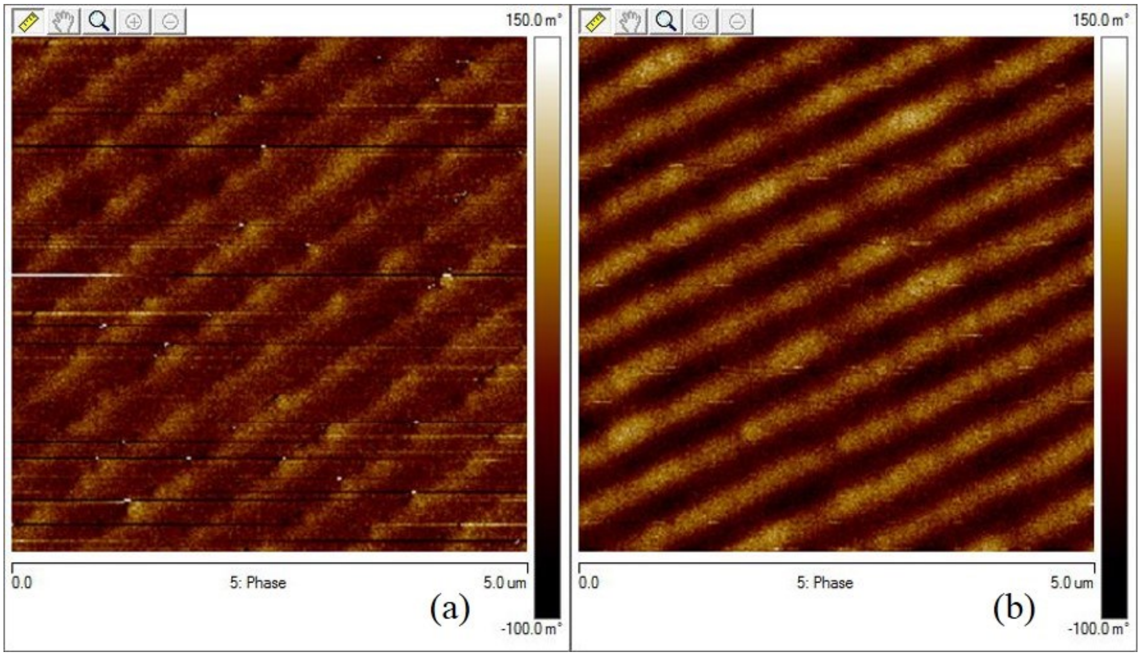

Figure 42. MFM images of the thermally evaporated Ni stripes with a 100 nm width, a 100 nm height and a 500 nm period (a) and Ni stripes with a 100 nm width, a 250 nm height and a 500 nm period (b).

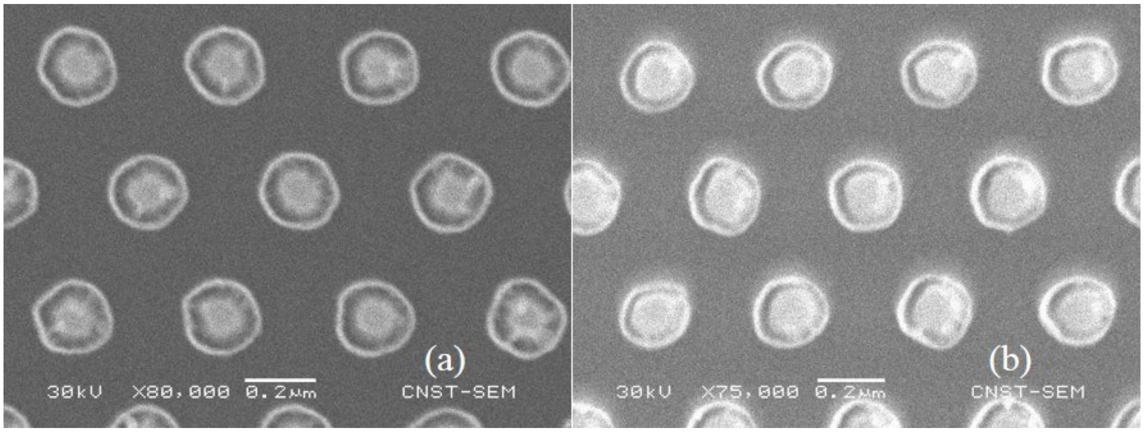

Figure 43. SEM images of the thermally evaporated Ni nanorods (a) and Co nanorods (b).

Figure 43 (a) shows an SEM image of the thermally evaporated Ni nanorods with a 200 nm diameter, 300 nm height, and 400 nm period and Figure 43 (b) shows the SEM image of the Co nanorods. Both the Ni and Co nanorod arrays are well-defined.

The magnetization of the Co is about three times greater than that of the Ni, and they show magnetic anisotropy, as shown in Figure 9 in subchapter 1.4 [25, 26]. Magnetic properties of the thermally evaporated Ni and Co nanorods were characterized with an S-VSM (Vibrating Sample Magnetometer) from Quantum Design. The results of measured magnetic properties of the Ni nanorods in Figure 43 (a) and Co nanorods in Figure 43 (b) are given in Figures 44 (a) and (b), respectively. Both the Ni and Co nanorods exhibited hysteretic behavior. The magnetization of the Co nanorods is about four times greater than that of the Ni, as shown in Figure 44. Thus, various magnetic effects could be expected on FSH from the dependence of ferromagnetic materials. Magnetic properties of Ni and Co were already discussed in subchapter 1.4.

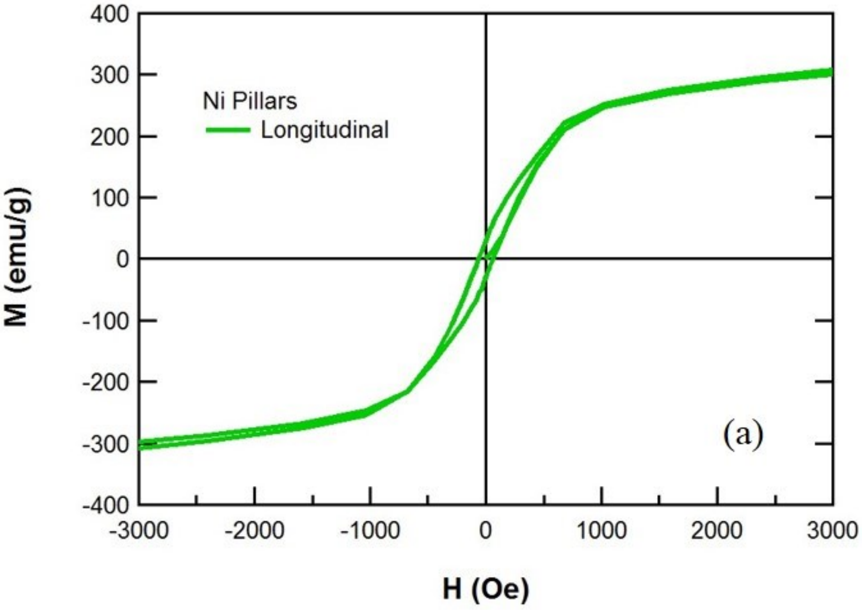

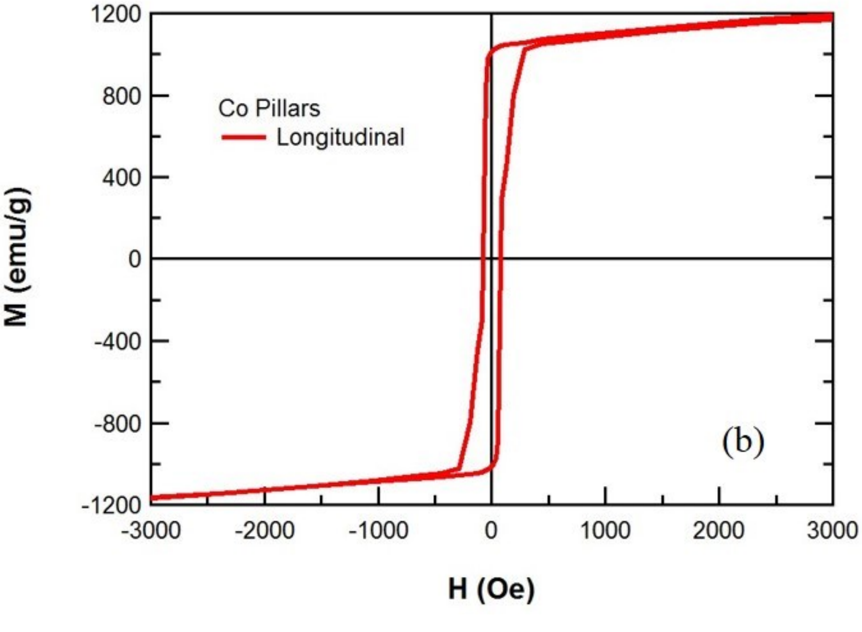

Figure 44. Magnetic properties of the thermally evaporated Ni (a) and Co nanorods (b).

In order to fabricate high aspect ratio nanoscale ferromagnetic structures, two main issues should be solved.

An angled SEM image in Figure 45 (a) shows that one of the main problems is a poor lift-off process after metallization. The Ni evaporated on the sidewalls of the patterned PMMA. Although the substrate was gently shaken in an acetone bath by hand during the lift-off process, the unwanted evaporated Ni on the PMMA was not effectively removed. A sonication could be used to remove the unnecessary Ni structures on the PMMA; however, the superconducting thin films less than 100 nm underneath the nanosized ferromagnetic structures might be damaged by sonication.

Another angled SEM image, as shown in Figure 45 (b), displays the other problem. When the aspect ratio of the patterned cylinders is too high, conical Ni nanorods with hollow cylinders were grown by the thermal evaporation process. This is because the patterned holes were gradually closed with increasing thickness of the depositing metal layer, as shown in Figure 45 (c). This is called the non-conformal step-coverage problem. In general, the step-coverage is not a problem for a low aspect ratio; for instance a 100 nm height with a 500 nm width trench. However, for a high aspect ratio, the step coverage problem dominates [55, 89, 90]. For the non-conformal step-coverage, the mean free path of the molecules in the gas phase during the deposition at low pressure is greater than the step dimensions of the patterns on the substrate. Also, there is no surface migration of the molecules. The solid angles associated with points at the sidewalls when the step has a trench shape with a high aspect ratio, because of a supplementary step coverage caused by the other side of the trench. Then, the step coverage is predicted to deteriorate with the increasing aspect ratios of the trench. The mean free path of the surface migration normally rises with the temperature. Consequently, the step coverage can be improved by increasing deposition temperature [91-94]. As mentioned earlier, superconducting thin films were deposited by thermal quench condensation. Thus, increasing the deposition is not an appropriate solution in this research. To avoid the non-conformal step coverage on the high aspect ratio EBL patterns, another fabrication technology is needed to produce high aspect ratio nanostructures.

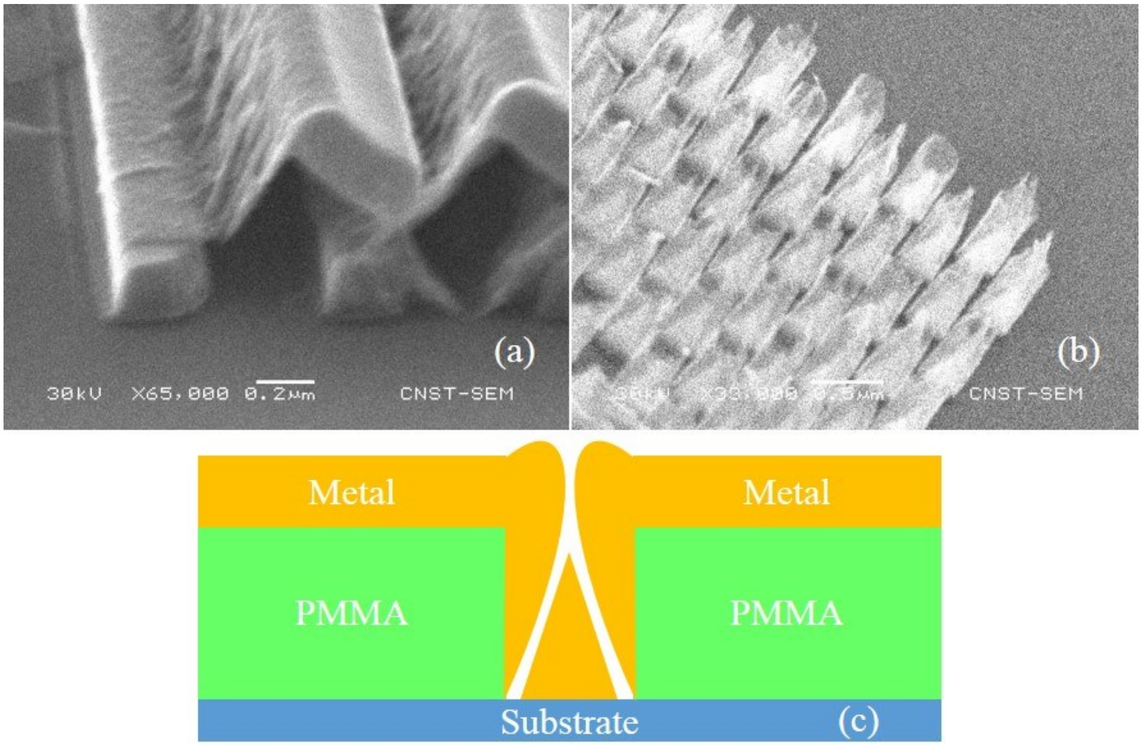

Figure 45. An angled SEM image of the thermally evaporated Ni nanostripes (a) and nanorods (b), and a schematic of the non-conformal step-coverage (c).

3.3 Electroplated ferromagnetic nanostructures

An electroplating technique was chosen in order to avoid the non-conformal step-coverage. Standard electrode reaction potential depends on the materials in the electroplating process [75, 95]. This means that all materials have a different reaction potential. In order to find the appropriate conditions for the Ni or Co electroplating, various constant potentials were applied for testing.

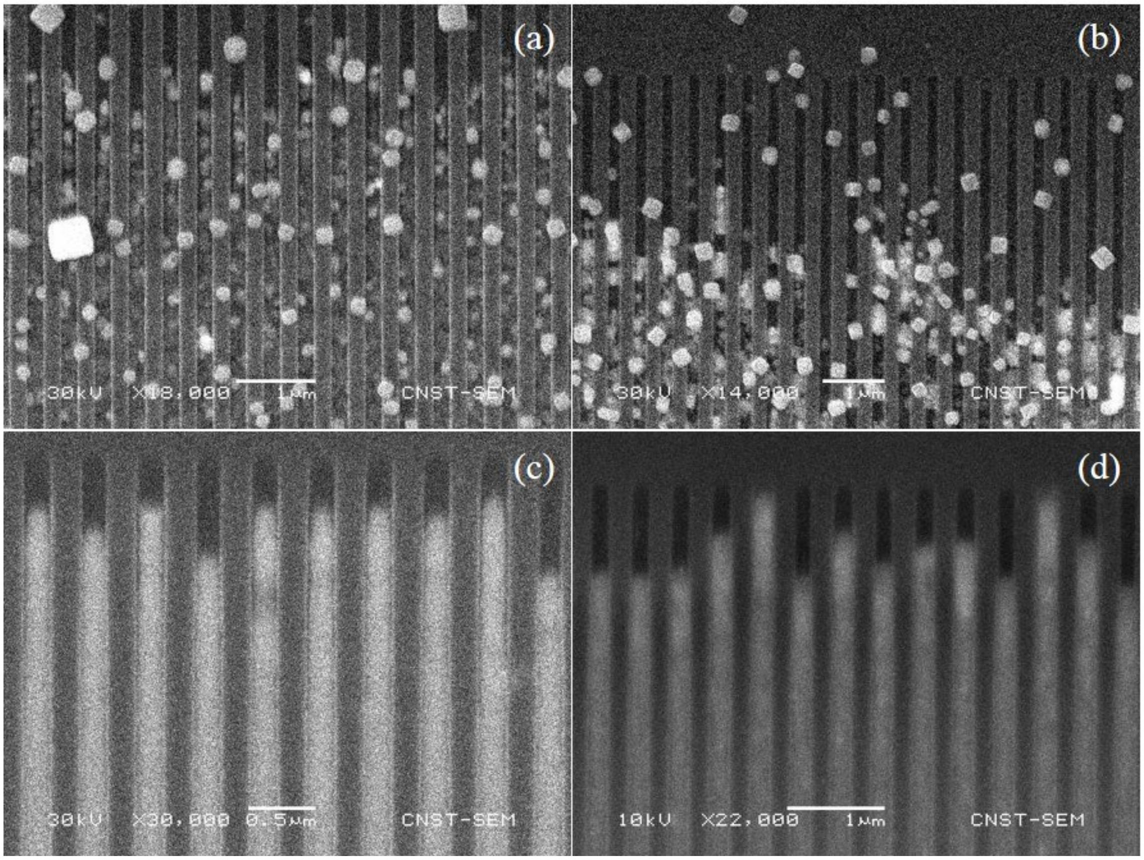

Figure 46. SEM images of the Ni nanostripes at various electroplating potentials for five seconds: -1.0V (a), -1.1 V (b), -1.2 V (c), and -1.3 V (d).

For optimization of the Ni electroplating, different constant potentials such as -1.0 V, -1.1 V, -1.2 V, and -1.3 V were applied to the electrodes for five seconds. Ni stripes electroplated at several potentials are shown in Figure 46. The EBL patterns were created with a 200 nm width and a 400 nm period. Figures 46 (a) and (b) show that an applied potential of -1.0 V and -1.1 V, respectively, were inappropriate for the Ni electroplating, resulting in unfilled patterns. Although Figure 46 (d) seems to contain successfully electroplated nanostripes, closer analysis revealed that using a potential of -1.3 V resulted in Ni overgrowth. The potential is hard to control in the deposition time of five seconds. Hence, a constant potential of -1.2 V, as shown in Figure 46 (c), is suitable for the Ni electroplating with a longer electroplating time (12 seconds) for better control of the height of the Ni nanostripes.

In order to optimize Co electroplating, -0.8 V, -0.9 V, and -1.0 V were applied to the electrodes for 70 seconds. Figure 47 depicts SEM images of the electroplated Co on the EBL patterned substrate. Figures 47 (e) and (f) show overgrown Co nanostructures meaning that the magnitude of potential, applied to the electrodes, was too high. Since the nanostripes have to be separate, the electroplated Co should not be overgrown. Figure 47 (a) indicates a smoother surface in comparison with Figure 47 (c). Therefore, -0.8 V is the proper potential for electroplating Co nanostructures.

Figure 48 shows the overgrown Co stripes and rods. These SEM images illustrate that either the electroplating potential or time was not appropriately adjusted. These Co samples demonstrate poor electroplating condition for the EBL patterns. However, the electroplated nanostructures indicate that the developed EBL patterns indeed had a high

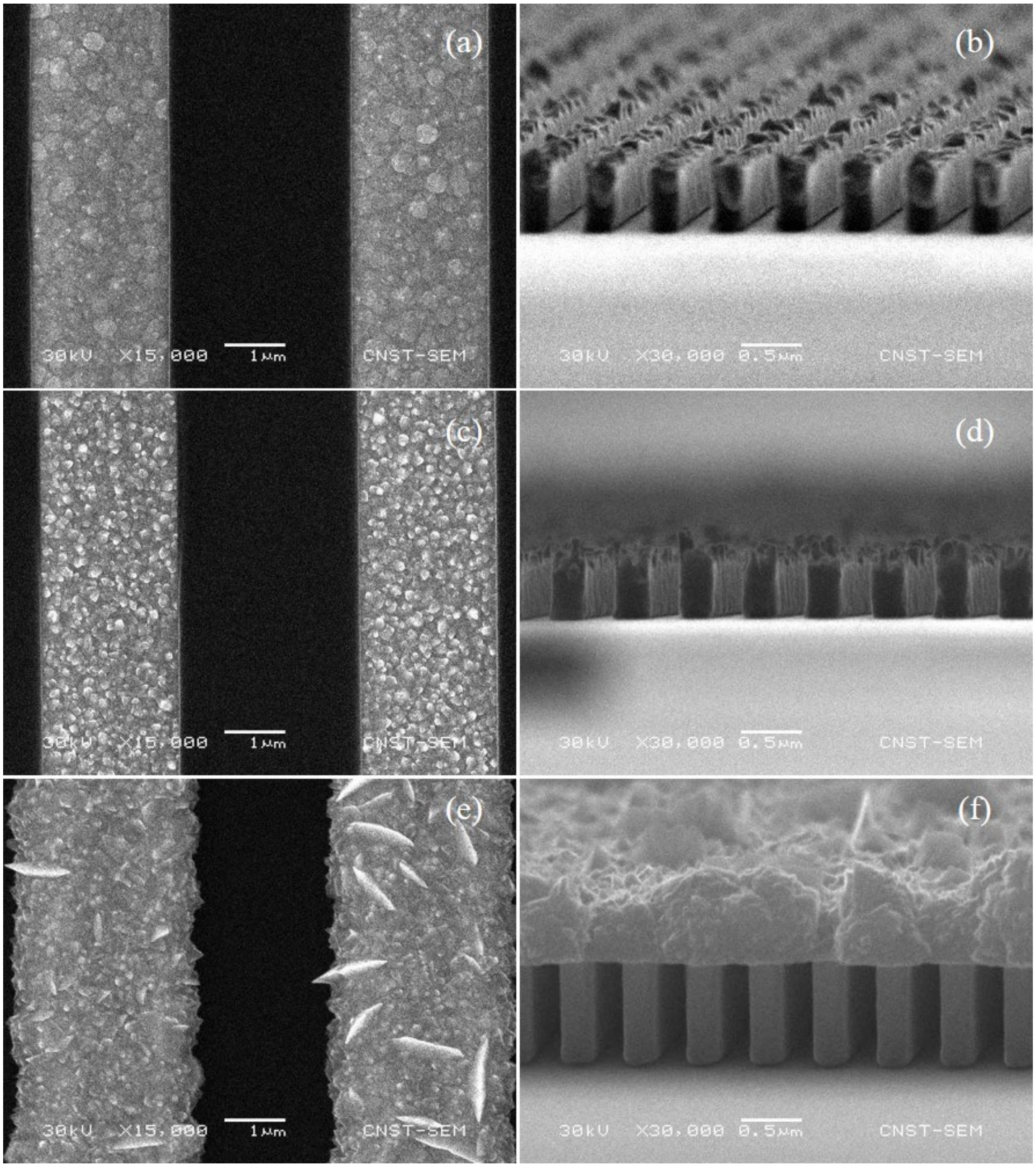

Figure 47. SEM images of the Co nanostripes with various electroplating potential for 70 sec with: -0.8V top view (a) and angled view (b), -0.9 V top view (c) and angled view (d), -1.0 V top view (e) and angled view (f).

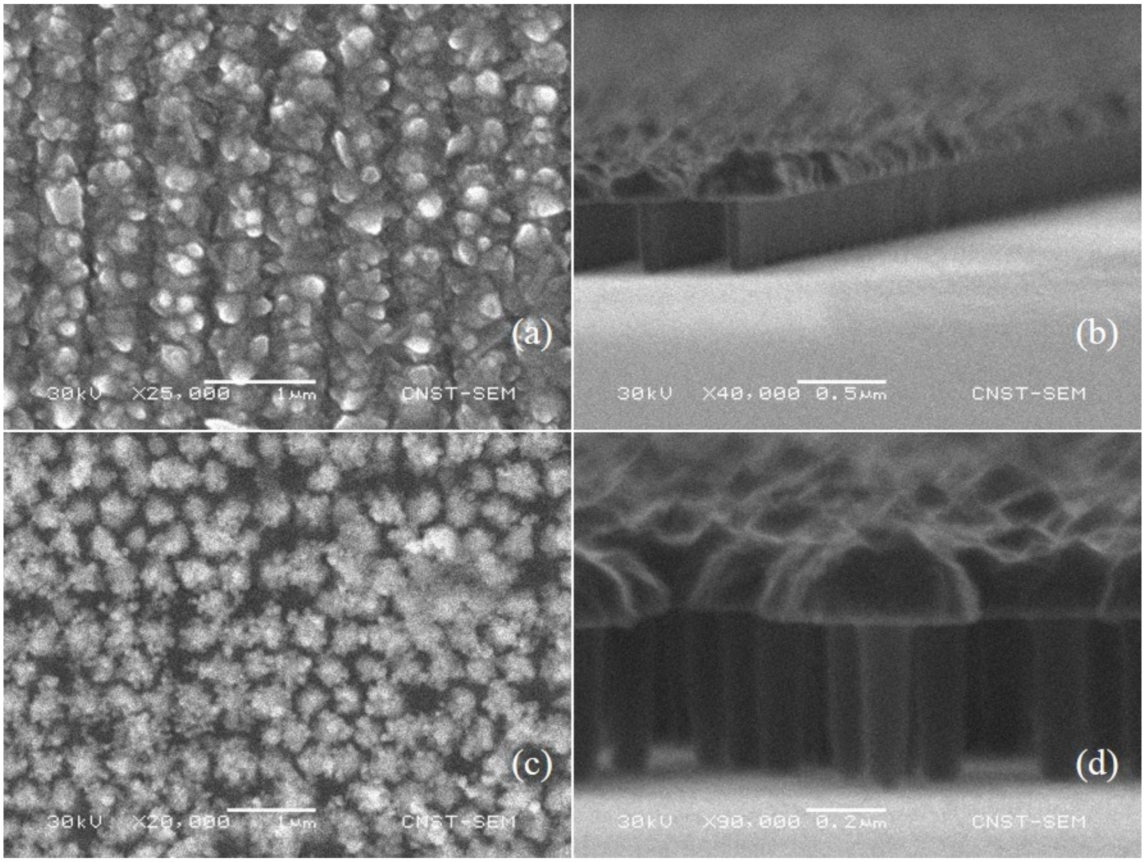

Figure 48. SEM images of the electroplated overgrown Co nanostripes of top view (a) and angled view (b), and nanorods top view (c) and angled view (d).

aspect ratio around 1:3.8.

Finally, -1.2 V was applied for 12 seconds for a 200 nm diameter and a 400 nm period nanorod array pattern to grow electroplated Ni nanorods, as shown in Figures 49 (a) and (b). The top surfaces of the nanorods are uniform, as shown in Figure 49 (a), and the height of the nanorods is around 750 nm in Figure 49 (b). The same conditions were used on the nanostripes patterns for the electroplated Ni nanostripes. In Figures 49 (e) and (f), the Ni nanostripes were separately created and well-defined.

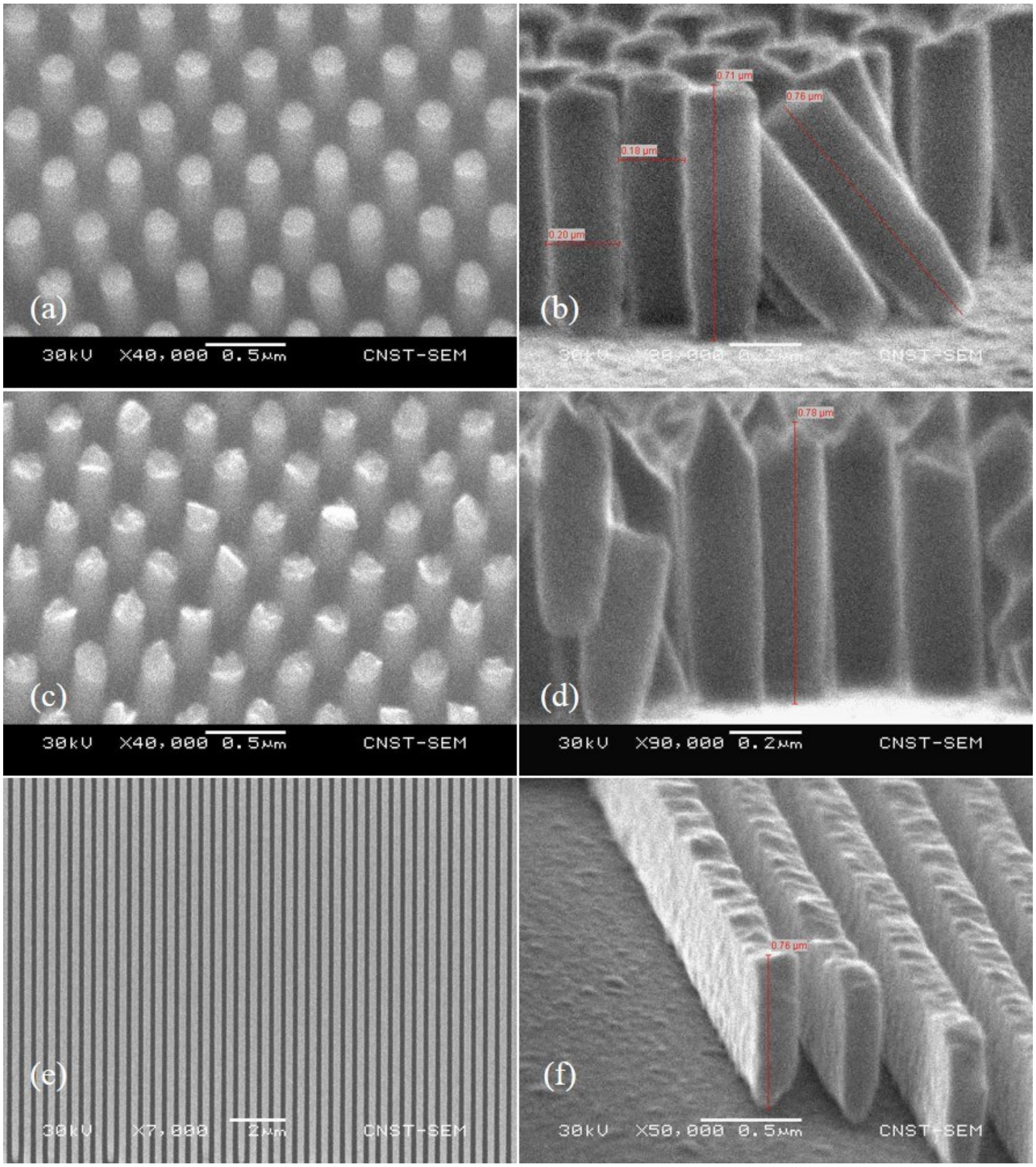

Figure 49. SEM images of the electroplated Ni nanorods of 45° angled view (a) and 85° angled view (b), Co nanorods of 45° angled view (c) and 85° angled view (d), and Ni nanostripes of top view (e) and 45° angled view (f).

In a similar way, the Co nanorod array was well-defined for a 200 nm diameter and a 400 nm period patterns, as displayed in Figures 49 (c) and (d). Constant potential was applied at -0.8 V for 120 seconds. The top surfaces of the Co nanorods were rougher in comparison to those of Ni nanorods. The surface roughness of the electroplated Co can be controlled by adding organic additives in the electrolyte [77, 96, 97]. These electroplating conditions will be used for the FSH samples.

3.4 Ferromagnet-Superconductor Hybrid samples

Ferromagnetic nanostructures such as Ni nanostripes and nanorods or Co nanostripes and nanorods were fabricated on top of superconducting thin films or embedded into the superconducting thin films. These ferromagnetic nanoscale structures were fabricated on the Sn, $Pb_{82}Bi_{18}$, or YBCO superconducting thin films. Although they all look the same, each of the three were created with different materials. Sn FSH sample is shown for the insulated FSH, and a $Pb_{82}Bi_{18}$ FSH sample is shown for the embedded FSH in this subchapter. SEM images of complete FSH nanostripes sample are displayed in Figure 50. The thermally evaporated superconducting thin films cover the Au contact pads for four-probe measurements. An example of the contacts between the Au pads and the superconducting thin films is circled in red in Figure 50 (a).

Figures 50 (c) and (d) show the thermally evaporated Ni nanostripes in a direction parallel and perpendicular to an applied current in the two Sn thin films, respectively. The white arrows in Figures 50 (c) and (d) indicate the direction of the applied current during the resistance measurement. The dimensions of the Ni nanostripes were a 100 nm width and a 121 nm height. Their period was 500 nm.

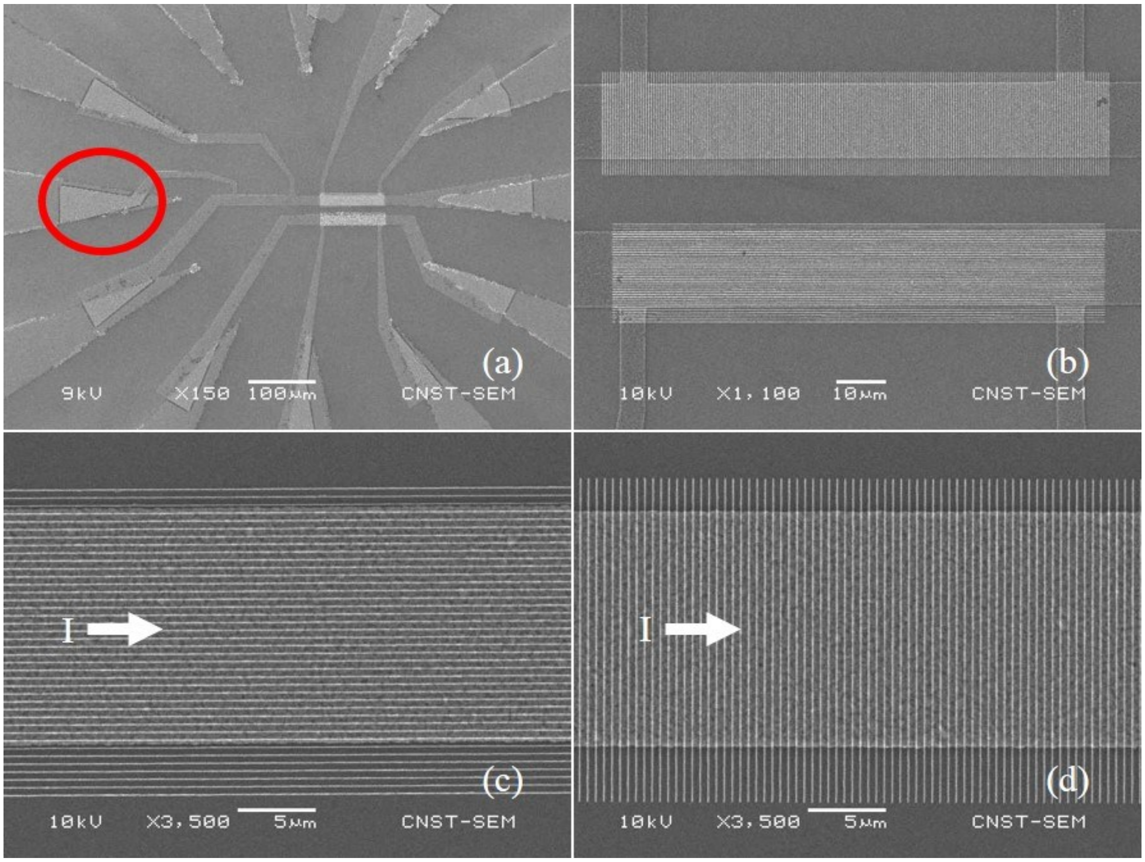

Figure 50. SEM images of the final Sn FSH sample for nanostripes at magnification at 150x (a), at 1,100x (b), at 3,500x for parallel stripes (c), and at 3,500x for perpendicular stripes (d).

Furthermore, Figure 51 shows an FSH sample with electroplated Ni and Co nanorods. The nanorods were generated on top of the superconducting thin films. Figure 51 (a) shows a top view SEM image of the FSH sample at low magnification (500x).

Figures 51 (b) and (c) are 45° angled SEM images of FSH samples with the Ni nanorods and the Co nanorods on top of Sn thin films, respectively. The electroplated Ni and Co nanorods were formed with a 200 nm diameter and a 750 nm height pattern. The nanorods were arrayed as triangular lattice, and the lattice constant was a 400 nm. The PMMA layers were not removed after the electrodeposition in order to support the high aspect ratio electroplated Ni and Co nanorods. Thus, the ferromagnetic nanorods are

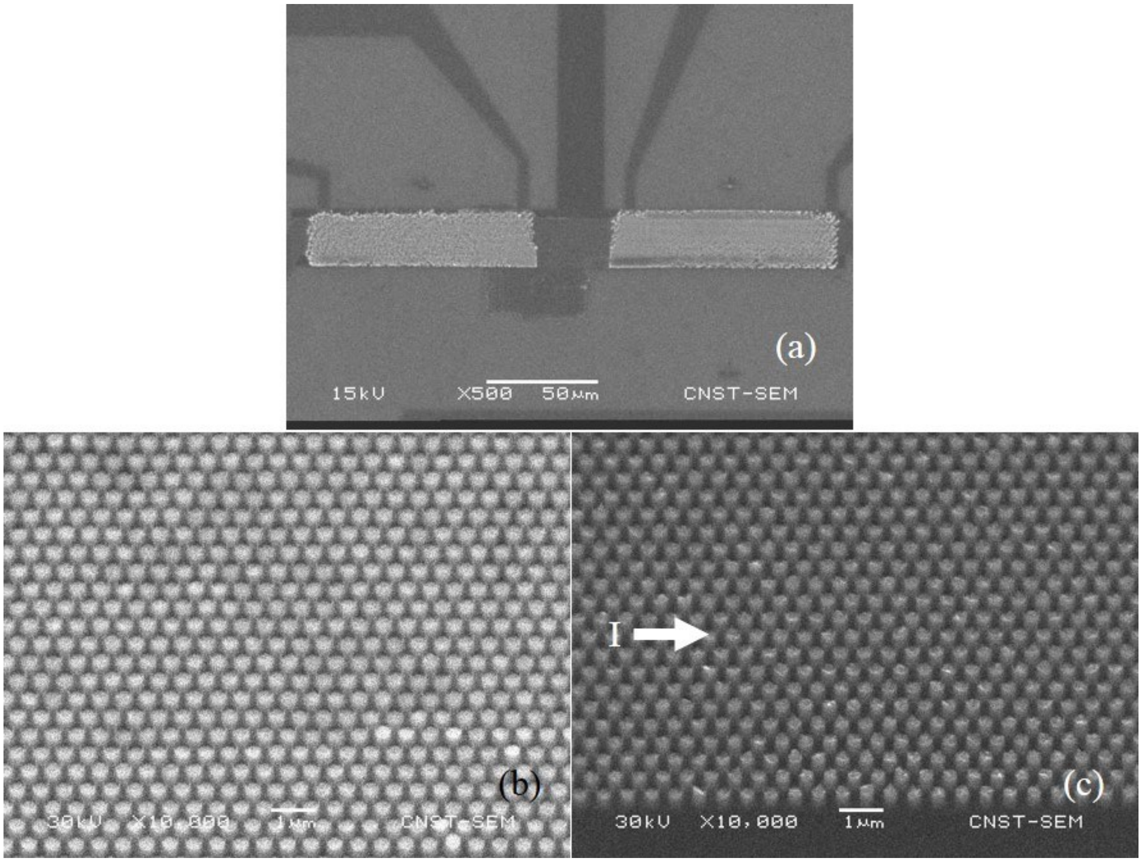

Figure 51. SEM images of the final Sn FSH sample for nanorods magnification at 500x (a), Ni nanorods at 10,000x with 45° angled view (b), and Co nanorods at 10,000x with 45° angled view (c).

oriented perpendicular to the superconducting thin films, i.e. the electroplated nanorods are parallel to the applied external magnetic fields. The PMMA layer did not interfere with the superconducting and magnetic properties of the FSH samples.

Lastly, SEM images of electroplated Ni nanorods embedded into a $Pb_{82}Bi_{18}$ thin film FSH are shown in Figure 52. Figure 52 (a) is a top view SEM image of the FSH, and Figure 52 (b) is a 45° angled view SEM image of the FSH. The tops of the Ni nanorods look rough, because the $Pb_{82}Bi_{18}$ thin film was thermally evaporated after fabricating the electroplated Ni nanorods. Thus, the top of the Ni nanorods were covered by the $Pb_{82}Bi_{18}$ thin film.

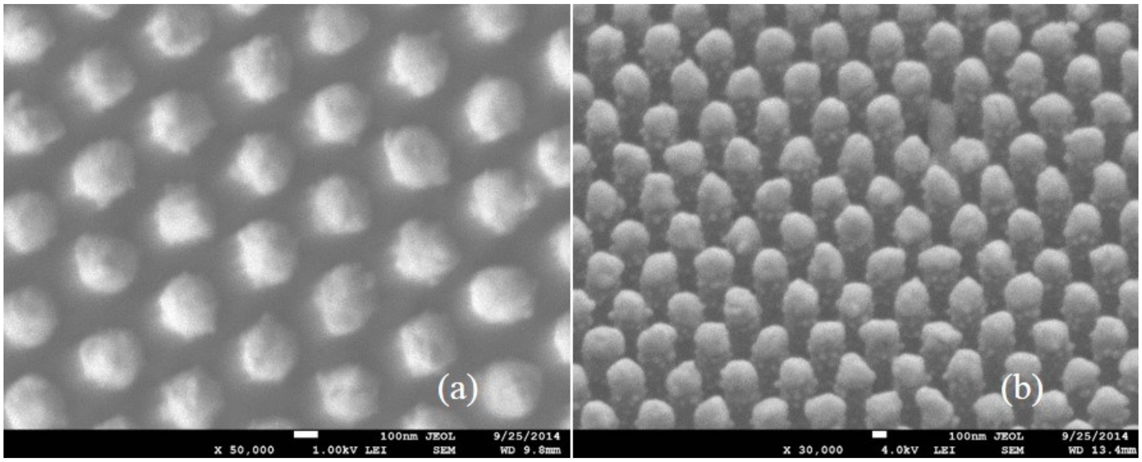

Figure 52. SEM images of the embedded electroplated Ni nanorods into the $Pb_{82}Bi_{18}$ thin film: top view (a) and 45° angled view (b).

4. CHARACTERIZATION OF THE CONTROL SAMPLES

A fundamental property of an equilibrium state of superconductors is the magnetic structure which occurs when external magnetic fields are applied. The equilibrium states of type I and type II superconductors are different, i.e. the intermediate and vortex states, respectively. The equilibrium state of the superconductors depends on the materials and its geometry. Even though a superconducting material in bulk may be type I with the intermediate state, the material can become a type II superconductor with a two-dimensional vortex state if its shape is a sufficiently thin film. When external magnetic fields are applied perpendicular to superconducting thin films, the magnetic properties even for type I material strongly depend on the thickness of the film. Therefore, thin films of type I superconductors, whose value of κ is smaller than $\frac{1}{\sqrt{2}}$, can be type II superconductors if thickness of the thin films are satisfied below the critical thicknesses [98-101]. The experimental results of the critical thicknesses of several materials were reported. The values for the critical thicknesses were obtained from magnetic structure observations. The critical thickness is 180 nm for Sn and 250 nm for Pb [99].

Measurement results of superconducting properties of Sn, $Pb_{82}Bi_{18}$, and YBCO control thin films (without ferromagnetic structures) are discussed in this chapter. The properties of the thin films were measured in the PPMS which can apply external magnetic fields up to 9 T and cool down to 1.8 K with liquid helium and a vacuum system. The control samples were electrically connected to the PPMS through Au wires with In pressing on the Au or Ag contact pads. The applied external magnetic fields by the PPMS were perpendicular to the thin films.

4.1 Sn thin films

In subchapter 3.1, three different thicknesses (D) of the control Sn thin films below Sn's critical thickness (180 nm) were fabricated on cleaned SiO_2 substrates by the thermal evaporation with the quench condensation: D=30 nm, 50 nm, and 100 nm. The dependence on the Sn thin film thickness is discussed with the experimental results. Figure 53 displays an SEM image that shows that the control Sn films were fabricated with an 84.33 μm length (L) with a 15.50 μm width (W). Thickness of the samples was controlled by the deposition time as mentioned earlier.

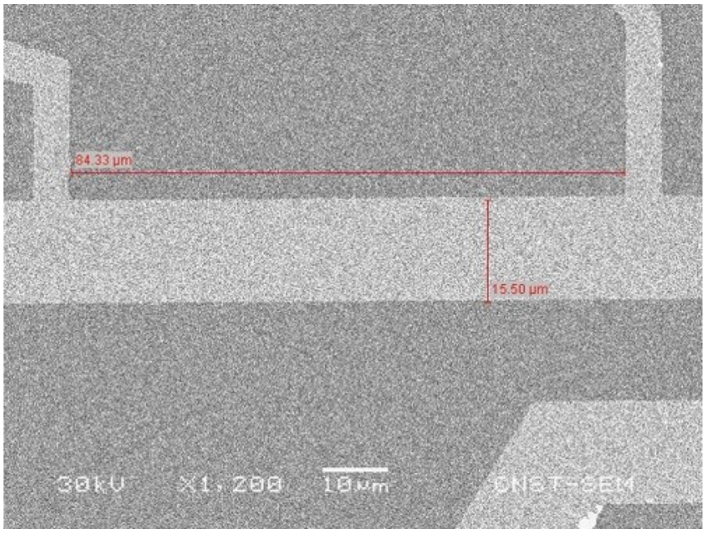

Figure 53. An SEM image of the Sn control sample.

In order to find resistance (R) of the control samples in the PPMS, a 1.0 μA alternating current was applied to each sample, and the voltage at zero field was measured. Temperatures were decreased during the R measurement to obtain the resistivity (ρ) versus temperature curves, as shown in Figure 54. The value of ρ was computed from R and the measured geometrical dimensions of the samples

$$\rho = R\frac{WD}{L} \tag{31}$$

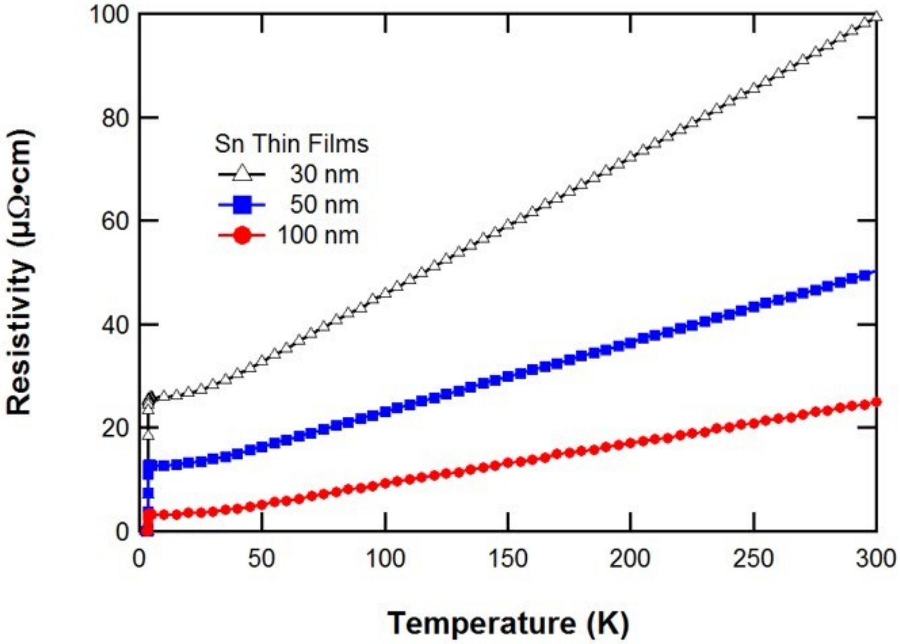

Figure 54. ρ-T of the Sn thin films.

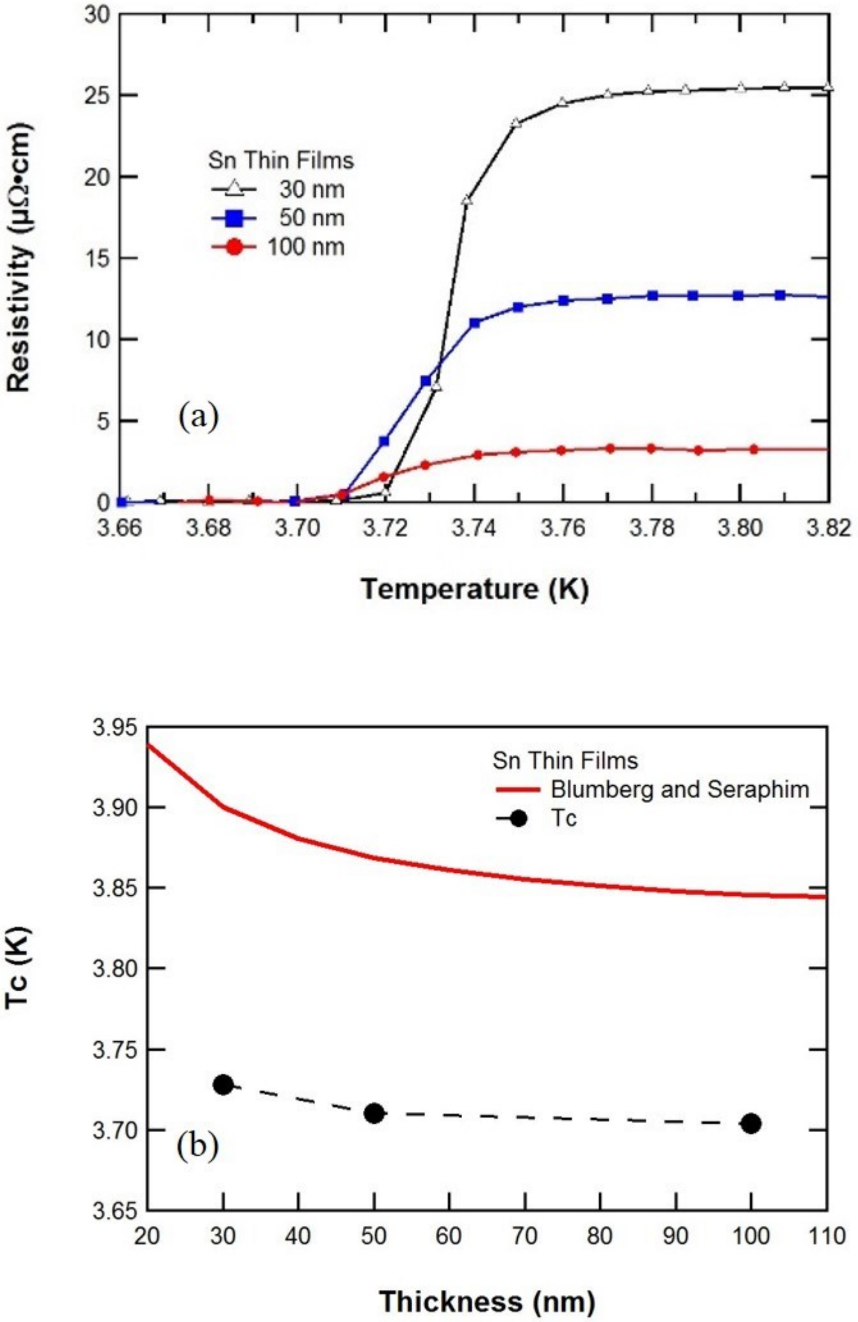

Figure 55. ρ-T of the Sn thin films near T_C (a) and T_C as a function of film thickness (b). Lines are drawn between the three data points as a guide.

The 30 nm Sn film has a relatively high ρ in comparison with the ρ of 50 nm and 100 nm of Sn films from room temperature to T_C. The relation between the film thickness and ρ will be discussed. Figure 55 (a) shows the measured ρ versus temperature (ρ-T) curves near T_C. Each T_C of the three samples was defined by linear extrapolations. T_C for thickness of 30 nm, 50 nm, and 100 nm correspond to 3.728 K, 3.710 K, and 3.705 K, respectively. Dependence of T_C on the Sn film thickness have been reported in the literature [18, 102, 103]. Several references indicate decreasing film thickness increases T_C in many LTS. The trend of the decrease in the transition temperature with increasing film thickness is shown in Figure 55 (b) for films in this study. T_C rapidly increases with decreasing thickness when the Sn films are thinner than 100 nm [103]. Lock explained that the increase in T_C is related to stresses in the films [104]. When T_C is higher, the coefficient of expansion of the substrate material is lower than that of the Sn. On the other hand, when T_C in the film is lower, the coefficient of expansion of the substrate material is higher than that of the Sn. In conclusion, the changes in T_C of the Sn films were due to strains caused by differential contraction of the Sn films and substrates upon cooling from room temperature to the transition temperature [104]. The stress effect of the thin films' thickness on variation of T_C can be written as

$$\Delta T_C = 1.673\left(\frac{\partial T_C}{\partial \sigma_C}\sigma_0 + \frac{\partial T_C}{\partial \sigma_C}\alpha \cdot \frac{Gb}{t}\right) \tag{32}$$

where σ_0 is an intrinsic critical shear stress, α is a constant of magnitude near 0.5, G is the shear modulus, t is thickness of the film, and b is the appropriate Burgers vector [102, 105]. ΔT_C is defined as a change in between thin film's T_C and bulk's T_C. T_C of bulk Sn is 3.722 K [106]. Blumberg and Seraphim [102] had chosen σ_0= 1,250 atm, αG=0.5x10^5 atm, and $\frac{\partial T_C}{\partial \sigma_C}$=4.8x$10^{-5}$ K/atm to express the simple numerical estimates from equation (32). The Burgers vector *b* is chosen as 0.583 nm, which is a lattice constant in the *a*-*a* plane in the tetragonal structure of Sn. Thus, equation (32) becomes

$$\Delta T_C = 0.1 + \frac{2.3413\times10^{-8}}{t} \tag{33}$$

Therefore, it is known that the thickness of thin films affects T_C which is proportional to $\frac{1}{t}$. The trend in the critical temperature is shifted to somewhat lower temperature (about 0.14 K lower than their results) [102], as displayed in Figure 55 (b). The shifted curve may be due to lower deposition rates (0.10 nm/sec) as compared to their deposition rates (10 nm/sec). Even though, the T_C versus thickness curve of Sn is shifted toward lower temperature, the trend of experimental result in this research is in good agreement with their theoretical estimation.

Figure 56 indicates normalized *R* as a function of external magnetic fields at 3.50 K. The normalized *R* was calculated by dividing all *R* by the residual resistance *R* in the normal state near T_C. The applied current during the *R* measurement was 1.0 µA and the magnetic fields were swept from +300 Oe to -300 Oe and then back to +300 Oe. *R* in the *R*-*H* curve of the 100 nm Sn shows appreciable noise because the measured *R* was much lower than that for the other thicknesses. The 100 nm Sn film's *R* was about 1.75 Ω in the normal state. In order to determine H_{C2} of the Sn thin films, a linear extrapolation (green line in Figure 56) of *R*(*H*) to *R*=0 was used.

The extracted H_{C2} of the samples is plotted as a function of the reduced temperature (T/Tc), as shown in Figure 57 (a). Black open triangles, blue closed squares, and red closed circles are experimental data, and the trend lines are drawn by curve fitting. The coefficients of determination (R^2) were 0.997±0.002 that means the regression line fitted the experimental data well. By extrapolation of the curve fitting lines in Figure 57 (a), $H_{C2}(0)$ of the Sn films can be obtained. The estimated $H_{C2}(0)$ of 30 nm, 50 nm, and 100 nm are 800.39 Oe, 718.92 Oe, and 451.34 Oe, respectively.

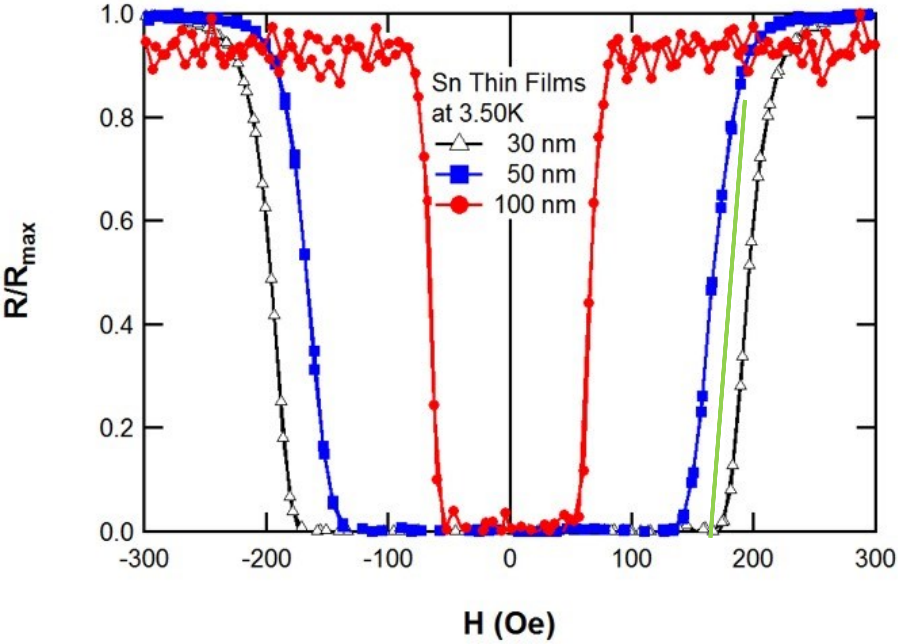

Figure 56. Normalized R as a function of external magnetic fields of the Sn thin films.

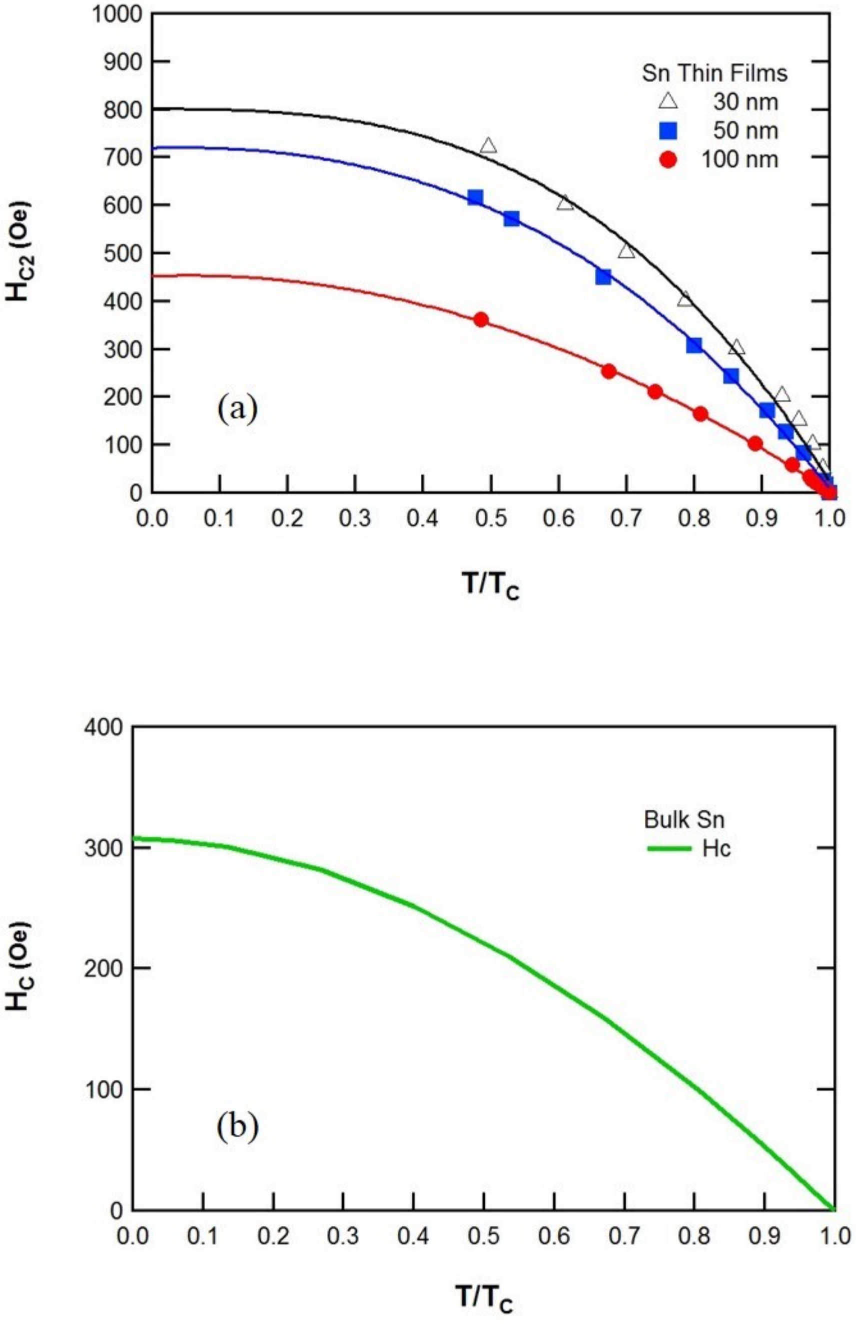

Figure 57. H_{C2} as a function of the T/T_C of the Sn thin films (a) and H_C as a function of the T/T_C of bulk Sn (b).

A green line in Figure 57 (b) indicates H_C as a function of the T/Tc of bulk Sn which is written as

$$H_C(T) = 1.225T^3 - 26.8T^2 + 307.3 \tag{34}$$

where T is temperature and $H_C(0)$ is 307.3 Oe [107].

The coherence length ξ, which is one of the characteristic lengths in superconductors as introduced in subchapter 1.3, was calculated from the experimental results of the R-H curves of the control Sn thin films. Why the dirty limit has been chosen will be shown in the next page. By combining equations (13) and (22), the ξ near T_C in the dirty limit becomes

$$H_{C2} = \frac{\phi_0}{2\pi(0.855)^2\xi_0 l} \cdot \frac{T_C - T}{T_C} \tag{35}$$

From equation (35), the derivative with respect to T gives

$$\frac{dH_{C2}}{dT} = -\frac{\phi_0}{2\pi(0.855)^2\xi_0 l} \cdot \frac{1}{T_C} \tag{36}$$

Equation (36) can be written as

$$\xi_0 = -0.21771 \frac{\phi_0}{T_C l \cdot \frac{dH_{C2}}{dT}} \tag{37}$$

where $\frac{dH_{C2}}{dT}$ was determined from Figure 57 (a) in a range between $0.97T_C$ and T_C. The coefficient of determination (R^2) was 0.995±0.002. Finally, the BCS ξ_0 of the Sn films were calculated. The estimated ξ_0 are 8.67 nm, 12.78 nm, and 21.64 nm, as shown in

Table 4. They correspond to the Sn 30 nm, 50nm, and 100 nm, respectively. It is known that the ξ_0 of the Sn films are much less than their thicknesses.

In order to estimate mean free paths of the Sn thin films, equation (38) can be used

$$l = v_F \tau \tag{38}$$

where v_F is the Fermi velocity and τ is the relaxation time. The relaxation time is expressed by

$$\tau = \left(\frac{0.22}{\rho}\right)\left(\frac{r_s}{a_0}\right)^3 \times 10^{-14} \tag{39}$$

where ρ is the resistivity in μΩ·cm, r_s is the electronic density, and a_0 is the Bohr radius. For Sn, ρ is 11.5 μΩ·cm at 273 K (bulk Sn), $\frac{r_s}{a_0}$ is 2.22, and v_F is1.90 x 10^6 m/sec [108]. Thus, the estimated l for bulk Sn at 273 K is 3.976 nm. The resistivity of thin films relates to the mean free path, according to

$$\rho l = \rho' l' \tag{40}$$

where ρ' is the resistivity of the thin film and l' is the mean free path of the film [109, 110]. Since ρ, ρ', and l are estimated, l' can be computed for the Sn films. The resistivity of the thin films were chosen for the calculation from Figure 55 (a) at 3.80 K. The Sn films were in the normal state and slightly above their T_Cs at the temperature. The estimated l's at 3.80 K are shown in Table 4. Shorter l' in a thinner film may be due to skin effect.

The London penetration depth at zero temperature by BCS is expressed as [5]:

$$\lambda_L(0) = \frac{\phi_0}{0.8165\pi^2\xi_0 H_C(0)} \tag{41}$$

All the parameters from the experimental results are known to estimate $\lambda_L(0)$ of the Sn films. The estimations are in Table 4.

Table 4. Estimated values of the characteristic lengths of the Sn thin films.

Thickness (nm)	$\lambda_L(0)$ (nm)	ξ_0 (nm)	l' (nm)	κ	l'/ξ_0
30	369.56	8.67	1.80	146.79	0.21
50	279.37	12.78	3.61	55.33	0.28
100	262.73	21.64	14.13	13.29	0.65

The ratio of $\frac{l\prime}{\xi_0}$ is smaller than 1, as shown in Table 4. This ratio demonstrates that the Sn films in this study are in the dirty limit. Type I superconductors can function as type II superconductors when the thickness of the material is below the critical thickness, as mentioned earlier in this subchapter.

Now, the Sn thin films can be classified as type I or type II superconductors by investigating the ratio of

$$\kappa = \frac{\lambda_{eff}(l,T)}{\xi_0(T)} = 0.715\frac{\lambda_L(0)}{l} \tag{42}$$

where l denoted l' of Sn thin films. Equation (42) is obtained from equation (13) and (20).

The values of the κ of the Sn films are given in Table 4. As a result, the κ is much greater than $\frac{1}{\sqrt{2}}$, therefore all the Sn films in this research indeed behave as type II superconductors. κ decreases with increasing thickness of the Sn thin films. It can be expected that thicker film or bulk samples have lower κ than 1, and the samples turn out to be Type I superconductors.

Figure 58 (a) displays computed ξ as a function of the T/T_C near T_C based on equation (13). Moreover, when the Sn film thickness increases, a similar increase occurs in ξ at the same temperature, as shown in Figure 58 (a) and Figure 59. The penetration depth of the specific thicknesses of the Sn thin films were estimated by equation (20). The form has been chosen rather than equation (19), because the Sn films are in the dirty and near T_C limit. The l in equation (20) denotes calculated l', and $\lambda_L(0)$ is given in Table 4. The $J(0,T)$ is defined as 1.33 at $T \approx T_C$. Hence, the penetration depth of the Sn films near their T_C may be computed. Figure 58 (b) indicates the estimated penetration depth as a function of the T/Tc. λ increases to infinity near T_C. This means that superconducting areas decrease in the films, and the external magnetic field penetrates all the thin films. Also, this means that the Sn films transfer to the normal state. The estimated penetration depth is inversely proportional to the film thickness, as shown in Figure 58 (b) and Figure 59. The values of penetration depth are much greater than the film thicknesses near their T_C.

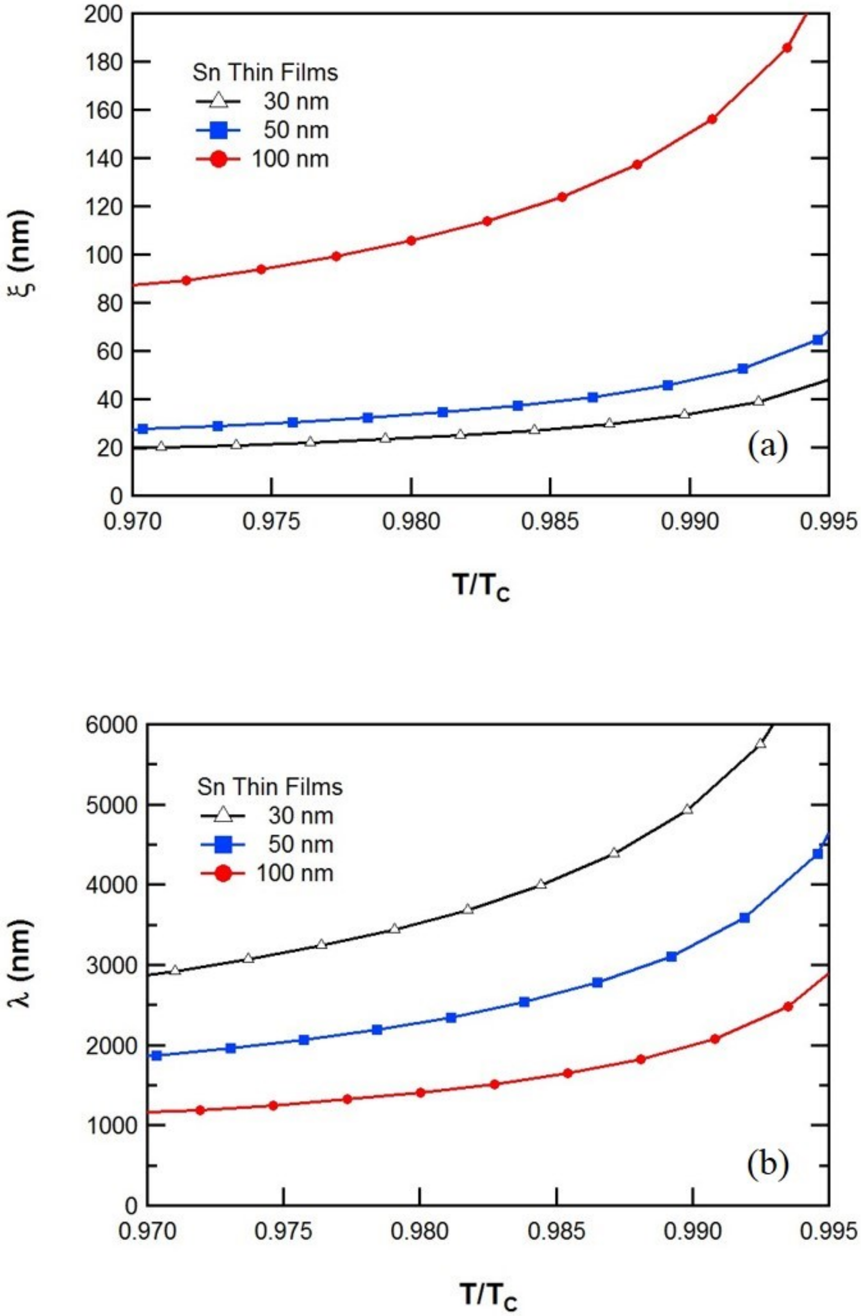

Figure 58. Calculated ξ as a function of the T/T_C of the Sn thin films (a) and calculated λ as a function of the T/T_C of them (b).

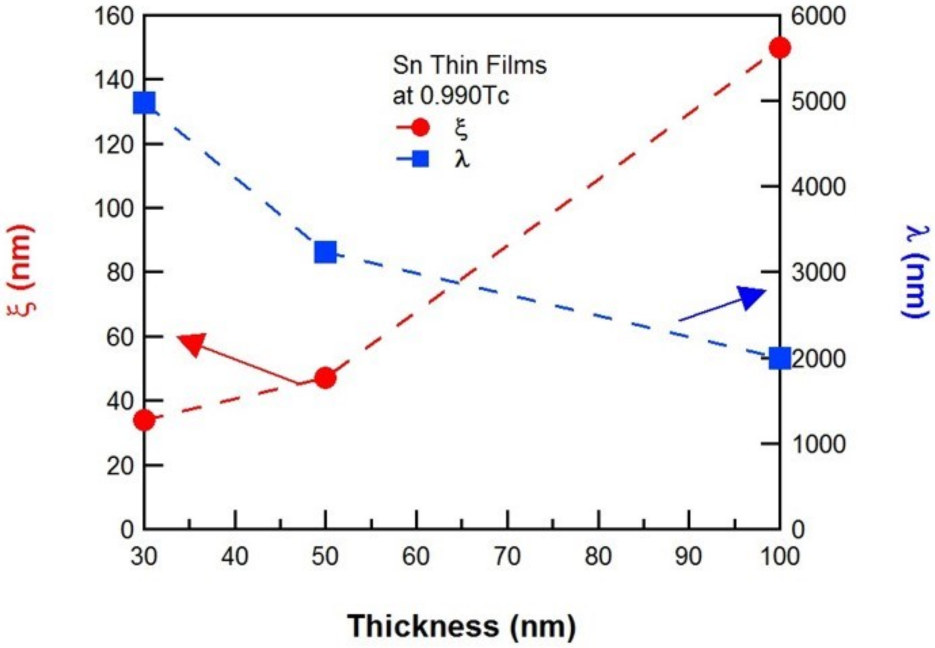

Figure 59. A correlation between the ξ and λ as a function of the Sn films thicknesses.

In general, there is some vortex pinning so that there is a region where V=0 for finite I. At some current, some of the vortices become unpinned and start to move. This is the flux flow regime with $V \propto I$, but less than IR_N where R_N is the normal state resistance at that temperature and external magnetic field. That current is called a flux flow critical current (I_{Cff}). At some higher current, the superconductor goes into the normal state and $V=IR_N$ above that. The field energy plus the kinetic energy of the superconducting current equals the condensation energy at that point. That current is in essence I_{Ci} as a function of temperature and external magnetic field, which is called an intrinsic critical current. The practical I_C as a function of temperature and external magnetic field is due to flux flow. Note that I_C denotes I_{Cff} in this research, and J_C is calculated with I_{Cff}.

Measurements of the *I-V* characteristics were done on the 30 nm Sn film at 50 Oe at 3.50 K. The film exhibits the superconducting state when I is below 0.12 mA (I_{Cff}), as shown in Figure 60. The flux flow regime is between 0.12 mA and 0.16 mA (I_{Ci}), and V gradually increases in the regime. Above the I_{Ci}, the film becomes a normal conductor. The red and blue arrows indicate I_{Cff} and I_{Ci} in Figure 60, respectively.

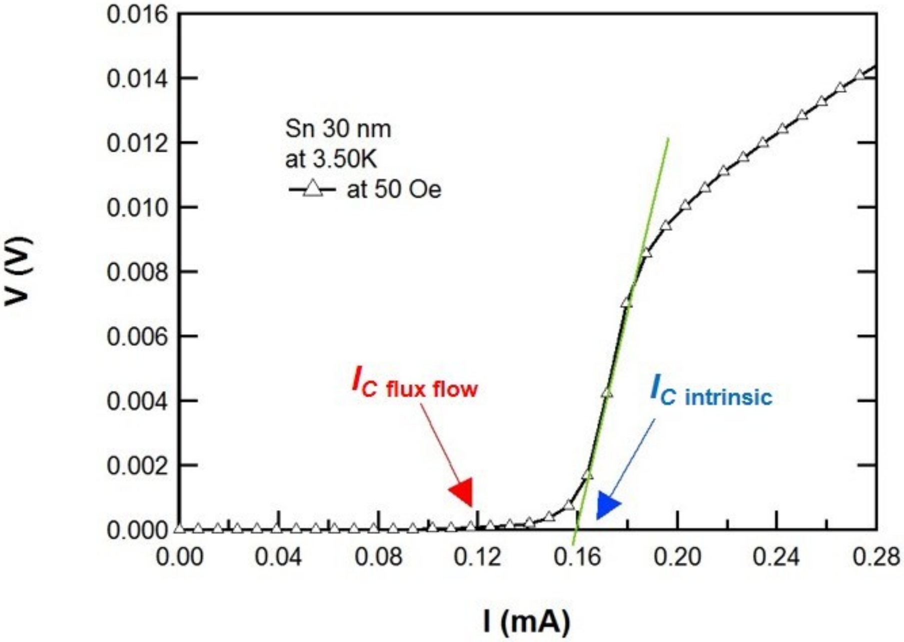

Figure 60. *I-V* curves of the 30 nm Sn film at 50 Oe at 7.43 K.

Critical current density (J_C) was calculated from the measured I_{Cff} at 3.50 K with cross-sectional dimension of the Sn films. Figure 61 (a) shows J_C of the Sn films as a function of external magnetic field. J_C for the 100 nm Sn film indicates the greatest value at zero field, however the J_C decreases abruptly around 55 Oe. In contrast, J_C of the 30 nm Sn film has a relatively lower value, and J_C goes to zero near 160 Oe. Figure 61 (b) depicts I_C as a function of the T/T_C for these films. I_C increases with decreasing temperature. I_C of the 100 nm Sn film is 8.6 times greater than that of the 30 nm Sn film. It is clear that variation of I_C is strongly related to the film thickness with the thicker films having larger I_C in a range between 30 nm and 100 nm.

Figure 62 (a) shows a correlation between the surface roughness and ρ the Sn films at 3.78 K of as a function of their thicknesses. At 3.78 K, the Sn films in this research are all in the normal state residual resistance region. As the thickness of Sn thin films increases from 30 nm to 100 nm, the surface roughness also increases from 5.08 nm to 14.75 nm. In contrast, ρ decreases from 25.22 μΩ·cm to 3.29 μΩ·cm in the same thickness range. In this case, scattering on the surface of the Sn thin films is considered to play a key role in approximately 7.7 times increase in the ρ of Sn films [111, 112]. In accordance with the Fuchs and Sondheimer [113, 114] theory, the resistivity dependence on the thickness is due to the effect of electron scattering at the thin film surface and interface [112, 115].

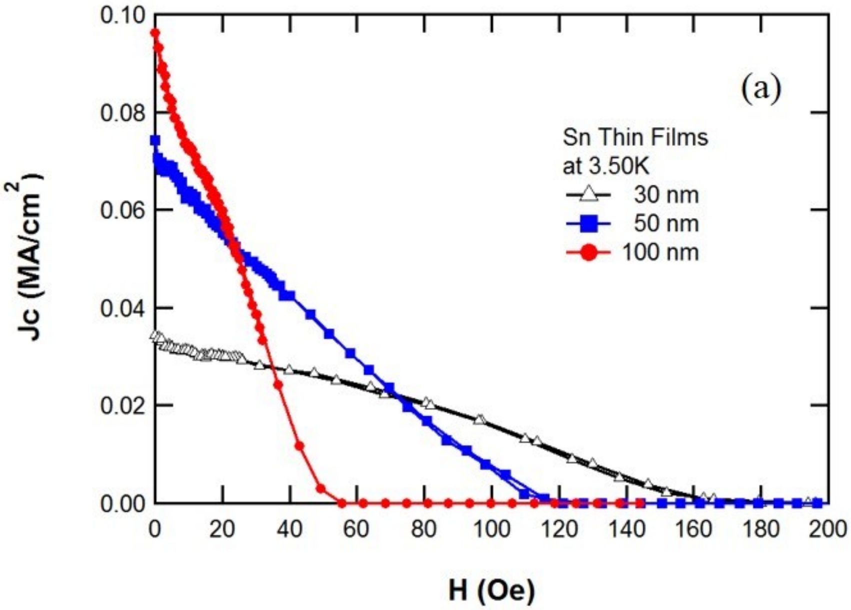

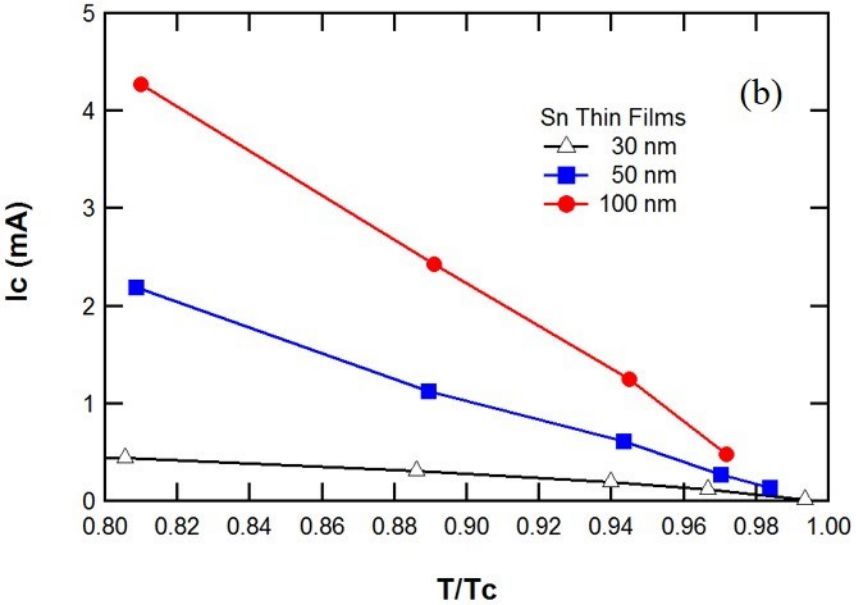

Figure 61. J_C as a function of external magnetic fields of the Sn thin films (a) and I_C as a function of the T/T_C of the Sn thin films (b).

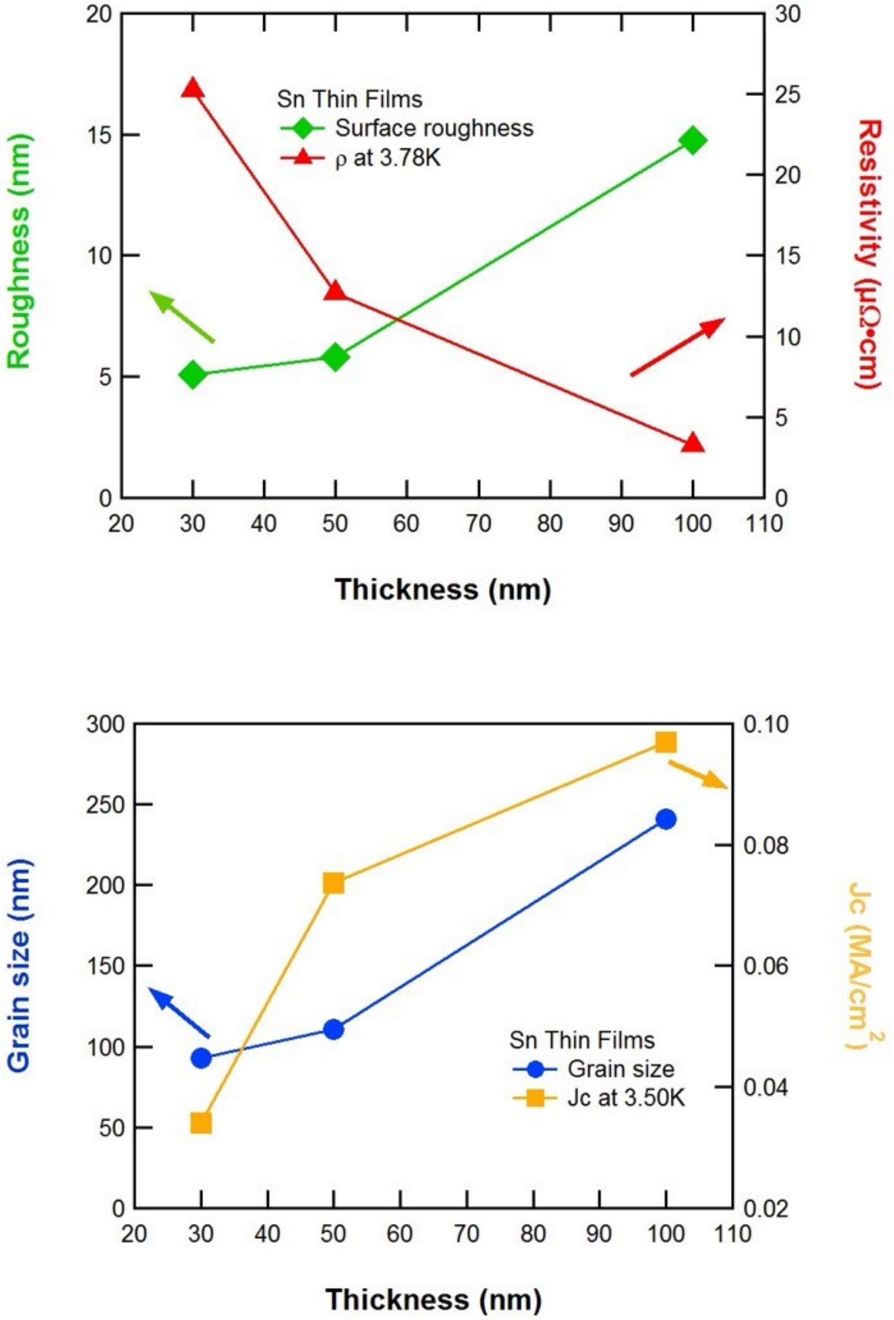

Figure 62. A correlation between surface roughness and ρ as a function of the Sn thin films thicknesses (a) and a correlation between grain size and J_C as a function of ρ (b).

From their theory, the simplified ρ_s of the thin film can be written as

$$\rho_s = \rho_0 \left\{ 1 + \frac{3}{8k}(1-p) \right\} \tag{43}$$

where ρ_0 is the bulk metal resistivity and p is the specularity coefficient. k is defined as $k = \frac{d}{l}$, where d is the film thickness, and l is the electron mean free path. The specularity coefficient p determined as $p \approx 0$ for polycrystalline films and $p \approx 1$ for single crystal films [116]. Therefore, it is known that resistivity of the thin films is inversely proportional to the thickness of the thin films from equation (43). Figure 62 (b) depicts that the grain size increases from 92.83 nm to 240.65 nm, and J_C also increases from 0.097 MA/cm^2 to 0.034 MA/cm^2 when the thickness of the Sn films increases from 30 nm to 100 nm. Hence, increasing the grain size with thicken Sn films seems to enhance the J_C.

4.2 $Pb_{82}Bi_{18}$ thin film

An evaporation source for a $Pb_{82}Bi_{18}$ alloy was made by arc melting pure Pb and Bi metals at this atomic ratio in an argon atmosphere. A 100 nm thin film of $Pb_{82}Bi_{18}$ was evaporated on to an EBL patterned substrate by thermal quench condensation with liquid nitrogen. The deposition rate was 0.3 nm/sec. The dimensions of the film are 84.33 μm long and 15.50 μm wide, the same as of the Sn films shown in Figure 53. The superconducting properties of the film were characterized using a four-probe measurement in the PPMS. The properties of the film are discussed with the experimental results in this subchapter.

In order to measure *R* of the 100 nm $Pb_{82}Bi_{18}$ film (without ferromagnetic nanostructures) in the PPMS, a 1.5 μA alternating current was applied, and the voltage at zero field was measured. Temperature was decreased from room temperature to below its T_C during the *R* measurement to determine *R* as a function of temperature. Figure 63 demonstrates that the film exhibits superconducting properties with a clear and sharp resistance drop near its T_C.

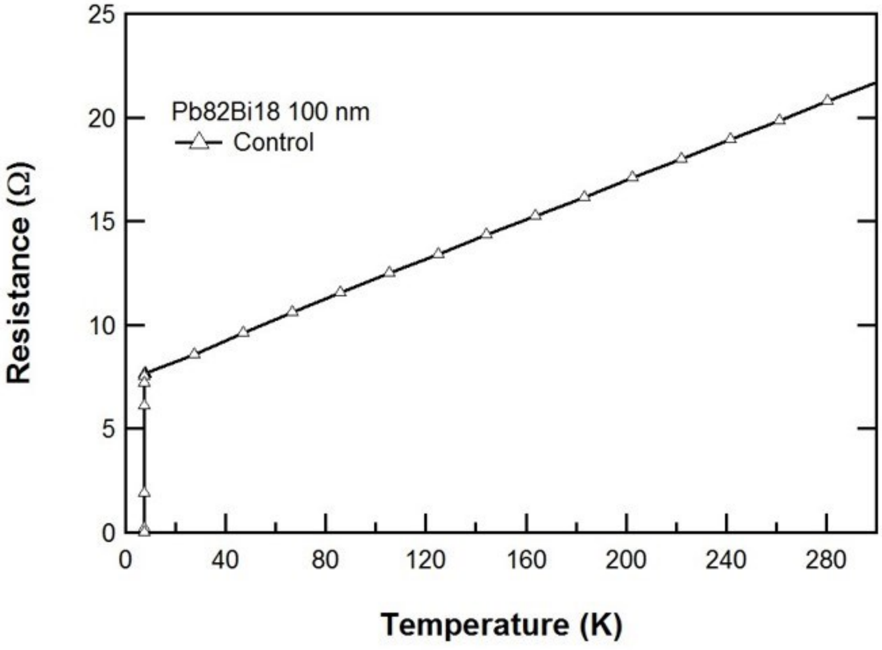

Figure 63. An *R*-*T* curve of temperature from 0 K to 300 K of the $Pb_{82}Bi_{18}$ film.

The mean free path, l, of the $Pb_{89}Bi_{11}$ thin film can be considered with an l of pure Pb thin film as a function of the film thickness and an l of contents of Bi. In $Pb_{82}Bi_{18}$ case, Bi is the impurity in Pb thin films, hence the 100 nm $Pb_{82}Bi_{18}$ film is in dirty limit. The l(d) is estimated by using the Matthiessen's rule,

$$\frac{1}{l(d)} = \frac{1}{l_{Pb}} + \frac{1}{l_{impurity}} \tag{44}$$

where l is a function of film thickness, d, $l_{\mathrm{Pb}}=2d$ is the mean free path by boundary scattering, and l_{impurity} is the mean free path by impurity scattering [117]. The l of pure Pb films is linearly proportional to the film thickness. On the other hand, the l of Pb_xBi_{1-x} is saturated at a suitable value. According to Ozer's results, the l_{impurity} of $Pb_{89}Bi_{11}$ and $Pb_{80}Bi_{20}$ are 20 nm and 9 nm, respectively [117]. For $Pb_{82}Bi_{18}$, 11.45 nm has been chosen for the value of l_{impurity}. As a result, equation (44) can be written as

$$\frac{1}{l(d)} = \frac{1}{2d} + \frac{1}{11.45} \tag{45}$$

where d is from 0.05 nm to 10 nm. Equation (45) can be plotted, as displayed in Figure 64. The l depends on the film thickness and temperature. From Schiller and Bulow's results [118], l of a 100 nm Pb thin film can be estimated as 3 nm below 25 K. This corresponds to 1.5 nm of Pb film thickness [117]. Finally, the l of the 100 nm $Pb_{82}Bi_{18}$ film may be computed at the same temperature with the same thickness. Thus, the value is 2.38 nm, which is a red dot in Figure 64.

κ is investigated using equation (42) in order to classify the 100 nm $Pb_{82}Bi_{18}$ film as a type I superconductor or type II superconductor. For the $Pb_{82}Bi_{18}$ film, $\lambda_L(0)$ is 32.36 nm from equation (41), which is valid in the dirty limit and near T_C. From equation (42), κ is 9.72 which is much greater than $\frac{1}{\sqrt{2}}$. Thus, the calculated κ demonstrates that the film indeed operates as a type II superconductor.

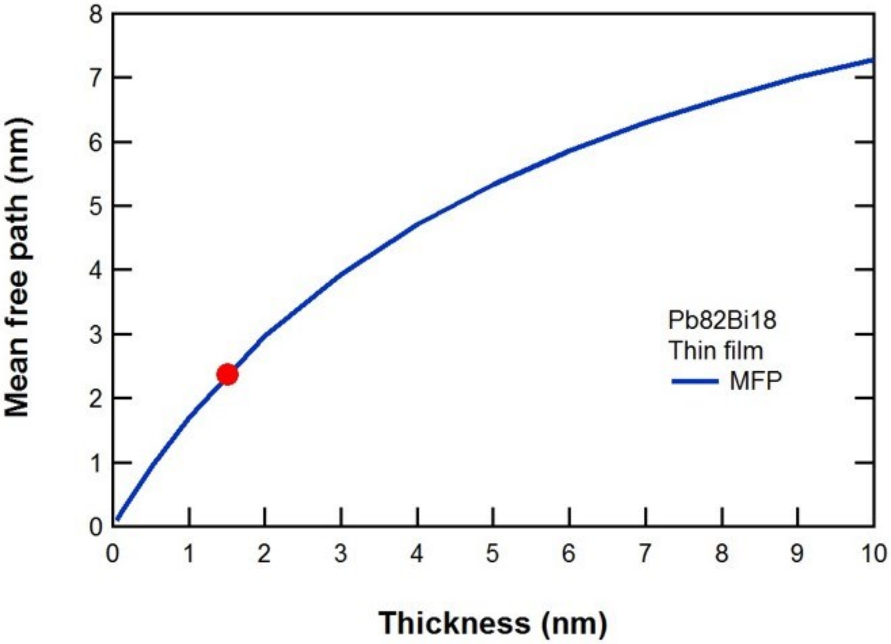

Figure 64. Electronic mean free path as a function of thickness for the $Pb_{82}Bi_{18}$ film.

Figure 65 (a) illustrates reduction of the superconducting transition temperatures by increasing the external magnetic field. T_C of the $Pb_{82}Bi_{18}$ film at zero field is 7.574 K by a linear extrapolation. In order to determine $H_{C2}(T)$ of the film, the linear extrapolation was used again on all the curves in Figure 65 (a). As a result, the estimated $H_{C2}(T)$ as a function of the T/Tc is plotted in Figure 65 (b). The slope of $H_{C2}(T)$ as a function of the T/T_C is linear in a range between $0.950T_C$ and T_C.

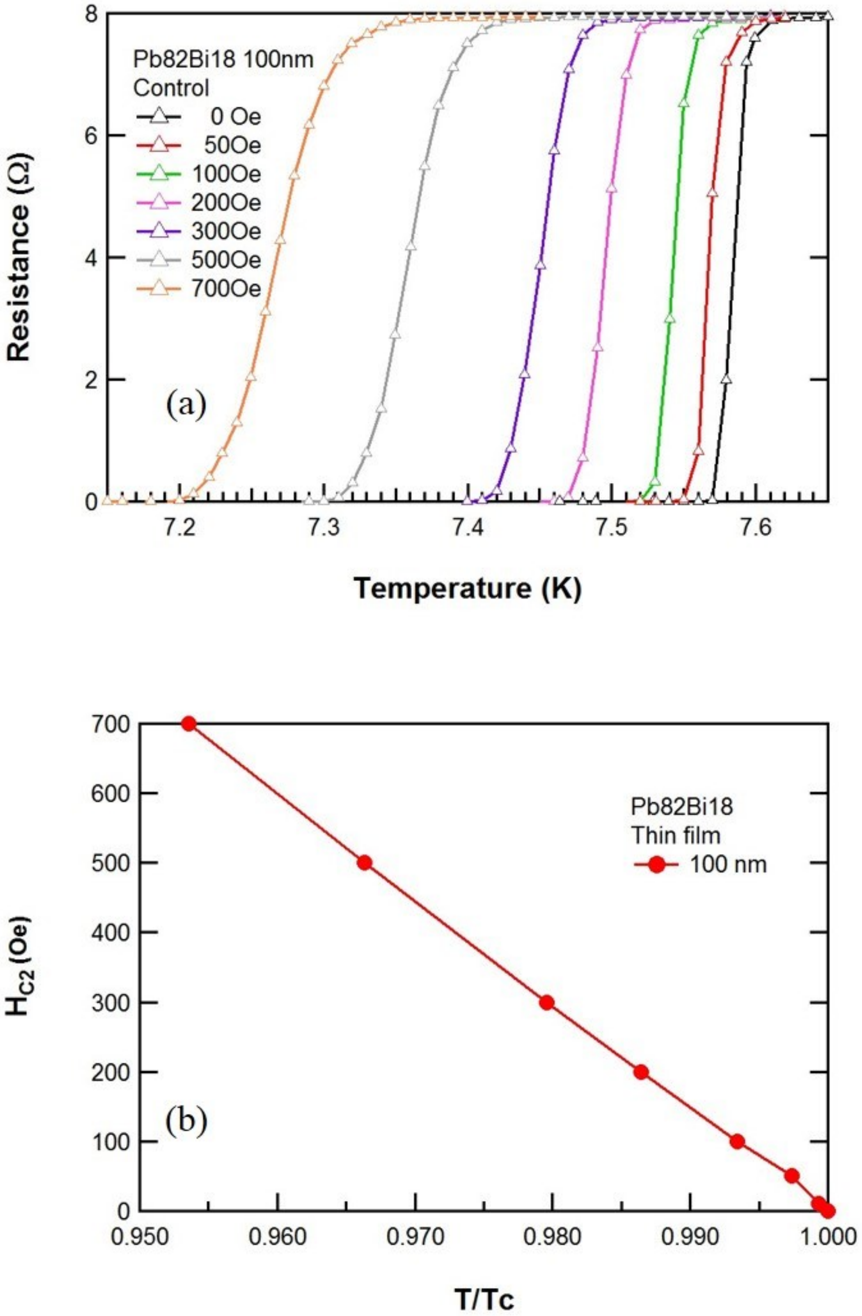

Figure 65. *R*-*T* curves depending on external magnetic fields of the $Pb_{82}Bi_{18}$ film (a) and its H_{C2} as a function of the T/T_C (b).

ξ_0 of the $Pb_{82}Bi_{18}$ film can be computed by using equation (37) because ϕ_0, l, T_C, and $\frac{dH_{C2}}{dT}$ have been estimated. The calculated ξ_0 is 5.20 nm. Thus, ξ_0 is greater than l, and the film fits the dirty limit. In addition, by the equation (13), ξ of the thin film as a function of the T/Tc near T_C can be plotted, as shown in Figure 66 (a). Also, Figure 66 (b) expresses λ as a function of the T/Tc with the equation (20). As expected, both ξ and λ increase to infinity near T_C. This means that superconducting areas reduce in the thin film, and the external magnetic fields penetrate into the thin film. Also, this means that the thin film transfers to the normal state. At $0.990T_C$, $\kappa = \frac{\lambda}{\xi}$ is 11.16. This also proves that the thin film is a type II superconductor near T_C. This value of κ is almost the same in comparison with calculation by the equation (42). Furthermore, ξ_0 is much smaller than the film thickness, and λ is comparable with the thin film's thickness at $0.987T_C$.

Applied external magnetic fields were swept from +300 Oe to -300 Oe and back to +300 Oe during the I_C measurement for the $Pb_{82}Bi_{18}$ film at 7.43 K, 7.48 K, and 7.53 K. J_C has been determined as the measured I_{Cff} divided by the cross-sectional area (WD) of the thin film. The value of J_C as a function of the external magnetic field is shown in Figure 67 (a). J_C at 7.43 K of this film has the greatest value at zero field, and the J_C at 7.53 K is the lowest value at zero field in Figure 67 (a). J_C dramatically rises below ±50 Oe in the J_C-H curves, and they are symmetric as well. No J_C in high magnetic fields (above ±250 Oe) in the J_C-H curves means that the thin film lost the superconducting properties. J_C increases with decreasing the magnetic fields, and J_C decreases with

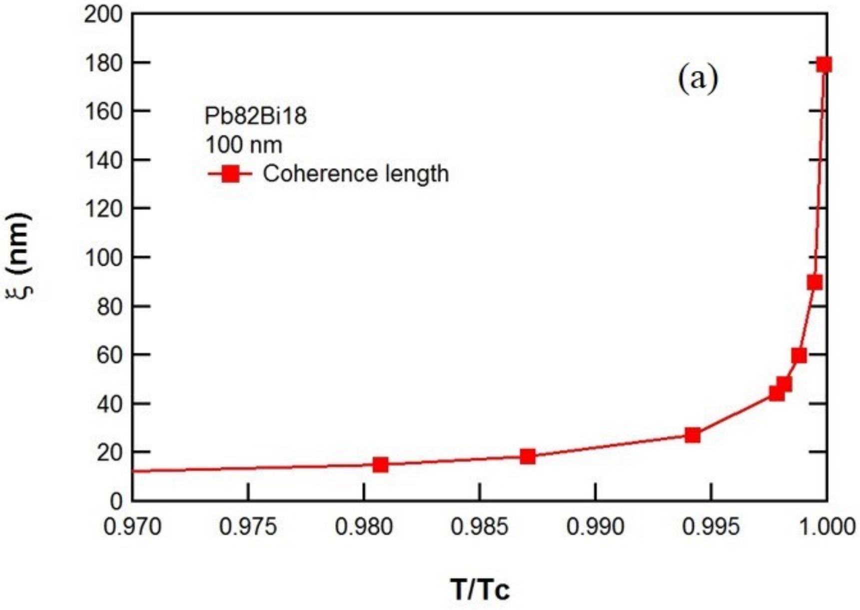

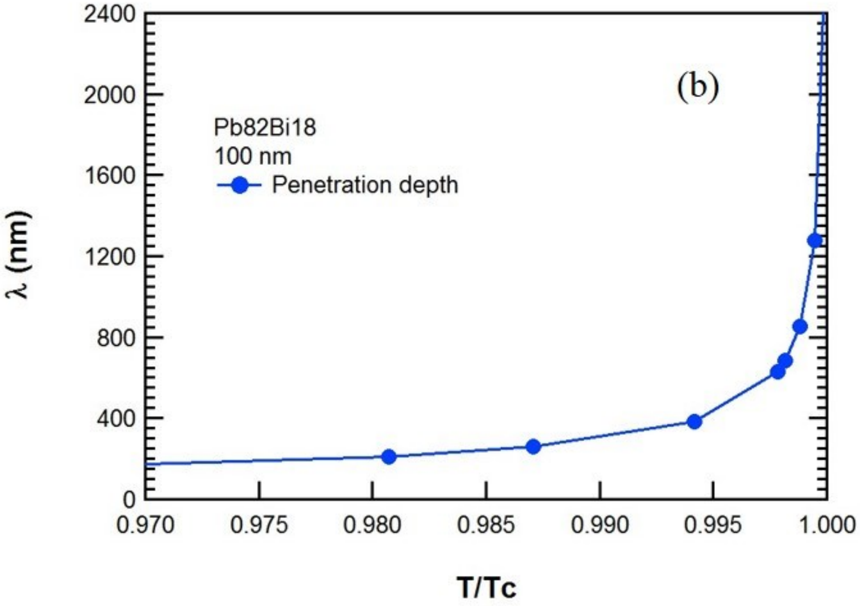

Figure 66. ξ as a function of the T/T_C of the $Pb_{82}Bi_{18}$ film (a) and its λ as a function of the T/T_C (b).

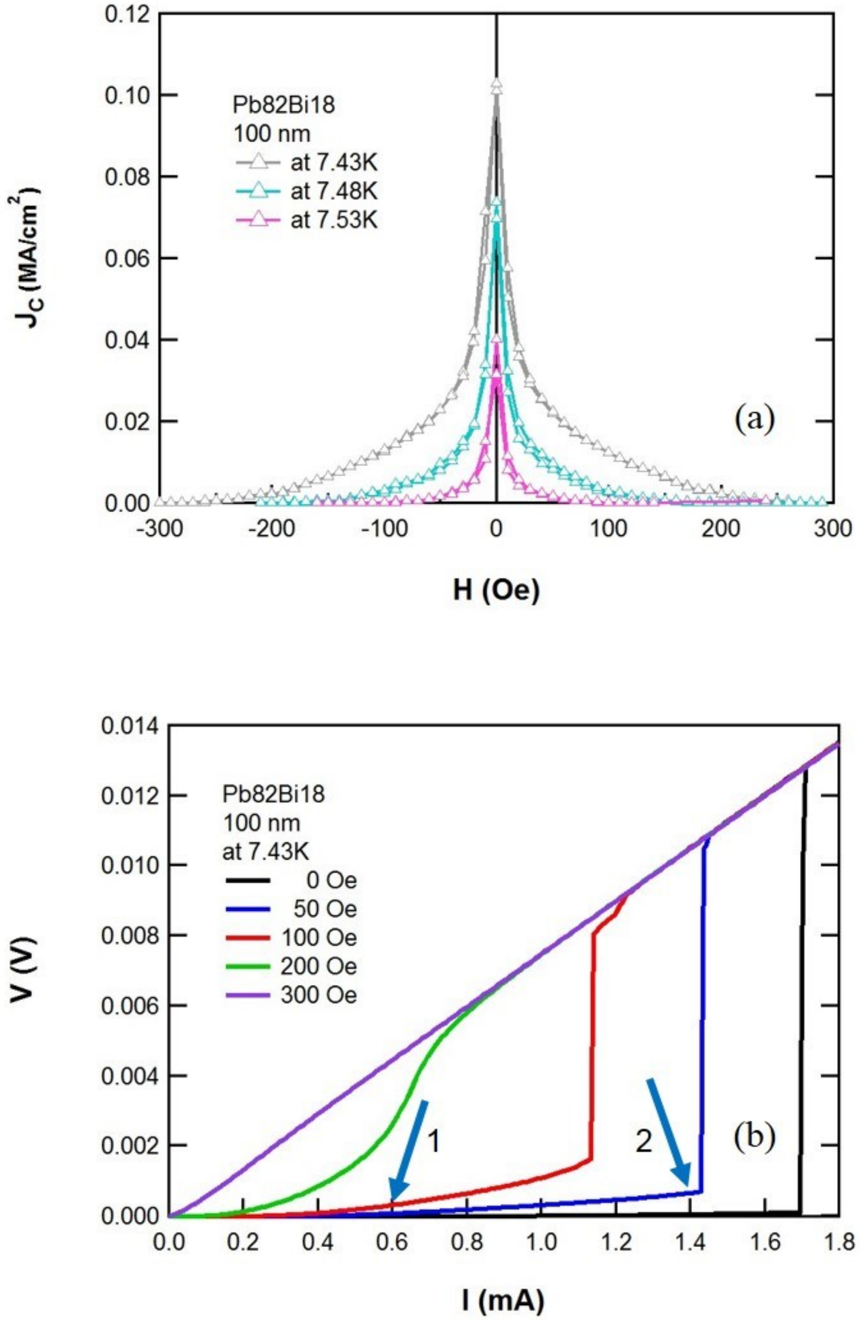

Figure 67. J_C as a function of external magnetic fields of the $Pb_{82}Bi_{18}$ film (a) and its I-V curves with different external magnetic fields at 7.43 K (b).

decreasing temperature from the J_C-H curves of the thin film. In other words, the J_C of the film strongly depends on the applied magnetic fields and the temperatures.

Figure 67 (b) shows *I-V* characteristics of the film at 7.43 K in various external magnetic fields. Each *I-V* curves correspond to the J_C-H curves at 7.43 K. At 50 Oe (blue line) in Figure 67 (b), the thin film exhibits the superconducting state, and the V is zero with zero resistance when the I is below 0.43 mA. There is the flux flow regime between 0.43 mA and 1.43 mA, and the V gradually increases in the regime. Even though the V is not zero in the flux flow regime, the film is still a superconductor [2]. The thin film transists to the normal state above 1.43 mA. The blue arrows indicate I_{Cff} (1) and I_{Ci} (2) in Figure 67 (b). The phase transition is no longer sharp in high external magnetic field regime such as at 200 Oe.

In order to obtain I_C at various temperatures, I was applied, and V was measured. Figure 68 (a) illustrates *I-V* curves of the thin film at zero field with different temperatures from 7.000 K to 7.565 K. I_C can be determined by the current when the voltage has non-zero value in the *I-V* curves. I_C increases in all temperature ranges when the temperature decreases. The slope in the *I-V* curves above the sharp transition indicates that the thin film is in the normal state, and the value of the slope is 7.98 Ω. This value corresponds with the R in the normal state right above T_C of the thin film in Figure 65 (a). The voltage is zero when the thin film is in the superconducting state.

The I_C, which is estimated from Figure 68 (a), as a function of the T/Tc is plotted in Figure 68 (b). I_C enhances towards lower temperature. The I_C is proportional to $\left(\frac{T_C-T}{T_C}\right)^{\frac{3}{2}}$, and this condition is effective near the film's T_C [5]. Hence, the I_C versus the

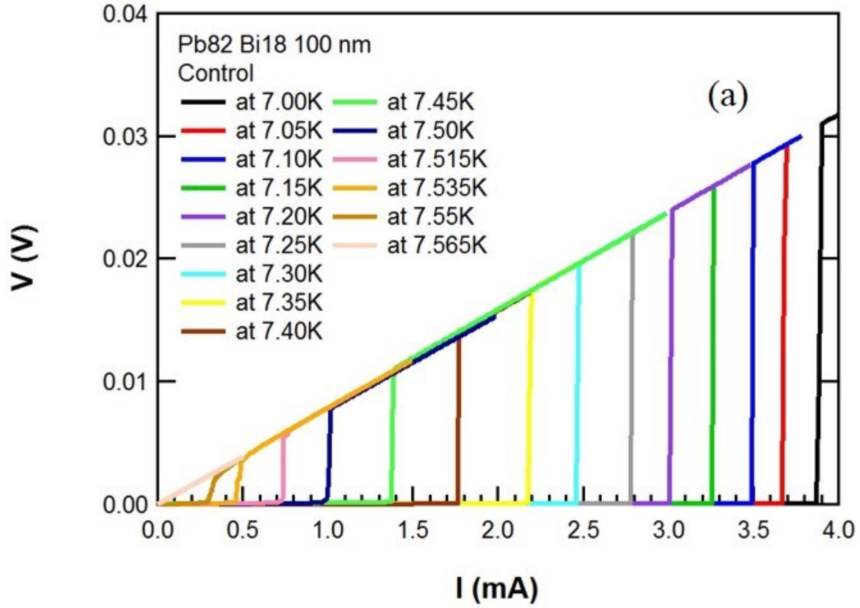

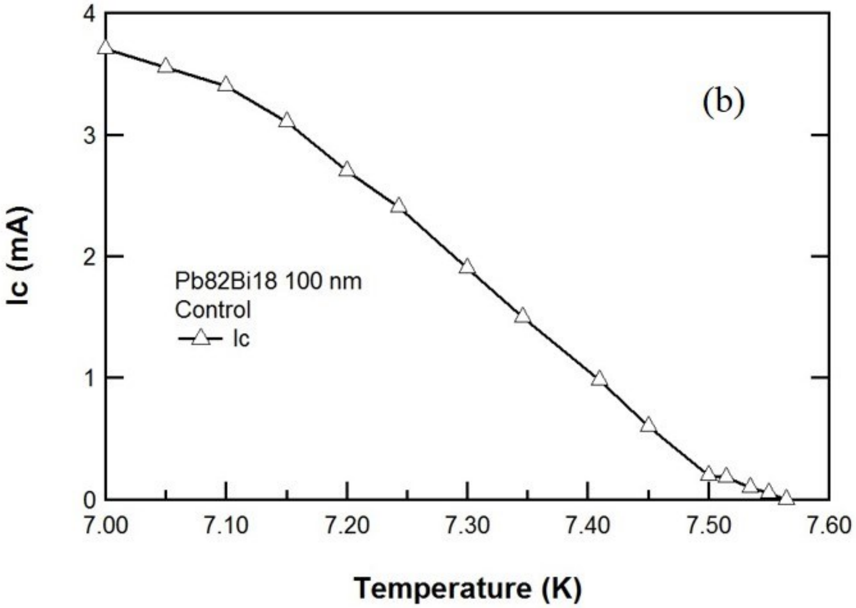

Figure 68. *I*-*V* curves of the $Pb_{82}Bi_{18}$ film with different temperatures (a) and I_C as a function of the T/T_C (b).

T/T_C transition is in good agreement with that the I_C increases when the temperature decreases.

4.3 YBCO thin films

100 nm thin films of epitaxial YBCO on STO substrates were purchased from MTI Corporation. The film was patterned by using a photolithography technique, and etched in a diluted nitric acid (about 1%). Figure 69 displays an optical microscope image to show geometrical dimensions of the film. The film has a 1 mm length and a 100 μm width, and there are no ferromagnetic nanostructures on it.

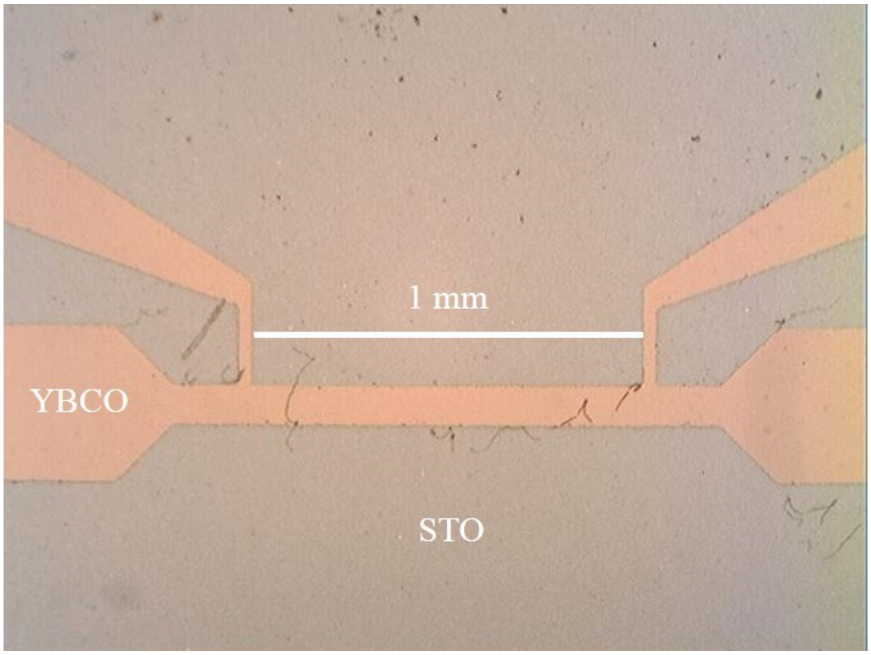

Figure 69. An optical microscope image of the YBCO film.

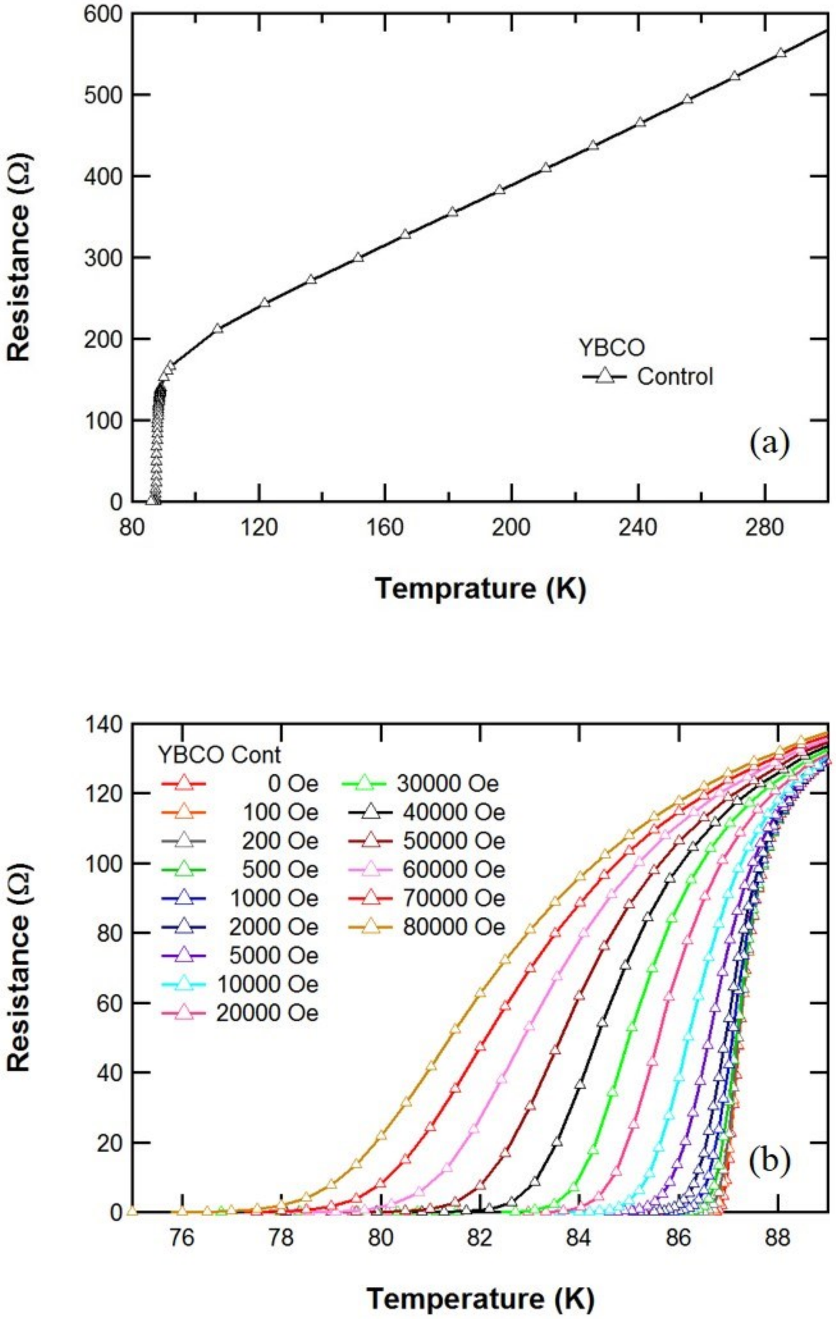

Figure 70. An *R*-*T* curve of the YBCO film (a) and its *R*-*T* curves with applied external magnetic fields near its T_C (b).

R of the YBCO film was measured in the PPMS. A 3.0 μA alternating current was applied, and the voltage at zero field was measured as a function of temperature. Temperature was reduced from room temperature to below T_C of the thin film during the *R* measurement. Figure 70 (a) shows the measured *R* of the thin film as a function of temperature. It demonstrates that the *R* of the film suddenly drops near its T_C.

Figure 70 (b) shows that the T_C of the film shifts toward lower temperature as magnitude of the external magnetic field is raised to 80,000 Oe. The magnetic field was applied perpendicular to the film. In order to determine $H_{C2}(T)$ of the thin film, the linear extrapolation was applied again on all the *R*-*T* curves in Figure 70 (b). As a result, $H_{C2}(T)$ as a function of the T/T_C is plotted in Figure 71 (a).

Coherence length ξ was calculated from the experimental results of the *R*-*H* curves. Why the clean limit has chosen will be explained in the next page.

T_C of the thin film at zero field is 86.90 K as measured by a linear extrapolation. ξ near T_C in the clean limit is given by

$$H_{C2} = \frac{\phi_0}{2\pi(0.74\xi_0)^2} \cdot \frac{T_C - T}{T_C} \tag{46}$$

by combining equations (12) and (22). From equation (46), the derivative of H_{C2} with respect to *T* is

$$\frac{dH_{C2}}{dT} = -\frac{\phi_0}{2\pi(0.74\xi_0)^2} \cdot \frac{1}{T_C} \tag{47}$$

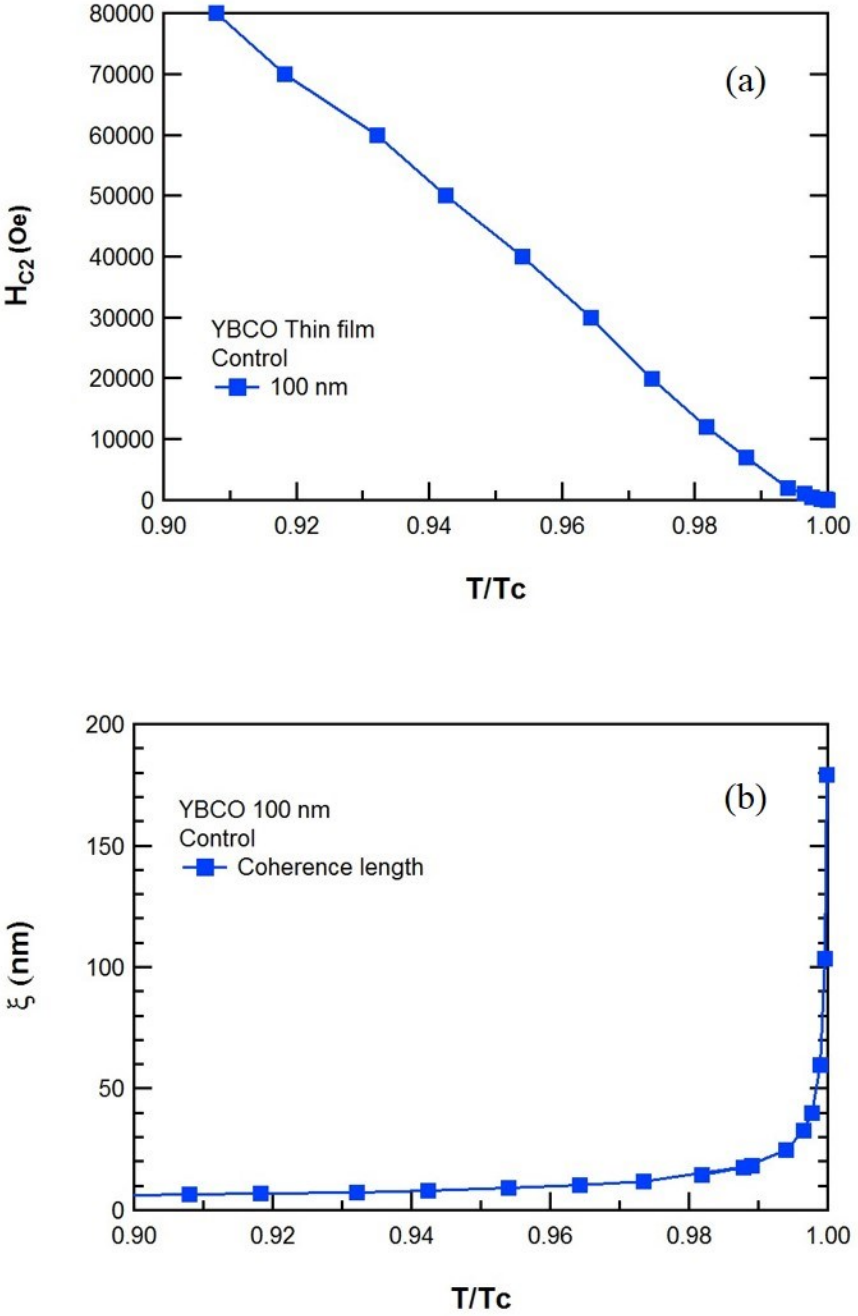

Figure 71. H_{C2} as a function of the T/T_C of the 100 nm thin film of YBCO (a) and its ξ as a function of the T/T_C (b).

Equation (47) can be written as

$$\xi_0 = \left(-\frac{\phi_0}{3.44067T_C \cdot \frac{dH_{C2}}{dT}}\right)^{\frac{1}{2}} \tag{48}$$

where $\frac{dH_{C2}}{dT}$ was obtained from Figure 71 (a) in the range from 0.908T_C to T_C. The coefficient of determination (R^2) was 0.9977. The YBCO film has an anisotropic coherence length within the superconducting state such as ξ_{ab} and ξ_c [119, 120].

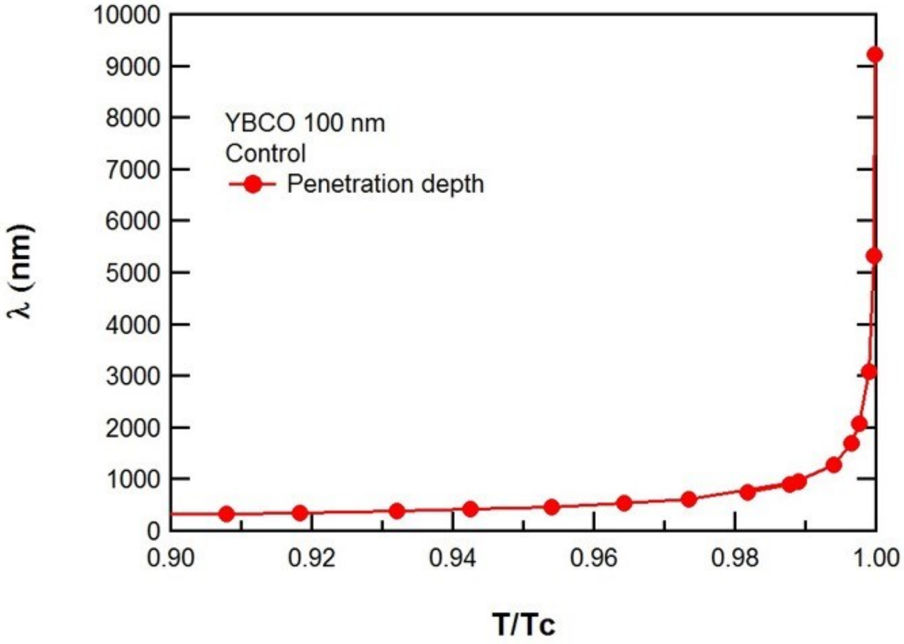

Figure 72. λ as a function of the T/T_C of the 100 nm thin film of YBCO.

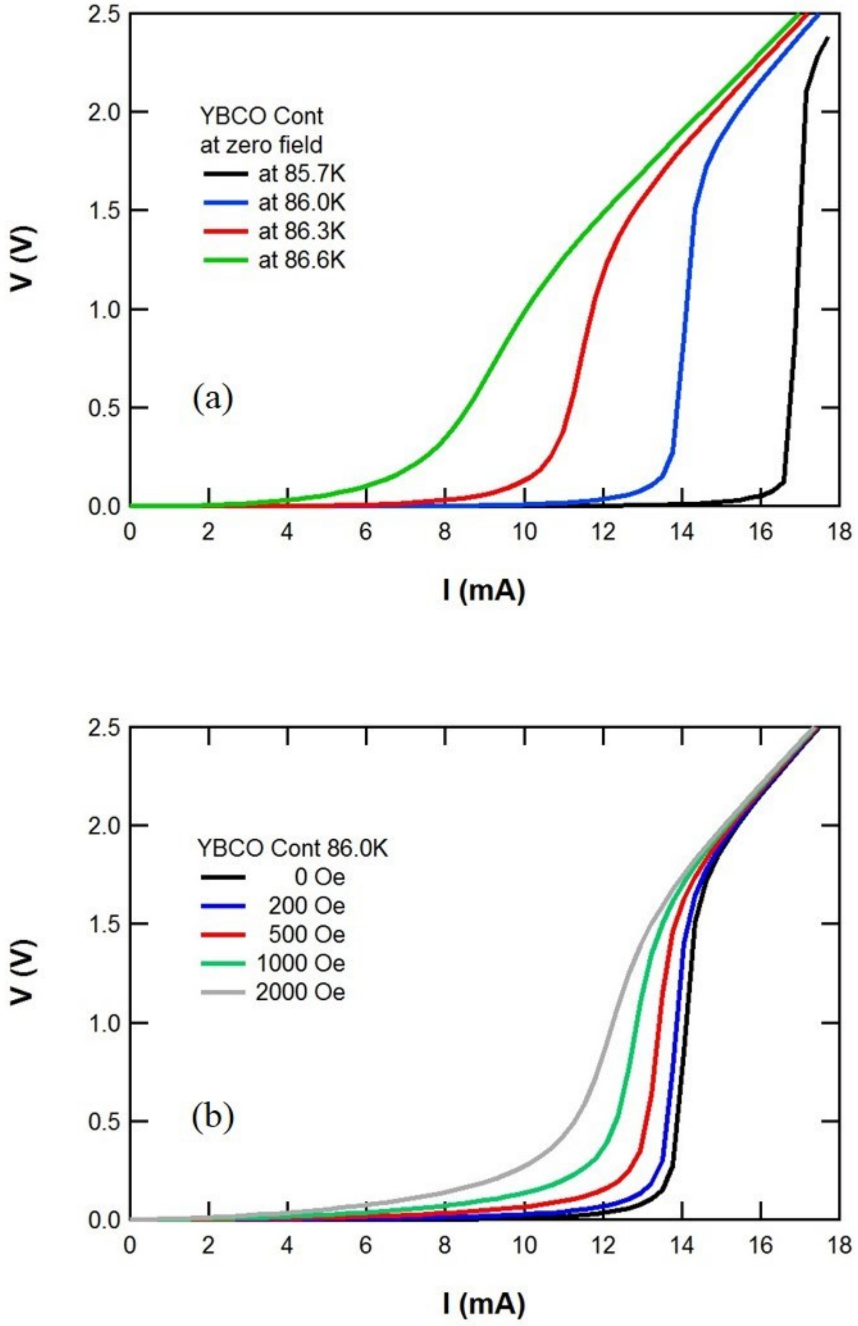

Figure 73. *I*-*V* curves of the YBCO film with different temperatures (a) and its *I*-*V* curves with different external magnetic fields (b).

Welp *et al* [120] obtained ξ_{ab}=1.6 nm and ξ_c=0.3 nm from their experimental results. Since ϕ_0, *T*$_C$, and $\frac{dH_{C2}}{dT}$ of the film are known, ξ_{0ab} of the film can be computed by using equation (48), if the orientation of the 100 nm YBCO film is c-axis. As a result, the calculated ξ_{0ab} is 2.59 nm. The ξ_{0ab} from the experimental results in this study is 1.6 times greater than their calculation. If thickness of the YBCO thin films is in a range between 25 nm and 200 nm, its mean free path right above T_C is as 7 nm [119, 121]. As a result, it is easy to know $\xi_0 < l$ (2.59 nm < 7 nm) for the 100 nm YBCO film, hence the film fits the clean limit.

If the 100 nm YBCO film characterizes the superconducting properties in the *a*-*b* plane, $\lambda_{ab}(0)$ is estimated 140 nm from the experimental results [122, 123]. Equation (19) can be employed to estimate the penetration depth depending on temperature, because the thin film is in the clean limit. Figure 72 depicts the calculated penetration depth as a function of the *T/Tc*. By calculating ξ_{0ab} and $\lambda_{ab}(0)$, κ is 51.48. This value is much greater than $\frac{1}{\sqrt{2}}$, and the value elucidates that the 100 nm YBCO film is a type II superconductor.

The *I-V* curves were measured to determine I_C at various temperatures. Figure 73 (a) shows *I-V* characteristics of the film with different temperatures from 85.7 K to 86.6 K at zero field. I_C has been determined by the current when the voltage has non-zero value in the *I-V* curves. The I_C increases with decreasing the temperature. The phase transitions from the superconducting state to the normal state in Figure 73 (a) are not sharp. *R* is absolutely zero below 10 mA, in contrast *R* is not zero above 10 mA at 86.0 K (blue line). There is a transition to the vortex state between 10 mA to 14 mA. The *V* gradually increases as the 100 nm $Pb_{82}Bi_{18}$ film in subchapter 4.2. This experimental result is one of the evidences that the 100 nm YBCO film is a type II superconductor.

In order to investigate the dependence of external magnetic fields on I_C for the YBCO film, I-V characteristics were measured at 86.0 K. Figure 73 (b) shows the I-V curves of the film with different applied magnetic fields from zero field to 2,000 Oe at T=86.0 K. As the applied magnetic field increases, I_C decreases at this temperature. Although the magnetic fields were applied up to 2,000 Oe, the thin film still has remained superconducting properties, as shown in Figure 73 (b).

The slope of the I-V curves above I_{Ci} indicates the resistance of the YBCO film in normal state, and the value of slope is 142.85 Ω. This value corresponds with the resistance at the normal state right above the T_C of the film in Figure 70 (b). From the results of I-V characteristics, the YBCO film has higher I_C at higher temperatures compared with the I_C of $Pb_{82}Bi_{18}$ film in Figure 68 (b). For this reason, YBCO is considered to be a good candidate for use in superconducting power cables at high temperatures.

5. EFFECTS OF NANOSIZED FEEROMAGNETS WITH SUPERCONDUCTING THIN FILMS

FSH samples have been successfully fabricated by photolithography, EBL, thermal evaporation, and electroplating techniques. In chapter 5, effects of ferromagnetic nanostructures with Sn, $Pb_{82}Bi_{18}$, and YBCO thin films are discussed. The nanostructures were created to have stripes or rods arrays. Several different nanostructures in the FSH of Sn films will be introduced in subchapters: anisotropy of the thermally evaporated Ni nanostripes, dependence on thickness of the Sn films with the thermally evaporated Ni nanostripes, anisotropy of the high aspect ratio electroplated Ni nanostripes, and the electroplated Ni nanorods. Also, electroplated Ni nanorods on $Pb_{82}Bi_{18}$ films and embedded Ni nanorods into $Pb_{82}Bi_{18}$ films will be discussed. Finally, an evaporated Ni nanorod array on YBCO films will be introduced.

5.1 Thermally evaporated Ni nanostripes on Sn thin films

Ferromagnetic structures were separated from the superconducting film by an insulating layer to evade the proximity effect and mechanical deformations of the thin film present when it is fabricated directly on the ferromagnetic structures [6, 7, 9, 10]. A $Pb_{82}Bi_{18}$ thin film with 25 μm iron (Fe) stripe showed a strong anisotropy in the vortex pinning [124]. In addition, a $Pb_{82}Bi_{18}$ thin film covering a nanosized ferromagnetic stripe array and an FSH sample exhibited strong anisotropy [11]. Some of the FSH samples included an insulating layer between the superconducting $Pb_{82}Bi_{18}$ thin film and two types of ferromagnetic stripes. Thus, the superconducting thin film and the ferromagnetic stripes only interact via the applied external magnetic field. The magnetic interaction of vortices with the magnetic stripes leads to the anisotropy in the I_C for the ferromagnetic stripes. The main source of the pinning potential with a one-dimensional symmetry is due to the magnetic interaction of vortices with the artificial ferromagnetic stripes. The Lorentz force applied on vortices is perpendicular to the ferromagnetic stripes when the applied current is parallel to the stripes. On the other hand, the Lorentz force becomes parallel to the stripes when the current is perpendicular to the stripes. The periodic potential barrier from the magnetic stripes inhibits motion of vortices that is perpendicular to the stripes. Thus, magnetic stripes parallel to the current flow in the superconducting film enhance its critical current; whereas, those stripes perpendicular to the current have little effect [124].

In this subchapter, the FSH sample consisted of 30 nm films of Sn with thermally evaporated Ni nanostripes. The nanostripes were either parallel to the applied current or perpendicular to it, as shown in Figures 50 (c) and (d), respectively. Three Sn thin films were deposited simultaneously on the same substrate by thermal quench condensation with liquid nitrogen. A 20 nm insulating layer of Ge was then deposited by thermal evaporation atop the Sn film. The Ni nanostripes were fabricated a 100 nm width and a 120 nm height. The period (center to center) of the Ni nanostripes was 500 nm. In order to characterize R of the FSH sample in the PPMS, a 1.0 µA alternating current was applied, and the voltage was measured for the three samples. An external magnetic

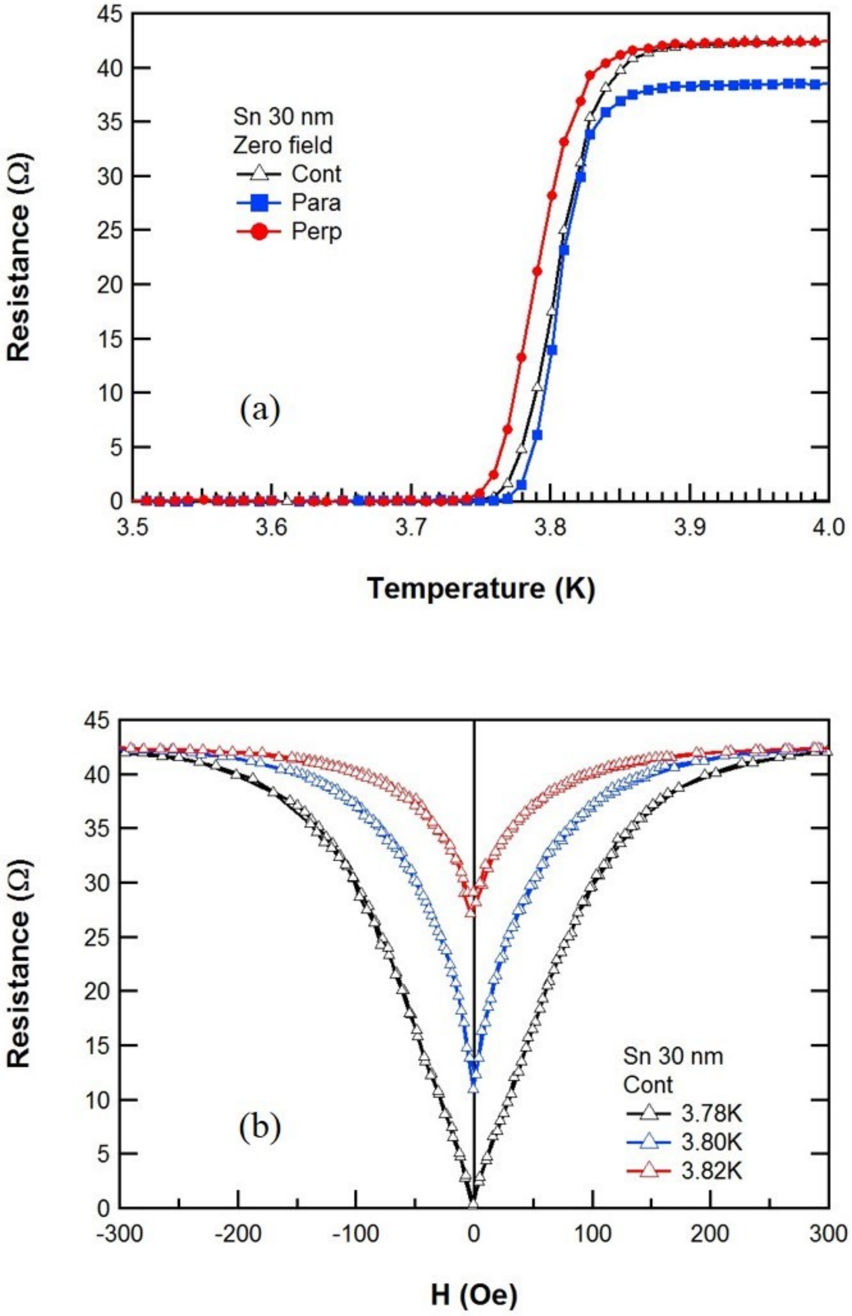

Figure 74. *R*-*T* curves of the Sn FSH and control samples around their T_Cs (a) and *R*-*H* curves of the Sn control sample slightly above its T_C (b).

field was applied perpendicular to the Sn thin films. The three samples were exposed in either +1 T or -1 T, and the Ni nanostripes were magnetized. The external magnetic field was swept from +800 Oe to -800 Oe. Afterwards, the magnetic field was returned to +800 Oe to complete a full cycle.

The temperature was reduced from room temperature to below their T_C during the *R* measurement. *R*-*T* curves in a zero magnetic field are shown in Figure 74 (a): the black open triangles are *R* of the control sample, the blue closed squares are *R* of the Ni nanostripes parallel to the applied current (the parallel FSH sample), and the red closed circles are *R* of the Ni nanostripes perpendicular to the applied current (the perpendicular FSH sample). Even though the two FSH samples (the parallel and perpendicular samples) had Ni nanostripes on top of Sn thin films, they showed similar superconducting properties to the control sample in a zero magnetic field. The control sample does not exhibit hysteretic behavior in the *R*-*H* curves, as shown in Figure 74 (b). The control sample has conventional superconducting properties between 3.78 K and 3.82 K: the *R* depends on the external magnetic fields and the temperatures.

Since the aspect ratio of the Ni nanostripes is greater than one, they tend to be magnetized along the direction parallel to the external magnetic fields. Unlike the control sample, the magnetized Ni nanostripes dramatically change the superconducting properties of the FSH samples. Even though the control sample was exposed in the external magnetic field, the sample's T_C was not changed at zero field by comparing Figure 74 (a) with (b) (see results at 3.78 K). On the other hand, after magnetizing the Ni nanostripes, both the parallel and perpendicular FSH samples' T_Cs are shifted towards lower temperatures. At 3.74 K, the parallel sample had a zero resistance in Figure 74 (a), however it had a flux flow resistance in Figure 75 (a). Similarly, at 3.70 K, the perpendicular sample had a zero resistance in Figure 74 (a), however it had a flux flow resistance in Figure 75 (a).

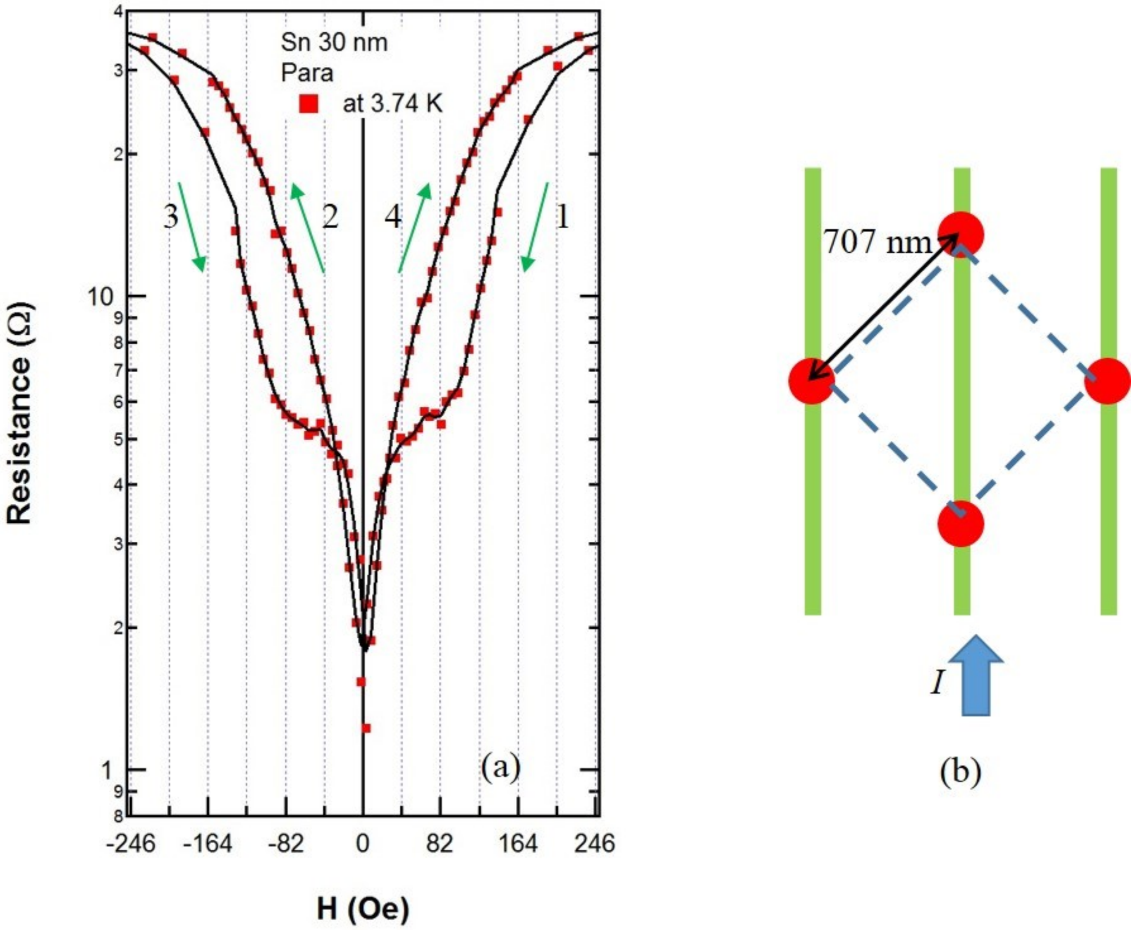

Figure 75. An *R*-*H* curve of the parallel FSH sample slightly above T_C (a) and a square commensurate vortex lattice (707 nm) (b).

The two FSH samples show strong hysteretic behavior in *R*-*H* curves, as shown in Figure 75 (a) and Figure 76 (a). The *R*-*H* curves of both the parallel FSH sample and perpendicular FSH sample are shifted to a non-zero magnetic field. The *R*-*H* curves are also shifted in the same direction as positive or negative direction of the magnetized Ni nanostripes. Green arrows in the figures indicate the sweep direction of the magnetic fields. The decreasing H branch (arrow 1 in Figure 75 (a)) always has a larger H_{C2} than that of the increasing H branch (arrow 4 in Figure 75 (a)). The two FSH samples have larger H_{C2} than the control sample in the whole temperature range. A magnetic hysteretic behavior in various FSH structures is a common property [7, 43, 125-127]. This phenomenon can be understood as the field compensation effect, as explained in subchapter 1.6. When the Ni nanostripes are magnetized in a direction parallel to the external magnetic field, the magnetization of the Ni nanostripes will reduce the magnetic field in the parts of the Sn thin film between the Ni nanostripes.

The parallel FSH sample shows vortex pinning properties near its T_C. The vortex pinning is represented by a one-dimensional periodic pinning potential for vortices. This phenomenon was observed by experiments [128] and discussed in theory [129]. As the period of the vortex lattice is commensurate with the period of the potential, the vortex pinning can be increased. Figure 75 (b) illustrates that the strongest vortex pinning on the parallel FSH sample is expected when all vortices can be placed into potential minima. The I indicates the direction of an applied current. In Figure 75 (a), the first matching field is approximately 41 Oe. The parallel FSH sample shows two kinks for the matching fields. The square vortex lattice constant of vortices on the Ni nanostripes of the parallel FSH sample is 707 nm. The first matching field, which corresponds to one flux quantum per unit cell, is 41.37 Oe by equation (30). The value of first matching field by the experimental results is in excellent agreement with the theoretical calculation. Analogously, the perpendicular FSH sample also shows a vortex pinning effect, as displayed in Figure 76 (a). The first matching field of the perpendicular FSH

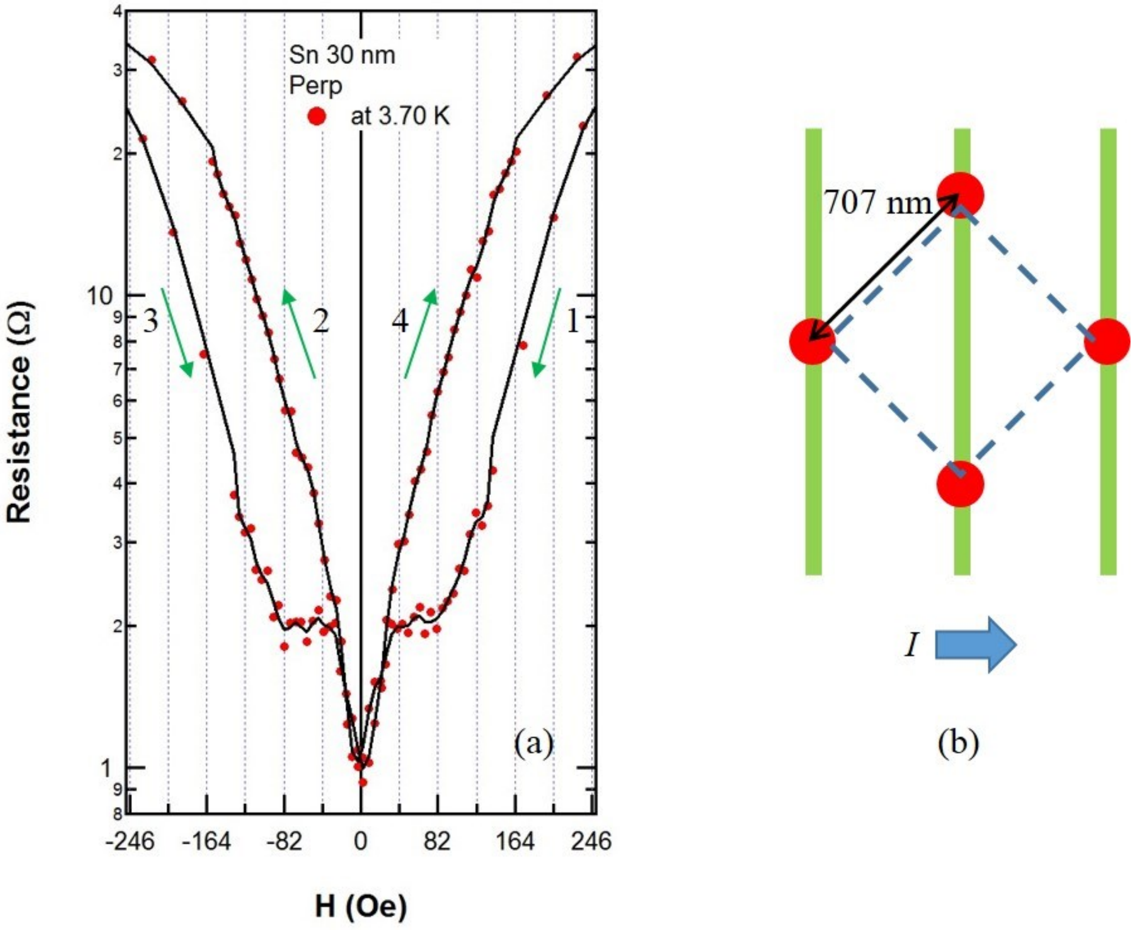

Figure 76. An *R*-*H* curve of the perpendicular FSH sample slightly above T_C (a) and a square commensurate vortex lattice (707 nm) (b).

sample is also approximately 41 Oe. Even though the *MR* does not sharply drop at the matching fields, three kinks are observed for the matching field effect in the perpendicular FSH sample. Figure 76 (b) illustrates vortex pinning in Ni nanostripe arrays, and the *I* indicates the direction of the applied current. The parallel FSH sample shows larger *MR* variations than the perpendicular FSH samples between the zero field and the first matching field. Furthermore, the matching field effect is clearly seen as the temperature is close to their T_Cs. Although the ratio of *MR* drops are smaller than the results of magnetic dots on Niobium (Nb) thin films [38, 39], the margin of error for theoretical and experimental field matching values are much smaller than the previous results [11].

In Figure 77 (a), the typical phase transitions by the external magnetic fields in *R*-*H* curves for the FSH samples and the control sample at 3.60 K are displayed. The control sample exhibits the superconducting state in the range of about ±300 Oe. In contrast, the range of the superconducting state in the FSH samples is enhanced to about ±400 Oe. The magnetized Ni nanostripes provide hysteretic behavior in the FSH samples. This results in the expansion of the superconducting state. Figure 77 (b) shows H_{C2} as a function of temperature near their T_C. The data points were extracted by linear extrapolation of the *R*-*H* curves of the Sn FSH and control samples. The external magnetic fields were scanned from +800 Oe to 0 Oe after the Ni nanostripes were magnetized at +1T. H_{C2} as a function of temperature shows that the magnetized Ni nanostripes enhanced the FSH samples' superconductivity compared to the control

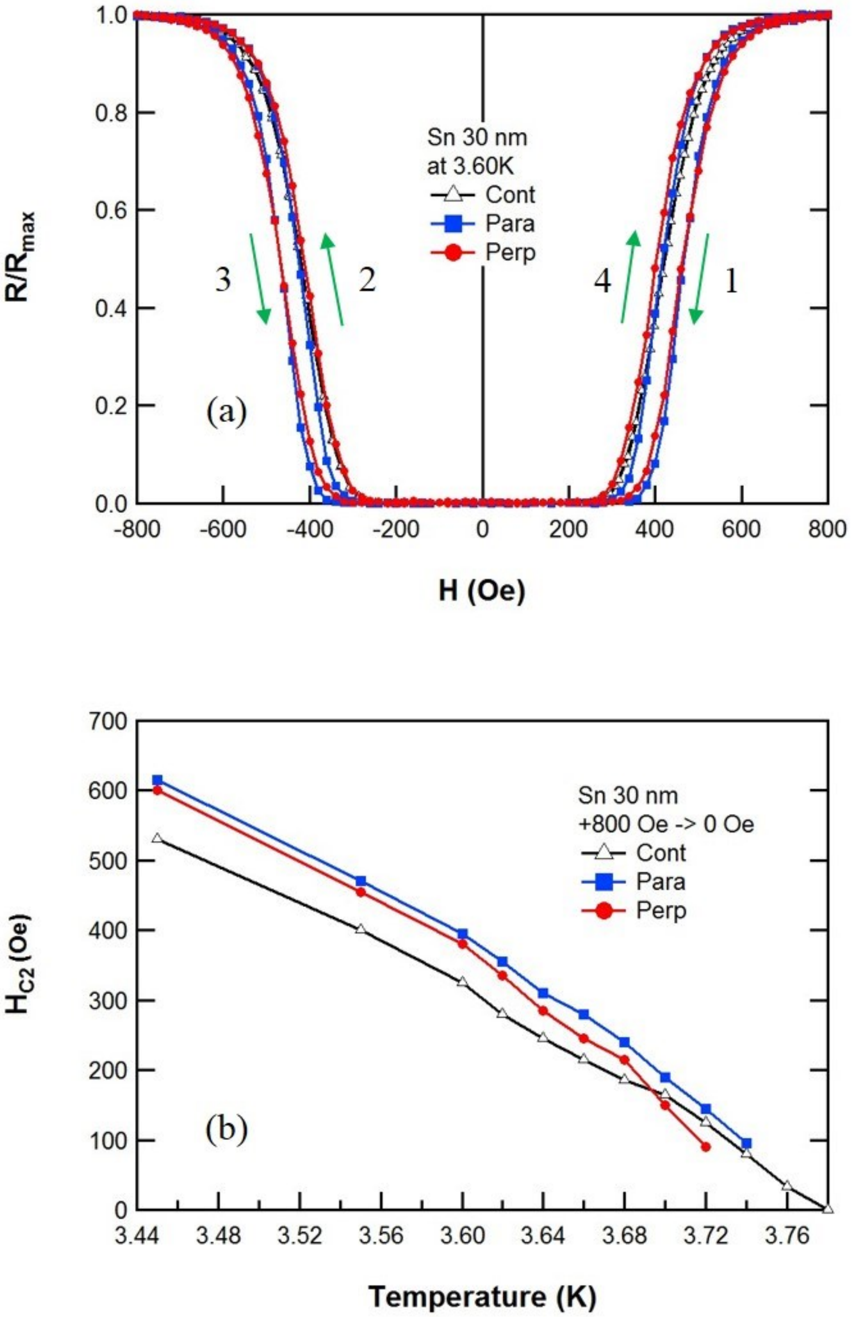

Figure 77. *R*-*H* curves of the Sn FSH and control samples at 3.60 K (a) and their H_{C2} as a function of temperature (b).

sample over a large temperature range. These phase diagrams are similar to those predicted by mean field theory [130]. The parallel FSH sample has larger H_{C2} than that of the perpendicular FSH sample at the same temperature. This is because vortex pinning is stronger when the direction of the applied current is parallel to the Ni nanostripes rather than perpendicular to the nanostripes [11].

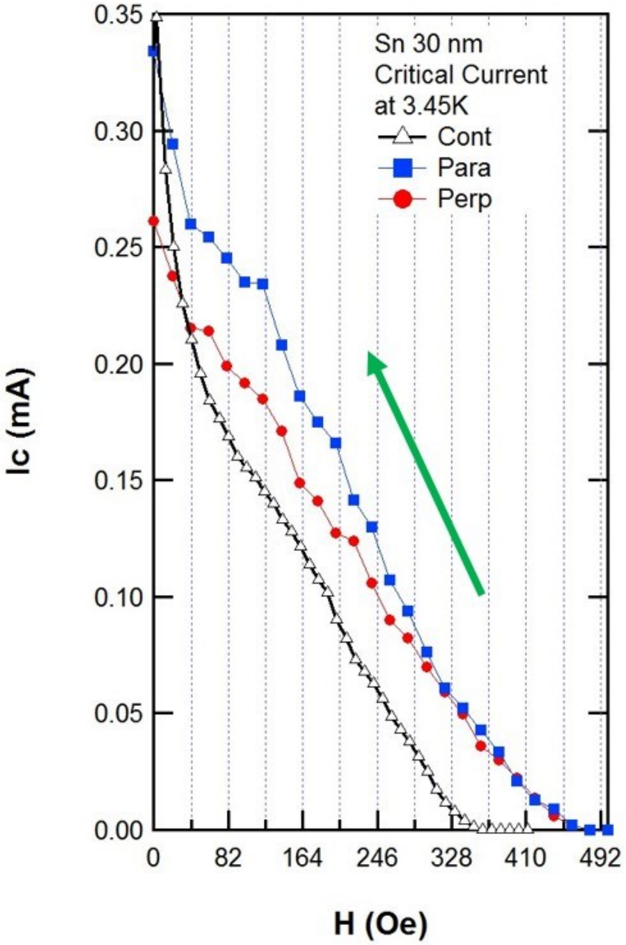

Figure 78. I_C as a function of the external magnetic fields at 3.45 K for the Sn FSH and control samples.

I_C of the FSH and control samples were measured with various external magnetic fields from +500 Oe to 0 Oe after the Ni nanostripes were magnetized at +1 T. Figure 78 shows I_C as a function of the magnetic fields at 3.45 K. The curve (blue squares) for the parallel FSH sample demonstrates enhanced superconductivity compared with the perpendicular FSH sample. The magnetized Ni nanostripes of the parallel FSH sample increases I_C by 30%. Vortices in the Sn thin films strongly interact magnetically with the Ni nanostripes. Hence, the vortices have different barriers for motion parallel and perpendicular to the nanostripes. This results in a strong anisotropy of the I_C [11].

In addition, the matching field effect is also seen in the I_C curves, and the values of the matched fields corresponds to the values in the R-H curves in Figure 75 (a) and Figure 76 (a) for the parallel and perpendicular FSH samples, respectively. On the contrary, the matching fields are not apparent in the I_C curve for the control sample. The existing number of data points is not enough to investigate clear matching fields for multiple of 41 Oe in the I_C curves. Shallow peaks may be due to the strong influence of thermal fluctuations [11].

Ni nanostripes exhibited an enhancement of superconductivity and vortex matching fields with the Sn films when the nanostripes were magnetized. The parallel FSH sample had higher I_C than the perpendicular FSH sample due to strong anisotropy of the magnetized Ni nanostripes.

5.2 Dependence of the thickness of the Sn thin films

In this subchapter, different thicknesses of the Sn FSH samples are introduced. These FSH samples consisted of thermally evaporated Ni nanostripes on 50 nm or 100 nm thin films of Sn. Nanostripes were fabricated either parallel or perpendicular to an applied current, as given in Figures 50 (c) and (d), respectively. There were four types of the FSH samples: the parallel FSH with 50 nm Sn film, the perpendicular FSH with 50 nm Sn film, the parallel FSH with 100 nm Sn film, and the perpendicular FSH with 100 nm Sn film. The same thickness of the Sn films were deposited simultaneously on the same substrate by thermal quench condensation. A 20 nm insulating film of Ge was deposited by the thermal evaporation atop the Sn film. The Ni nanostripes were created on top of the Ge film to form 100 nm width and 120 nm height stripes. The period (center to center) of the Ni nanostripes was 500 nm.

A 1.0 μA alternating current was applied, and the voltage was measured in the PPMS to obtain R of the FSH samples. An external magnetic field was applied perpendicular to the FSH samples, i.e. along the height of the Ni nanostripes, and the nanostripes were magnetized at 1 T. The external magnetic field was then swept from +300 Oe to -300 Oe. Afterwards, the magnetic field was returned to +300 Oe to complete a full cycle.

Figure 79 shows phase transitions of the FSH samples in a range of temperatures from 3.60 K to 3.85 K. In Figure 79, 0 T means that the FSH samples were not exposed to an external magnetic field, on the other hand 1 T means that the FSH samples were

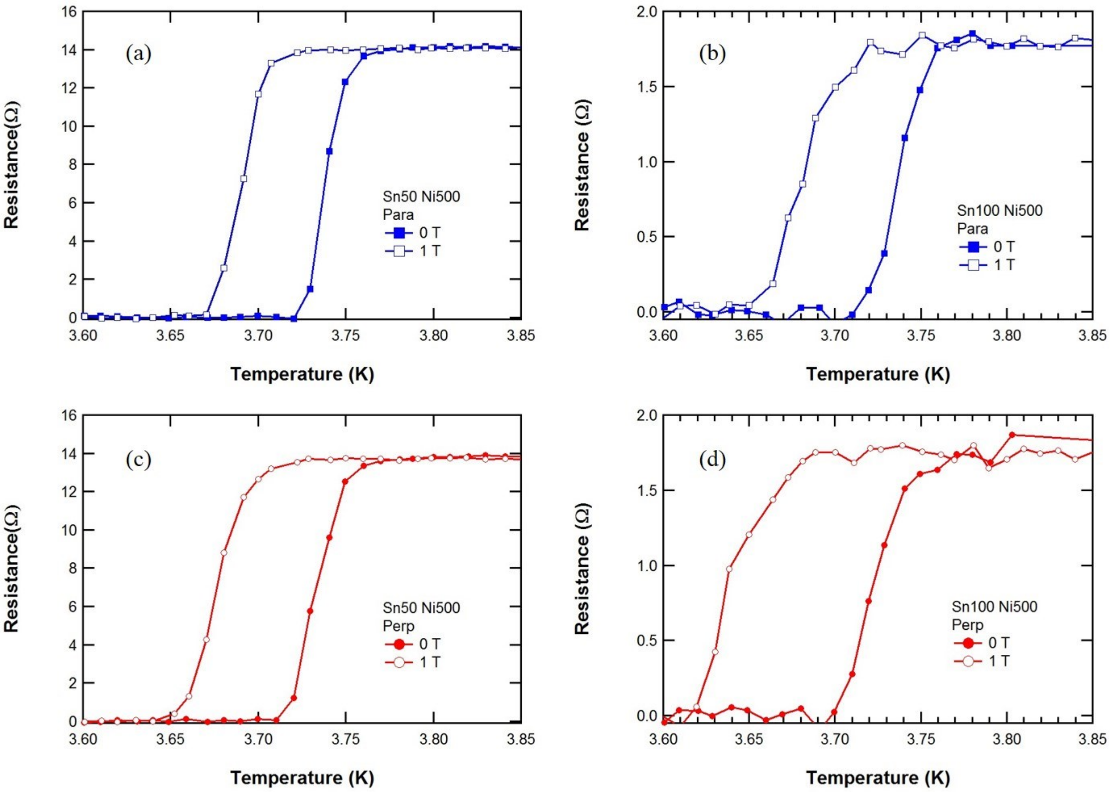

Figure 79. Effect of magnetized the Ni nanostripes on *R*-*T* curves of the parallel FSH sample with 50 nm Sn film (a), the parallel FSH sample with 100 nm Sn film (b), the perpendicular FSH sample with 50 nm Sn film (c), and the perpendicular FSH sample with 100 nm Sn film (d).

magnetized at +1 T, and the field was returned to 0 T before measuring the *R*. The normal state resistance was the same for samples of the same Sn thickness despite the different Ni nanostripe directions, as can be seen by comparing either Figures 79 (a) and (c) or Figures 79 (b) and (d). The Ni nanostripes of the FSH samples were magnetized at +1 T before taking *R* measurements. The T_Cs of all the FSH samples were shifted towards lower temperatures when the Ni nanostripes were magnetized, as shown in Figures 79 (a) through (d). Although all the FSH samples' T_Cs are reduced, the slope of their *R*-*T* curves in the transition region were not changed. The transport properties were dramatically changed by the magnetized nanostripes; open squares and circles [131]. Effect of the magnetized nanostripes on the Sn films are similar in all the *R*-*T* curves.

Figures 80 (a) and (b) illustrate *R*-*H* curves for the FSH samples at 3.60 K. The *R* are normalized with each R_{max}, which means *R* in the normal state slightly above their

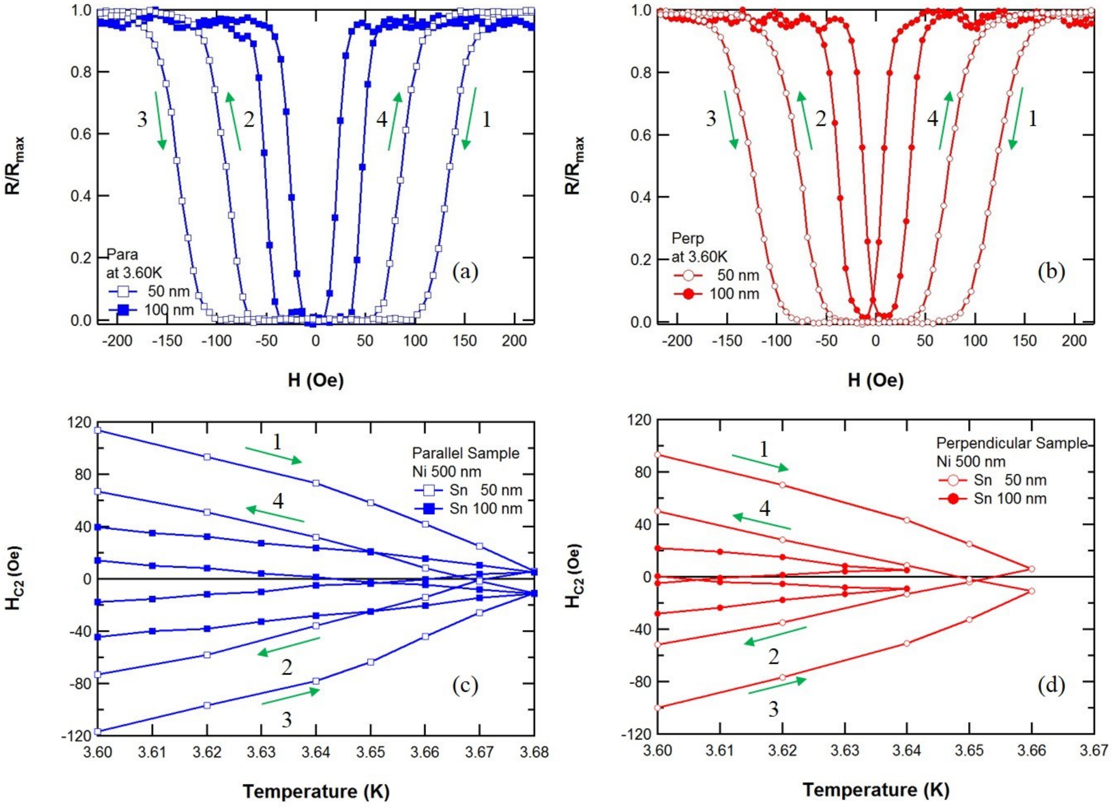

Figure 80. Comparison of *R*-*H* curves of the parallel FSH samples with the 50 nm and 100 nm Sn films (a), the perpendicular FSH samples with the 50 nm and 100 nm Sn films (b), H_{C2} as a function of temperature of the parallel FSH samples with the 50 nm and 100 nm Sn films (c), and H_{C2} as a function of temperature of the perpendicular FSH samples with the 50 nm and 100 nm Sn films (d).

T_C. The green arrows indicate the direction of the magnetic field sweep in Figure 80. All the FSH samples on 50 nm Sn films and 100 nm Sn films show a strong hysteretic behavior. However, the parallel FSH sample with the 50 nm Sn film indicates a larger hysteretic behavior in the *R-H* curves than that with the 100 nm Sn film, as shown in Figure 80 (a). The parallel FSH with the 50 nm Sn film remains the superconducting in ±100 Oe at 3.60 K; on the other hand, the parallel FSH with the 100 nm Sn film remains superconducting in ±30 Oe at the same temperature. A similar phenomenon occurs in the perpendicular FSH samples with the 50 nm Sn film and the 100 nm Sn film, as shown in Figure 80 (b). Phase diagrams in the H_{C2} as a function of temperature near T_C are depicted in Figure 80 (c) for the parallel FSH samples and (d) for perpendicular FSH samples. The resulting phase diagrams demonstrate strong hysteresis due to the hysteresis of the Ni nanostripes, and the phase diagrams are similar to those predicted by mean field theory [130]. The magnetic field distribution is created by the magnetic nanostripe array. The array on the superconducting thin film is exposed to this inhomogeneous magnetic field. The magnetic field distribution depends on the properties of the nanostripes and the thickness of the superconducting thin films. The magnetic field from the nanostripe array magnetized along their height with an in-plane period a drops as $e^{-\frac{2\pi z}{a}}$ where z is the distance from the template surface [132]. The ratio of the thickness of the superconducting thin films (d) and the width of the Ni nanostripes (w) is significant. If $\frac{d}{w}$ is smaller than 1, the direction of the magnetic field inside the superconducting thin film is normal to the thin film surface. Also, the magnetic field inside the superconducting thin film is close to the field at the surface of the nanostripes. Therefore, the direction of the magnetic field between the nanostripes will be changed. In this case, a field compensation effect can be expected [36]. The ratio of $\frac{d}{w}$ for 50 nm FSH samples is less than the ratio for 100 nm FSH samples. Therefore, both the parallel and perpendicular FSH samples of 50 nm Sn films show about twice as large as hysteretic behavior than that of 100 nm Sn films. In addition, the FSH samples exhibit anisotropy in the H_{C2} as a function of temperature. The parallel FSH samples show a larger H_{C2} at the same temperature. This anisotropic behavior can be explained by vortices in the Sn films interacting magnetically with the magnetized Ni nanostripes. Therefore, the vortices have different barriers for directions of motion parallel and perpendicular to the nanostripes.

Figure 81 shows J_C as a function of the external magnetic field for the FSH samples at 3.60 K. For the parallel FSH samples, the J_C for the FSH with 100 nm Sn

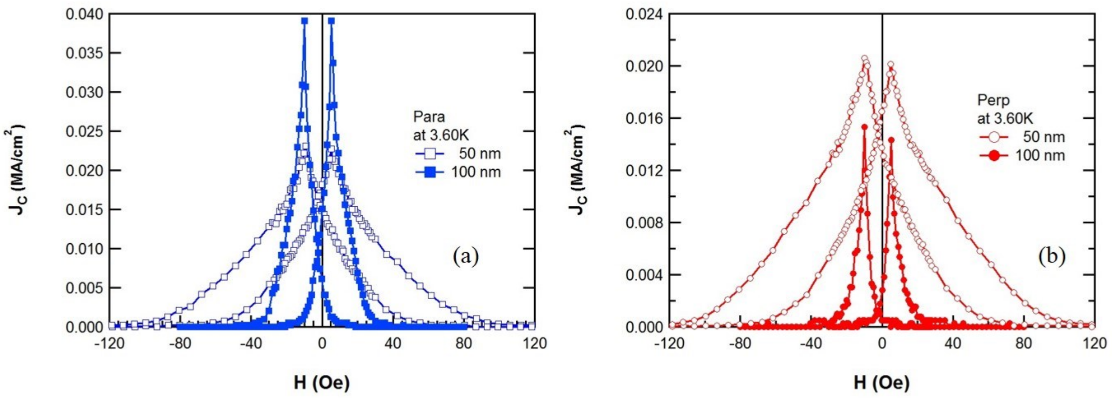

Figure 81. J_C as a function of the external magnetic fields for the parallel FSH with the 50 nm and 100 nm Sn films (a) and the perpendicular FSH with the 50 nm and 100 nm Sn films (b).

films is twice the value for the FSH with 50 nm Sn films near the peaks at ±20 Oe at 3.60 K, as shown in Figure 81 (a). A non-zero J_C for the 100 nm Sn film exists between ±30 Oe, while that for the 50 nm Sn film exists between ±100 Oe at 3.60 K. These external magnetic field ranges correspond to Figure 80 (a). Although a similar phenomenon occurs in the perpendicular FSH samples, the 50 nm Sn film has a greater maximums J_C than the 100 nm film at ±20 Oe at 3.60 K, as shown in Figure 81 (b).

The superconducting properties of the FSH samples depended on the thickness of the Sn films. The thinner Sn films indicated enhanced superconductivity and strong hysteretic behavior near their T_C when the structures of Ni nanostripes are the same, as shown in Figures 80 (c) and (d). Also, both the parallel and perpendicular FSH samples showed anisotropy when the Ni nanostripes are magnetized.

5.3 Anisotropy of the electroplated Ni nanostripes on the Sn thin films

In order to increase the amplitude of *MR* variations by the magnetic fields applied to the superconducting thin films by the magnetic nanostripes, a high aspect ratio of the nanostripes such as 1:3 is required. Nanosized EBL patterns with a high aspect ratio cannot be properly filled in by thermally evaporated materials. Typically, the thermal evaporator is appropriate for growing low aspect ratio nanostructures, as discussed in subchapter 3.2. An electroplating system was utilized to fabricate high aspect ratio Ni nanostripes. In this subchapter, the experimental results of high aspect

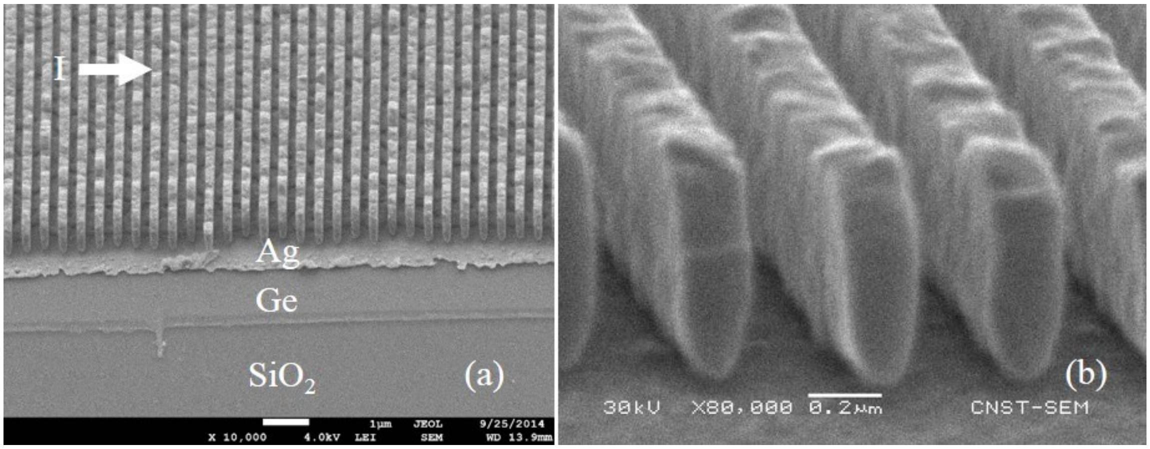

Figure 82. SEM images of the electroplated Ni nanostripes of 45° angled view for the perpendicular FSH sample (a) and 85° angled view for it (b).

ratio Ni nanostripes on Sn films will be compared with the previous results in subchapter 5.2.

A FSH sample, in this subchapter, consisted of 100 nm thin films of Sn with electroplated Ni nanostripes. The nanostripes were fabricated to be parallel to an applied current or perpendicular to an applied current, as given in Figures 50 (c) and (d), respectively. The Sn thin films were evaporated simultaneously on the same substrate by thermal quench condensation with liquid nitrogen. The electroplated Ni nanostripes were isolated from the Sn thin films by insulating layers to eliminate the proximity effect and mechanical deformations of the thin film are introduced when the thin film is fabricated directly on the magnetic nanostructures [6, 7, 9, 10]. A 5 nm thin film of thermally evaporated Ge was used as the insulating layer between the Sn thin film and the Ni nanostripes, and a 15 nm thin film of Ag was thermally evaporated on it as the electrode for electroplating, as shown in Figure 82 (a). A constant voltage of -1.2 V was applied between the electrodes for ten seconds to grow the Ni nanostripes. The Ni nanostripes were fabricated to have a 200 nm width and a 750 nm height whose aspect ratio is 1:3.75, as shown in Figure 82 (b). Spacing between the Ni nanostripes was 200 nm; therefore, the nanostripes have a 400 nm period (center to center). In order to define *R* of the FSH in the PPMS, a four-probe measurement was employed by applying an alternating current of 1.0 µA. The *R* of the three samples were measured at the same time in the PPMS. The external magnetic field was applied perpendicular to the Sn thin films in the FSH samples. Since the aspect ratio of the Ni nanostripes is 1:3.75, the Ni nanostripes can be magnetized along the direction of their heights. The Ni nanostripes were magnetized at either +1 T or -1 T. The hysteresis was observed in the region from +400 Oe to -400 Oe, as shown in Figure 83 (b).

The temperature was reduced from room temperature (at 300 K) to below the sample's T_C during the *R* measurement. *R* was normalized by *R* at 3.90 K. The normalized *R* as a function of temperature curves in a zero magnetic field are shown in Figure 83 (a): the black open triangles are data of the control sample, the blue closed squares are data for the Ni nanostripes parallel to the applied current (the parallel FSH sample), and the red closed circles are data for the Ni nanostripes perpendicular to the applied current (the perpendicular FSH sample). The magnetized Ni nanostripes on the Sn thin films dramatically change the transport properties of the FSH samples, as depicted in Figure 83 (a). Hysteretic behavior in *R*-*H* curves, as shown in Figure 83 (b), was observed. The behavior indicates an enhancement of superconductivity. As a result, the magnetized Ni nanostripes in the FSH samples enhanced H_{C2} by 68% compared with

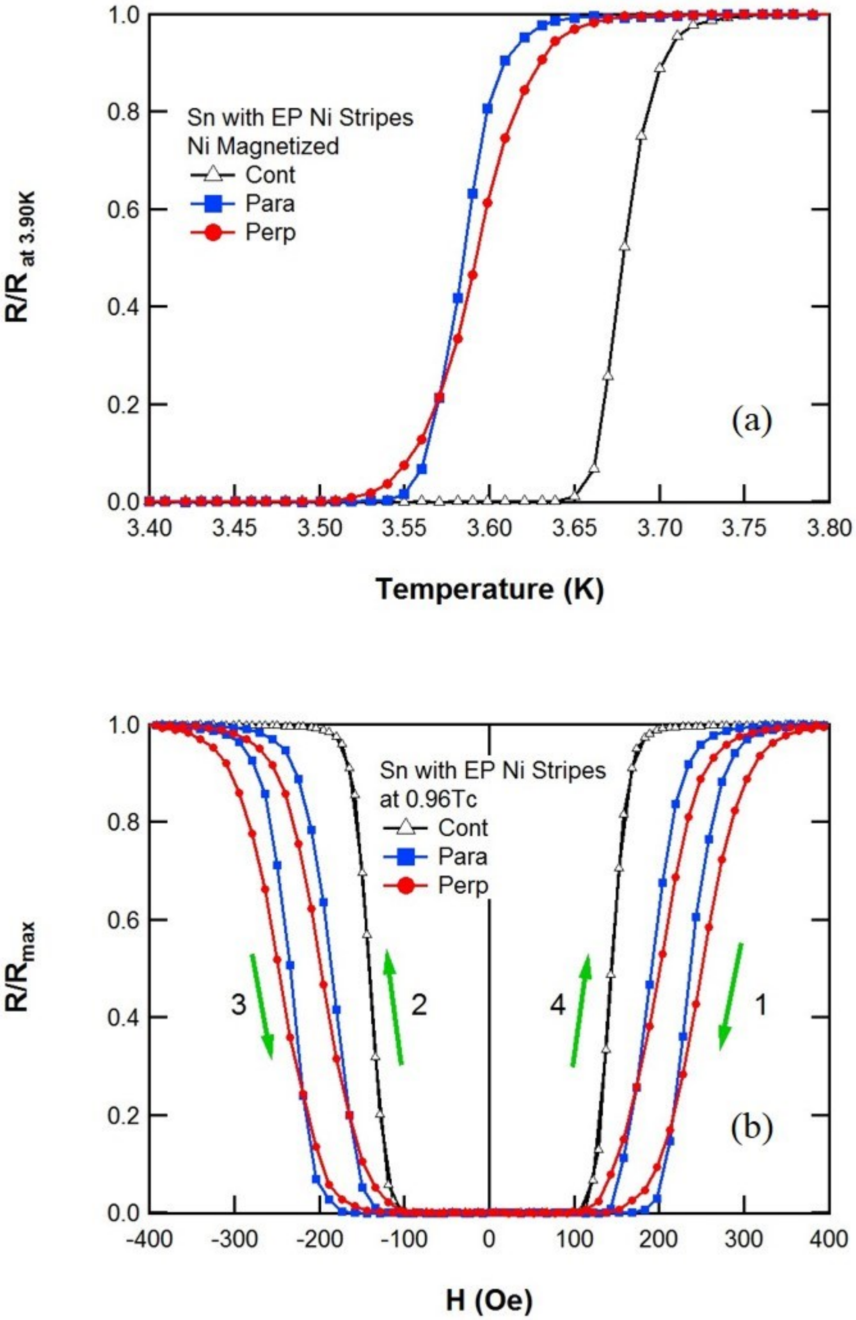

Figure 83. Normalized *R* as a function of temperature curves of the Sn FSH and control samples around their T_Cs (a) and their *R*-*H* curves at $0.96T_C$ (b).

the control sample at 0.96T_C. The decreasing H branch (arrow 1) of the FSH samples always has a larger H_{C2} than the increasing H branch (arrow 4), as seen in Figure 83; however, this behavior does not occur in the control sample. This phenomenon can be explained as the field compensation effect [36], as mentioned in subchapter 1.6. When the Ni nanostripes are magnetized in a direction parallel to the external magnetic fields, the magnetization of the nanostripes will reduce the magnetic fields in the parts of the Sn thin film between them [11]. Increase of the aspect ratio from 1:1.2 to 1:3.75 enhanced

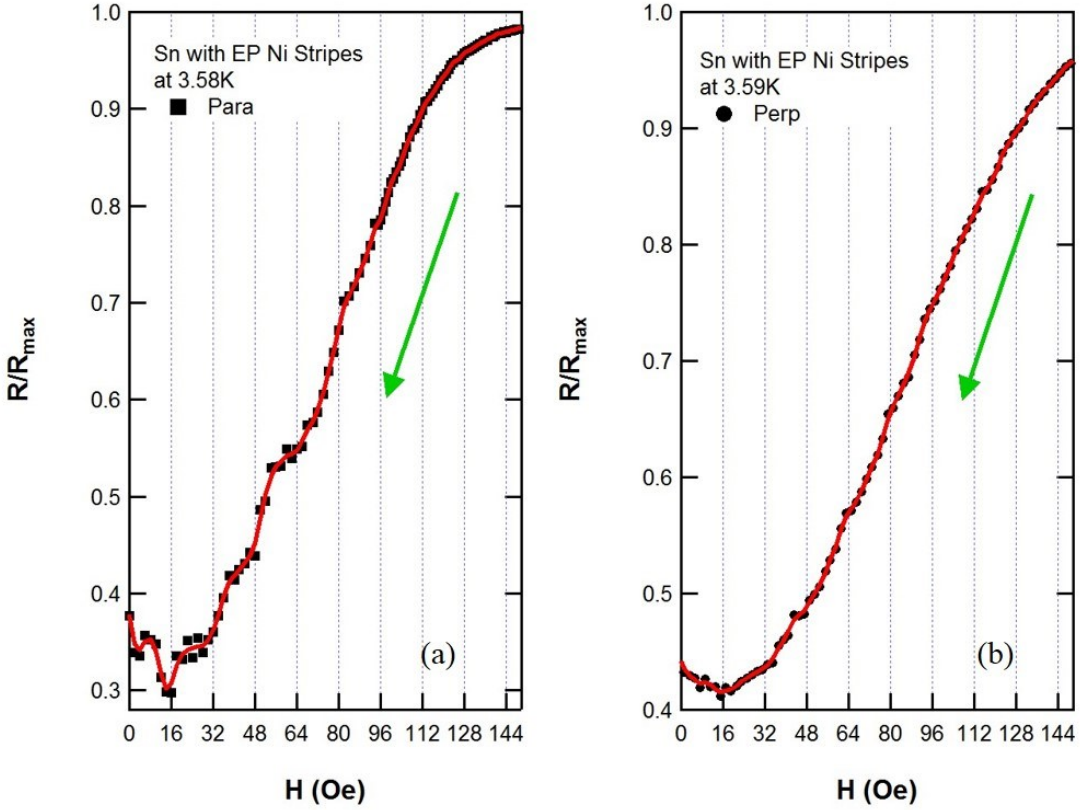

Figure 84. *R-H* curves of the parallel FSH sample at 3.58 K (a) and *R-H* curves of the perpendicular FSH sample at 3.59 K (b).

the hysteretic behavior in the *R*-*H* curves. As a result, the shifted phase diagram in the *R*-*H* curves represented in Figure 83 is twice as larger as that for the parallel FSH sample with 100 nm wide Ni nanostripes in Figure 80.

Both the parallel FSH sample and the perpendicular FSH sample exhibit vortex pinning properties near T_C, as shown in Figure 84. Vortex pinning is presented in a one-dimensional periodic pinning potential has been theoretically [129] and experimentally [128] discussed. An increase of vortex pinning occurs when the period of the vortex lattice is commensurate with the period of the potential. The vortex pinning on the FSH samples is expected when all vortices can be placed into potential minima. Figure 87 (a) depicts that the expected square vortex lattice on the Ni nanostripes of the FSH samples is 1,131 nm. The first matching field of the FSH samples is 16 Oe, and the green arrow indicates the sweep direction of the external magnetic field, as shown in Figure 84. The first matching fields of the samples are in excellent agreement with the theoretical calculation (16.15 Oe) by equation (30). The *R*-*H* curves in Figure 84 illustrate the integral multiples of 16 Oe of the FSH samples. There are five and six kinks for the parallel and perpendicular FSH samples, respectively. The magnitude of visible oscillations in Figure 84, which means the ratio of *MR* drops, is less than those in hybrid systems with arrays of magnetic dots embedded in a superconducting film [39]. These kinks may be due to the strong influence of thermal fluctuations. Even though Ni nanostripes on $Pb_{82}Bi_{18}$ thin films [11] did not show a periodic field matching effect, the electroplated Ni nanostripes on Sn thin films manifest the effect. This is due to the well-defined high aspect ratio Ni nanostripes.

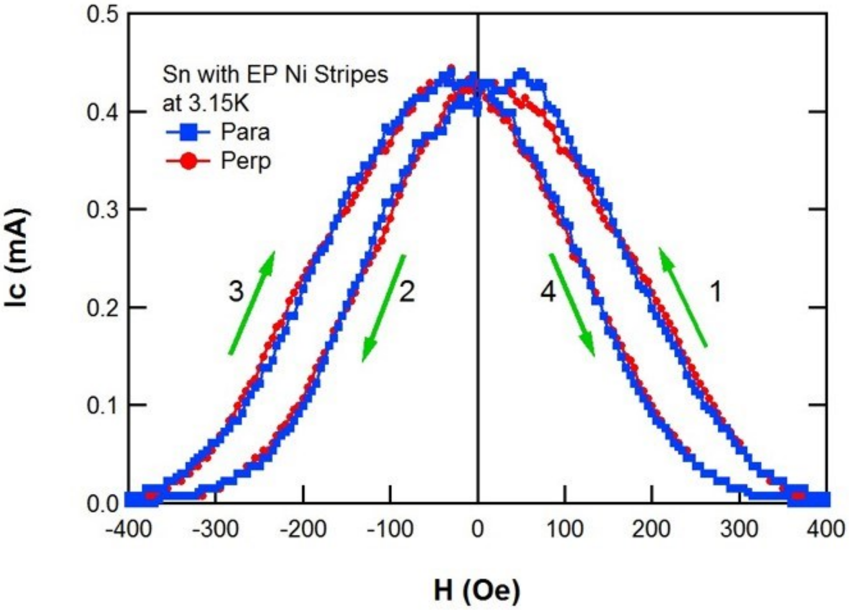

Figure 85. I_C-H curves of the parallel and perpendicular FSH samples at 3.15 K.

Figure 85 depicts the I_C for the parallel FSH sample (blue closed squares) and the perpendicular FSH sample (red closed circles) at 3.15 K. Strong hysteresis in the field dependence of the I_C demonstrates magnetic pinning of the vortices by the Ni nanostripes. This was observed in previous results [124, 131]. Note that the strongly magnetized nanostripes (arrow 1) has a higher I_C than those that are weakly magnetized them (arrow 4). The I_C for the parallel FSH sample is slightly greater than the perpendicular FSH sample near the zero field. A 30% greater I_C was observed when the magnetic nanostripes were parallel to the applied current rather than perpendicular to it. This effect was explained by the larger spacing between the Ni nanostripes used in the previous report [131].

Figure 86 displays a part of I_C-H curves of the parallel FSH sample and the perpendicular FSH sample at 3.15 K. The green arrows in Figures 86 (a) and (b) correspond to the arrow 1 in Figure 85. The matching field effect was observed in both FSH samples. One flux quantum per unit cell corresponds to 37.33 Oe for the FSH samples by equation (29) when the vortices are pinned on a triangular lattice with an 800 nm lattice constant. The simplified vortex lattice orientation is shown in Figure 87 (b).

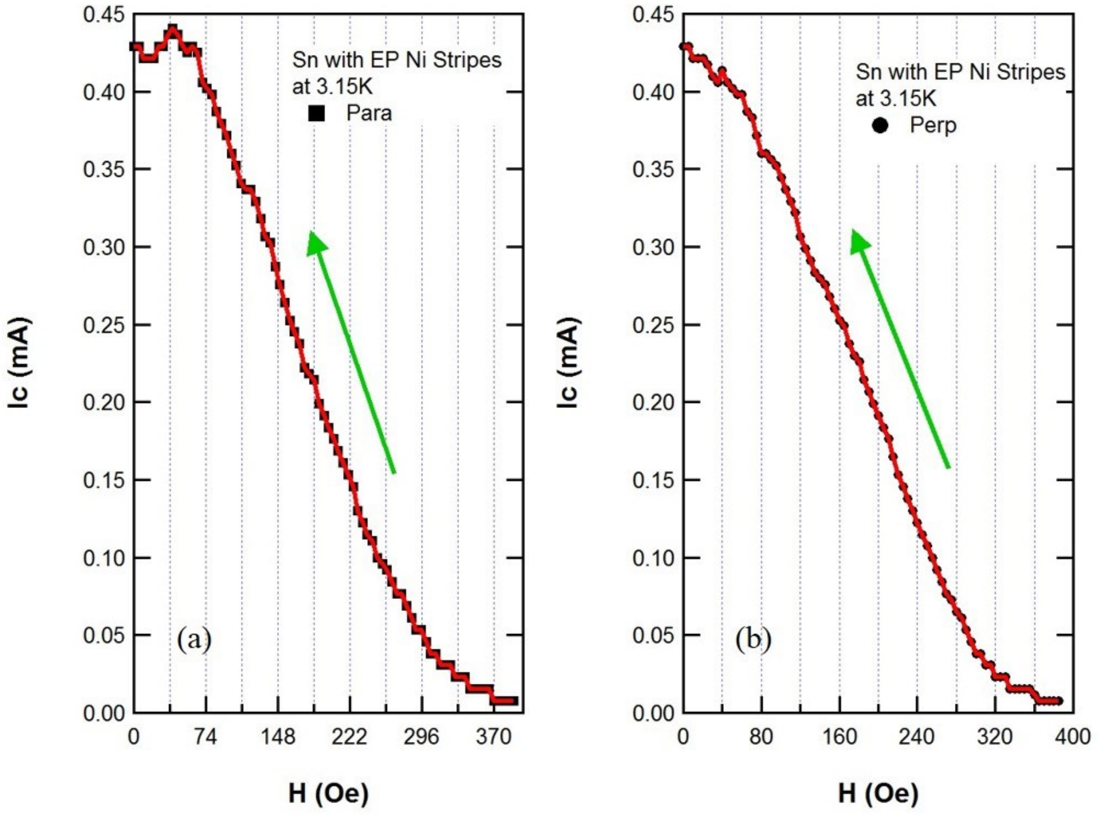

Figure 86. A part of I_C-H curves of the parallel FSH sample at 3.15 K (a) and the perpendicualr FSH sample at 3.15 K (b).

Figures 86 (a) and (b) demonstrate good correlation of the I_C variations up to six matching fields (37 Oe) and five matching fields (40 Oe), respectively. When the vortex lattice period is commensurate with the potential period, the vortex pinning increases. When all vortices are placed into potential minima, the strongest vortex pinning is expected. Due to the thermal fluctuations, the pinning potential abruptly drops near the T_C for large values of commensurability [11].

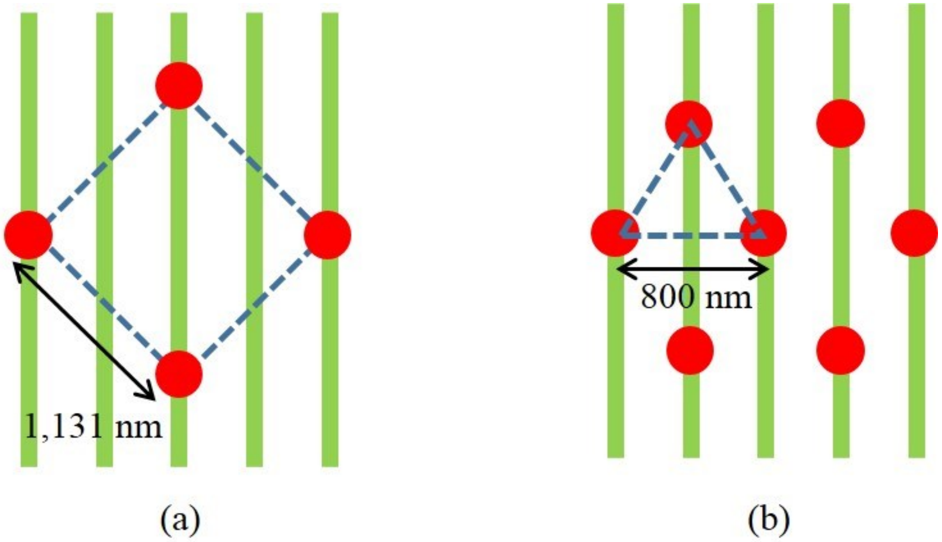

Figure 87. A square commensurate vortex lattice (1,131 nm) (a) and a triangular commensurate vortex lattice (800 nm) (b).

The difference between Figures 87 (a) and (b) demonstrates the rearrangement of the vortices by temperatures. Figure 87 (a) corresponds to Figure 84. For Figure 84 (a) and (b), the temperature during the R measurement is above their T_C, and the normal state starts above 200 Oe. On the other hand, Figure 87 (b) corresponds to Figure 86. For Figures 86 (a) and (b), the temperature during the I_C measurement is below their T_C, and the normal state starts above 400 Oe. Therefore, although the vortices are pinned by the magnetized Ni nanostripes, the vortex lattice may be rearranged by the temperature during the measurement. Also, the existence of the normal state at high magnetic fields indicate an increase of the value of its matching field.

5.4 Effect of the electroplated Ni nanorods on the Sn thin films

Thin magnetic structures (pancake-like) were created on superconducting thin films, or covered by superconducting thin films. The magnetic structures with superconducting thin films systems dramatically change and improve their superconducting properties [6, 7, 9, 10]. However, it is difficult to know from the systems whether the contribution of proximity effect, mechanical distortion, and magnetic interaction affect the changed properties or not [11]. Vortex pinning and matching field effect in an embedded Ni nanorod array into a $Pb_{82}Bi_{18}$ thin film was observed [43]. In contrast to that previous FSH system, an electroplated Ni nanorod array was isolated from a superconducting Sn thin film by an insulating Ge layer with the Ag electrode film on top of it to avoid the mechanical deformations and proximity effect of the Ag film present when it is fabricated directly on the ferromagnetic structures. Hence, the superconducting Sn thin film and the Ni nanorod array only interact via the magnetic field created by the nanorods.

In this subchapter, the FSH sample consisted of a 100 nm Sn film and the array of electroplated Ni nanorods. The two Sn films of the FSH sample and a control sample were thermally evaporated simultaneously on the same substrate with thermal quench condensation. A 5 nm insulating layer of Ge was deposited by thermal evaporation on the Sn film. There is an additional 15 nm film of thermally evaporated Ag to act as the electrode to electroplate the Ni nanorod array. A constant voltage of -1.2 V was applied to the electrodes for ten seconds to grow the Ni nanorods. The Ni nanorod array was fabricated to have a triangular lattice on the Ag film. Each nanorod had a 200 nm diameter and a 750 nm height. The period (center to center) of the Ni nanorods was 500 nm, as shown in Figure 88. During the fabrication process, 0.23% of the nanorods of the FSH sample were lost.

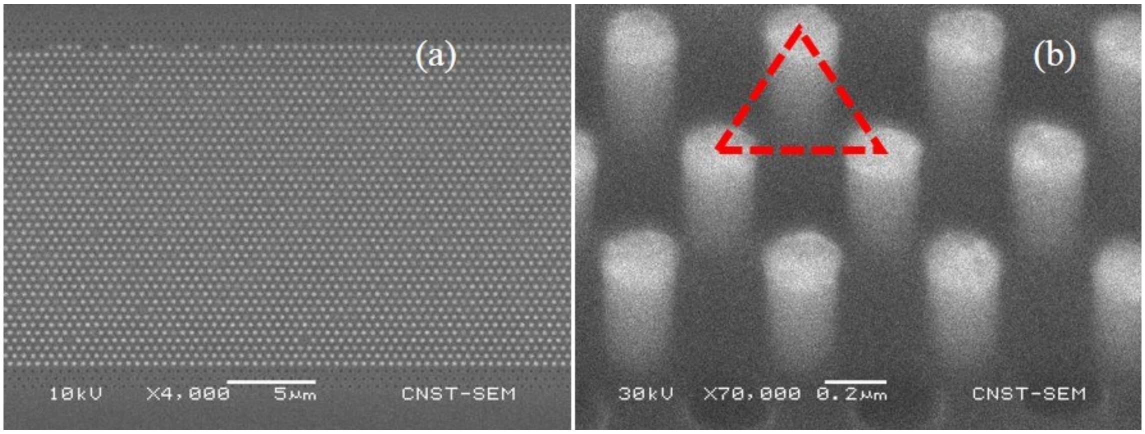

Figure 88. SEM images of top view of the electroplated Ni nanorod array in a triangular lattice at 4,000x (a) and its 45° angled view at 70,000x (b).

A 1.5 μA alternating current was applied, and the voltage at zero field was measured to obtain *R* of the FSH and control samples in the PPMS. The *R* of the FSH and the control sample were measured at the same time. An external magnetic field was then applied perpendicular to surface of the Sn films. The Ni nanorods were magnetized along the longitudinal direction due to shape anisotropy. The magnitude of the external magnetic fields for magnetizing of the Ni nanorods were at either +1 T or -1 T. The external magnetic fields were swept from zero to ±500 Oe.

The temperature was reduced from room temperature to below their T_C when the *R* was measured. Figure 89 (a) displays the phase transition of the FSH sample in a range of temperatures from 3.20 K to 3.80 K: *R*-*T* curves of the FSH sample in a zero magnetic field (blue open squares) and after magnetizing the Ni nanorods at +1 T (blue closed squares). The T_C of the FSH sample is reduced when the Ni nanorods were in a 1 T applied field, as shown in Figure 89. The FSH sample's T_C was shifted towards lower temperature due to the magnetized nanorods. Slope of the *R*-*T* curve during phase transition is reduced when the Ni nanorods were magnetized by comparing with the *R*-*T* curve of non-magnetized Ni nanorods. This phenomenon is different from Figure 79 where the slope of the *R*-*T* curves do not depend on the magnetization of the Ni nanostripes.

The control sample does not exhibit hysteretic behavior in the *R*-*H* curve, as shown in Figure 89 (b). The *R*-*H* curve of the control sample (black open triangles) indicates typical dependence of resistance on magnetic fields at 3.59 K. The *MR* in the *R*-*H* curve sharply drops to zero-resistance, and the control sample transists to the

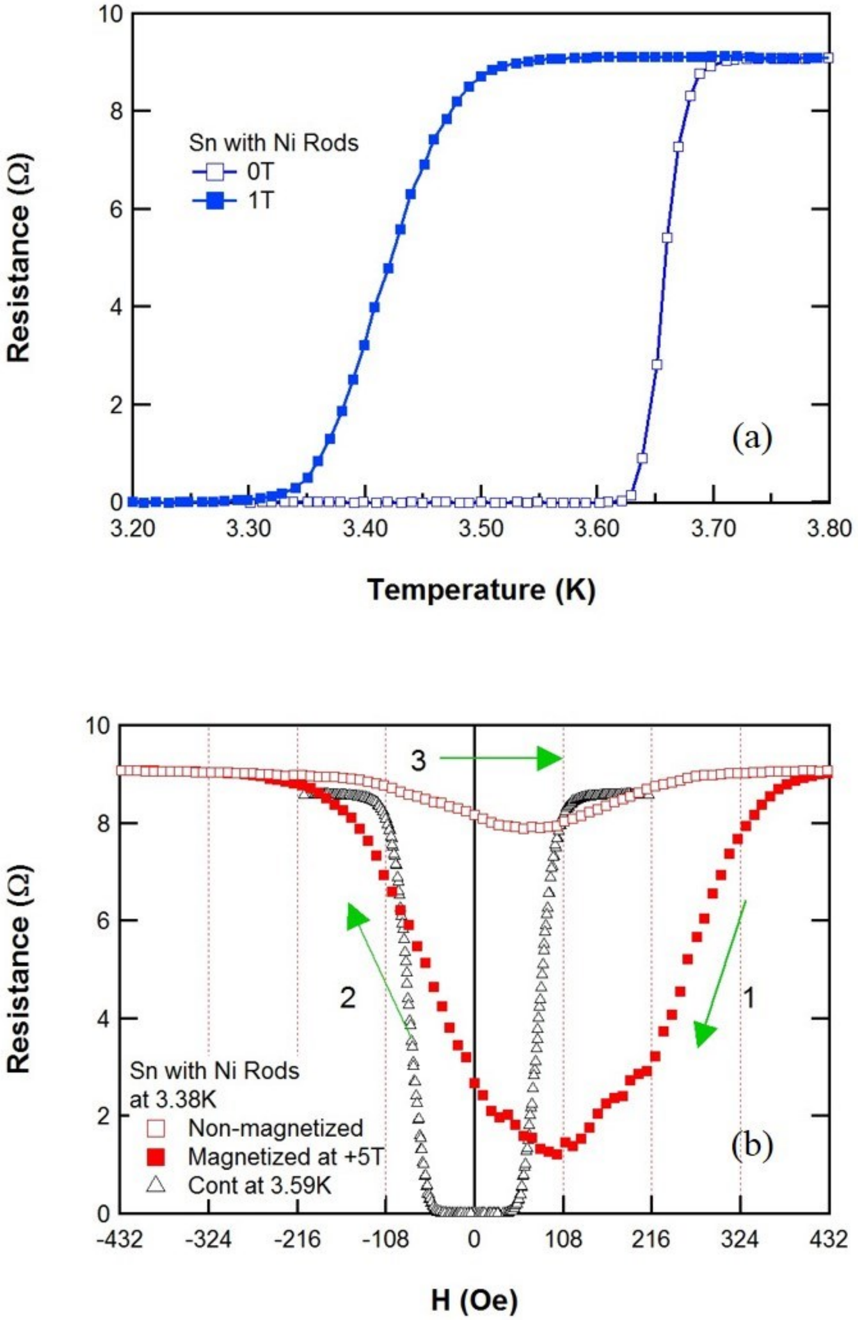

Figure 89. *R*-*T* curves of the Sn FSH sample around its T_C (a) and *R*-*H* curves of the Sn FSH and control samples at 3.38 K and 3.59 K, respectively (b).

superconducting state when the external magnetic field is between +110 Oe and -110 Oe. Also, the *R*-*H* curve of the control sample is symmetric with respect to the zero field line. On the other hand, the *R*-*H* curve of the FSH sample exhibits interesting properties when its Ni nanorod array was magnetized at +5 T before taking *R* measurements. Red closed squares in Figure 89 (b) displays the measured *MR* of the FSH sample at 3.38 K. The green arrows indicate the direction of the magnetic field sweep. After magnetizing the Ni nanorods at +5 T, the field was scanned from arrow 1 to 2. The *R*-*H* curve (red closed square) shows hysteretic behavior. The *R*-*H* curve is shifted in the direction of the magnetized Ni nanorods. This phenomenon can be understood as the field compensation effect, as introduced in subchapter 1.6. A Ni nanorod array with magnetic moments aligned along the positive z direction (parallel to the rods and perpendicular to the Sn films) is placed on top of the Sn film. The magnetic stray field of each rod has a positive z component of the magnetic induction B_Z under the nanorods and a negative one in the parts between the nanorods. On the other hand, when an external magnetic field is applied, the stray field between the nanorods in the opposite direction to the external field are attenuated. Thus, the magnetic nanorods in the FSH sample provide an opportunity to observe the field compensation effect in which the external magnetic field is applied parallel to the nanorods. The magnetization of the nanorods reduces the magnetic field in the parts of the Sn film between the nanorods [36]. This phenomenon also occurred in FSH samples of Ni nanostripes on Sn films in previous subchapter 5.1 through 5.3.

The so-called first matching field H_1 corresponds to the one flux quantum per unit cell at 95.58 Oe. The value was calculated for a 500 nm triangular vortex lattice with equation (29). When the Ni nanorods were positively magnetized, the experimental result shows that the first matching field is +108 Oe, and second matching field is +216 Oe. These values of the matching field effect are in reasonable agreement with the

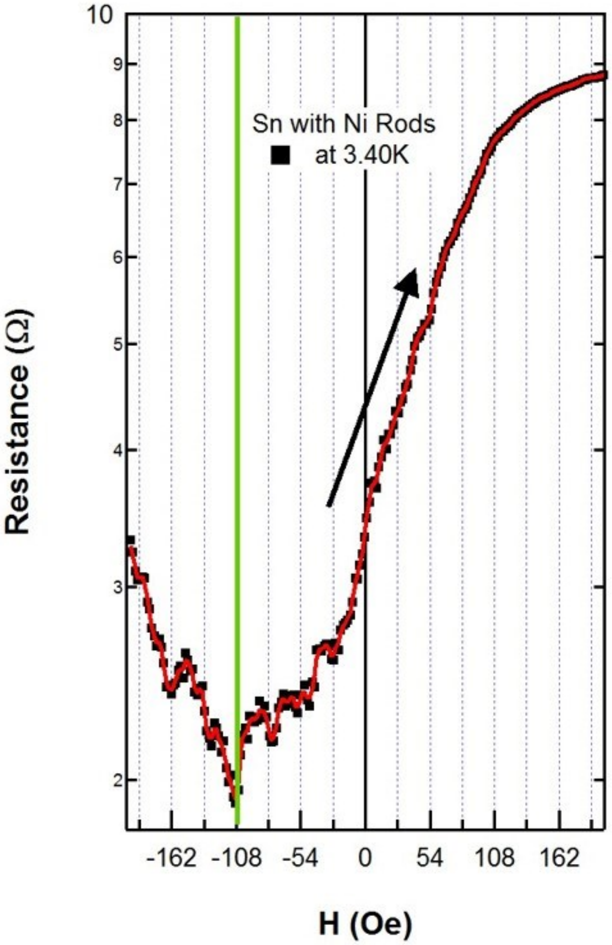

Figure 90. *R*-*H* curve of the Sn FSH sample at 3.40 K after negatively magnetizing the Ni nanorods.

theoretical estimation. A minimum in *R*-*H* is observed when there is an integer number of vortices per unit cell in the magnetic nanorod array, as shown in Figure 89 (b). Moreover, the magnetized Ni nanorods on the Sn film enhanced H_{C2} in the *R*-*H* curves. Within the sweeping range between -500 Oe and +500 Oe (arrow 3 in Figure 89 (b)) of the FSH sample (red open squares) the Ni nanorods were not magnetized at -5 T. Positive magnetic moments were still dominant in the Ni nanorods in the sweep direction. Non-magnetized Ni nanorods indicate higher values of *MR* than that of magnetized Ni nanorods. Hence, magnetized Ni nanorods enhance superconductivity and increase the value of H_{C2} at lower temperatures.

The external magnetic field was applied up to -1 T to negatively magnetize the Ni nanostripes of the FSH sample. The magnetic field was swept from -200 Oe to +200 Oe. Figure 90 demonstrates that *R*-*H* curve is shifted in the opposite direction of the field compensation effect. Interestingly, Figure 90 also shows another periodic oscillation near the first matching field. The resistance of the sample was measured at every 2 Oe to examine the small periodic matching fields at 3.40 K. Several dissipation minima are observed in the vortex state of the FSH sample at this temperature. However, the qualitative behavior is quite different from samples with pancake-like magnetic dots with a rectangular lattice [38] or a triangular lattice [39]. Two types of minima are clearly presented. The first matching field $-H_1$, -108 Oe (green line), is the same when the Ni nanorods were positively magnetized, as shown in Figure 89 (b). There are additional periodic *MR* oscillations in the interval between two consecutive minima. The period of the *MR* oscillation is 27 Oe which is close to the 24 Oe for one flux quantum per unit cell on a 1,000 nm triangular vortex lattice estimated with equation (29). The values of experimental results for the matching fields are in good agreement with the theoretical estimations. The triangular vortex lattice constant is 500 nm for red circles and 1,000 nm for blue circles, as shown in Figure 91. In this vortex lattice, 500 nm and 1,000 nm triangular vortex lattices coexist. Both types of triangles occupy the lattice equivalently. The results for the triangular arrays indicate that critical matching between the vortex lattice and the Ni nanorod array originates at the local scale. The two types of triangles responsible for a particular matching field are found scattered all over the array.

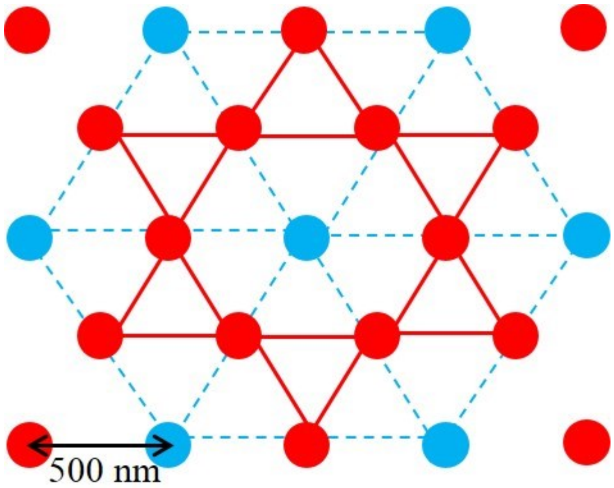

Figure 91. Coexistence of triangular commensurate vortex lattices of 500 nm (red circles) and 1,000 nm (blue circles).

Figure 92 shows that I_C for the FSH sample (red closed squares) and the control sample (black open triangles) depends on external magnetic field at 2.60 K and 3.50 K, respectively. The shifted I_C curve is due to the strong hysteresis effect in the FSH sample by the magnetized Ni nanorods. The strong matching field effect (blue arrows) in the I_C-H curve for the FSH sample is also observed at the same temperature. However, the existing number of data points is not enough to investigate the additional periodic matching fields for 27 Oe. This artificial degeneracy results in an I_C peak close to the

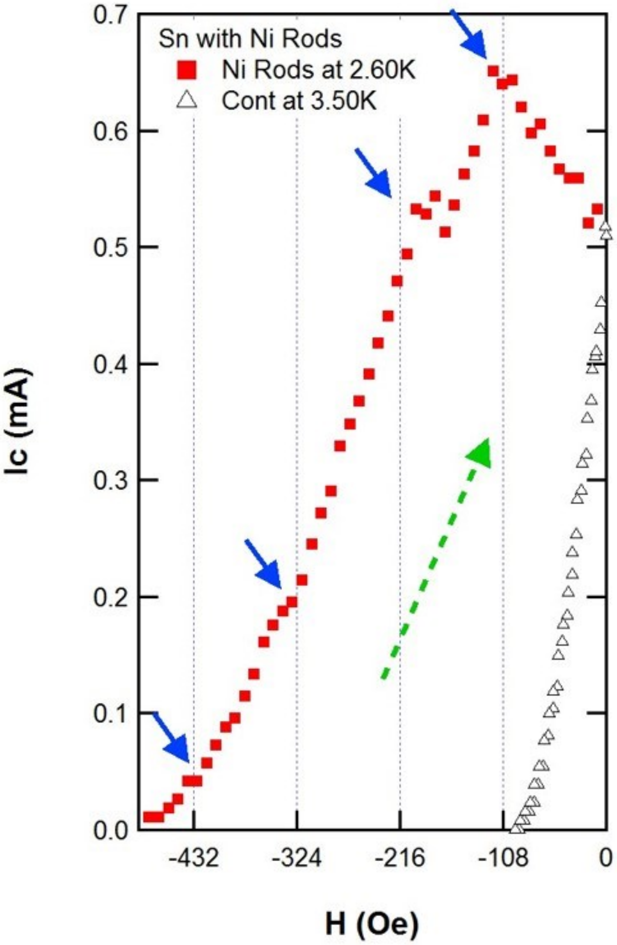

Figure 92. I_C-H curves of the Sn FSH sample at 2.60 K and the control sample at 3.50 K.

zero external field [43]. Figure 92 also displays the important feature of magnetic pinning of vortices by the Ni nanorods. A similar phenomenon was observed in previous research [43, 133]. The order of magnitude actually increases the range of magnetic fields with a significant value of the I_C.

Measurement of the *I-V* characteristics were done on the FSH sample with a direct current. The influence of an external magnetic field on the FSH sample was observed on the *I-V* curves. Figure 93 shows the *I-V* characteristics of the FSH sample at 2.50 K. Figure 93 (a) is the result for non-magnetized Ni nanorods, and Figure 93 (b) is the results for Ni nanorods magnetized at +1 T. When the Ni nanorods were not magnetized, the *I-V* characteristics exhibit typical superconductor behavior, which means that I_C decreases with increasing the external magnetic field. In contrast, when the nanorods were positively magnetized at +1 T, the *I-V* curves are dramatically changed by the magnetized Ni nanorods. This is an interesting property. A comparison of Figure 93 (a) with (b) clearly shows that I_C was significantly increased at the same external magnetic field. In particular, the value of I_C at +100 Oe (blue curve) is increased about 200% by the magnetized Ni nanorods. Furthermore, the *I-V* curves after magnetizing Ni nanorods in the FSH sample demonstrate a hysteresis in the I_C-H curves. The *I-V* curve measured at +100 Oe has a higher I_C (blue curve) than the curve at 0 Oe (black curve), as seen in Figure 93 (b). Also, the curve measured at +200 Oe has a value of I_C close to that of the curve at 0 Oe. This phenomenon corresponds to the I_C-H curve of the FSH sample in Figure 92. A similar effect, increasing I_C in *I-V* curves by magnetized Ni nanostripes on a Sn thin film, was shown by Kim *et al* [131]. The last exciting feature is that three to

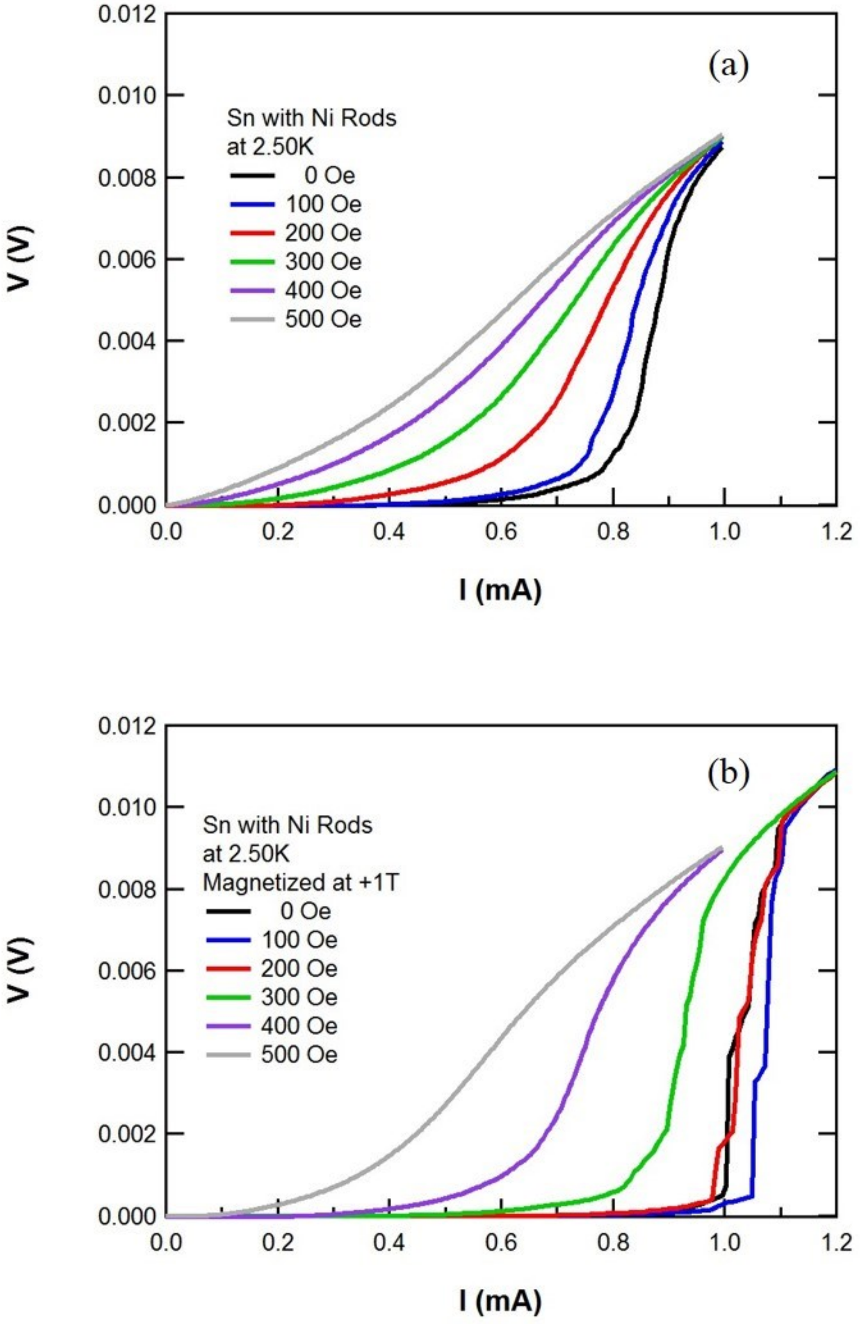

Figure 93. *I-V* charateristics of the Sn FSH sample without magnetization (a) and after magnetizing the Ni nanorods at +1 T (b).

five discrete steps occur in the *I-V* curves at low external magnetic fields. The steps were observed while approaching the normal state when the Ni nanorods were magnetized, as shown in Figure 93 (b). The voltage steps vanish when the applied external magnetic field is above +400 Oe. This phenomenon is similar to the voltage steps that were shown in one-dimensional superconductors. Diameters of those superconductors were comparable with their ξ. Several steps in the *I-V* curves were observed in Sn whiskers [134] and single Sn nanowires [135, 136]. All the voltage steps in the one-dimensional Sn nanowires merged into a single step when the magnetic field was increased above a certain value. These voltage steps in one-dimensional superconductors have been explained by phase-slip centers (PSCs) [134-137] and an increase of the charge imbalance distance (Λ_Q) [5] at relatively large magnetic fields. Due to the increase of Λ_Q, there is a lack in space for coexistence of two phase slip centers in Sn nanowires [135]. For the two-dimensional superconductors, phase-slip lines (PSLs) may occur [138] which is analogous with PSCs. Voltage steps in *I-V* curves in Sn films were observed by Dmitriev, *et al* [139]. In that reference, the authors showed that the steps in the *I-V* characteristics appear when the current is greater than the maximum current (I_m) for the existence of the Abrikosov vortex state. They assume that the *R* is due to the system of PSLs in the current region $I > I_m$. The *I-V* characteristics in Figure 93 (b) can be classified into three sections based on [140]: voltage steps in the curves due to PSLs from 0 Oe to +200 Oe, transitional curves at +300 Oe, and smooth nonlinear curves from +400 Oe to +500 Oe in Figure 93 (b). The voltage steps by PSLs are not affected by weak magnetic fields. On the contrary, the steps in the *I-V* curves of the PSLs were destroyed by strong magnetic fields. Also, the strong magnetic fields create vortex resistance [139, 140]. However, those systems do not have ferromagnetic structures. A single magnetic dot on a superconducting stripe shows the voltage steps in the *I-V* characteristics [141]. A PSL nucleates in the center of the superconducting stripe, and two more PSLs are shown on the left hand side and right hand side of the first PSL with a symmetry when the current increases. Finally, the PSLs in the superconducting thin film merge into one line, and the film drives the normal state. When the PSLs start to appear due to reduced superconductivity under the magnetized dot, this creates regions of the film is in the normal state [141]. Therefore, the voltage steps in the *I-V* curves manifested by magnetized Ni nanorods may be understood as the PSLs. Since voltage steps in *I-V* curves in low dimensional superconductor depend on temperature and external magnetic fields [135, 136], additional measurements are needed to test this interpretation.

The experimental data clearly show an enhanced superconductivity and pinning effect by the magnetization of the Ni nanorod array. The matching field effect demonstrates the relationship between the vortex lattice and the artificial array. Finally, voltage steps appear when the Ni nanorods are magnetized.

5.5 Effect of the electroplated Ni nanorods with $Pb_{82}Bi_{18}$ thin films

Vortex pinning has been studied with superconductor-ferromagnetic nanostructures to take advantages of the magnetic interaction between vortices and artificially defined nanomagnets. The magnetic nanodisks on superconducting thin film systems significantly change and enhance the superconducting properties [36, 38, 39]. Superconducting properties were enhanced in several hybrid systems of $Pb_{82}Bi_{18}$ thin films by ferromagnetic nanorods: Ni and Co nanorods embedded into the thin film [43, 133, 142] and Co nanorods on the thin film [143]. In contrast to the previous hybrid systems, in this subchapter an electroplated Ni nanorod array was isolated from a superconducting $Pb_{82}Bi_{18}$ thin film (sample A) by an insulating Ge layer to exclude the proximity effect and mechanical deformations. Thus, the $Pb_{82}Bi_{18}$ thin film and the Ni nanorod array only interact via an applied external magnetic field. Embedding ferromagnetic nanorod arrays into a superconducting thin film has been suggested by Lyuksyutov and Naugle [144] for more effective pinning than magnetic nanodisks on a superconducting thin film. So, the insulated FSH sample will be compared with the same structures of the Ni nanorod arrays embedded into a $Pb_{82}Bi_{18}$ thin film (sample B).

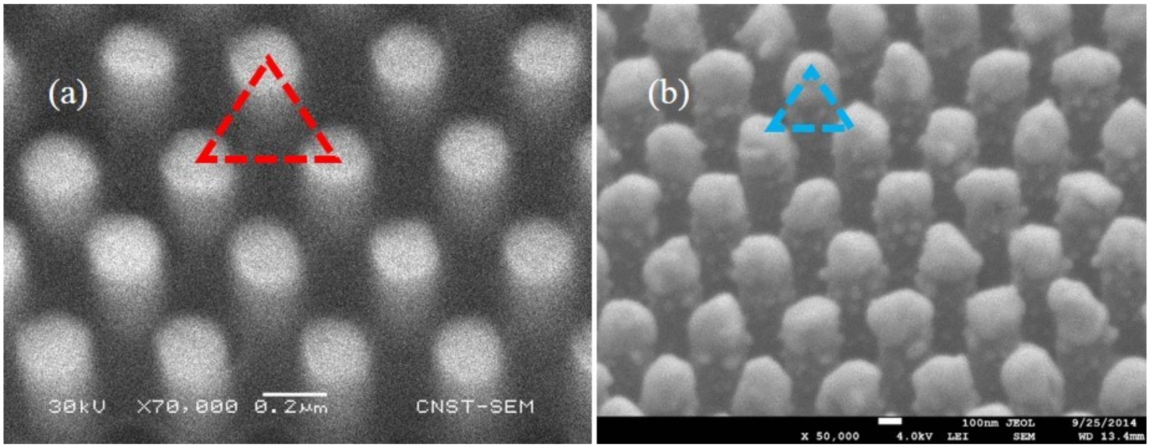

Figure 94. 45° angled view SEM images for samples A (a) and B (b).

Sample A consisted of a 100 nm thin film of $Pb_{82}Bi_{18}$ and an array of electroplated Ni nanorods, a control sample was prepared simultaneously on the same substrate by using thermal quench condensation. A 5 nm insulating layer of Ge was deposited by thermal evaporation on top of the $Pb_{82}Bi_{18}$ thin film. A 15 nm Ag thin film was thermally evaporated and functioned as the counter electrode for Ni electroplating.

Sample B consisted of a 70 nm thin film of $Pb_{82}Bi_{18}$ and an array of electroplated Ni nanorods. Sample B also had its own control sample fabricated with the same method as sample A's control sample. Ni nanorods were electroplated on the Ag thin film. The $Pb_{82}Bi_{18}$ thin film was evaporated by thermal quench condensation directly onto the nanorods for this sample. The dimension and arrangement of the Ni nanorods were the same in both samples A and B. A constant voltage of -1.2 V was applied between electrodes for ten seconds to grow the Ni nanorods. They were fabricated as array triangular lattices with a 400 nm lattice constant, as shown in Figure 94. Each nanorod had a 200 nm diameter and a 750 nm height.

Measurements of T_C for samples A and B with control samples were done by applying a 1.5 μA of alternating current and measuring the voltage at zero magnetic field in the PPMS. A 1 T external magnetic field was applied perpendicular to surface of the $Pb_{82}Bi_{18}$ films to magnetize the Ni nanorods before the T_C measurement. The nanorods tended to be magnetized along the longitudinal direction because of shape anisotropy. In order to magnetize the array, the magnetic field was applied either positively at +1 T or negatively at -1 T.

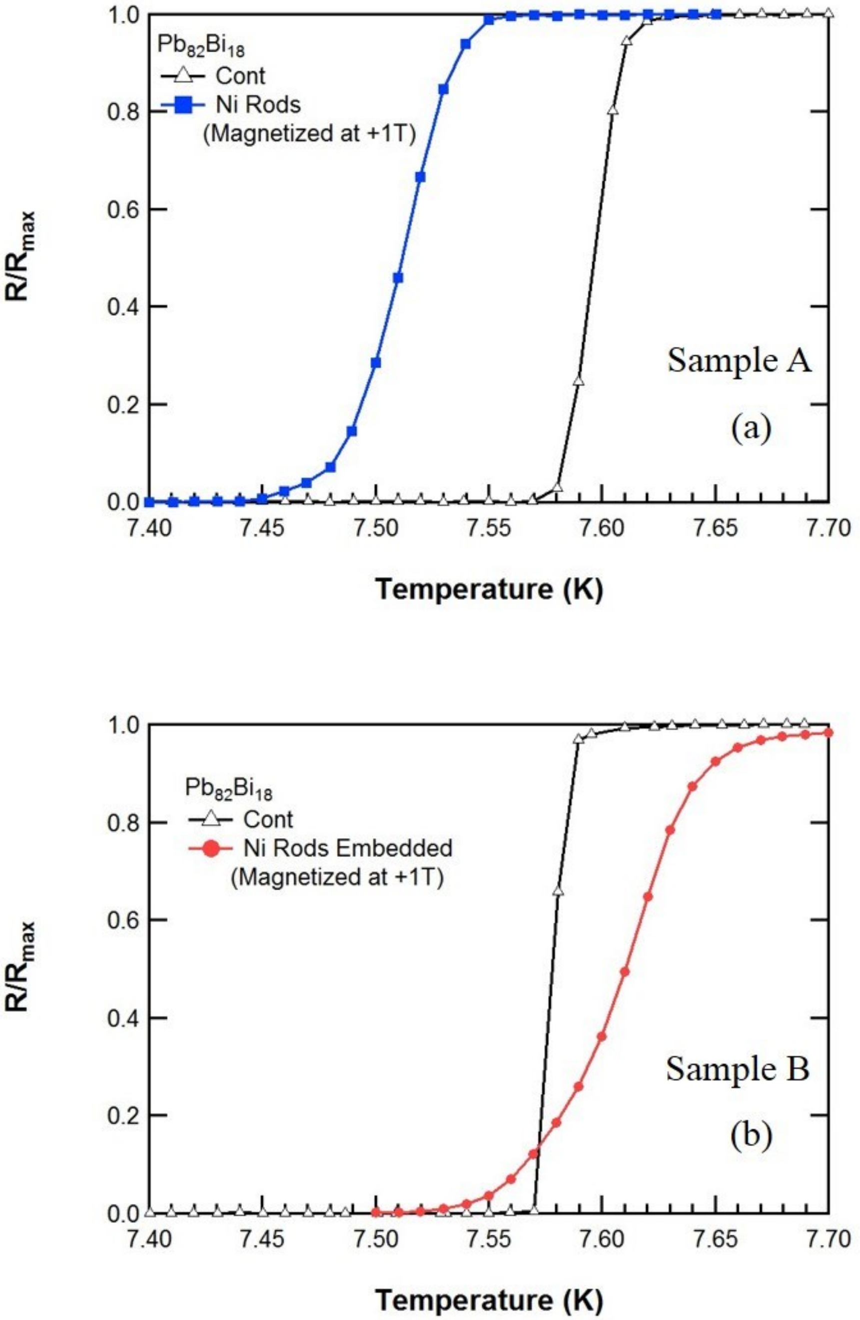

Figure 95. *R*-*T* curves around their T_Cs for samples A (a) and B (b) with control samples.

Figure 95 shows temperature dependence of R of samples A and B when the Ni nanorods were positively magnetized. Black open triangles express the R-T curves of control sample for samples A and B in Figures 95 (a) and (b), respectively. The R in figures are normalized at the R in the normal state slightly above their T_Cs. The magnetized Ni nanorods significantly change the phase transition of samples A and B in a range of temperatures from 7.40 K to 7.70 K: sample A is marked by blue closed squares in Figure 95 (a) and sample B is marked by red closed circles in Figure 95 (b). The T_Cs of both samples A and B are reduced by the magnetized Ni nanorods. The slope of the R-T curves for samples A and B during the phase transition are reduced when the Ni nanorods were magnetized as compared to the R-T curves of each control sample. Sample B shows an onset of superconductivity at a higher temperature than either its control or sample A. The dramatic changes in the R-T curves were similarly shown for Sn thin films with electroplated Ni nanorods in subchapter 5.4.

Figure 96 depicts R-H curves of samples A (a) and B (b) slightly below their T_Cs. The magnetic field sweeping range is ± 800 Oe and ± 2,000 Oe for samples A and B, respectively. The arrows indicate the direction of the magnetic field sweep in the figures. Hysteretic behavior in the R-H curves for both samples A and B is observed. The decreasing H branch (arrow 1) of samples A and B always has a larger H_{C2} than the increasing H branch (arrow 4); however, this phenomenon does not appear in the control samples. This is due to the pronounced field compensation effect described in subchapter 1.6. Since the R-H curves are shifted in the direction of magnetization of the Ni nanorods, the superconducting state of sample A exists in a larger magnetic field range

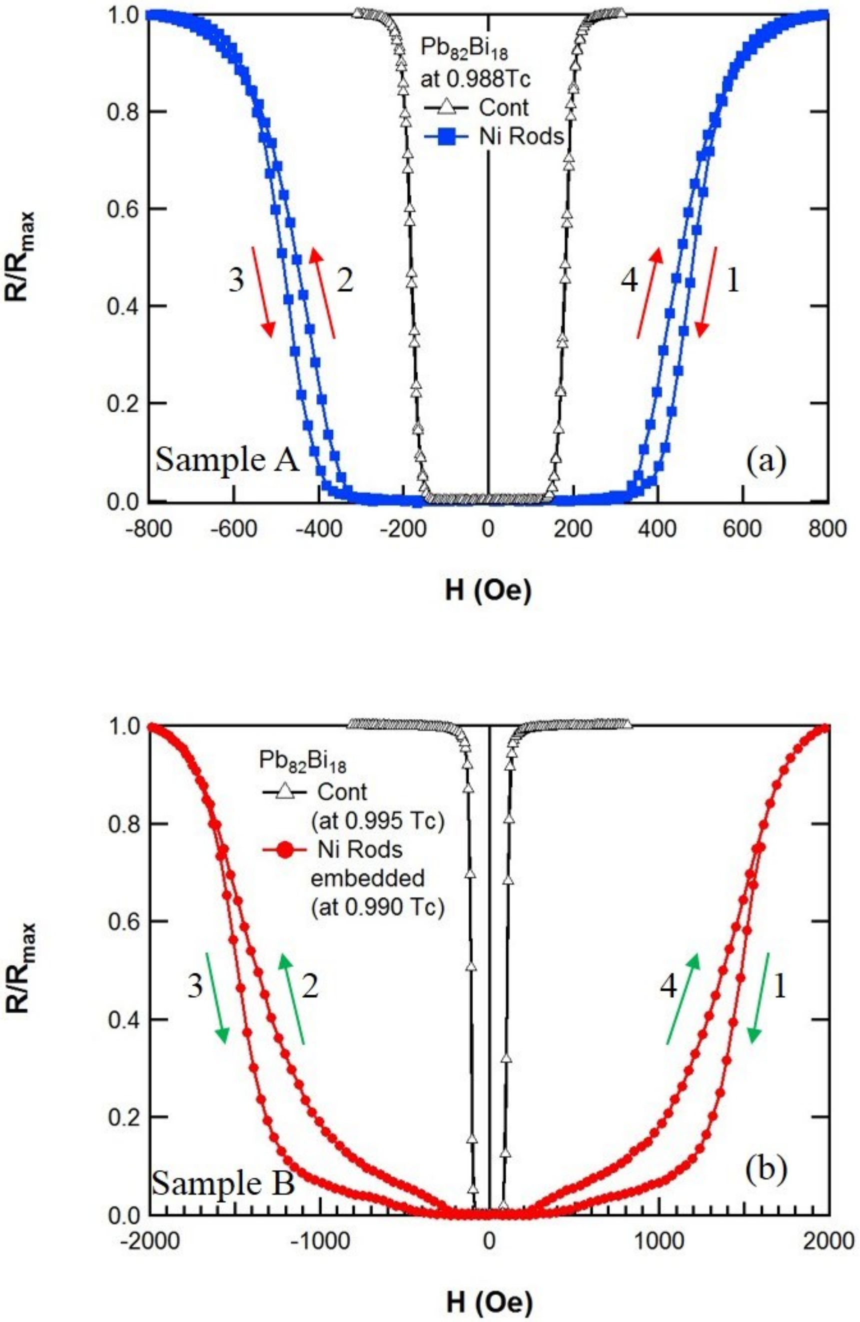

Figure 96. *R*-*H* curves of samples A (a) and B (b) with control samples below their T_Cs.

than its control sample with the same temperature, as displayed in Figure 96 (a). As a result, superconductivity of sample A is clearly enhanced. Although the temperature for sample B is slightly lower than that of its control sample, the magnetized Ni nanorods in sample B obviously also enhance its H_{C2}, as seen in Figure 96 (b). The reduced temperature difference between the *R*-*H* curves for samples A and B is $0.002T_C$; hence the results of their properties can be comparable. Sample B has a larger H_{C2} than sample A by comparing the *R*-*H* curves. This is due to the fact that the Ni nanorods for sample B penetrate the superconducting film. This will be discussed later.

Figure 97 illustrates the dependence of the *MR* on external magnetic fields of samples A (blue squares) and B (red circles) slightly above their T_Cs. This shows that the

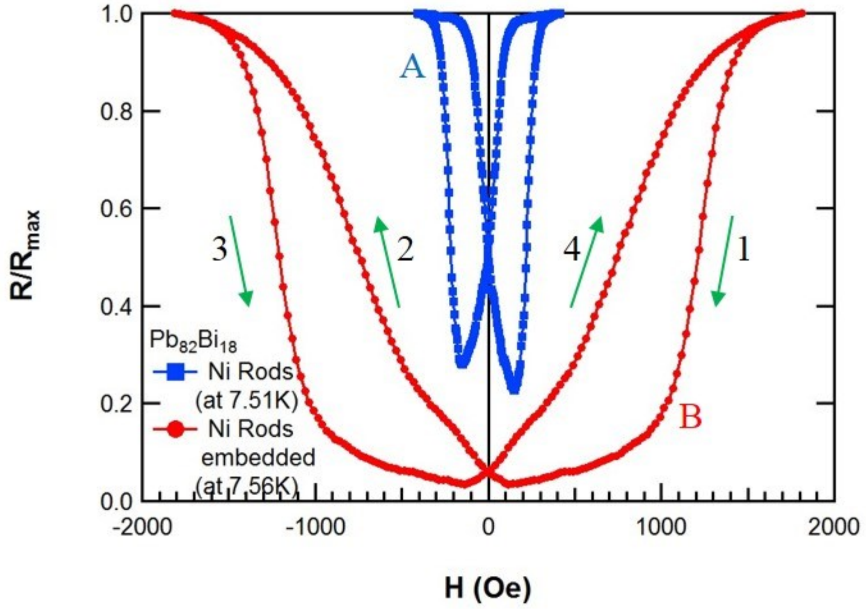

Figure 97. *R*-*H* curves of sample A and B above their T_Cs.

magnetized Ni nanorods in samples A and B provide hysteretic behavior in the *R*-*H* curves. The strongest vortex pinning can be expected when all vortices are placed into their respective local potential minima. The field matching effect appears at the same field for samples A and B, as expected since the 400 nm lattice constant of the Ni nanorod arrays is the same. The first matching field H_1 is 149.35 Oe as calculated from equation (29) in good agreement with the experimental location of the minima in Figure 97. No features can be seen, however, at integral multiples of 148 Oe in Figure 97.

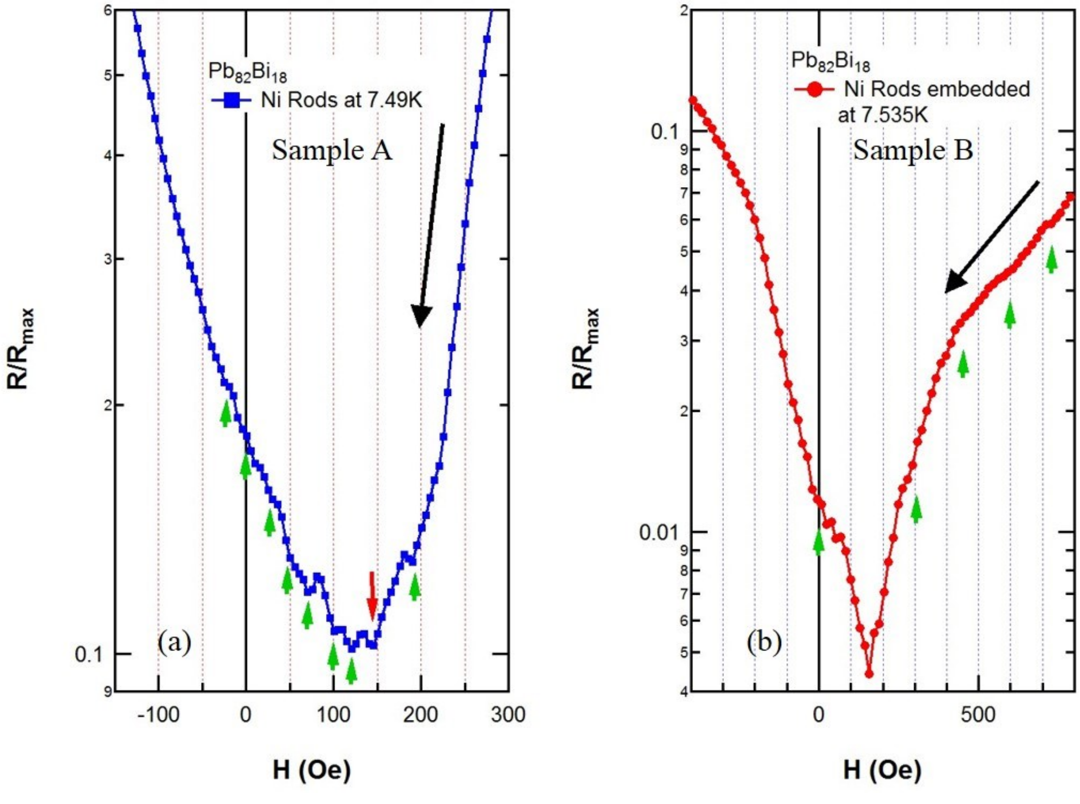

Figure 98. *R*-*H* curves of sample A (a) and B (b) after positively magnetizing their Ni nanorods.

Figures 98 (a) and (b) show detailed *R*-*H* curves after positively magnetizing the Ni nanorods for sample A at 7.490 K and sample B at 7.535 K, respectively. Black arrows in the figures indicate the sweep direction of the magnetic fields. Vortex pinning is increased when the vortex lattice is commensurate with the lattice of the magnetic pinning centers. Thus, the matching field effect is observed when the applied magnetic field is in the same direction with the magnetization of the Ni nanorods. For sample A, the *R*-*H* curves were measured between -150 Oe and +300 Oe. The main matching field is near +150 Oe with the red arrow. An additional matching field can be found around H_1; the periodic matching fields is approximately 24 Oe, which corresponds to 23.89 Oe for 1,000 nm triangular lattice constant. The additional periodic kinks (green arrows) are shown when the external magnetic field decreases after the main matching field (+150 Oe). Also, the matching fields for 24 Oe are dominant in the field range. For sample B, the *R*-*H* curves were measured between -400 Oe and +800 Oe. Similar to sample A, H_1 for sample B is also near +150 Oe. Although the *MR* does not drop abruptly at integer multiples of +150 Oe, one kink at 0 Oe and four more kinks between +150 Oe and +750 Oe appeared with green arrows, as shown in Figure 98 (b). Unfortunately, since the number of data points are too sparse, additional periodic matching fields for 24 Oe between the interval of main matching fields (+150 Oe) for sample B are not apparent. In previous results [43, 142], the embedded FSH systems were analogous to sample B. Additional oscillations around H_n, where n is an integer, were not observed; however, matching fields from H_1 to H_3 were stronger than those for sample B.

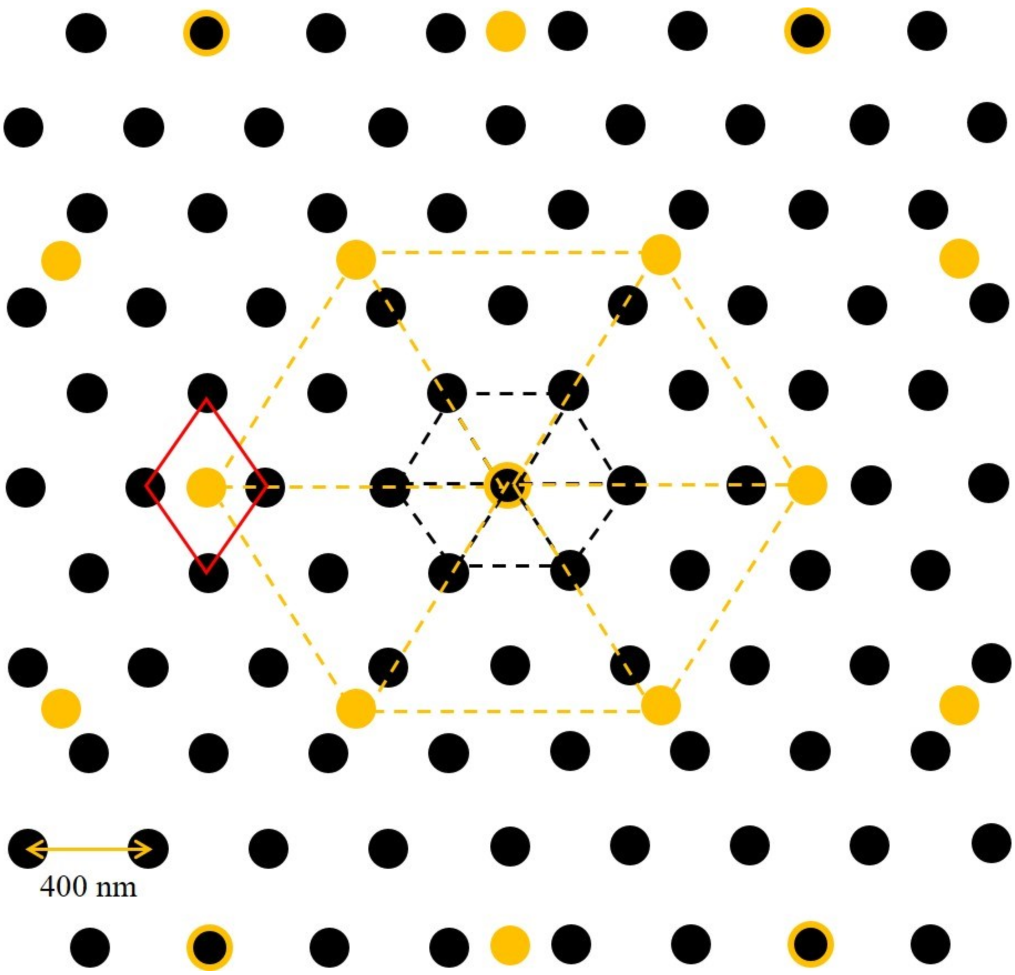

Figure 99. Coexistence of triangular commensurate vortex lattices of 400 nm (black circles) and 1,000 nm (yellow circles).

The 400 nm triangular vortex lattices coexist with the 1,000 nm triangular vortex lattices, as shown in Figure 99. Black circles indicate 400 nm lattices on the Ni nanorods, and yellow circles indicate the additional 1,000 nm lattices. Vortices on 400 nm lattices and 1,000 nm lattices are shared by three of them in a 2,000 nm triangular lattice, while most of the vortices inside the 2,000 nm triangular lattice are not shared. The black circles with a yellow ring show the share. For the 1,000 nm lattices, a vortex may be trapped in the middle of a unit lattice (the red diamond), as shown in Figure 99. Even though Figure 99 shows the coexistence of the vortex lattices, it is not clearly understood why the 1,000 nm vortex lattice is favored as compared to an 800 nm vortex lattice. Additional studies are needed to investigate this. These additional periodic matching fields were similarly shown on a Fibonacci array [145]. A similar hybrid system for the Sn thin films in subchapter 5.4 exhibits them.

Figure 100 illustrates schematic diagrams of an isolated FSH sample like sample A (a) and an embedded FSH sample like sample B (b). In the figures, FM indicates a ferromagnetic nanorods, and SC indicates the superconducting thin film. Moreover, IL is an insulating layer. Both structures can be expected to exhibit a field compensation

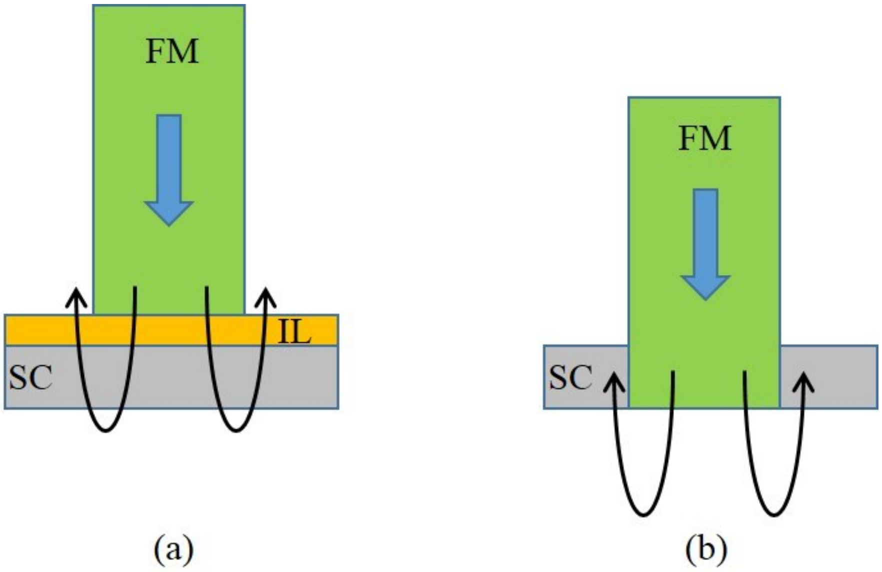

Figure 100. Schematic diagrams of isolated FSH sample (for sample A) (a) and embedded FSH sample (for sample B) (b).

effect and increase of I_C in comparison to the control samples [42, 43, 133, 144]. Figure 101 shows the dependence of I_C on the applied external magnetic field for sample B. I_C of the control sample (black open triangles) rapidly increases in the field range of ± 300 Oe at 7.47 K. The control sample shows typical superconducting properties with no hysteretic behavior. In contrast, I_C of sample B indicates strong hysteretic behavior at 6.00 K and 7.00 K due to the magnetized Ni nanorods in a range of ±1,500 Oe. Clear hysteresis is not observed above ± 1,500 Oe in sample B and in the previous report [142]. This occurs because values above ± 1,500 Oe for the external magnetic field exceed the saturation field of the Ni nanorods. The I_C-H curves of sample B demonstrate a greatly enhanced I_C except for the region extremely close to H=0.

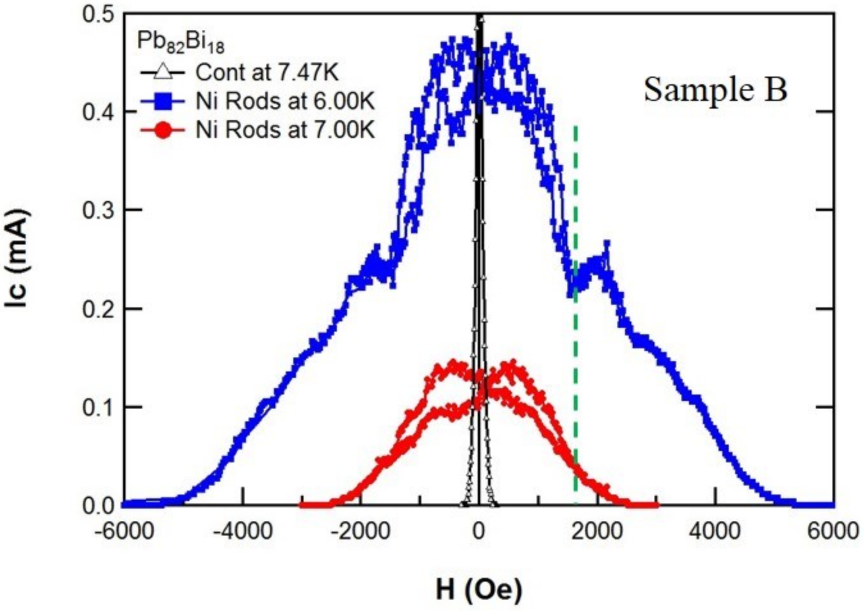

Figure 101. I_C-H curves of sample B and control sample.

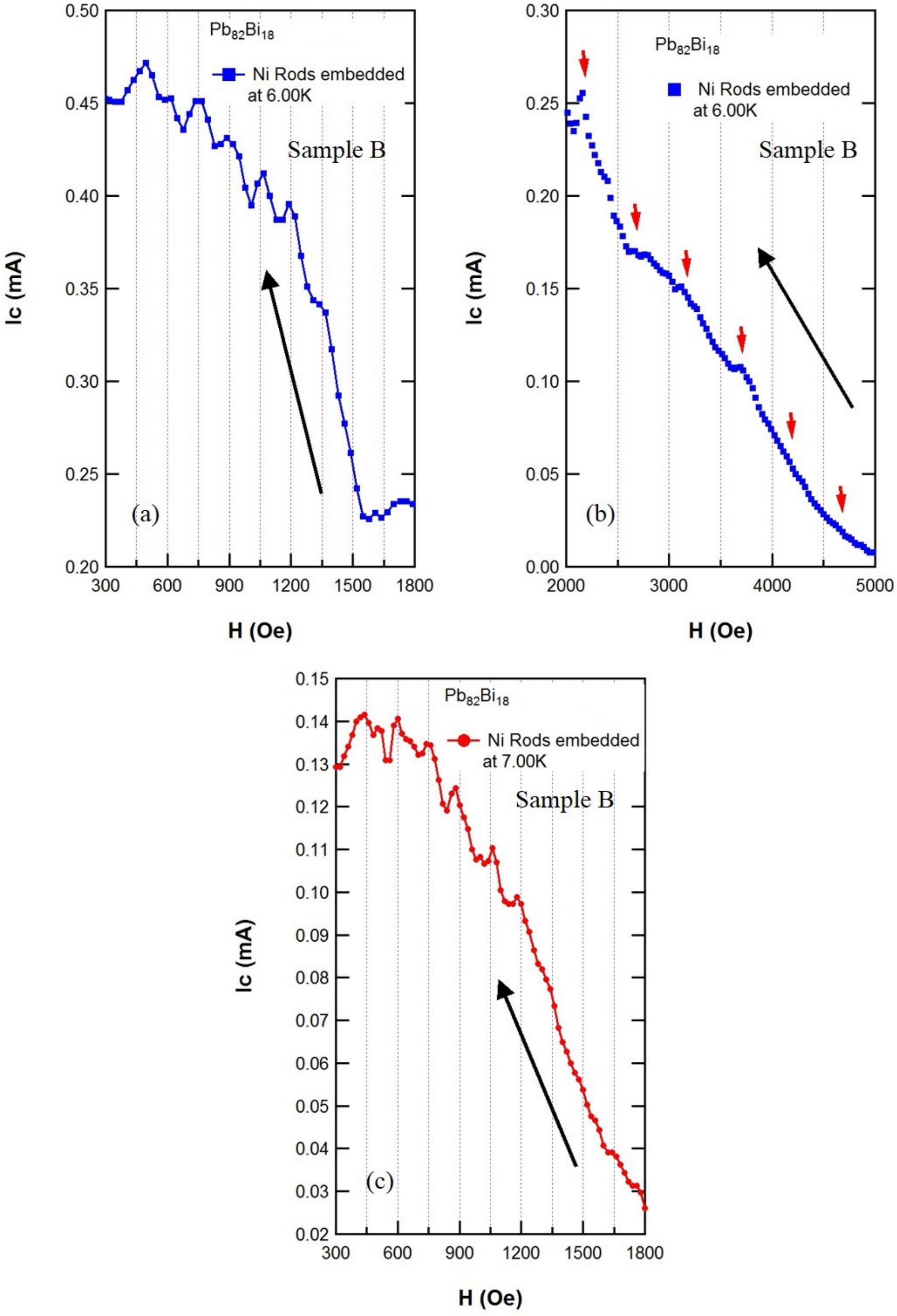

Figure 102. I_C-H curves of sample B at 6.00 K (a), in a high magnetic field at 6.00 K (b), and at 7.00 K (c).

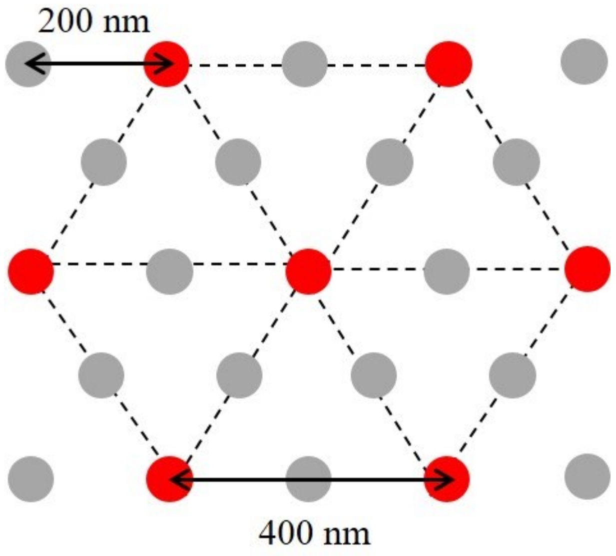

Figure 103. Coexistence of triangular commensurate vortex lattices of 400 nm (red circles) and 200 nm (gray circles).

Figure 102 displays detailed I_C-H curves of the sample B to investigate the matching field effect. The black arrows in the figures indicate the sweep direction of the external magnetic field after magnetizing the Ni nanorods at +1 T. A strong matching field effect in Figure 102 (a) is observed at roughly every 150 Oe between +450 Oe and +1,500 Oe at 6.00 K. There are six peaks and one kink. Furthermore, within the same range, six peaks and four kinks are displayed at 7.00 K in Figure 102 (c). This peak structure is much more pronounced than in the earlier results [43]. The I_C-H curve between +2,000 Oe and +5,000 Oe shows one peak and five kinks at periodicity of 500 Oe in Figure 102 (b). The matching field for 500 Oe corresponds to a 219 nm triangular lattice constant. This value of the lattice constant is close to 200 nm. A vortex would be added to each of the side of a triangular vortex lattice, as shown in Figure 103. Red circles and gray circles indicate the Ni nanorods and the additional unpinned vortices between the nanorods, respectively. This 200 nm vortex lattice configuration is less stable than that at 400 nm. Due to a shorter vortex-to-vortex distance, they interact more strongly and the pinning potential strength is too weak to provoke a vortex guiding on the nanorods. This suggests a reconfiguration and reduction of the vortex lattice, because the elastic energy becomes larger than the pinning energy at higher external magnetic fields [38].

I-V characteristics were measured on sample A by applying a direct current. Figure 104 (a) shows the *I-V* characteristics of the control sample at 7.43 K, 7.48 K and 7.53 K at zero field. The *I-V* curves exhibit a typical superconducting behavior; I_C of the control sample depends on temperature with I_C increases with decreasing temperatures. Also, the control sample rapidly transists from the superconducting state to the normal state. The *I-V* curves of sample A, however, are significantly different from the control sample at similar temperatures (7.25 K, 7.30 K, and 7.35 K) at zero field, as depicted in Figure 104 (b). The *I-V* characteristics of sample A show a broad phase transition from the superconducting state to the normal state after magnetization of the Ni nanorods at +1 T. Several voltage steps are revealed in between the two states. The number of voltage steps in sample A is reduced when the temperature is close to T_C. The steps near I_{Ci} show a larger transition than near the normal state at lower temperatures. Since depinning forces overcome pinning forces of the artificial pinning sites, destruction of the pinning of large clusters of vortices appears. Hence, the strength variation of the artificial pinning sites is possible so that different clusters of vortices are depinned at

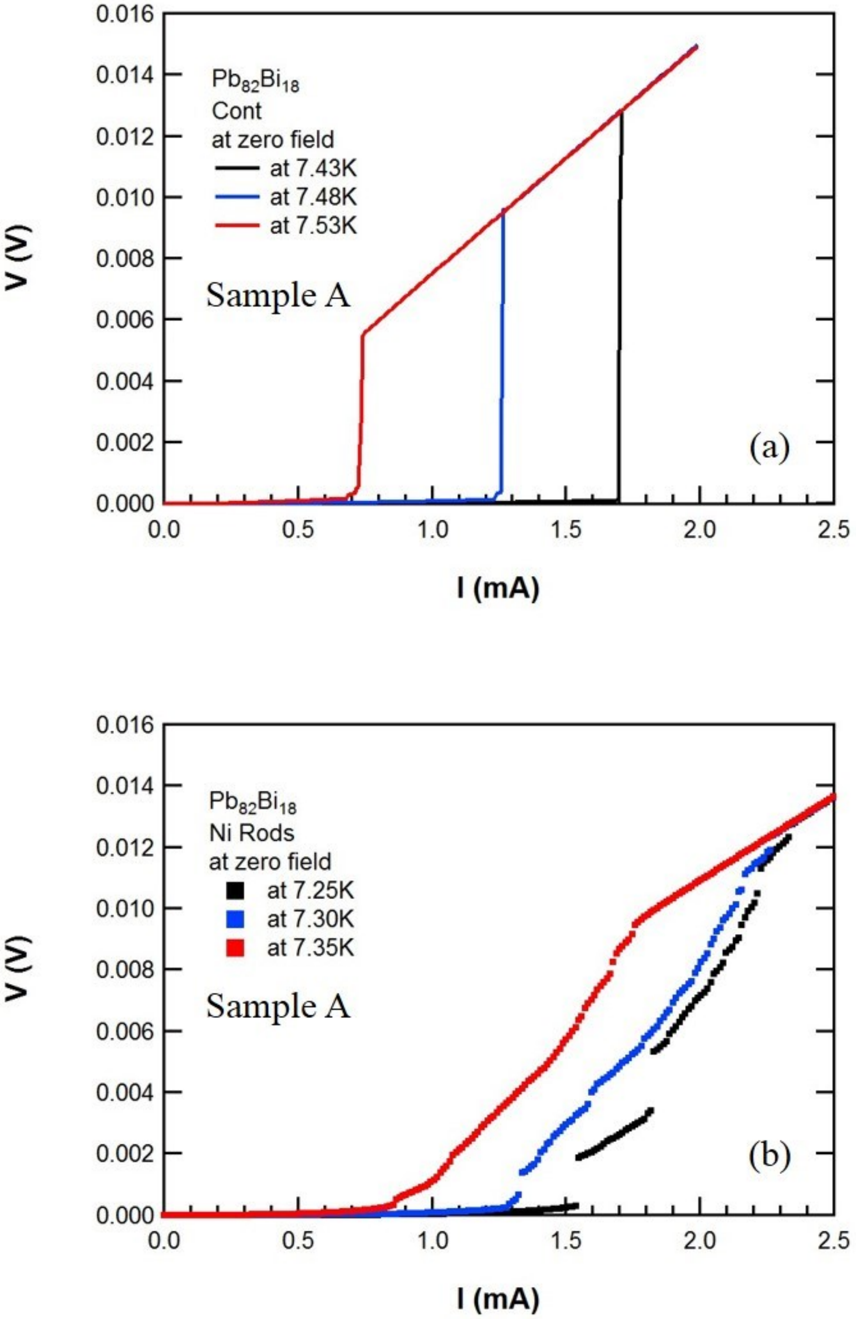

Figure 104. Temperature dependence of *I-V* curves for the control sample (a) and sample A (b).

different currents.

Although embedded Ni nanorods in the $Pb_{82}Bi_{18}$ film show a larger hysteretic behavior, both samples A and B demonstrate an enhancement of superconductivity and the pinning effect by the magnetization of the Ni nanorod array. The relationship between the vortex lattices and the artificial arrays are shown by the periodic matching field effect. The voltage steps occur in FSH sample A due to the magnetized Ni nanorods.

5.6 Effect of the evaporated Ni nanorods on the YBCO thin films

According to subchapter 4.3, a YBCO thin film, one of many high temperature superconductors, exhibits a relatively higher I_C than Sn and $Pb_{82}Bi_{18}$. Moreover, the YBCO thin film remains the superconducting state above liquid nitrogen temperature (77 K). These two advantages provide a great motivation to fabricate a FSH sample with a high temperature superconducting thin film. Some interesting properties can be expected if Sn or $Pb_{82}Bi_{18}$ thin films are replaced by YBCO thin films.

In this subchapter, a FSH sample with a YBCO thin film is introduced. The FSH sample consisted of a 100 nm thin film of YBCO and an array of thermally evaporated Ni nanorods. The nanorods were separated from the YBCO film by an Ag layer to avoid any chemical reaction at the interface.

After patterning nanorods on the YBCO film with EBL, 20 nm of Ag was evaporated to function as the barrier between the YBCO films and the Ni nanorods. The

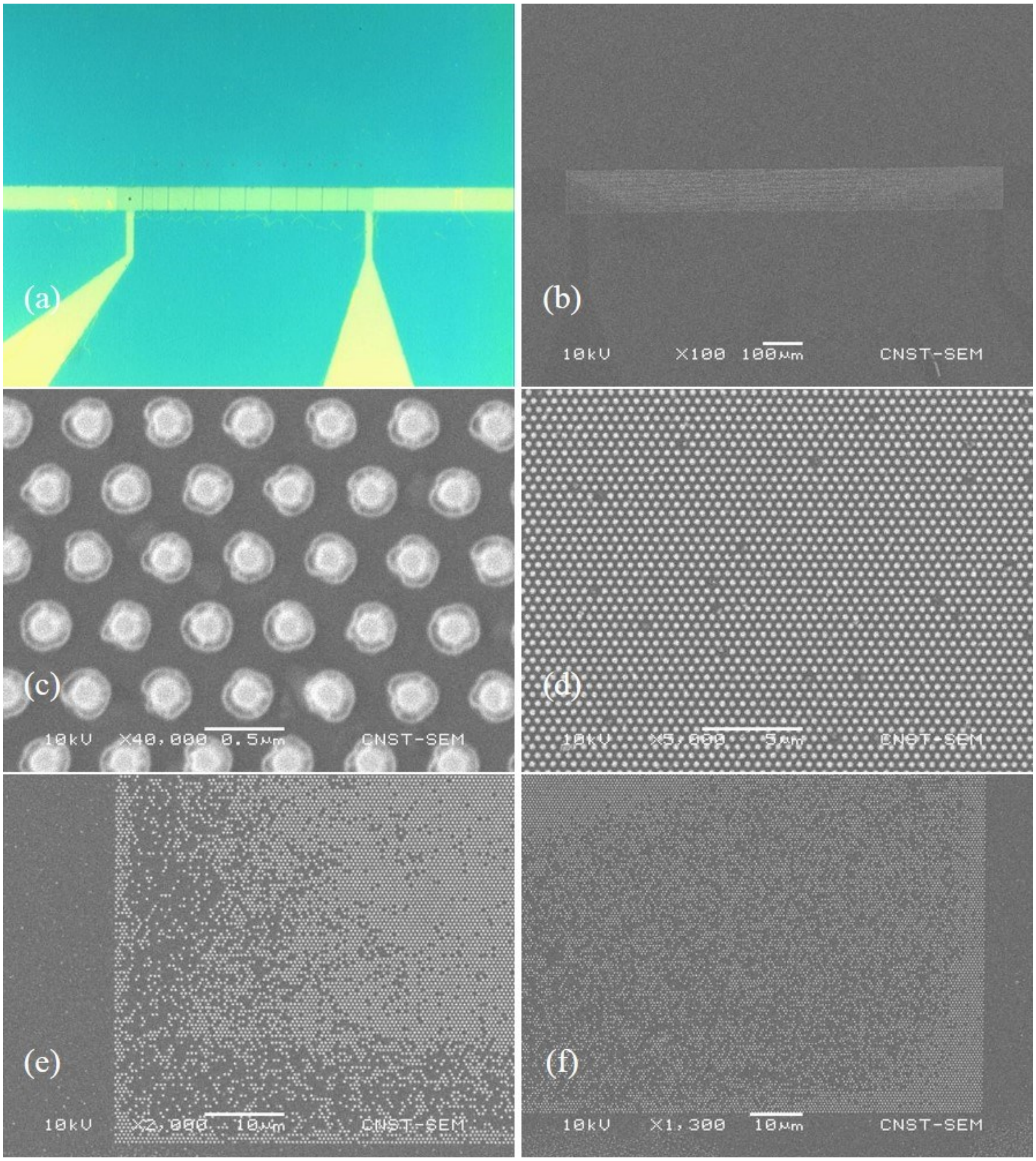

Figure 105. The YBCO FSH sample's optical microscopic image (a), SEM images at 100x (b), 40,000x (c), 5,000x (d), 2,000x (e), and 1,300x (e),

evaporated Ni filled the nanorod pattern after the Ag deposition. The Ni nanorod array had a 600 nm triangular lattice constant, and each nanorod had a 300 nm diameter and a 300 nm height, as seen in Figure 105 (c). Unfortunately, however, the thermally evaporated Ni nanorods formed as cones rather than cylinders. Since the nanorods were cones, the center of the nanorods were brighter than circumference of the nanorods in Figure 105 (c). This main drawbacks of the thermally evaporated nanostructures was discussed earlier in subchapter 3.2 and displayed in Figure 45 (b). Figures 105 (a) and (b) depict an optical microscope image and an SEM image of the FSH sample, respectively. During the fabrication process, 1% of the Ni nanorods of the FSH sample were lost in the center region, as shown in Figure 105 (d), and 50% of the nanorods were lost at the edge regions, as shown in Figures 105 (e) and (f).

A 3.0 μA alternating current was applied, and the voltage at zero field was measured to obtain R of the FSH and control samples in the PPMS. Figure 106 (a) shows the temperature dependence of R of the FSH and the control sample near their T_Cs. In order to magnetize the Ni nanorods, an external magnetic field was applied perpendicular to surface of the YBCO film at either +1 T or -1 T. In contrast to the previous results for R-T curves of Sn or $Pb_{82}Bi_{18}$ FSH samples, even though the Ni nanorods were positively magnetized, R-T curves of the YBCO FSH sample was not shifted or changed, as seen in Figure 106 (b). The magnetic field dependence of MR at 86.0 K is illustrated in Figure 106 (c). There is no interesting behavior, such as hysteresis or periodic MR shifts, induced by the magnetized Ni nanorods in a range of ±30,000 Oe. Moreover, the magnetized nanorods show no change in properties by Ni

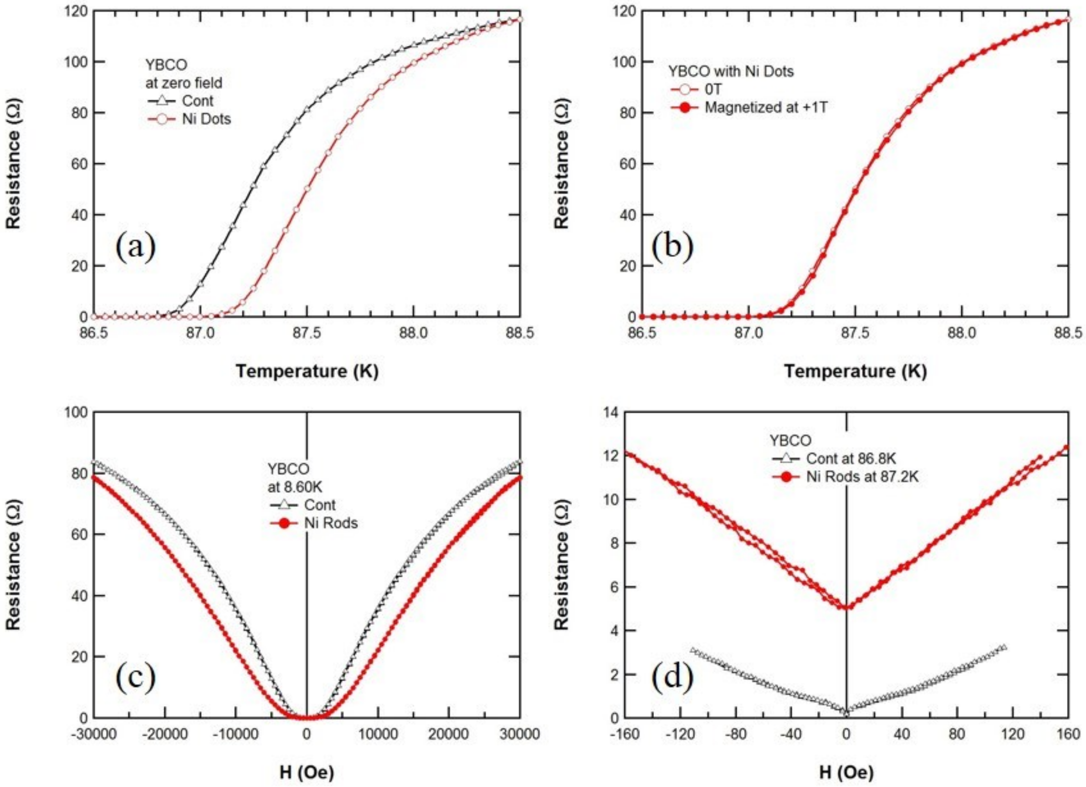

Figure 106. *R*-*T* curves of the YBCO FSH and control sample (a), *R*-*T* curves with magnetization for the FSH sample (b), *R*-*H* curves of the YBCO FSH and control sample below their T_Cs (c), and above their T_Cs (d).

nanorods on the FSH sample, as shown in Figure 106 (d).

The facts that the Ni nanorods were of conical shape and that many were missing on the edges may explain the absence of any significant effect on the YBCO. The Ni nanocones may not be magnetized in one direction by the applied external magnetic field. In order to observe interesting properties on the YBCO FSH samples, improvement of the fabrication procedures for nanoscale structures on YBCO thin films is needed.

6. CONCLUSION AND FUTURE WORK

Photolithography, EBL, thermal evaporation, and electroplating techniques were used to construct nanoscale ferromagnetic-superconductor hybrid (FSH) systems. Magnetic interaction between the ferromagnetic nanostructures and superconducting thin films were investigated using successfully fabricated nanosized FSH systems. The Ni nanostripes were thermally evaporated for a low aspect ratio (1:1.2) and electroplated for a high aspect ratio (1:3.75). The period of the stripes were 400 nm or 500 nm. The high aspect ratio Ni and Co nanorods were grown by electroplating. The nanorod arrays have triangular lattices, and the lattice constants were 400 nm or 500 nm. The FSH samples were characterized by the optical microscope, SEM, AFM, MFM, and PPMS.

Fabricated Sn, $Pb_{82}Bi_{18}$, and YBCO thin films (30-100 nm) for control samples were examined to elucidate their superconducting properties. Their experimental results proved that they behave as a type II superconductor.

The ferromagnetic nanostructures on the superconducting thin films in the FSH samples were isolated by an insulating layer. The FSH samples showed dramatically enhanced superconductivity and strong hysteretic behavior when the Ni nanostructures were magnetized. In addition, the FSH samples exhibited vortex pinning and a matching field effect. Furthermore, voltage steps were manifested in the *I-V* curves of the FSH samples due to the magnetization of the Ni nanostructures. Magnetic interaction in the FSH samples can be elucidated by the field compensation effect. High aspect ratio Ni nanostructures with thinner Sn films showed enhanced effects in the FSH systems. For

$Pb_{82}Bi_{18}$ thin films, the embedded FSH sample indicated a larger hysteretic behavior than the isolated FSH samples.

In order to analyze the relation between *MR* oscillations and the coexistence of two vortex lattices in the FSH samples, more data points of the *MR* measurements will be needed. The structures of the FSH systems in this study can be extended to high aspect ratio ferromagnetic nanostructures on high temperature superconducting thin films, such as Ni or Co nanostructures on YBCO thin films.

Superconducting power cables have no heat generation nor electrical losses. These power cables have the capability to carry three to five times more current compared to conventional cables in the same amount of physical space. However, their superconducting properties are lost when they are exposed to an external magnetic field above the material's H_{C2}. The H_{C2} of FSH systems in this research significantly increased when the ferromagnetic nanostructures on type II superconducting thin films were magnetized by applying an external magnetic field. Therefore, if the FSH system is integrated into superconducting power cables, the cables may be able to remain their superconductivity at a higher external magnetic field. In addition, vortex pinning by magnetized ferromagnetic nanostructures will be better controlled in such superconducting power cables. Vortex pinning enhances by a matching field phenomenon, which can be determined by size and geometry of ferromagnetic nanostructures and thickness modulation of type II superconducting thin films. Hence, the I_C in the cables may be increased at the matching fields. Furthermore, since liquid nitrogen is about 50 times cheaper than liquid helium, FSH systems created on high temperature (above liquid nitrogen temperature) superconducting thin films may be more cost efficient in the future, when similar facts in high temperature superconductors have been established.

REFERENCES

1. Kittel, C., *Introduction to solid state physics*. 8th ed. (2005), Hoboken, NJ: Wiley. xix, 680 p.

2. Lee, P. J., *Engineering superconductivity*. (2001), New York: Wiley-Interscience. x, 661 p.

3. Parks, R. D., *Superconductivity*. (1969), New York: M. Dekker.

4. Poole, C. P., *Superconductivity*. 2nd ed. (2007), Oxford: Academic. xxiii, 646 p.

5. Tinkham, M., *Introduction to superconductivity*. 2nd ed. International series in pure and applied physics. (1996), New York: McGraw Hill. xxi, 454 p.

6. Buzdin, A. I., "Proximity effects in superconductor-ferromagnet heterostructures." *Reviews of Modern Physics*, (2005), **77**(3), 935-976.

7. Lyuksyutov, I. F. and Pokrovsky, V. L., "Ferromagnet-superconductor hybrids." *Advances in Physics*, 2005. **54**(1), 67-136.

8. Aladyshkin, A. Y., Silhanek, A. V., Gillijns, W., and Moshchalkov, V.V., "Nucleation of superconductivity and vortex matter in superconductor-ferromagnet hybrids." *Superconductor Science and Technology*, (2009), **22**(5), 053001.

9. Vélez, M., Martín, J. I., Villegas, J. E., Hoffmann, A., González, E. N., Vicent, J. L., and Schuller, I. K., "Superconducting vortex pinning with artificial magnetic nanostructures." *Journal of Magnetism and Magnetic Materials*, (2008), **320**(21), 2547-2562.

10. Jaque, D., González, E. N., Martín, J. I., Anguita, J. V., and Vicent, J. L., "Anisotropic pinning enhancement in Nb films with arrays of submicrometric Ni lines." *Applied Physics Letters*, (2002), **81**(15), 2851-2853.

11. Ye, Z., Lyuksyutov, I. F., Wu, W., and Naugle, D. G., "Strongly anisotropic flux pinning in superconducting $Pb_{82}Bi_{18}$ thin films covered by periodic ferromagnet stripes." *Superconductor Science and Technology*, (2011), **24**(2), 024011.

12. Gourdon, C., Jeudy, V., Menant, M., Roditchev, D., Tu, L. A., Ivchenko, E. L., and Karczewski, G., "Magneto-optical imaging with diluted magnetic semiconductor quantum wells." *Applied Physics Letters*, (2003), **82**(2), 230-232.

13. Jeudy, V. and Gourdon, C., "Instability-driven formation of domains in the intermediate state of type-I superconductors." *Europhysics Letters*, (2006), **75**(3), 482-488.

14. Jeudy, V., Gourdon, C., and Okada, T., "Impeded growth of magnetic flux bubbles in the intermediate state pattern of type I superconductors." *Physical Review Letters*, (2004). **92**(14), 147001.

15. Essmann, U. and Träuble, H., "The direct observation of individual flux lines in type II superconductors." *Physics Letters A*, (1967). **A 24**(10),526-527.

16. London, F. and London, H., "The electromagnetic equations of the supraconductor." *Proceedings of the Royal Society of London Series A, Mathematical and Physical Sciences*, (1935), **149**(A866), 0071-0088.

17. Bardeen, J., Cooper, L. N., and Schrieffer, J. R., "Theory of superconductivity." *Physical Review*, (1957), **108**(5), 1175-1204.

18. Gubin, A. I., Il'in, K. S., Vitusevich, S. A., Siegel, M., and Klein, N., "Dependence of magnetic penetration depth on the thickness of superconducting Nb thin films." *Physical Review B*, (2005), **72**(6), 064503.

19. Abrikosov, A. A., "On the magnetic properties of superconductors of the second group." *Soviet Physics JETP*, (1957), **5**(6), 1174-1183.

20. Ginzburg. V. L., Landau, L. D., "On the theory of superconductivity." *Journal of Experimental and Theoretical Physics*, (1950), **20,** 1064.

21. Wu, M. K., Ashburn, J. R., Torng, C. J., Hor, P. H., Meng, R. L., Gao, L., Juang, Z., J., Qnag, Y. Q., and Chu, C. W., "Superconductivity at 93 K in a new mixed-phase Y-Ba-Cu-O compound system at ambient pressure." *Physical Review Letters*, (1987), **58**(9), 908-910.

22. Coalition for the Commercial Application of Superconductors, "*history of superconductor materials*." (2015), Available from: http://www.ccas-web.org/superconductivity/#image1.

23. Cullity, B. D. and Graham, C. D., *Introduction to magnetic materials*. (2009), IEEE/Wiley,: Hoboken, N.J., online resource (xvii, 544 p.).

24. Chikazumi, S. and Graham C. D., *Physics of ferromagnetism*. 2nd ed. The international series of monographs on physics. (1997), New York: Oxford University Press. xii, 655 p.

25. Kaya, S., "On the magnetisation of single crystals of cobalt." *Science Report Tohoku University*, (1928), **17**, 1157-1177.

26. Kaya, S., "On the magnetisation of single crystals of nickel." *Science Report Tohoku University*, (1928), **17**, 639-663.

27. Daldini, O., Martinoli, P., Olsen, J. L., and Berner, G., "Vortex-line pinning by thickness modulation of superconducting films." *Physical Review Letters*, (1974), **32**(5), 218-221.

28. Geoffroy, O., Givord, D., Otani, Y., Pannetier, B., and Ossart, F., "Magnetic and transport-properties of ferromagnetic particulate arrays fabricated on superconducting thin films." *Journal of Magnetism and Magnetic Materials*, (1993), **121**(1-3), 223-226.

29. Nozaki, Y., Otani, Y., Runge, K., Miyajima, H., Pannetier, B., Nozières, J. P, and Fillion, G., "Magnetic flux penetration process in two-dimensional superconductor covered with ferromagnetic particle array." *Journal of Applied Physics*, (1996), **79**(11), 8571-8577.

30. Otani, Y., Pannetier, B., Nozières, J. P, and Givord, D., "Magnetostatic interactions between magnetic arrays and superconducting thin films." *Journal of Magnetism and Magnetic Materials*, (1993), **126**(1-3), 622-625.

31. Baert, M., Metlushko, V. V., Jonckheere, R., Moshchalkov, V. V., and Bruynseraede, Y., "Composite flux-line lattices stabilized in superconducting films by a regular array of artificial defects." *Physical Review Letters*, (1995), **74**(16), 3269-3272.

32. Harada, K., Kamimura, O., Kasai, H., Matsuda, T., Tonomura, A., and Moshchalkov, V. V., "Direct observation of vortex dynamics in superconducting films with regular arrays of defects." *Science*, (1996), **274**(5290), 1167-1170.

33. Metlushko, V. V., Baert, M., Jonckheere, R., Moshchalkov, V. V., and Bruynseraede, Y., "Matching effects in Pb/Ge multilayers with the lattice of submicron holes." *Solid State Communications*, (1994), **91**(5), 331-335.

34. Moshchalkov, V. V., Baert, M., Metlushko, V.V., Rosseel, E., Van Bael M. J., Temst, K., and Bruynseraede, Y., "Pinning by an antidot lattice: The problem of the optimum antidot size." *Physical Review B*, (1998), **57**(6), 3615-3622.

35. Moshchalkov, V. V., Baert, M., Metlushko, V.V., Rosseel, E., Van Bael M. J., Temst, K., Jonckheere, R., and Bruynseraede, Y., "Magnetization of multiple-quanta vortex lattices." *Physical Review B*, (1996), **54**(10), 7385-7393.

36. Lange, M., Van Bael M. J., Bruynseraede, Y., and Moshchalkov, V. V., "Nanoengineered magnetic-field-induced superconductivity." *Physical Review Letters*, (2003), **90**(19), 197006.

37. Lange, M., Van Bael M. J., Morelle, M., Raedts, S., and Moshchalkov, V. V., "Field-induced superconductivity in films with magnetic dots." *Advances in Solid State Physics*, (2003), **43**, 721-730.

38. Martín, J. I., Vélez, M., Hoffmann, A., Schuller, I. K., and Vicent, J. L., "Artificially induced reconfiguration of the vortex lattice by arrays of magnetic dots." *Physical Review Letters*, (1999), **83**(5), 1022-1025.

39. Martin, J. I., Vélez, M., Nogués, J., and Schuller, I. K., "Flux pinning in a superconductor by an array of submicrometer magnetic dots." *Physical Review Letters*, (1997), **79**(10), 1929-1932.

40. Silhanek, A. V., Gillijns, W., Moshchalkov, V. V., Metlushko, V., Gozzini, F., Ilic, B., Uhlig, W. C., and Unguris, J., "Manipulation of the vortex motion in nanostructured ferromagnetic/superconductor hybrids." *Applied Physics Letters*, (2007), **90**(18), 182501.

41. Morgan, D. J. and Ketterson J. B., "Asymmetric flux pinning in a regular array of magnetic dipoles." *Physical Review Letters*, (1998), **80**(16), 3614-3617.

42. Ye, Z., Lyuksyutov, I. F., Wu, W., and Naugle, D. G., "Superconducting properties of $Pb_{82}Bi_{18}$ films controlled by ferromagnetic nanowire arrays." *Superconductor Science and Technology*, (2011), **24**(2), 024019.

43. Kim, K., Ozmetin, A. E., Naugle, D. G., and Lyuksyutov, I. F., "Flux pinning with a magnetic nanorod array." *Applied Physics Letters*, (2010), **97**(4), 042501.

44. Tinchev, S. S., "Interface superconductivity – Possible origin of high critical temperature in layered superconductors." *Physica C*, (2010), **470**, 626-629.

45. Levinson, H. J., *Principles of lithography*. 2nd ed. (2005), Bellingham, Wash.: SPIE Press. xii, 423 p.

46. Available from: http://www.ece.gatech.edu/research/labs/vc/theory/PosNegRes.html.

47. Shipley. *Microposit S1800 Series Photo Resists*. (2014), Available from: http://www.microchem.com/PDFs_Dow/S1800.pdf.

48. Thompson, L. F., Willson, C. G., and Bowden, M. J., *Introduction to microlithography : theory, materials, and processing*. ACS symposium series,. (1983), Washington, D.C.: The Society. ix, 363 p.

49. TAMU, *Instruction for the Mask Aligner (Quintel Q-4000IR)*. (2008), Available from: http://mcf.tamu.edu/docs/MaskAligner_Instructions_2-09.pdf.

50. Tandon, U. S. and Khokle, W. S., *Patterning of material layers in submicron region*. (1993), New York: J. Wiley. xii, 183 p.

51. Tseng, A. A., Chen, K., Chen, C. D., and Ma, K. J., "Electron beam lithography in nanoscale fabrication: recent development." *IEEE Transactions on Electronics Packaging Manufacturing*, (2003), **26**(2), 141-149.

52. Nabity, J. C., *Nanometer Pattern Generation System*. (2003), Available from: www.jcnabity.com.

53. Broers, A. N., Hoole, A. C. F., and Ryan, J. M., "Electron beam lithography-Resolution limits." *Microelectronic Engineering*, (1996), **32**(1-4), 131-142.

54. Vieu, C., Carcenac, F., Pépin, A., Chen, Y., Mejas, M., Lebib, A., Manin-Ferlazzo, L., Couraud, L., and Launois,. H., "Electron beam lithography: resolution limits and applications." *Applied Surface Science*, (2000), **164**(1-4), 111-117.

55. Franssila, S., *Introduction to microfabrication*. (2004), Chichester, West Sussex, England; Hoboken, NJ: J. Wiley. xvii, 401 p.

56. Reimer, L., *Scanning electron microscopy : physics of image formation and microanalysis*. 2nd completely rev. and updated ed. Springer series in optical sciences. (1998), Berlin; New York: Springer. xiv, 527 p.

57. Mohammad, M. A., Dew, S. K., Westra, K., Li, P., Aktary, M., Lauw, Y., Kovalenko, A., and Stepanova, M., "Nanoscale resist morphologies of dense gratings using electron-beam lithography." *Journal of Vacuum Science and Technology B*, (2007), **25**(3), 745-753.

58. Mohammad, M. A., Fito, T., Chen, J., Buswell, S., Aktary, M., and Stepanova, M., "Systematic study of the interdependence of exposure and development conditions and kinetic modelling for optimizing low-energy electron beam nanolithography." *Microelectronic Engineering*, (2010), **87**(5-8), 1104-1107.

59. Wang, M., ed. *Lithography*. Chapter 16. The Interdependence of Exposure and Development Conditions when Optimizing Low-Energy EBL for Nano-Scale

Resolution, ed. Mohammad, T. F., Mohammad, A., Chen, J., Buswell, S., Aktary, M., Dew, S. K., and Stepanova, M., (2010) Intech. 678.

60. Huang, X., Bernstein, G. H., Bazán, G., and Hill, D. A., "Spatial density of lines exposed in poly(methylmethacrylate) by electron beam lithography." *Journal of Vacuum Science and Technology A: Vacuum, Surfaces, and Films*, (1993), **11**(4), 1739.

61. Dai, Z. R., Pan, Z. W., and Wang, Z. L., "Novel nanostructures of functional oxides synthesized by thermal evaporation." *Advanced Functional Materials*, (2003), **13**(1), 9-24.

62. Harsha, K. S. S., *Principles of Vapor Deposition of Thin Films*. (2006), Oxford: ELSEVIER. xii, 1160 p.

63. Nemetschek, R., Prusseit, W., Holzapfel, B., Eickemeyer, J., Miller, U., and Maher, E., "Continuous tape coating by thermal evaporation." *IEEE Transactions on Applied Superconductivity*, (2003), **13**(2), 2477-2480.

64. Ohring, M., *Materials science of thin films: deposition and structure*. 2nd ed. (2002), San Diego, CA: Academic Press. xxi, 794 p.

65. Hablanian, M. H., *High-vacuum technology : a practical guide*. 2nd ed. Mechanical engineering. (1997), New York: Marcel Dekker. x, 551 p.

66. Hoffman, D. M., Singh, B., and Thomas, J. H., *Handbook of vacuum science and technology*. (1998), San Diego, CA: Academic Press. xxii, 835 p.

67. Hucknall, D. J., *Vacuum technology and applications*. 1991, Oxford ; Boston: Butterworth-Heinemann. vii, 319 p.

68. Mathis, R. D., *R.D. Mathis Company, High-Vacuum Evaporation Sources*. Available from: https://www.rdmathis.com/.

69. Buckel, W. and Hilsch, R., "Einfluß der Kondensation bei tiefen temperaturen auf den elektrischen widerstand und die supraleitung für verschiedene metalle." *Zeitschrift für Physik*, (1954), **138**(2), 109-120.

70. Buckel, W. and Hilsch, R., "Supraleitung und elektrischer widerstand neuartiger zinn-wismut-legierungen." *Zeitschrift für Physik*, (1956), **146**(1), 27-38.

71. Haviland, D. B., Liu, Y., and Goldman, A. M., "Onset of superconductivity in the two-dimensional limit." *Physical Review Letters*, (1989), **62**(18), 2180-2183.

72. Narlikar, A. V., *Frontiers in superconducting materials*. (2005), Berlin ; New York: Springer. xxxi, 1103 p.

73. Shalnikov, A., "Superconducting thin films." *Nature*, (1938), **142**, 74.

74. Bard, A. J. and Faulkner, L. R., *Electrochemical methods: fundamentals and applications*. 2nd ed. (2001), New York: John Wiley. xxi, 833 p.

75. Schlesinger, M. and Paunovic, M., *Modern electroplating*. 4th ed. Electrochemical Society series. (2000), New York: Wiley. xiv, 868 p.

76. Demortie. A and Bard, A. J., "Electrochemical Reactions of Organic Compounds in liquid-ammonia. I. reduction of benzophenone." *Journal of the American Chemical Society*, (1973), **95**(11), 3495-3500.

77. Bang, W. and Hong, K., "Planarity improvement and reduction of coercivity by organic additives in electroplated Ni-Fe permalloy thin films." *Electrochemical and Solid State Letters*, (2007), **10**(8), J86-J88.

78. Bang, W., Lee, J, Hong, K., Ko, Y., Chung, J., and Lee, H., "Permeability change of electroplated Ni-Fe permalloy thin films by a leveller added to the electrolyte." *Physica Status Solidi a-Applications and Materials Science*, (2007), **204**(12), 4067-4070.

79. Bang, W., Ko, Y., Lee, H., Hong, K., Chung, J., and Lee, H., "Effects of saccharine N-propane sulfonate on the microstructures, magnetic properties, and magnetoimpedance of electroplated Ni-Fe permalloy thin films." *Journal of the Electrochemical Society*, (2008), **155**(6), D429-D435.

80. Blondel, A., Meier, J. P., Doudin, B., and Ansermet, J. -Ph., "Giant Magnetoresistance of Nanowires of Multilayers." *Applied Physics Letters*, (1994), **65**(23), 3019-3021.

81. Bae, J., Bang, W., and Hong, K., "Reduction of coercivity in electroplated permalloy thin films utilizing a brightening agent." *ECS Transactions*, (2007), **3**(25), 101-104.

82. Baskaran, A. and Smereka, P., "Mechanisms of stranski-krastanov growth." *Journal of Applied Physics*, (2012), **111**(4), 044321.

83. Bündgens, N., Lüth, H., Mattern-Klosson, M., Spitzer, A., and Tulke, A., "Sn overlayers on GaAs(110): growth mechanism and band bending." *Surface Science*, (1985), **160**(1), 46-56.

84. Lüth, H., *Solid surfaces, interfaces and thin films*. 4th, rev. and extended ed. Advanced texts in physics. (2001), Berlin ; New York: Springer. xiii, 559 p.

85. Melo, L. L., Vaz, A. R., Salvadori, M. C., and Cattani, M., "Grain sizes and surface roughness in platinum and gold thin films." *Journal of Metastable and Nanocrystalline Materials*, (2004), **20-21**, 623-628.

86. Jadhav, N., Buchovecky, E. J., Reinbold, L., Kumar, S., Bower, A. F., and Chason, E., "Understanding the correlation between intermetallic growth, stress evolution, and Sn whisker nucleation." *IEEE Transactions on Electronics Packaging Manufacturing*, (2010). **33**(3), 183-192.

87. Kim, H., Horwitz, J. S., Kushto, G., Piqué, A., Kafafi, Z. H., Gilmore C. M., and Chrisey, D. B., "Effect of film thickness on the properties of indium tin oxide thin films." *Journal of Applied Physics*, (2000), **88**(10), 6021-6025.

88. Kumar, A., Singh, D., and Kaur, D., "Grain size effect on structural, electrical and mechanical properties of NiTi thin films deposited by magnetron co-sputtering." *Surface & Coatings Technology*, (2009), **203**(12), 1596-1603.

89. Madou, M. J., *Fundamentals of microfabrication: the science of miniaturization*. 2nd ed. (2002), Boca Raton, FL: CRC Press. 723 p.

90. Nishi, Y. and Doering R., *Handbook of semiconductor manufacturing technology*. (2000), New York: Marcel Dekker. xiv, 1157 p.

91. Blech, I. A., "Evaporated film profiles over steps in substrates." *Thin Solid Films*, (1970), **6**(2), 113-118.

92. Blech, I. A., Fraser, D. B., and Haszko, S. E., "Optimization of Al step coverage through computer simulation and scanning electron microscopy." *Journal of Vacuum Science and Technology*, (1978), **15**(1), 13-19.

93. Levin, R. M. and Evans-Lutterodt, K., "The step coverage of undoped and phosphorus-doped SiO_2 glass films." *Journal of Vacuum Science and Technology B*, (1983), **1**(1), 54-61.

94. Tsai, C. C., Knights, J. C., Chang, G., and Wacker, B., "Film formation mechanisms in the plasma deposition of hydrogenated amorphous silicon." J*ournal of Applied Physics*, (1986), **59**(8), 2998-3001.

95. Paunovic, M. and Schlesinger, M., *Fundamentals of electrochemical deposition*. The Electrochemical Society series. (1998), New York: Wiley. viii, 301 p.

96. Hong, K., Lee, J., Lee, J., Ko, Y., Chung, J., and Kim, J., "Property changes of electroplated Cu/Co alloys and multilayers by organic additives." *Journal of Magnetism and Magnetic Materials*, (2006), **304**(1), 60-63.

97. Bae, J., Bang, W., Kim, J., and Hong, K., "Effect of organic additives on magnetic properties of electroplated Cu/Co thin films." *ECS Transactions*, (2007), **2**(20), 33-37.

98. Boersch, H., Kunze, U., Lischke, B., and Rodewald, W., "Observation of mixed state in films of type-I superconductors (Pb)." *Physics Letters A*, (1973), **A 44**(4), 273-274.

99. Dolan, G. J. and Silcox, J., "Critical thicknesses in superconducting thin films." *Physical Review Letters*, (1973), **30**(13), 603-606.

100. Rodewald, W., "Triangular vortex lattice in thin films of type-I superconductors." *Physics Letters A*, (1975), **55**(2), 135-136.

101. Tinkham, M., "Effect of fluxoid quantization on transitions of superconducting films." *Physical Review*, (1963), **129**(6), 2413-2422.

102. Blumberg, R. H. and Seraphim, D. P., "Effect of elastic strain on superconducting critical temperature of evaporated tin films." *Journal of Applied Physics*, (1962), **33**(1), 163-168.

103. Toxen, A. M., "Size Effects in Thin Superconducting Indium Films." *Physical Review*, (1961), **123**(2), 442-446.

104. Lock, J. M., "Penetration of magnetic fields into superconductors III. Measurements on thin films of tin, lead and indium." *Proceedings of the Royal Society of London Series A, Mathematical and Physical Sciences*, (1951), **208**(1094), 391-408.

105. Cottrell, A. H., *Dislocations and plastic flow in crystals*. International series of monographs on physics. (1953), Oxford,: Clarendon Press. 223 p.

106. Lide, D. R., ed. *CRC Handbook of Chemistry and Physics*. 87th edition ed. (2006), Boca Raton, FL: Taylor & Francis Group. 2608 p.

107. Muench, N. L., "Effects of stress on superconducting Sn, in, Tl, and Al." *Physical Review*, (1955), **99**(6), 1814-1820.

108. Ashcroft, N. W. and Mermin, N. D., *Solid state physics*. (1976), New York: Holt, Rinehart and Winston. xxi, 826 p.

109. Andrew, E. R., "The size variation of resistivity for mercury and tin." *Proceedings of the Physical Society of London Section A*, (1949), **62**(350), 77-88.

110. Lovell, A. C. B., "The electrical conductivity of thin metallic films. I. Rubidium on pyrex glass surfaces." *Proceedings of the Royal Society of London Series A, Mathematical and Physical Sciences*, (1936), **157**(A891), 0311-0330.

111. Ke, Y., Zahid, F., Timoshevskii, V., Xia, K., Gall, D., and Guo, H., "Resistivity of thin Cu films with surface roughness." *Physical Review B*, (2009), **79**(15), 155406.

112. Plombon, J. J., Andideh, E., Dubin, V. M., and Maiz, J., "Influence of phonon, geometry, impurity, and grain size on copper line resistivity." *Applied Physics Letters*, (2006), **89**(11), 113124.

113. Fuchs, K., "The conductivity of thin metallic films according to the electron theory of metals." *Proceedings of the Cambridge Philosophical Society*, (1938), **34**, 100-108.

114. Sondheimer, E. H., "The mean free path of electrons in metals." *Advances in Physics*, (1952), **1**(1), 1-42.

115. Lim, J. W., Mimura, K., and Isshiki, M., "Thickness dependence of resistivity for Cu films deposited by ion beam deposition." *Applied Surface Science*, (2003), **217**(1-4), 95-99.

116. Anderson, J. C., *The use of thin films in physical investigations; a NATO Advanced Study Institute held at the Imperial College of Science and Technology, University of London, 19-24 July, 1965*. (1966), London, New York: Academic Press. xix, 462 p.

117. Özer, M. M., Jia, Y., Zhang, Z., Thompson, J. R., and Weitering, H. H., "Tuning the quantum stability and superconductivity of ultrathin metal alloys." *Science*, (2007), **316**(5831), 1594-1597.

118. Schiller, C. K. and Bulow, H., "Quenched thin Sn, Pb and Indium films: comparison of nominal crystallite size from electron diffraction experiments with electronic mean free paths calculated from H_C-Values." *Solid State Communications*, (1970), **8**(22), 1827-1829.

119. Flik, M. I., Zhang, Z. M., Goodson, K. E., Siegal, M. P., and Phillips J. M., "Electron scattering rate in epitaxial $YBa_2Cu_3O_7$ superconducting films." *Physical Review B*, (1992), **46**(9), 5606-5614.

120. Welp, U., Kwok, W. -K., Crabtree, G. W., Vadervoort, J. G., and Liu, J. Z., "Magnetic measurements of the upper critical field of $YBa_2Cu_3O_{7-\delta}$ single crystals." *Physical Review Letters*, (1989), **62**(16), 1908-1911.

121. Goodson, K. E. and Flik, M. I., "Electron and phonon thermal conduction in epitaxial high-T_C superconducting films." *Journal of Heat Transfer,Transactions of the ASME*, (1993), **115**(1), 17-25.

122. Krusin-Elbaum, L., Greene, R. L., Holtzberg, F., Malozemoff, A. P., and Yeshurun, Y., "Direct measurement of the temperature-dependent magnetic penetration depth in Y-Ba-Cu-O crystals." *Physical Review Letters*, (1989), **62**(2), 217-220.

123. Krusin-Elbaum, L., Malozemoff, A. P., Yeshurun, Y., Cronemeyer, D. C., and Holtzberg, F., "Temperature-dependence of lower critical fields in Y-Ba-Cu-O crystals." P*hysical Review B*, (1989), **39**(4), 2936-2939.

124. Ozmetin, A. E., Rathnayaka, K. D. D., Naugle, D. g., and Lyuksyutov, I. F., "Strong increase in critical field and current in magnet-superconductor hybrids." *Journal of Applied Physics*, (2009), **105**(7), 07E324.

125. Yang, Z. R., Lange, M., Volodin, A., Szymczak, R., and Moshchalkov, V. V., "Domain-wall superconductivity in superconductor-ferromagnet hybrids." *Nature Materials*, (2004), **3**(11), 793-798.

126. Vlasko-Vlasov, V., Welp, U., Karapetrov, G., Novosad, V., Rosenmann, D., Iavarone, M., Belkin, A., and Kwok, W. -K., "Guiding superconducting vortices with magnetic domain walls." *Physical Review B*, (2008), **77**(13), 134518.

127. Zhu, L. Y., Chen, T. Y., and Chien, C. L., "Altering the superconductor transition temperature by domain-wall arrangements in hybrid ferromagnet-superconductor structures." *Physical Review Letters*, (2008), **101**(1), 017004.

128. Martinoli, P., Nsabimana, M., and Racine, G. A., "Search for two-dimensional melting in a lattice of superconducting vortices." *Helvetica Physica Acta*, (1983), **56**(1-3). 765-785.

129. Lyuksyutov, I. F., Naumovets, A. G., and Pokrovsky, V. L., *Two-dimensional crystals*. 1992, Boston: Academic Press. 423 p.

130. Lyuksyutov, I. F., "Magnetic Nanorod-Superconductor Hybrids." *Journal of Superconductivity and Novel Magnetism*, (2010), **23**(6), 1047-1049.

131. Kim, K., Rathnayaka, K. D. D., Lyuksyutov, I. F., and Naugle, D. G., "Superconducting film with an array of magnetic nanostripes." *International Journal of Modern Physics B*, (2013), **27**(15), 1362020.

132. Lyuksyutov, I. F., "Nanoscale magnetic traps." *Modern Physics Letters B*, (2002), **16**(15-16), 569-576.

133. Lee, H., Kim, K., Rathnayaka, K. D. D., Lyuksyutov, I. F., and Naugle, D. G., "Superconducting film with embedded cobalt nanorods." *International Journal of Modern Physics B*, (2013), **27**(15), 1362005.

134. Meyer, J. and Minnigerode, G. v., "Instabilities in transition curve of current-carrying one-dimensional superconductors." *Physics Letters A*, (1972), **A 38**(7), 529-530.

135. Michotte, S., Matefi-Tempfli, S., Piraux, L., Vodolazov, D. Y., and Peeters, F. M., "Condition for the occurrence of phase slip centers in superconducting nanowires under applied current or voltage." *Physical Review B*, (2004), **69**(9), 094512.

136. Tian, M. L., Wang, J., Kurtz, J. S., Liu, Y., Chan, M. H. W., Mayer, T. S., and Mallouk, T. E., "Dissipation in quasi-one-dimensional superconducting single-crystal Sn nanowires." *Physical Review B*, (2005), **71**(10), 104521.

137. Patel, U., Xiao, Z. L., Gurevich, A., Avci, S., Hua, J., Divan, R., Welp, U., and Kwok, W. -K., "Magnetoresistance oscillations in superconducting granular niobium nitride nanowires." *Physical Review B*, (2009), **80**(1), 012504.

138. Sivakov, A. G., Glukhov, A. M., Omelyanchouk, A. N., Koval, Y., Müller, P. , and Ustinov, A. V., "Josephson behavior of phase-slip lines in wide superconducting strips." *Physical Review Letters*, (2003), **91**(26), 267001.

139. Dmitriev, V. M. and Zolochevskii, I. V., "Resistive current states in wide superconducting films in zero magnetic field." *Superconductor Science and Technology*, (2006), **19**(4), 342-349.

140. Ōgushi, T. and Shibuya, Y., "Flux flow in type I and II superconducting films." *Journal of the Physical Society of Japan*, (1972), **32**(2), 400-415.

141. Berdiyorov, G. R., Milošević, M. V., and Peeters, F. M., "Tunable kinematics of phase-slip lines in a superconducting stripe with magnetic dots." *Physical Review B*, (2009), **80**(21), 214509.

142. Kim, K., Lyuksyutov, I. F., and Naugle, D. G., "Magnetic nanorod-superconductor hybrid near the superconducting transition temperature." *Superconductor Science and Technology*, (2011), **24**(2), 024013.

143. Ye, Z., Naugle, D. G., Wu, W., Lyuksyutov, I. F., "Superconducting properties of Pb/Bi films quench-condensed on a porous alumina substrate filled with Co nanowires." *Journal of Superconductivity and Novel Magnetism*, (2010), **23**(6), 1083-1085.

144. Lyuksyutov, I. F. and Naugle, D. G., "Frozen flux superconductors." *Modern Physics Letters B*, (1999), **13**(15), 491-497.

145. Villegas, J. E., Montero, M. I., Li, C. P. and Schuller, I. K., "Correlation length of quasiperiodic vortex lattices." *Physical Review Letters*, (2006), **97**(2), 027002.

146. Sellmyer, D. J., Zheng, M., and Skomski, R., "Magnetism of Fe, Co and Ni nanowires in self-assembled arrays." *Journal of Physics:Condensed Matter*, (2001), **13**(25), R433-R460.

147. Ye, Z., Liu, H., Luo, Z., Lee, H., Wu, W., Naugle, D. G., and Lyuksyutov, I. F., "Thickness dependence of the microstructures and magnetic properties of electroplated Co nanowires." *Nanotechnology*, (2009). **20**(4), 045704.

148. Bang, W., Kim, K., Rathnayaka, K. D. D., Teizer, W., Lyuksyutov, I. F., and Naugle, D. G., "Manipulating superconducting films with magnetic nanostripes." *Physica C:Superconductivity and Its Applications*, (2013), **493**, 89-92.

149. Kim, K., Rathnayaka, K. D. D., Lyuksyutov, I. F., and Naugle, D. G., "Transport properties of a superconducting film with magnetic nanostripes." *International Journal of Modern Physics B*, (2013), **27**(15), 1362025.

150. Ozmetin, A.E., Yapici, M. K., Zou, J., Lyuksyutov, I. F., and Naugle, D. G., "Micromagnet-superconducting hybrid structures with directional current flow dependence for persistent current switching." *Applied Physics Letters*, (2009), **95**(2), 022506.

151. Wei, Z., Ye, Z., Rathnayaka, K. D. D., Lyuksyutov, I. F., Wu, W., and Naugle, D. G., "Superconductivity of a Sn film controlled by an array of Co nanowires." *Physica C:Superconductivity and its Applications*, (2012), **479**, 41-44.

152. Bang, W., Teizer, W., Rathnayaka, K. D. D., Lyuksyutov, I. F., and Naugle, D. G., "Using electrochemical fabrication to grow external arrays of magnetic nanostripes to manipulate superconductivity in the thin film." *International Journal of Modern Physics B,* (In press).

153. Bang, W., Teizer, W., Rathnayaka, K. D. D., Lyuksyutov, I. F., and Naugle, D. G., " Controlling superconductivity in thin film with an external array of magnetic nanostructures." *International Journal of Modern Physics B,* (In press).

APPENDIX

Appendix 1. Manipulating superconducting films with magnetic nanostripes*

The transport properties of a 90 nm $Pb_{82}Bi_{18}$ thin films and 50 nm Sn thin film with an array of parallel Ni or Co magnetic nanostripes (500 nm period) deposited on the top of a 20 nm Ge insulating layer covering the superconducting film surface. The I_C parallel to the stripes is significantly larger than I_C perpendicular to the stripes for $Pb_{82}Bi_{18}$ thin film.

Figure 107 (a) shows the SEM image of the cross-like $Pb_{82}Bi_{18}$ superconducting film with thickness 90 nm and a set of parallel Ni stripes with the cross-section 120 x 120 nm^2 evaporated atop the 20 nm thick Ge insulating layer. The control film, fabricated simultaneously without the Ni array, is less than 200 μm away on the same chip. Such geometry ensures the smallest possible difference in the thickness and quality of the hybrid and control films. Figure 107 (b) show the central part of the similar cross for Sn film to demonstrate the quality of the Co nanostripe array.

The samples were coupled to the PPMS with Au wires attached by pressed In for a four-probe measurement.

In order to determine the T_C, R of the samples was measured with a DC current

---

* Reprinted with permission from "Manipulating superconducting films with magnetic nanostripes" by W. Bang, K. Kim, K. D. D. Rathnayaka, W. Teizer, I. F. Lyuksyutov, D. G. Naugle, 2013. *Physica C*, 493, 89-92, Copyright [2015] by Elsevier [148].

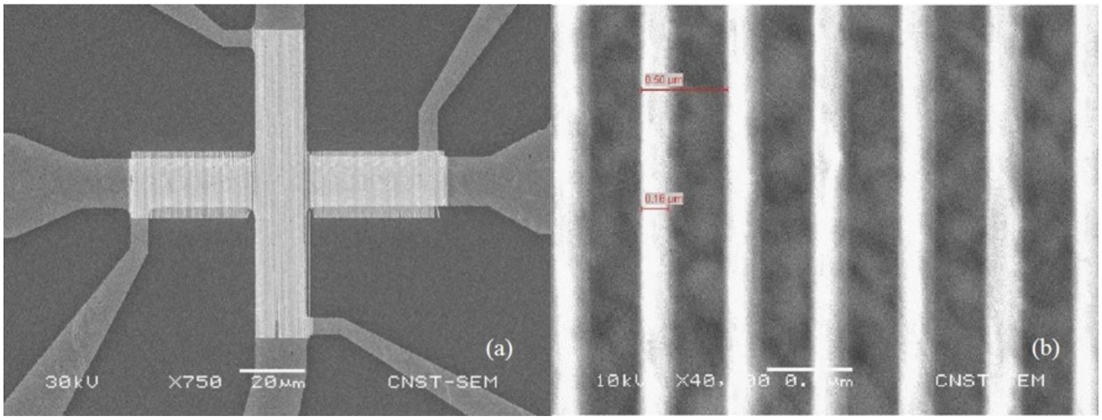

Figure 107. SEM image of the cross-like Pb$_{82}$Bi$_{18}$ superconducting film with thickness 90 nm and a set of parallel Ni stripes with the cross-section 120 x 120 nm^2 evaporated atop the 20 nm thick Ge insulating layer (a). The part of the Co stripe array to demonstrate the quality of the array atop Sn film with thickness 50 nm (b).

of 1 μA while the samples were cooled from a temperature (*T*) where the samples were in the normal states to a *T* where the samples were in the superconducting state. An up to 1 T string external magnetic field (*H*) was applied to magnetized the Ni/Co stripes and then reduced to zero before the temperature sweep for the *R* vs. *T* characterization.

The *R*-*T* curves are shown in Figure 108. *R*-*T* curves for non-magnetized hybrid samples are close to that for the control samples as shown in Figure 108 (a) for the Pb$_{82}$Bi$_{18}$/Ni system. Similar behavior was observed for Co/Sn system. Figures 108 (b) and (c) indicate that T_C for both current directions (parallel and perpendicular to the stripes) in the hybrid films are close to each other. Note that in both systems, there is a difference ΔT_C in T_C for hybrid and control samples. The relative value of $\Delta T_C/T_C$ is almost four times larger for Sn/Co system than for Pb$_{82}$Bi$_{18}$/Ni system.

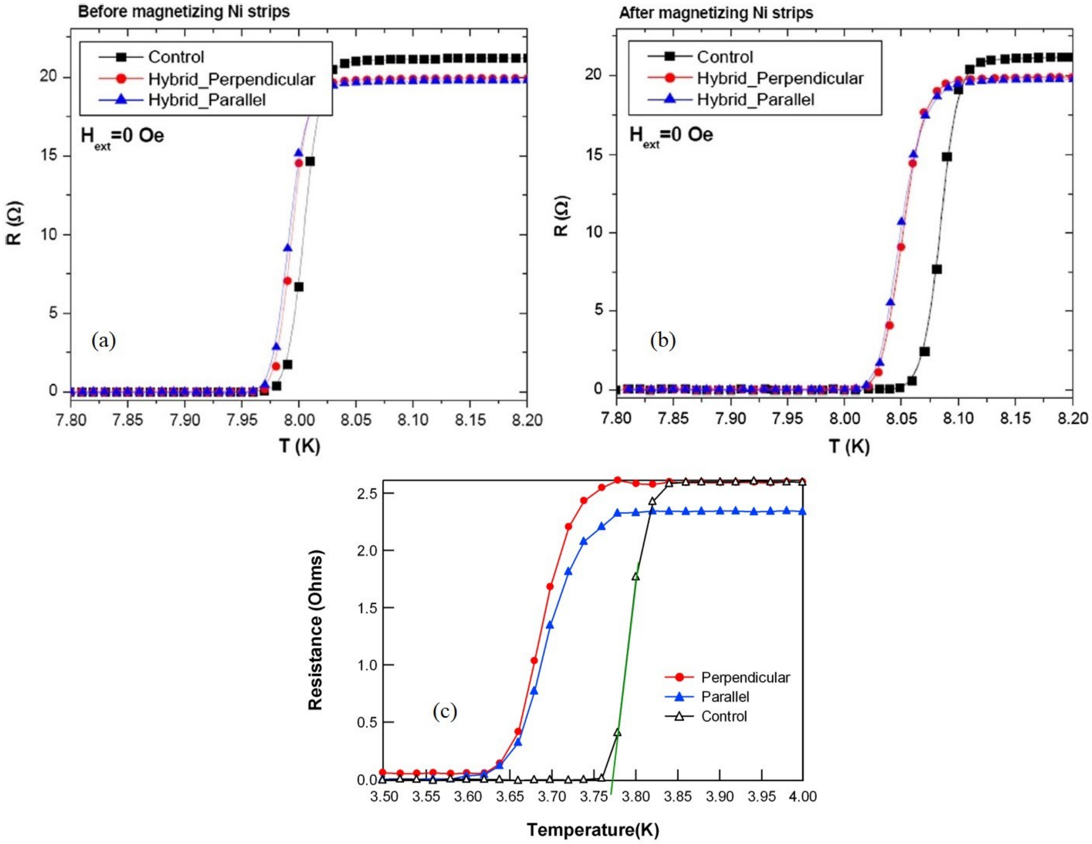

Figure 108. *R*-*T* curves of the hybrid and $Pb_{82}Bi_{18}$ control samples before (a) and after (b) magnetizing Ni stripes. *R*-*T* curves for magnetized hybrid Sn/Co and control Sn samples (c). Measuring current=1 µA.

Figure 109 (a) shows *R*(*H*) curves of the hybrid and control samples of the $Pb_{82}Bi_{18}$/Ni system measured at *T*=8.06 K during complete cycles of the field sweep. Maximum magnetic field is 10,000 Oe, and measuring current is a 1 µA. Figure 109 (b) shows the same curves for Sn/Co system at *T* =3.70 K. In both systems the *T* is above T_C for the hybrid samples, and it is below T_C for Sn/Co system and very close to T_C for $Pb_{82}Bi_{18}$/Ni system. There are two main differences between systems: (i) strong hysteresis for $Pb_{82}Bi_{18}$/Ni system and (ii) much stronger magnetic field influence on

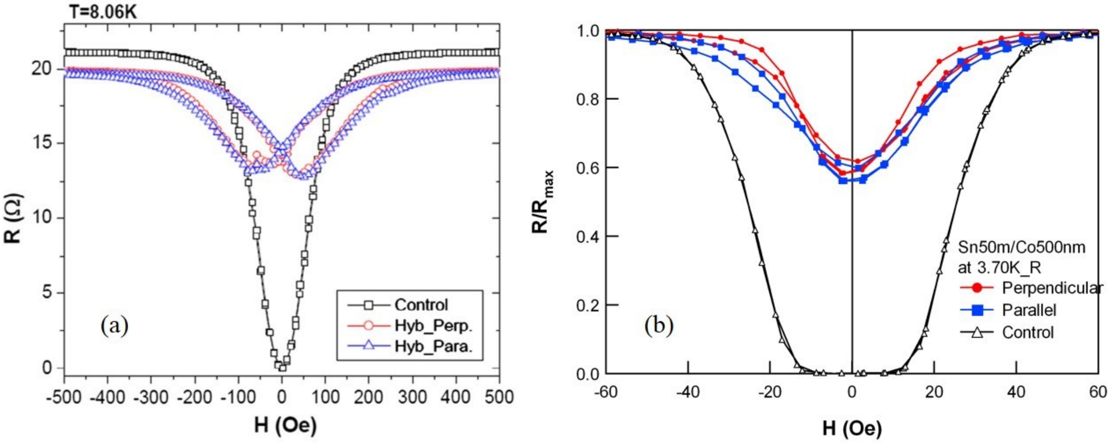

Figure 109. *R*-*H* curves of the hybrid and control $Pb_{82}Bi_{18}$ samples measured at *T*=8.06 K during complete cycles of the field sweep (a). H_{max}=10,000 Oe and measuring current=1 µA. Similar curves for Sn/Co system at *T*=3.70 K (b).

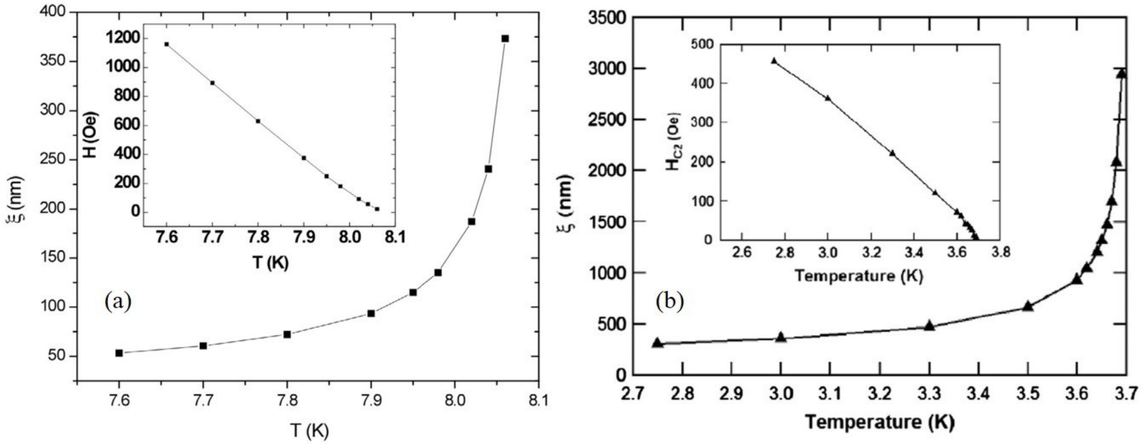

Figure 110. ξ and phase diagram (inset) for the control $Pb_{82}Bi_{18}$ film (a) and for the Sn film (b).

$Pb_{82}Bi_{18}$/Ni system.

Figure 110 shows phase diagrams ($H_{C2}(T)$) and $\boldsymbol{\xi}$ vs. *T* for $Pb_{82}Bi_{18}$ and Sn films.

Note that Sn coherence length values reach almost an order of magnitude larger than those for $Pb_{82}Bi_{18}$, and it exceeds the film thickness and magnetic array period several times.

I_C of the hybrid samples were determined from I-V curves which were obtained during a complete cycle of the magnetic field sweep carried out at a fixed temperature of 7.7 K. Current sweeps for the I-V curves were performed every 5 Oe increment (or decrement, depending on the field sweep-direction) of the external magnetic field over the range 0 Oe to ±300 Oe. The maximum of the applied field during the process was 1 T. The I_C was defined in I-V measurements as the values at which the induced voltages across the samples become 10 μV and plotted as a function of H in Figure 111 for the $Pb_{82}Bi_{18}$/Ni system.

The magnetic interaction of vortices with the stripe magnetic structure results in the anisotropy in the I_C and I-V curves. When the current is parallel to the magnetic stripes, the Lorentz force acts on vortices in the direction perpendicular to the stripes, when current is perpendicular, the force is parallel to the stripes. The magnetic interaction of vortices with the magnetic stripes provides a periodic potential barrier for vortex motion in the direction perpendicular to the stripes (see [42] for discussion). This explains the higher value of I_C in the direction parallel to the stripes in comparison to the direction perpendicular to the stripes, as shown in Figure 111. The “magnetic” origin of the pinning effect is proven by the strong hysteresis in the I_C dependence on magnetic field. The maximum of the I_C is observed at a finite magnetic field (H_1) when the stripes are magnetized. The average value of H_1 for two peaks is close to 60 Oe. This is close to the value of the field (45 Oe), which creates a vortex lattice with a period equal to the

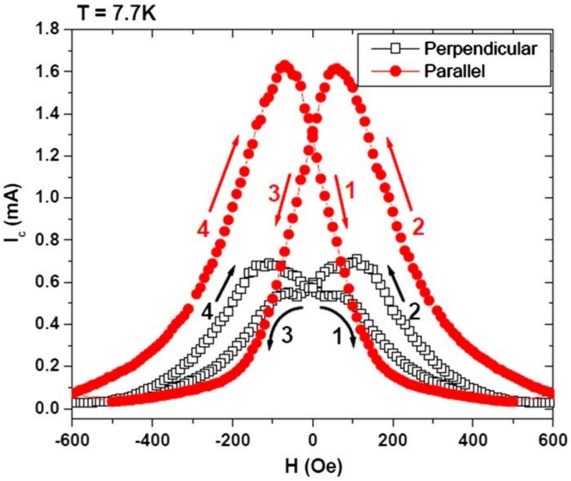

Figure 111. I_C ($V_{threshold}$=10 μV) of the hybrid $Pb_{82}Bi_{18}$/Ni system measured as a function of magnetic fields at 7.7 K, during complete cycle of the field sweep. Arrows indicate the field sweep direction.

period of the stripe structure as explained by Fig. 6 in Ref. [42].

The system $Pb_{82}Bi_{18}$/Ni shows behavior similar to what was observed previously in Ref. [42]. In contrast, the Sn/Co system shows different behavior: no hysteresis, no pronounced vortex pinning, but much stronger relative influence of magnetic Co nanostripes on the I_C. This can be explained by two factors: (i) weak stray magnetic field from Co stripes and (ii) large value of coherence length, which exceeds several times Co stripes period near transition temperature. Weak stray field from Co stripes contradicts observed bulk magnetic properties [146] and Co nanowires magnetic properties [147]. In conclusion, this effect is probably due to the fabrication procedure (evaporation). Both factors (i) and (ii) results in the weak interaction of the Co stripes with vortices (which have cores several times larger than structure period). This weak interaction means that all effects in magnetic field related with vortices will be weak.

Appendix 2. Using electrochemical fabrication to grow external arrays of magnetic nanostripes to manipulate superconductivity in the thin film*

This results on electrochemical fabrication of arrays of magnetic nanostripes atop a thermally evaporated 100 nm Sn film covered with an insulating 20 nm Ge layer. Electroplated Ni nanostripes had a 200 nm wide by a 750 nm high, and their period was 400 nm, as shown in Figure 112 (a). The nanostripes are either parallel or perpendicular to an applied current. Their transport properties and superconducting T_C is reported. The transport properties demonstrate strong hysteresis as a function of the magnetic field.

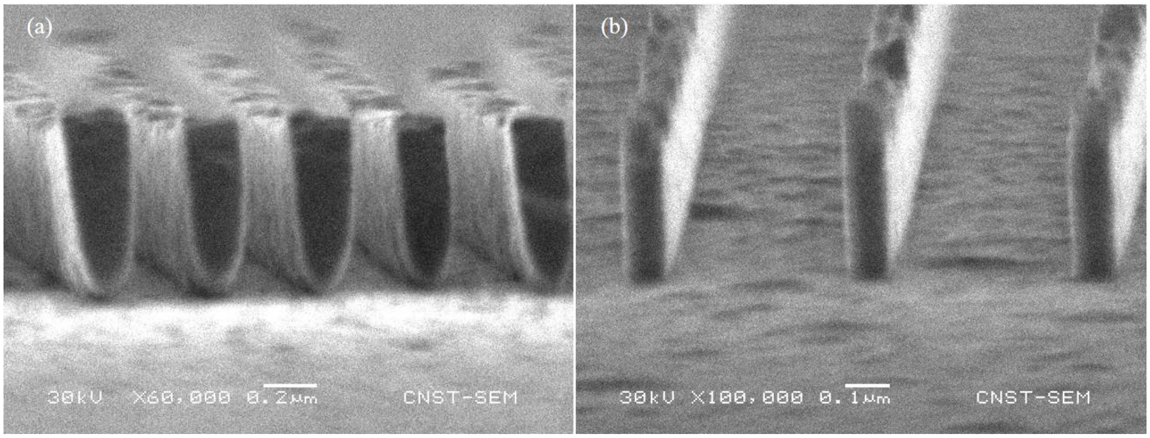

Figure 112. SEM images of the Ni nanostripe arrays (a) and Co nanostripe arrays (b).

---

[*] Appendix 2 is in press "Using electrochemical fabrication to grow external arrays of magnetic nanostripes to manipulate superconductivity in the thin film" by Wonbae Bang, W. Teizer, K. D. D. Rathnayaka, I. F. Lyuksyutov, D. G. Naugle, 2015. *International Journal of Modern Physics B* [152].

In order to determine T_C, R of the samples was measured with an AC current of 1.5 μA while the samples were cooled from a temperature where the samples were in the normal state to a temperature where they were in the superconducting state.

A 1 T external magnetic field was applied to magnetize the Ni nanostripes and then reduced to zero before the temperature sweep. Decrease of T_C for the samples with magnetized Ni nanostripes is natural due to the magnetic field from magnetized nanorod array which was observed in previously studied systems [11, 124, 131, 148-150].

Figure 113 (a) shows R-H curves slightly below T_C for a sample with current perpendicular to the Ni nanostripe array. It demonstrates strong hysteresis and a "field compensation effect" [6-9]. Figure 113 (b) also shows a new feature, variation of $R(H)$ with an interval of about 12 Oe not previously observed for arrays of magnetic

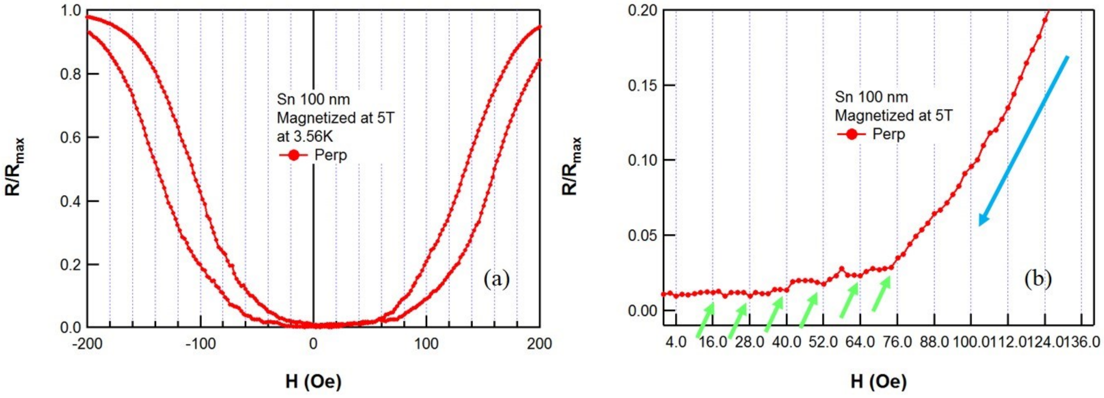

Figure 113. R-H curves of the hybrid Sn film measured at T=3.56 K during a complete cycle of the field sweep. The current is perpendicular to the Ni nanostripe array (a). Enlarged part of the R-H curve, and green arrows indicate features which appear with approximately a 12 Oe interval (b). H_{max}=50,000 Oe and measuring current=1.5 μA.

nanostripes. Figures 114 (a) and (b) show $R(H)$ curves for the sample with current parallel to the Ni nanostripe array. The main features are similar to those for the sample with current perpendicular to the Ni nanostripe array.

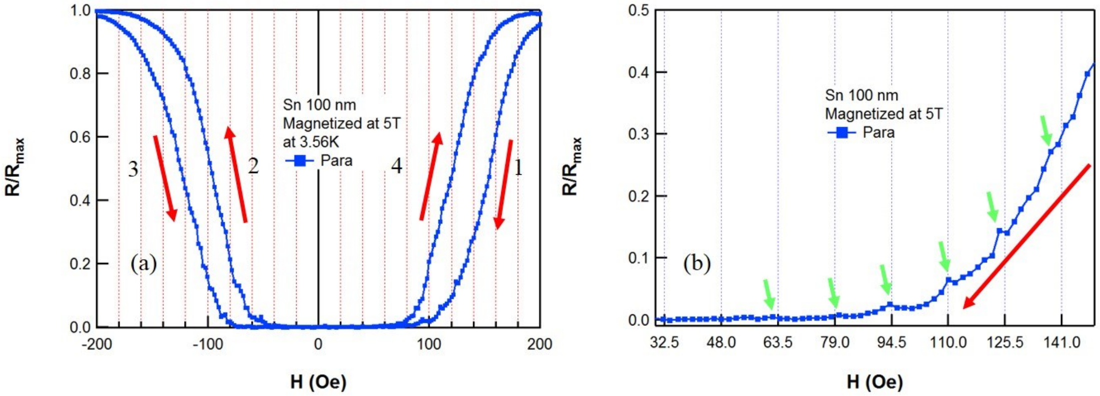

Figure 114. *R*-*H* curves of the hybrid Sn film measured at T=3.56 K during a complete cycle of the field sweep. The current is parallel to the Ni nanostripe array (a). Enlarged part of the *R*-*H* curve, and green arrows indicate features which appear with approximately a 15.5 Oe interval (b). H_{max}=50,000 Oe and measuring current=1.5 μA.

Figure 115 (a) shows the I_C for hybrid systems with the current perpendicular (red filled circles) and parallel (blue filled squares) to the magnetic Ni nanostripes at 3.00 K. Strong hysteresis in the field dependence of the I_C demonstrates magnetic pinning of the vortices by an array of magnetic nanostripes observed previously in [11, 124, 131, 148-150]. Note that the strongly magnetized array (arrow 1) has a higher I_C than the weakly magnetized (arrow 4). For both orientations of current with respect to magnetic nanostripes the I_C is essentially the same. This behavior was already observed previously [148] for a Sn film. This explains in [148] by the large value of the Sn coherence length, which is comparable with nanostructure's period.

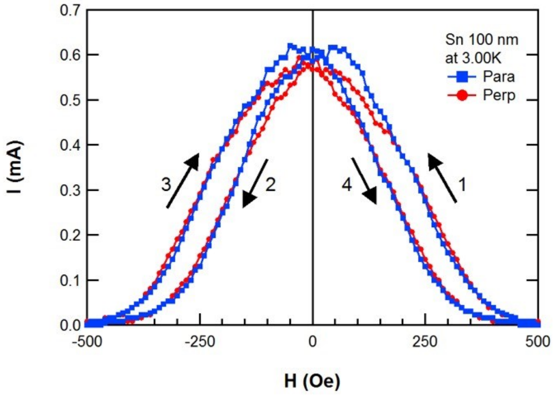

Figure 115. I_C for Sn films with an array of Ni nanostripes perpendicular (red filled circles) and parallel (blue squares) to the current at 3.00 K.

How this electroplated Ni nanostripes affects magnetic pinning of vortices in a Sn thin film superconductor is studied. This electrochemically grown configuration exhibits several interesting properties, which are reported for the first time. The Sn/Ni system [131] with a similar Sn thickness (90nm) was previously studied, but with a nanostripe array with 120 x 120 nm^2 cross-section and a 800nm period fabricated by evaporation. The Sn film dimensions, T_C for the control and the hybrid samples and the values of I_C were similar to those in this work. However, in [131], a 30% stronger I_C has been observed when it was parallel to the nanostripes rather than perpendicular to them. This explains an effect by the larger period of the magnetic nanostructure used in [131].

Appendix 3. Controlling superconductivity in thin film with an external array of magnetic nanostructures [*]

A new type of Magnet-Superconductor Hybrid was fabricated: an ordered array of Magnetic Nanorods atop a superconducting film electrically insulated from the array. Transport properties of this Magnet-Superconductor Hybrid, *R*(*T*) and *R*(*H*) are reported. These results are compared with those for a superconducting film atop an alumina template with an array of magnetic nanowires [42, 143, 151].

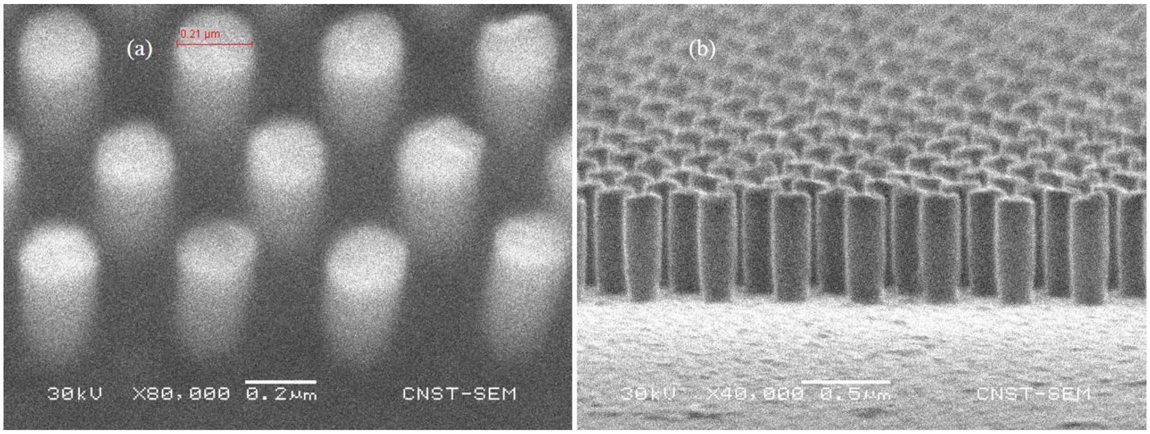

Figure 116. SEM images of the Ni nanorods with a 200 nm diameter and a 400 nm array period (a) and a larger part of the Ni nanorod array to demonstrate the quality of the array (b).

---

[*] Appendix 3 is in press "Controlling superconductivity in thin film with an external array of magnetic nanostructures" by Wonbae Bang, W. Teizer, K. D. D. Rathnayaka, I. F. Lyuksyutov, D. G. Naugle, 2015. *International Journal of Modern Physics B* [153]

A 100 nm Sn film was thermally evaporated with quench condensation on a Si substrate. A 5 nm Ge film was deposited at 45 degree angles to prevent a short at the edge of the Sn thin film. Afterwards, a Ag film was deposited on top of the Ge layer for a CE for Ni electroplating. Electroplated Ni nanorods had a 200 nm wide by a 750 nm high, and their period was 400 nm, as shown in Figure 116.

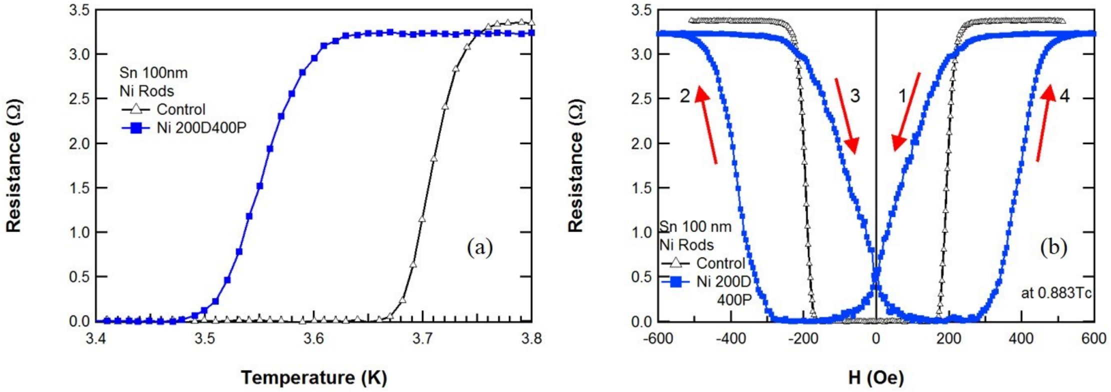

Figure 117. *R*-*T* curves of the hybrid and control samples (a). *R*-*H* curves of the hybrid and control samples measured at T=0.883T_C during complete cycle of the field sweep (b). H_{max}=10,000 Oe and measuring current=1.5 μA.

The T_Cs were determined from *R*-*T* curves in Figure 117 (a). Prior to the temperature sweep ±1 T magnetic field was applied to magnetize the Ni nanorods and then reduced to zero. The lower T_C for the hybrid sample is due to the field from the Ni nanorods. Figure 117 (b) shows *R*-*H* curves below T_C for both samples. The hybrid sample exhibits strong hysteresis: several times larger than that for nanorod arrays in an alumina template [42, 143, 151]. The width of hysteresis is comparable with that for embedded magnetic nanorod arrays [43, 133, 142], but its sign is different. The origin of hysteretic behavior of the *R*-*H* curves was previously discussed [43, 130].

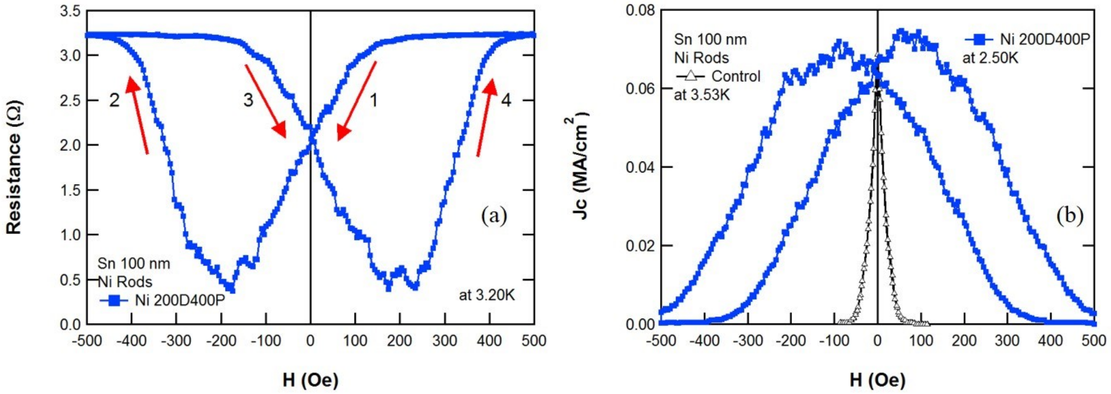

Figure 118. An *R*-*H* curve for the hybrid sample measured at T=3.20 K (above T_C) during a complete field sweep cycle (a). H_{max}=10,000 Oe and measuring current = 1.5 µA. J_C for hybrid and control samples (b).

Figure 118 (a) shows an *R*-*H* curve just above T_C. This curve dramatically differs from those for superconducting thin films on alumina templates with magnetic nanorods [42, 143, 151]. In that case, the *R*-*H* curves were smooth with no internal structures. The *R*-*H* curve in Figure 118 (a) is in some sense intermediate between those for arrays of magnetic nanorods embedded into superconducting film [142] and those for films on alumina templates [42, 143, 151]. For embedded rods, the *R*-*H* curves demonstrate clear oscillations with a period close to a flux quantum per unit cell of the magnetic nanostructure. Figure 118 (a) displays a rather irregular internal structure. The J_C for the control sample at 3.53 K and for the hybrid sample at 2.50 K is shown in Figure 118 (b). This figure also shows the important feature of magnetic pinning of vortices by magnetic nanorods given previously [43, 133]. The order of magnitude increase in the range of magnetic fields with a significant value of J_C.

The direction of the magnetic fields in the superconducting thin film is opposite to the nanorods' magnetization direction. As a result, the external magnetic fields can be compensated by the field from the rods, and the I_C for the magnetized nanorods is higher than that for the control sample [43, 133]. Thickness of the superconducting thin film in this experiment is comparable to the diameter of the Ni nanorods, and where the stray field has a significant parallel component. No field compensation effect can be expected in this case. R-H curves in Figure 117 (b) exhibit the same sign of the hysteresis as those for samples 1 and 3 in Ref. [42], where the diameter of the magnetic nanorods is close to the thickness of the superconducting film. Magnetic nanorods create a highly inhomogeneous internal fields inside the superconducting film. Using data for the magnetic field on the surface of the cross-section of a Ni nanorod [146], i.e. 0.3 T, the estimated flux from a single 200 nm diameter nanorod is of the order of five flux quanta. However, the actual magnetic field at the magnetic nanorod's surface can be several times smaller than that due to the shape anisotropy and due to a value of magnetization smaller than the saturation magnetization. In addition, not all flux generated by a nanorod penetrates normal to the superconducting film. As a result, the average field penetrating through the superconducting film can be an order of magnitude smaller than the ideal value 0.3 T. This estimation fits the experimental value of the hysteresis width in the *R*-*H* curve Figure 118 (a) and the width of the hysteresis in the I_C data in Figure 118 (b) reasonably well.

An electrochemically grown array of magnetic Ni nanorods on a superconducting film exhibits interesting properties that were observed for the first time with magnetic nanostructures placed outside the superconducting film. But also, several similarities with hybrid systems with magnetic nanowires in an alumina template [42, 143, 151] (hysteresis) and with nanorods embedded in the superconducting film [43, 133] (I_C dependence on magnetic fields) were observed. A change of the hysteresis sign is expected by decreasing Sn and $Pb_{82}Bi_{18}$ films' thickness from 100 nm to 30 nm.